MODELLING TROPOSPHERIC GRADIENTS AND PARAMETERS FROM NWP MODELS: EFFECTS ON GPS ESTIMATES

REZA GHODDOUSI-FARD

February 2009

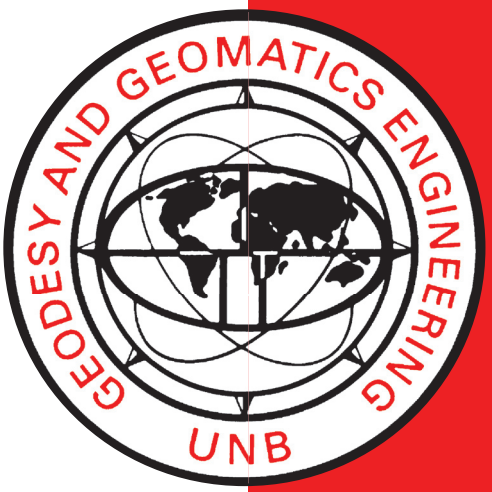

TECHNICAL REPORT
NO. 264

MODELLING TROPOSPHERIC GRADIENTS AND PARAMETERS FROM NWP MODELS: EFFECTS ON GPS ESTIMATES

Reza Ghoddousi-Fard

Department of Geodesy and Geomatics Engineering
University of New Brunswick
P.O. Box 4400
Fredericton, N.B.
Canada
E3B 5A3

February 2009

PREFACE

This technical report is a reproduction of a dissertation submitted in partial fulfillment of the requirements for the degree of Doctor of Philosophy in the Department of Geodesy and Geomatics Engineering, February 2009. The research was supervised by Dr. Peter Dare, and funding was provided by the Natural Sciences and Engineering Research Council of Canada, the Canada Foundation for Innovation, the New Brunswick Innovation Foundation, Northern Scientific Training Program of Indian and Northern Affairs Canada, and the Royal Institution of Chartered Surveyors Education Trust.

As with any copyrighted material, permission to reprint or quote extensively from this report must be received from the author. The citation to this work should appear as follows:

Ghoddousi-Fard, Reza (2009). *Modelling Tropospheric Gradients and Parameters from NWP Models: Effects on GPS Estimates*. Ph.D. dissertation, Department of Geodesy and Geomatics Engineering, Technical Report No. 264, University of New Brunswick, Fredericton, New Brunswick, Canada, 216 pp.

ABSTRACT

The neutral atmosphere delay still remains one of the most limiting accuracy factors in global navigation satellite systems (GNSS) and other radiometric space-geodesy techniques. Due to the fact that the neutral atmosphere is a non-dispersive medium, the use of dual frequency approaches cannot eliminate the effect of neutral atmosphere delay at radio frequencies.

In recent years the use of numerical weather prediction (NWP) models has been investigated to mitigate the neutral atmosphere delay on GNSS signals. However, due to the practical issues NWP-based approaches have not yet been widely used by GNSS users. A spherically symmetric atmosphere has been a common assumption in GNSS processing for a long time. As NWP models provide the 3-D state of the neutral atmosphere, the motivation has been raised to consider the asymmetry of the neutral atmosphere in GNSS processing.

In this dissertation recent developments in NWP-based modeling of neutral atmosphere delay are reviewed and compared. As an example of an NWP-for-GNSS operational service an online ray tracing package has been developed which has been accessible to the public for the past 2 years. Routine 3-hourly global maps of zenith delay, gradients and comparison with climate-based models have been also generated.

Asymmetry of the hydrostatic part of the neutral atmosphere has been modeled based on a dual radiosonde ray tracing approach developed for part of North America. An approach based on a semi-3-D retrieval of delays from NWP models also has been developed. The NWP-based parameters including zenith delays, mapping functions and gradients have been implemented in the Bernese GPS software. This made the software capable of correcting pseudorange observables in all related processing options.

Modified software has been employed to study the effect of the implemented NWP-based processing on GPS estimated parameters. The result of a month-long precise point positioning experiment shows millimetre-level improvement in the latitude component at most of the stations when hydrostatic gradients are introduced as a priori. Height and zenith tropospheric delay parameters are also affected by implementing NWP-based gradients as well as by implementing zenith delay values and mapping functions even though the effects were not found to be systematic.

Based on the results of this dissertation research, implementing NWP-based parameters in GPS processing for high accuracy applications such as geodynamics, realization of terrestrial reference frames, and climatology are suggested. This is now possible with the modified Bernese software which is capable of considering NWP hydrostatic, non-hydrostatic and total gradients as a priori in GPS observables as well as zenith delay and mapping functions based on NWP models in all processing strategies.

ACKNOWLEDGEMENTS

I would like to thank my supervisor Dr. Peter Dare for his support, patience and opportunities throughout my PhD studies. I would also like to thank Dr. Richard Langley for his comments during weekly GPS group meetings. Thanks also go to Dr. Don Kim and other members of the examination committee: Dr. William Ward from UNB's Department of Physics and Dr. Johannes Boehm from Institute of Geodesy and Geophysics at the Vienna University of Technology, Austria.

The financial support from Canada's Natural Sciences and Engineering Research Council, Canada Foundation for Innovation, the New Brunswick Innovation Foundation, Northern Scientific Training Program of Indian and Northern Affairs Canada, and the Royal Institution of Chartered Surveyors Education Trust are acknowledged.

The Chair and staff at UNB's Ocean Mapping Group are thanked for providing support during my data collection exercise onboard the Canadian research icebreaker Amundsen during her 2005 Canadian Arctic and Hudson Bay expedition. Environment Canada's Meteorological Service of Canada, and its Canadian Meteorological Centre, the U.S. National Oceanic and Atmospheric Administration, and the International GNSS Service are thanked for providing data access. I also thank the Atlantic Computational Excellence Network for providing computing resources.

Thanks also go to office staff of the Department of Geodesy and Geomatics Engineering and UNB's Integrated Technology Services for their support. I would like to express my thanks to all fellow graduate students in the Geodetic Research Laboratory for their friendship.

Finally, I wish to thank my parents for their endless support during my life. This work is dedicated to them.

Table of Contents

List of Tables

List of Figures

List of Abbreviations

CCGS ……Canadian Coast Guard Ship

CMC……..Canadian Meteorological Centre

DoY……Day of Year

EW…….East-West

ECDF……..Empirical Cumulative Distribution Function

ECMWF…….European Centre for Medium-range Weather Forecasts

GDAS……...Global Data Assimilation System

GEM…….Global Environmental Multiscale

GMF……Global Mapping Functions

GNSS……...Global Navigation Satellite Systems

GPT……..Global Pressure and Temperature

GRIB……...GRidded BInary

IGS……International GNSS Service

IMF……...Isobaric Mapping Functions

MSL…….Mean Sea Level

NMF……..……Niell Mapping Functions

NS……..North-South

NWP……..Numerical Weather Prediction

PPP…….Precise Point Positioning

RAOB……...RAdiosonde OBservation

RUC……...Rapid Update Cycle

SD……Slant Delay

VLBI……..…Very Long Baseline Interferometry

VMF……...…Vienna Mapping Functions

WVR……Water Vapour Radiometer

WMO……World Meteorological Organization

ZHD……...Zenith Hydrostatic Delay

ZWD…….Zenith non-hydrostatic (Wet) Delay

ZTD……Zenith Tropospheric Delay

Chapter 1: Introduction

1.1- Background and Motivation

Radiometric space geodesy systems such as Global Navigation Satellite Systems (GNSS) and Very Long Baseline Interferometry (VLBI) are affected by the Earth's atmosphere. Due to the different physical characteristics, the atmospheric effects are studied based on two separate parts: the electrically charged ionosphere and the neutral atmosphere. The ionosphere is a dispersive medium at radio frequencies and hence its effect is dependent on the frequency of the signal. This means that by using dual-frequency radiometric techniques the ionospheric effect can be almost fully eliminated. The neutral atmosphere, however, is a non-dispersive medium. Hence the effect of the neutral atmosphere on radiometric signals is frequency independent. This makes dealing with the neutral atmosphere more problematic as it is not possible to eliminate its effect using dual-frequency techniques.

While neutral atmospheric delay in GNSS analysis is a nuisance parameter for positioning and navigation applications, it is a valuable parameter for meteorological applications. However, even if the neutral atmosphere is being treated as a valuable parameter to be used for meteorological or climate studies, it is still necessary to have a priori information on the neutral atmosphere in order to have accurate estimates of the desired parameters. While meteorological data or empirical models are crucial for dealing

with the neutral atmosphere in radiometric space techniques including GNSS, these techniques themselves are becoming a valuable source of data for the meteorology community including weather prediction models. Furthermore, the availability of long term continuous GNSS measurements, at a large number of locations, makes them a valuable source of information for climate studies as well.

The propagation delay due to the neutral atmosphere has two components: the *hydrostatic* component mainly due to dry gases and the *non-hydrostatic* component due to water vapour. The hydrostatic component in the zenith direction is usually predictable to high accuracy if accurate surface pressure is available. The non-hydrostatic component is highly variable both temporally and spatially and cannot be accurately predicted with surface measurements. The problem gets more challenging as signals with different azimuths and elevation angles received by GNSS receivers are affected by a different amount by the neutral atmosphere. Due to the fact that each signal passing through the neutral atmosphere includes an "unknown" amount of delay, it is virtually impossible to estimate delays in all received signals together with desired parameters (e.g. receiver coordinates) due to lack of redundancy. Hence, one should consider some assumptions or external information to overcome this lack of redundancy in the estimation process.

A "known" mapping function is usually used to map the neutral atmosphere delay from any direction to the zenith. While this reduces several unknown delays at each epoch to only one unknown delay parameter in the zenith direction, some uncertainties result from

the assumptions made by introducing the mapping function concept. Commonly used mapping functions are dependent on elevation angle and some location-based parameters. The main assumption in this type of mapping function is the symmetry of the neutral atmosphere. This assumption can be violated in situations involving the passage of weather fronts, for example. Furthermore, as the thickness of the atmosphere decreases toward the poles, the neutral atmosphere may show an average systematic asymmetry in the north-south (NS) direction. Such a systematic behaviour may affect the estimated parameters systematically, and hence degrade the subsequent interpretation of results.

Due to its high variability with location and time, real-time and accurate knowledge of the neutral atmosphere is necessary if high accuracy GNSS results are desired. RAdiosonde OBservation (RAOB) is still an important source of data for neutral atmosphere studies as it provides direct measurement of parameters which can impact the neutral atmospheric delays. Furthermore, GNSS researchers have taken advantage of numerical weather prediction (NWP) models for neutral atmosphere delay mitigation. NWP models provide the 3-D state of the lower part of the neutral atmosphere at virtually any location and time. Currently, operational NWP centres produce initial conditions through a statistical combination of observation and short-range forecasts. This approach has become known as “data assimilation” and involves the optimal use of all the available information to determine as accurately as possible the state of the atmospheric (or oceanic) flow [Kalnay, 2003].

There are several NWP model approaches, all with the ultimate aim of improving the numerical model that is used to forecast the weather. These models, developed by national weather offices, may cover a region or the entire world. Among the models that have been used by the GNSS research community are the Canadian Global Environmental Multiscale (GEM) models, the European Centre for Medium-range Weather Forecasts (ECMWF) models and the US Rapid Update Cycle (RUC) models, to name a few.

Schüler [2001] used an NWP model with $1^{\circ} \times 1^{\circ}$ resolution (111 km at the equator) and 26 vertical pressure layers to derive neutral atmospheric delays. The NWP data were validated with a few GPS stations that also had precise meteorological sensors. Jupp et al. [2003] investigated the spatial and temporal properties of meteorological features on GPS neutral atmospheric delay. They used the UK Met Office's global NWP model (~60 km resolution at mid-latitudes and ~90 km in the tropics) as well as a UK area mesoscale model (~12 km resolution). They found that the NWP model could reflect accurately the progression of weather fronts across the UK. Cucurull et al. [2002] studied the application of NWP models in a short time series analysis of GPS observables. They applied their approach to GPS data gathered at permanent stations in the UK. Pany [2002] calculated slant delays from the NWP model of the ECMWF. Compared to GPS-derived values, he found 10-20 mm agreement (RMS value) in the zenith non-hydrostatic (wet) delay (ZWD) and 1-2 mm in zenith hydrostatic delay (ZHD). Jensen [2002] did some initial verification of zenith delays based on a regional NWP model and suggested

the implementation of a ray tracer for low elevation angle signals. Seko et al. [2003] evaluated the GPS positioning error due to the inhomogeneous distribution of atmospheric delay using a NWP model data in Japan. Their study was performed using simulated fields rather than observed data. de Haan and van der Marel [2004] studied the influence of the NWP slant delays on simulated GPS estimates at a single GPS site in The Netherlands. They focused on a cold front passage effect and showed that the differences between the Niell [1996] mapping functions, the NWP model and radiosonde mapping functions influence the estimated zenith tropospheric delay (ZTD), clock error and height. It was concluded that the use of Niell mapping functions could introduce systematic errors in the estimated geodetic parameters, including ZTD which is used for meteorological applications. Niell [2000, 2003] and Boehm et al. [2006] have developed mapping functions partly based on NWP models to tune the mapping function based on the real-time state of the atmosphere.

Even though during the past few years NWP models have been used for deriving zenith delay values or mapping functions by researchers, there are some practical issues such as storage requirement, calculation time, accuracy of models, etc, that may make using NWP models impractical for public GPS users. Assuming the NWP models are the best available estimate of the state of the atmosphere, the ultimate benefit of an NWP model for GNSS neutral atmosphere modeling may be expected through ray tracing the entire paths of the signals to the GNSS satellites at every observation epoch. However, despite computational costs (computational time and resources), the introduction of 3-D ray

tracing has not shown a significant improvement in the precision of estimated parameters (see e.g. Hobiger et. al [2008]) - hence it may not be worthwhile to carry out such calculations. Nevertheless, algorithms and approaches partly based on NWP models seem to be practically feasible.

During the past two decades a large amount of work has focussed on zenith delay modelling and mapping functions, and there have been fewer studies on the effect of atmospheric gradients on estimates derived from GNSS observations. Furthermore, many of the past work in this area was research oriented i.e. they may not be feasible or practical for the user community. Chen and Herring [1997] studied gradients using 3-D ray tracing through a low resolution NWP model and detected common mean NS gradients at mid-latitudes. They also developed methods for estimation of gradients from VLBI analysis. Bar-Sever et al. [1998] showed that the inclusion of estimates of gradients in GPS processing improves the accuracy and precision of the estimated quantities. Ifadis and Savvaidis [2001] used 5 radiosonde sites to study the horizontal variations of the atmosphere. However, they were unable to model the delay variation in their case study. Niell [2001] proposed the use of NWP models for asymmetric mapping functions. Iwabuchi et al. [2003] reported that the differences between estimated ZTD in precise point positioning (PPP) with and without gradient estimation were correlated with the NS components of the estimated gradients. Also, in a simulated study, they concluded that a NS horizontal gradient of 1 mm (see Chapter 5 for a discussion on gradient units) gave

rise to negative ZTD biases of about 1 mm. Boehm and Schuh [2007] used a 3-profile approach to calculate the gradients from the ECMWF model for VLBI analysis.

One of the objectives of this dissertation research is studying and comparing recent developments in NWP-assisted GNSS processing and further development of optimized algorithms for considering atmospheric gradients and NWP-based mapping functions in the GNSS processing. In addition, the effect of these developments on individual GPS estimated parameters has been quantified. In other words, a main question to be answered was: How much change in the GPS estimated parameters might one expect from implementation of NWP data?

Canadian regional and global NWP models have been used extensively in this research both for several case studies and also for the development of continuous automatic processing routines. Comparison of neutral atmospheric delays calculated from these models with independent observations is one way to validate the accuracy of these models for GNSS applications. In this research, Canadian NWP models have been validated at several locations including the data-sparse regions of the Canadian Arctic.

As a part of the research of this dissertation, an online ray tracing package has been developed capable of using RAOB and NWP models as well as producing near-real-time global maps of zenith delay, gradients and comparisons with climate-based models. The

online package is an example of what an NWP-for-GNSS operational service could provide the GNSS community – it has been accessible to the public for the past 2 years.

The possibility of using RAOB for statistical modeling of neutral atmospheric gradients over a region has been investigated by deriving a regional hydrostatic gradient model using non-linear least-squares fits to semi-3D ray tracing results. For investigating day-to-day variations an algorithm has been developed to retrieve gradients from Canadian NWP models. All NWP products, including zenith delays, NWP-based mapping functions and gradients are implemented in the well-known Bernese software. This made the software capable of using NWP data as an a priori neutral atmospheric delay in all processing strategies. The effect of NWP-derived parameters on GPS estimated parameters was investigated using GPS data sets at a number of stations.

1.2- Dissertation Contribution

The main contributions of this dissertation can be summarized as follows:

- Review and comparison of recent mapping functions based on NWP models.

- Review and discussion of asymmetric mapping functions.

- Validation of NWP neutral atmospheric products with an independent approach using observations at different locations.

- Development of an online ray tracing package capable of using RAOB and NWP models which also produces near-real-time global maps of zenith delays, gradients and comparisons with climate-based models as an example of an operational service.

- A study of the asymmetry of the neutral atmosphere over most of North America using a dual radiosonde ray tracing approach. An averaged hydrostatic gradient model was derived, based on a created database of two sets of 4,244,695 slant delays from 71 radiosonde sites over one year.

- Development of an algorithm for the calculation of horizontal delay gradients from NWP models.

- Implementation of zenith delay, mapping functions and gradients from NWP models in scientific GNSS software.

- Quantification of the effect of implemented parameters using a month-long GPS dataset, processed at a number of stations under different a priori neutral atmospheric scenarios.

1.3- Dissertation outline

In Chapter 1 (current chapter) the dissertation topic is introduced. The most significant contributions and developments to date are briefly reviewed. The direction that is followed in the research is outlined in this chapter.

Chapter 2 reviews the theoretical aspects of the neutral atmosphere with emphasis on its effect on GNSS signals. Some of the past zenith delay models and mapping functions are briefly reviewed as well.

In Chapter 3 recent mapping functions based on NWP models are reviewed and compared with each other. Commonly used asymmetric mapping functions are also discussed.

In Chapter 4 the ray tracing algorithms used in this dissertation are reviewed. The practical use of ray tracing in space geodesy techniques is presented by introducing a web-based ray tracing package as an example of an operational service.

Chapter 5 includes the modeling of gradients in a statistical sense using a dual radiosonde ray tracing approach and the development of an algorithm to retrieve gradients from NWP models. Studying temporal behaviour of gradients using an NWP model is detailed;

discussion of GPS-estimated gradients and the effect of estimation interval size are also addressed in this chapter.

Implementing the NWP-based parameters in Bernese GNSS software and investigating the effects of these parameters on GPS estimates are the main parts of Chapter 6.

Conclusions based on the research documented in this dissertation as well as recommendations are given in Chapter 7.

Chapter 2: Effect of the Neutral Atmosphere on GNSS Signals

The delay induced by the neutral part of the atmosphere on GNSS signals still remains one of the most important accuracy limiting factors in high precision positioning applications. In this chapter theoretical aspects of the neutral atmosphere delay are reviewed. Basic GNSS observables with emphasis on the neutral atmospheric term will be discussed. Current zenith delay models and older mapping functions will be briefly reviewed.

2.1- The Neutral Atmosphere

The lower part of the Earth's atmosphere affects the propagation of electromagnetic signals due to the presence of neutral atoms and molecules. This part (henceforth called the neutral atmosphere) is illustrated in Figure 2.1. When GNSS signals pass through the neutral atmosphere, they are affected by the variability of the refractive index of this region. Refractive index is the ratio of the speed of light in vacuum to the phase velocity in the atmosphere, usually represented by n. However due to the fact that n is just slightly larger than 1 the more convenient quantity (namely refractivity) is defined as $N = 10^6(n-1)$. The refractive index is greater than unity and, therefore, it causes an excess path delay and bending of the ray (which is significant for signals coming from low elevation angles; at a 5 degree elevation angle it can be more than 20 cm while for

elevation angles above 15 degrees it is usually below 1 cm). The combination of path delay and ray bending is called neutral atmosphere delay; this can be expressed as:

$$d_{na} = 10^{-6} \int_{ray} N ds + \left[\int_{ray} ds - \int_{vac} ds \right] \tag{2.1}$$

where d_{na} is the slant delay due to the neutral atmosphere,

N is the refractivity,

ds is differential increment in slant distance,

ray is the path of the signal through the neutral atmosphere, and

vac is the virtual path of the signal through vacuum.

The formula for the total refractivity of moist air was given by Thayer [1974] as follow:

$$N = k_1 \frac{p_d}{T} Z_d^{-1} + k_2 \frac{p_{wv}}{T} Z_{wv}^{-1} + k_3 \frac{p_{wv}}{T^2} Z_{wv}^{-1} \tag{2.2}$$

where p_d is the partial pressure of dry air (hPa),

p_{wv} is the partial pressure of water vapour (hPa),

T is absolute temperature (K),

Z_d and Z_{wv} are the compressibility factors of dry air and water vapour respectively, and

k_1, k_2 and k_3 are empirically determined constants.

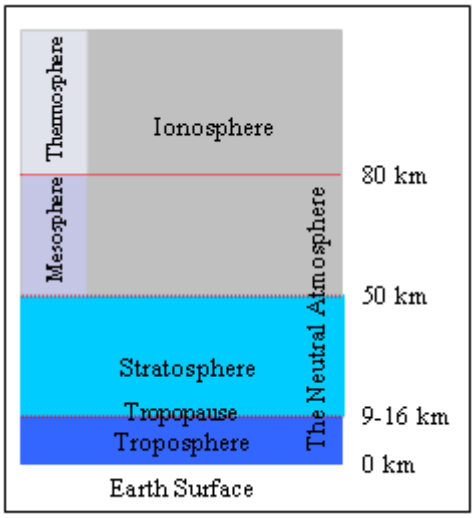

Figure 2.1- The Earth's atmospheric layers and the neutral atmosphere (after Langley [1998, p. 126]).

Davis et al. [1985] derived an alternative formula as follows:

$$N = k_1 R_d \rho + k_2' \frac{p_{wv}}{T} Z_{wv}^{-1} + k_3 \frac{p_{wv}}{T^2} Z_{wv}^{-1} \tag{2.3}$$

where ρ is the total mass density and

$$k_2' = k_2 - k_1 \frac{R_d}{R_{wv}} \tag{2.4}$$

where R_d and R_{wv} are the specific gas constants for dry air and water vapour respectively.

Unlike equation (2.2), the first term in equation (2.3) is no longer a pure dry component as the total mass density contains the contribution of water vapour. Hence the first term in equation (2.3) is referred to as hydrostatic component as opposed to dry. The rest of the terms in equation (2.3) are referred to as the non-hydrostatic (or wet) component.

Various researchers have determined values for the k_1, k_2 and k_3 constants. Bevis et al. [1994] compared constant values determined by different authors, and determined new constant values as well. Those determined by Bevis et al. [1994], which have been adopted for related calculations in this dissertation are:

$$k_1 = 77.60 \pm 0.05 \quad K\,hPa^{-1} \tag{2.4.a}$$

$$k_2 = 70.4 \pm 2.2 \quad K\,hPa^{-1} \tag{2.4.b}$$

$$k_3 = 3.739 \pm 0.012 \quad 10^5 K^2 hPa^{-1} \tag{2.4.c}$$

$$k_2' = 22.1 \pm 2.2 \quad K\,hPa^{-1} \tag{2.4.d}$$

Figures 2.2 shows, as an example, hydrostatic and non-hydrostatic refractivities calculated based on equation (2.3) from RAOB data. The exponential decay of hydrostatic refractivity as seen in Figure 2.2.a is a result of hydrostatic equilibrium which is the state of the atmosphere in normal conditions[1]. This is the key point in the fact that zenith hydrostatic delay is accurately predictable with only surface pressure measurements. Also one should note the horizontal scale difference between Figures 2.2.a and 2.2.b. The hydrostatic refractivity at the surface of the Earth is usually about one order of magnitude larger than the non-hydrostatic one. Furthermore, as can be seen in Figures 2.2, non-hydrostatic refractivity usually becomes ignorable at altitudes higher

[1] In the atmosphere vertical pressure gradient is usually in balance with gravity. However during strong vertical winds, which usually occur in and near thunderstorms, the balance between the gravitational and the vertical pressure gradient forces can be disrupted [Ackerman and Knox, 2007].

than about 10-15 km, far below the contribution of the atmosphere to the hydrostatic refractivity.

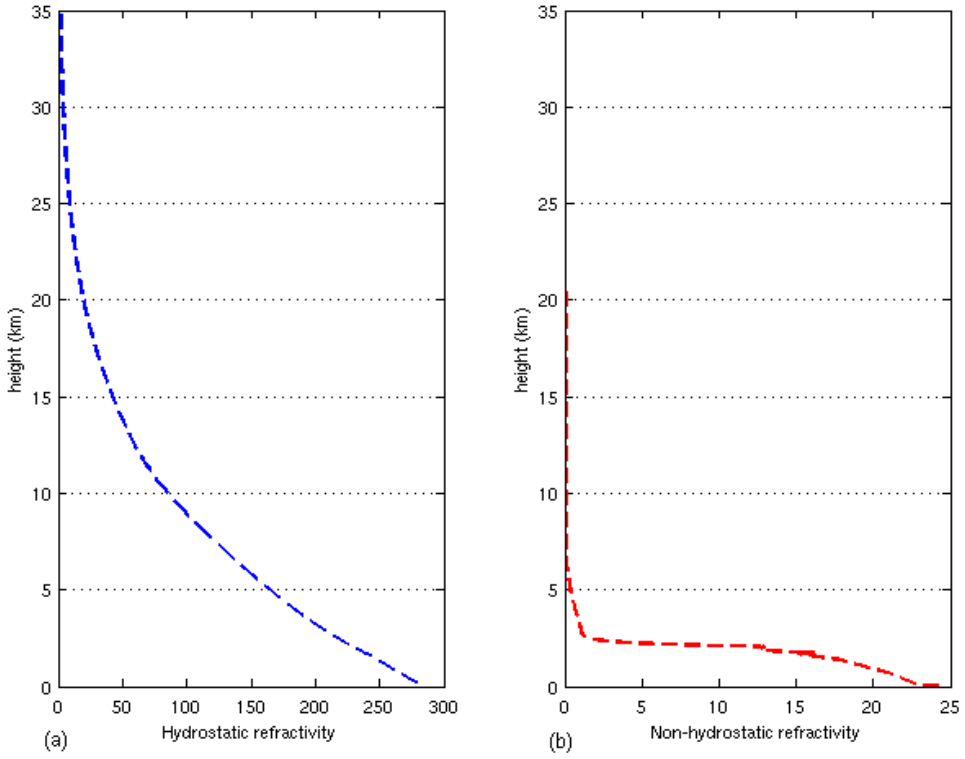

Figure 2.2- Refractivity calculated from RAOB at Churchill, MB, Canada, at 0 UTC, DoY 155, 2007. a) Hydrostatic. b) Non-hydrostatic.

Inverse compressibility factors can be determined by formulae originally given by Owens [1967]. These formulae as rearranged by Thayer [1974] are as follows:

$$Z_d^{-1} = 1 + p_d \cdot [57.90 \cdot 10^{-8} (1 + \frac{0.52}{T}) - 9.4611 \cdot 10^{-4} \cdot \frac{t}{T^2}] \tag{2.5}$$

$$Z_{wv}^{-1} = 1 + 1650 \cdot (\frac{p_{wv}}{T^3}) \cdot (1 - 0.01317 \cdot t + 1.75 \cdot 10^{-4} \cdot t^2 + 1.44 \cdot 10^{-6} \cdot t^3) \tag{2.6}$$

where t is the temperature in degree Celsius, p_d and p_{wv} are in hPa, and T is in kelvins.

Inverse compressibility factors calculated from RAOB at Churchill at 0 UTC, DoY 155, 2007 are plotted in Figures 2.3 as examples. As can be seen in Figure 2.3 the inverse compressibility factors are very close to 1. The effect of inverse compressibility factors in the zenith delay calculations is about 0.1-0.2 mm [Mendes, 1999] and may only affect non-hydrostatic refractivity (see equation (2.3)). Hence, for most applications, they may be safely ignored.

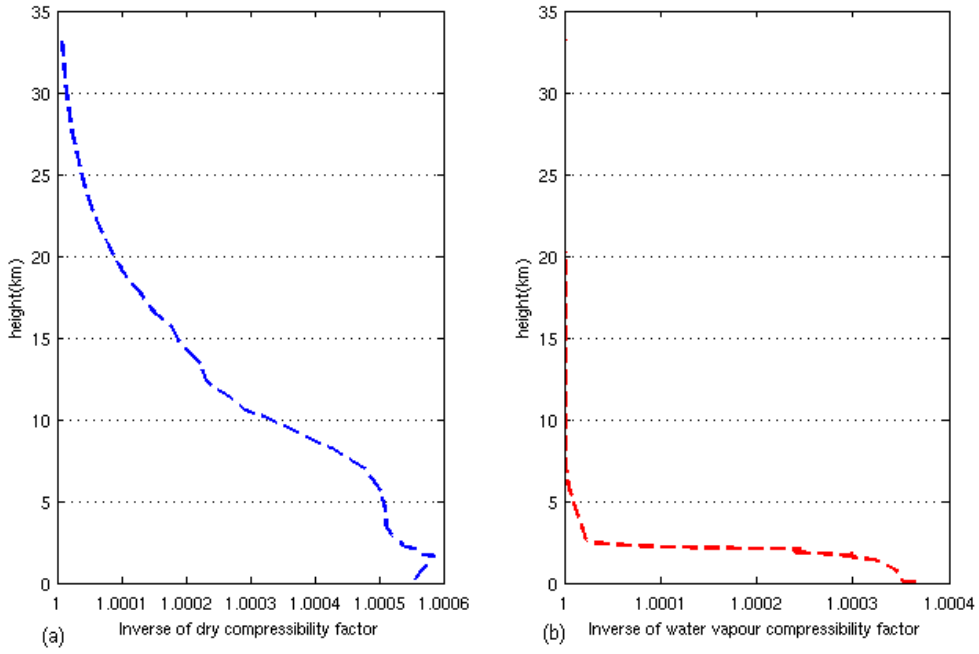

Figure 2.3- Inverse compressibility factors calculated from RAOB at Churchill, MB, Canada, at 0 UTC, DoY 155, 2007. a) Dry b) Water vapour

Direct calculation of the neutral atmospheric delay requires solving integrations in equation (2.1). In practice numerical integration approaches are used rather than analytic. Numerical integration of path delay (namely ray tracing) will be discussed in Chapter 4.

2.2- Neutral Atmospheric Delay in GNSS Observables

Following Leick [2004] code pseudorange and carrier phase observables can be written in terms of length as follows:

$$P_{i,r}^{s}(t_r) = \rho_r^s(\hat{t}^s) + c(d\bar{t}^s - d\underline{t}_r) + I_{i,r,P}^{s}(t_r) + T_r^s(t_r) + \delta_{i,r,P}^{s}(t_r) + \varepsilon_{i,P} \quad (2.7)$$

$$\phi_{i,r}^{s}(t_r) = \rho_r^s(\hat{t}^s) + \lambda_i N_{i,r}^{s} + c(d\bar{t}^s - d\underline{t}_r) + \lambda_i I_{i,r,\varphi}^{s}(t_r) + T_r^s(t_r) + \lambda_i \delta_{i,r,\varphi}^{s}(t_r) + \lambda_i \varepsilon_{i,\varphi} \quad (2.8)$$

where:

- subscript i identifies the frequency (f_1 or f_2) with wavelength λ_i, r and s indicate receiver and satellite respectively, c is velocity of light, N is carrier phase ambiguity and
- t_r is the nominal time, i.e., the receiver clock reading which is in error by $d\underline{t}_r$;
- $\rho_r^s(\hat{t}^s)$ is the geometric vacuum distance between satellite s and receiver r at true time of transmission of $\hat{t}^s$ (which is in error by $d\bar{t}^s$);
- $I_{i,r,P}^{s}$ and $I_{i,r,\varphi}^{s}$ are ionospheric code delay and ionospheric carrier phase advance respectively which are a function of frequency (i) and ionospheric condition along the path;
- T_r^s is the neutral atmospheric delay which is independent of the frequency;

- $\delta^s_{i,r,P}$ and $\delta^s_{i,r,\varphi}$ are hardware delays and multipath effects in code and carrier phase respectively;
- $\varepsilon_{i,P}$ and $\varepsilon_{i,\varphi}$ are code and carrier phase measurement noise respectively.

Several linear combinations can be made from code and/or carrier phase observables. Each may be eligible for a specific application or processing scenario. Common linear combinations that have been employed in GNSS software (e.g. Bernese) include: ionosphere-free, geometry-free, wide-lane and Melbourne-Wübbena. Among these, the ionosphere-free linear combination is the most popular one in many processing strategies including PPP and double differencing. Since the ionospheric code delay and carrier phase advance are frequency dependent, it is possible to eliminate the ionospheric effects using dual-frequency observations with this linear combination. The ionosphere-free linear combination for code and phase can be written as follows:

$$P^s_{IF,r}(t_r) = \frac{1}{f_1^2 - f_2^2}(f_1^2 P^s_{1,r}(t_r) - f_2^2 P^s_{2,r}(t_r)) = \\ \rho^s_r(\hat{t}^s) + c(d\bar{t}^s - d\underline{t}_r) + T^s_r(t_r) + \delta^s_{IF,r,P}(t_r) + \varepsilon_{IF,P} \tag{2.9}$$

$$\phi^s_{IF,r}(t_r) = \frac{1}{f_1^2 - f_2^2}(f_1^2 \phi^s_{1,r}(t_r) - f_2^2 \phi^s_{2,r}(t_r)) = \\ \rho^s_r(\hat{t}^s) + \frac{cf_1}{f_1^2 - f_2^2} N^s_{1,r} - \frac{cf_2}{f_1^2 - f_2^2} N^s_{2,r} + c(d\bar{t}^s - d\underline{t}_r) + T^s_r(t_r) + \lambda_i \delta^s_{IF,r,\varphi} + \lambda_i \varepsilon_{IF,\varphi} \tag{2.10}$$

where the subscript *IF* denotes the ionosphere-free linear combination. One can see that ionospheric terms have been eliminated on the right-hand side of the equations (2.9) and (2.10). However, the neutral atmosphere delay remains unchanged as a result of this

combination. The neutral atmosphere delay can be separated into hydrostatic and non-hydrostatic parts. Distinguishing between the azimuthally symmetric and asymmetric parts, the neutral atmosphere delay in full detail can be given by the following expression:

$$\begin{aligned} &T_r^s(t_r,\varepsilon_r^s,az_r^s) = ZHD_{t_r}\cdot mfh_{t_r}(\varepsilon_r^s) + ZWD_{t_r}\cdot mfnh_{t_r}(\varepsilon_r^s) + \\ &mfGh(\varepsilon_r^s)\cdot(Gh_{ns_{t_r}}\cdot\cos(az_r^s) + Gh_{ew_{t_r}}\cdot\sin(az_r^s)) + \\ &mfGnh(\varepsilon_r^s)\cdot(Gnh_{ns_{t_r}}\cdot\cos(az_r^s) + Gnh_{ew_{t_r}}\cdot\sin(az_r^s)) \end{aligned} \tag{2.11}$$

where:

- $T_r^s(t_r,\varepsilon_r^s,az_r^s)$ is the total slant neutral atmosphere delay of the incoming signal from satellite s to receiver r at epoch t_r with elevation angle ε_r^s and azimuth az_r^s;
- ZHD_{t_r} and ZWD_{t_r} are ZHD and ZWD respectively at epoch t_r;
- $mfh_{t_r}(\varepsilon_r^s)$ and $mfnh_{t_r}(\varepsilon_r^s)$ are hydrostatic and non-hydrostatic symmetric mapping functions respectively at epoch t_r and elevation angle ε_r^s;
- $mfGh(\varepsilon_r^s)$ is the hydrostatic gradient mapping function at elevation angle ε_r^s;
- $mfGnh(\varepsilon_r^s)$ is the non-hydrostatic gradient mapping function at elevation angle ε_r^s;
- $Gh_{ns_{t_r}}$ and $Gh_{ew_{t_r}}$ are NS and EW hydrostatic horizontal gradients at epoch t_r; and
- $Gnh_{ns_{t_r}}$ and $Gnh_{ew_{t_r}}$ are NS and EW non-hydrostatic horizontal gradients at epoch t_r.

For high precision applications and when low elevation angle measurements are used, the estimation of gradients has been suggested (see e.g. Meindl et al. [2004], Emardson and Jarlemark [1999], Bar-Sever et al. [1998] and Chen and Herring [1997]). Equation (2.11) includes separated hydrostatic and non-hydrostatic gradient components. These probably can not be estimated separately in the parameter estimation process [Chen and Herring, 1997] due to the increased number of unknown parameters. Hence a more practical expression for the neutral atmospheric delay in GNSS signal observables is given by:

$$T_r^s(t_r, \varepsilon_r^s, az_r^s) = ZHD_{t_r} \cdot mfh_{t_r}(\varepsilon_r^s) + ZWD_{t_r} \cdot mfnh_{t_r}(\varepsilon_r^s) + mfG(\varepsilon_r^s) \cdot (G_{ns_{t_r}} \cdot \cos(az_r^s) + G_{ew_{t_r}} \cdot \sin(az_r^s)) \quad (2.12)$$

where $mfG(\varepsilon_r^s)$ is the total gradient mapping function and $G_{ns_{t_r}}$ and $G_{ew_{t_r}}$ are the total NS and EW horizontal gradients respectively at epoch t_r .

2.3- Neutral Atmospheric Models and Mapping Functions

Over the last few decades, several neutral atmospheric models have been developed to provide a priori values for zenith hydrostatic and non-hydrostatic delays as well as several mapping functions. The performance of models and mapping functions (which have been derived based on a standard atmosphere) degrades when the weather conditions differ significantly from normal climatic conditions. A brief review of some of the models is provided in the following sections. For a comprehensive comparison of the models available up to the last decade, one can refer to Mendes [1999].

2.3.1- Zenith Hydrostatic (and Dry) Delay Models

Hopfield [1969] derived a dry delay model based on a refractivity model. Saastamoinen [1972a, 1972b, 1973] and Baby et al. [1988] developed hydrostatic delay models based upon a theoretical definition of hydrostatic delay and a hydrostatic equilibrium assumption. Later, Davis et al. [1985] slightly improved the Saastamoinen model. These hydrostatic delay models differ due to the choice of the refractivity constant and on the modelling of the height and latitude dependence of gravity acceleration [Mendes, 1999] but all follow the same theoretical procedures. Mendes [1999] concluded that zenith hydrostatic delay can be predicted from surface pressure measurements with a total error below 5 mm and concluded that of the mentioned models, the Saastamoinen model performance is far better than the other hydrostatic models. This conclusion was based on the fact that predictions obtained with this model agreed with his ray tracing results at the sub-millimetre level whereas the other models agreed at the millimetre level.

2.3.2- Zenith Non-Hydrostatic (and Wet) Delay Models

Due to the difficulty of modelling the water vapour profile, there are more models for the zenith non-hydrostatic and wet delay than for the hydrostatic delay. Mendes [1999] compared a number of these models and concluded that the Ifadis [1986] and Saatamoinen [1972a, 1972b, 1973] models have better performance. However, it was mentioned that these models are highly correlated. It was also mentioned that the zenith

non-hydrostatic delay cannot be predicted using surface meteorological values to an accuracy of better than a few centimetres.

2.3.3- Mapping Functions

A large number of mapping functions have been developed. These are either total mapping functions or purely hydrostatic and non-hydrostatic functions. Recent mapping functions are usually based on the truncated form of a continued fraction. Mendes [1999] carried out a comprehensive comparison among the mapping functions developed up to 1996 and concluded that Ifadis [1986], MTT [Herring, 1992] and Niell [1996] hydrostatic and non-hydrostatic mapping functions perform best. In general, the Niell mapping function (which is independent of meteorological measurements) was recommended. This mapping function has been widely used in GPS software. However, studies by Niell and Petrov [2003] indicate that use of the hydrostatic Niell mapping function for elevation angles below 10 degrees significantly increases the height uncertainty. Guo and Langley [2003] developed a mapping function for elevation angles down to 2 degrees (namely UNBabc) and recommended it for a GNSS receiver built-in mapping function due to its simplicity with respect to Niell mapping functions.

In order to overcome some of the detected biases due to missmodelling of the meteorological parameters and also the fact that mapping functions like Niell are not based on real-time parameters, some recent mapping functions use information from

NWP models. In Chapter 3 new symmetric mapping functions based on NWP models as well as gradient mapping functions are explained and compared.

2.3.4- Modeling the Meteorological Parameters

Most of the zenith delay models and some mapping functions need measurements of surface meteorological parameters. However, most users do not have access to such data. Due to this fact a number of studies have been carried out on the subject of modelling the meteorological parameters.

Collins [1999] developed a number of tropospheric models for aircraft users of GPS. Among those, the UNB3 model has been widely used for many GPS applications. The UNB3 model is the basis for the RTCA, Inc. (formerly, Radio Technical Commission for Aeronautics) satellite-based augmentation system minimum operational performance standards neutral atmosphere delay model [RTCA, 2006], which is used for the Wide Area Augmentation System, the European Geostationary Navigation Overlay Service, and other satellite-based augmentation systems. This model is based on the works of Saastamoinen [1972a, 1972b, 1973] and Niell [1996] for zenith delay and mapping functions respectively. A look-up table of atmospheric parameters based on the 1966 U.S. Standard Atmosphere is used in the UNB3 model. The model input parameters are day of year, elevation angle, height and latitude. UNB3m [Orliac, 2002; Leandro et al., 2008] improves on UNB3 through an improved handling of the wet delay.

Schüler et al. [2001] proposed a tropospheric correction model namely GTN (Global Tropospheric Navigation model). In contrast to UNB3, this model not only includes a latitudinal correction data field, but also a longitudinal one with a higher horizontal resolution which accounts for regional variations. The GTN models were derived from analyses of GDAS (Global Data Assimilation System) numerical weather fields.

Leandro et al. [2006] developed a wide area neutral atmosphere model for North America (namely UNBw.na). They reported that the new grid-based model could perform better than models based only on latitude (such as UNB3m) even though the improvement may not be spectacular.

Boehm et al. [2007a] developed a global model of pressure and temperature for geodetic applications namely GPT (Global Pressure and Temperature). GPT is based on spherical harmonics up to degree and order nine and provides pressure and temperature for any site at or near the Earth's surface. This model was derived from 3 years of 15°×15° global grids of monthly mean profiles for pressure and temperature from the ECMWF 40 years reanalysis data.

2.4- Summary

In this chapter, theoretical aspects of neutral atmosphere effects on GNSS signals have been addressed. Some zenith delay models and mapping functions have also been briefly reviewed. One may refer to e.g. Mendes [1999] for a more comprehensive theoretical

background and historical review of the older models. In Chapter 3 recent developments in mapping functions based on NWP models as well as gradient mapping functions will be discussed in detail.

Chapter 3: Recent Developments in Neutral Atmosphere Mapping Functions

In this chapter recent mapping functions based on NWP models as well as commonly used gradient mapping functions are reviewed. Older mapping functions which were not based on (or derived from) NWP model data have been compared and reviewed comprehensively by Mendes [1999]. However, as mentioned in the previous chapter, among older mapping functions, Niell [1996] is still being used by many software products and analysis centres and is relevant for introducing the newer mapping functions. Hence, in this chapter, in addition to newer mapping functions based on NWP models, the Niell mapping functions are also reviewed.

3.1- Recent Symmetric Mapping Functions

3.1.1- Niell Mapping Functions

Niell mapping functions (NMF) use the continued fractional form as presented first by Marini [1972] as follow:

$$m_i(\varepsilon) = \frac{1+\dfrac{a_i}{1+\dfrac{b_i}{1+c_i}}}{\sin\varepsilon+\dfrac{a_i}{\sin\varepsilon+\dfrac{b_i}{\sin\varepsilon+c_i}}} + H_s \cdot 10^{-3}\left[\frac{1}{\sin\varepsilon} - \frac{1+\dfrac{a_{ht}}{1+\dfrac{b_{ht}}{1+c_{ht}}}}{\sin\varepsilon+\dfrac{a_{ht}}{\sin\varepsilon+\dfrac{b_{ht}}{\sin\varepsilon+c_{ht}}}}\right] \qquad (3.1)$$

where ε is the vacuum (unrefracted) elevation angle and *i* is replaced by *h* or *nh* standing for hydrostatic and non-hydrostatic respectively. The second term of the above equation, in which H_s is the orthometric height of the station in metres, is a height correction term and only applied to the hydrostatic mapping function. The *ht* terms for the height correction part are:

$$a_{ht} = 2.53e^{-5} \tag{3.2.a}$$

$$b_{ht} = 5.49e^{-3} \tag{3.2.b}$$

$$c_{ht} = 1.14e^{-3} \tag{3.2.c}$$

The coefficients for the hydrostatic part are functions of the station latitude and day of year as follow[1]:

$$a_h(\varphi_i, DoY) = a_{h_{avg}}(\varphi_i) - a_{h_{amp}}(\varphi_i)\cos\left(2\pi\frac{DoY - 28}{365.25}\right) \tag{3.3.a}$$

$$b_h(\varphi_i, DoY) = b_{h_{avg}}(\varphi_i) - b_{h_{amp}}(\varphi_i)\cos\left(2\pi\frac{DoY - 28}{365.25}\right) \tag{3.3.b}$$

$$c_h(\varphi_i, DoY) = c_{h_{avg}}(\varphi_i) - c_{h_{amp}}(\varphi_i)\cos\left(2\pi\frac{DoY - 28}{365.25}\right) \tag{3.3.c}$$

where coefficients with subscripts *avg* and *amp* are determined for the five latitudes as presented in Table 3.1 and are obtained by linear interpolation for non-tabulated latitudes.

[1] Note that these equations are the corrected ones as oppose to some earlier publications in which the two terms in the equations were added together.

Parameters for latitudes from 0 to 15° are the same as those for 15°. Parameters for latitudes above 75° are also the same as those for 75°. The mapping function is symmetric with respect to the equator except for the coefficients in equations (3.3) in which a phase of π is added for the southern hemisphere to account for seasonal differences.

Table 3.1- Coefficients for NMF

Coeff.	Latitude				
	15°	30°	45°	60°	75°
$a_{h_{avg}}$	$1.2769934e^{-3}$	$1.2683230e^{-3}$	$1.2465397e^{-3}$	$1.2196049e^{-3}$	$1.2045996e^{-3}$
$b_{h_{avg}}$	$2.9153695e^{-3}$	$2.9152299e^{-3}$	$2.9288445e^{-3}$	$2.9022565e^{-3}$	$2.9024912e^{-3}$
$c_{h_{avg}}$	$62.610505e^{-3}$	$62.837393e^{-3}$	$63.721774e^{-3}$	$63.824265e^{-3}$	$64.258455e^{-3}$
$a_{h_{aamp}}$	0	$1.2709626e^{-5}$	$2.6523662e^{-5}$	$3.4000452e^{-5}$	$4.1202191e^{-5}$
$b_{h_{aamp}}$	0	$2.1414979e^{-5}$	$3.0160779e^{-5}$	$7.2562722e^{-5}$	$11.723375e^{-5}$
$c_{h_{aamp}}$	0	$9.0128400e^{-5}$	$4.3497037e^{-5}$	$84.795348e^{-5}$	$170.37206e^{-5}$
a_{nh}	$5.8021897e^{-4}$	$5.6794847e^{-4}$	$5.8118019e^{-4}$	$5.9727542e^{-4}$	$6.1641693e^{-4}$
b_{nh}	$1.4275268e^{-3}$	$1.5138625e^{-3}$	$1.4572752e^{-3}$	$1.5007428e^{-3}$	$1.7599082e^{-3}$
c_{nh}	$4.3472961e^{-2}$	$4.6729510e^{-2}$	$4.3908931e^{-2}$	$4.4626982e^{-2}$	$5.4736038e^{-2}$

The popularity of NMF apart from higher accuracy than the older mapping functions is due to the fact that it does not require meteorological parameters and hence is rather easy to use. As an example, NMF values at day of year 182 for 5 degree elevation angle for the whole world have been calculated at the surface grid points of the global high resolution Canadian NWP model and presented at Figures 3.1 and 3.2.

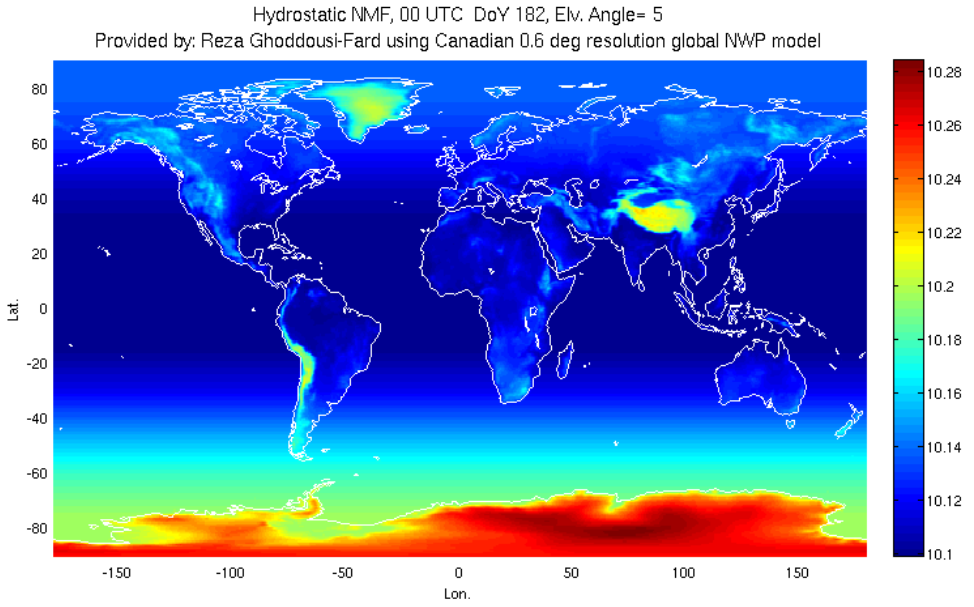

Figure 3.1– Hydrostatic NMF at 5 degree elevation angle on DoY 182 calculated on all grid points of the Canadian high resolution global NWP model

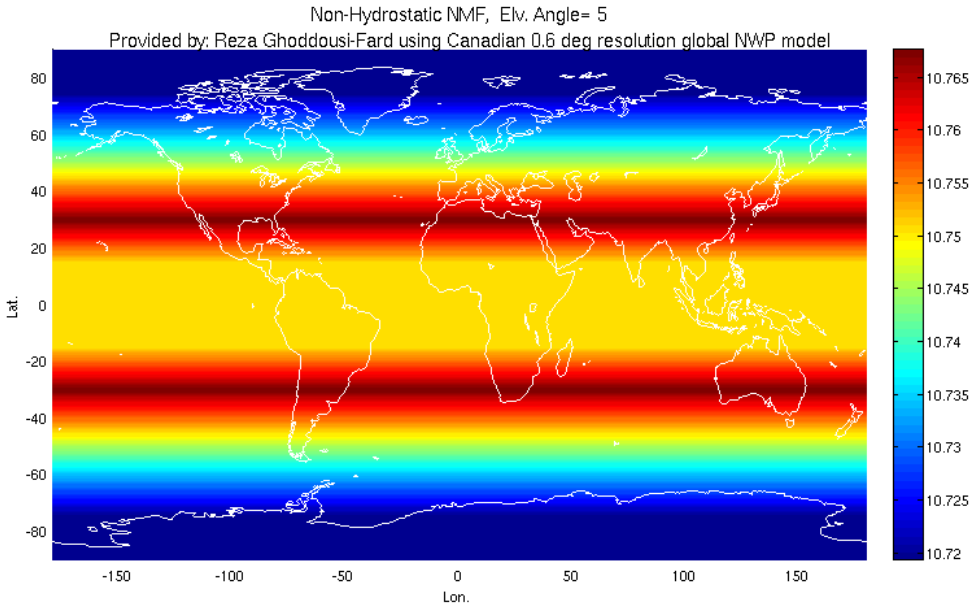

Figure 3.2– Non-hydrostatic NMF at 5 degree elevation angle calculated on all grid points of the Canadian high resolution global NWP model

While NMF has been a popular mapping function in the GNSS community, it suffers from some systematic biases mainly in the southern hemisphere (see section 3.1.5 and Chapter 6). As can be seen in Figure 3.2, the non-hydrostatic NMF is symmetric with respect to the equator. It should also be mentioned that the non-hydrostatic NMF is not dependent on day of year and hence what is represented in Figure 3.2 are mapping factor values for any epoch. Apart from a height correction, the hydrostatic NMF differs between northern and southern hemispheres by a phase change in the coefficients (as mentioned before in equations (3.3)).

3.1.2- Isobaric Mapping Functions

Niell [2000] proposed new mapping functions based on parameters from numerical weather models, namely Isobaric Mapping Functions (IMF). He studied the correlation of isobaric heights with radiosonde-derived hydrostatic mapping functions and reported that the 200 hPa level shows the highest correlation with the mapping function at 5°. Similar to NMF a continued fraction with three coefficients was adopted as follows:

$$m(\varepsilon) = \frac{1 + \dfrac{a}{1 + \dfrac{b}{1 + c}}}{\sin\varepsilon + \dfrac{a}{\sin\varepsilon + \dfrac{b}{\sin\varepsilon + c}}} \tag{3.4}$$

The coefficients for the hydrostatic mapping function are as follows (Niell [2003]):

$$a = a_\varphi + \zeta_\varphi \cdot (z_{200} - z_r) \tag{3.5.a}$$

$$b = 0.002905 \tag{3.5.b}$$

$$c = 0.0634 + 0.0014 \cdot \cos(\varphi) \tag{3.5.c}$$

where:

$$a_\varphi = 0.00124 + 0.00004 \cdot \cos(2 \cdot (\varphi - 2)) \tag{3.6.a}$$

$$\zeta_\varphi = 0.000000074 - 0.000000016 \cdot \cos(2\varphi) \tag{3.6.b}$$

$$z_r = 11836 + 619 \cdot \cos(2 \cdot (\varphi - 3)) \tag{3.6.c}$$

where φ and z_{200} are the latitude and height of the 200 hPa level above the site. A height correction similar to the one for NMF should also be applied here.

The coefficients for the non-hydrostatic (wet) mapping function are as follows (Niell [2003]):

$$a = (mf_3 - 15.5) \cdot (-0.00020795 + 0.00068827 - 0.0000001658 \cdot h) \tag{3.7.a}$$

$$b = (mf_3 - 15.5) \cdot 0.00018882 + 0.0013503 \tag{3.7.b}$$

$$c = (mf_3 - 15.5) \cdot 0.0048581 + 0.0039647 \tag{3.7.c}$$

where mf_3 is the mapping function at 3° elevation calculated using ray tracing of numerical weather model grids and h is the height of the site.

As an example, the hydrostatic IMF at 5 degree elevation angle has been calculated at all grid points of the Canadian global high resolution NWP model at DoY 182, 2008 and are presented in Figure 3.3.

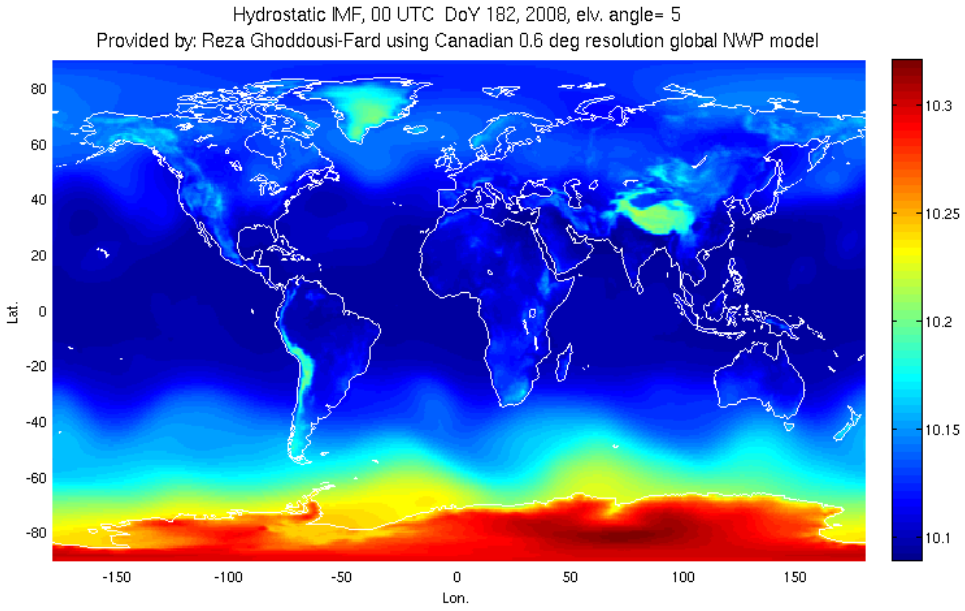

Figure 3.3 – Hydrostatic IMF at 5 degree elevation angle on DoY 182 calculated on all grid points of Canadian high resolution global NWP model

3.1.3- Vienna Mapping Functions

Vienna mapping functions (VMF) introduced by Boehm and Schuh [2004] use the *b* and *c* coefficients of IMF for the hydrostatic part, and those of NMF at 45° latitude for the non-hydrostatic part (i.e.: $b_{nh} = 0.00146, c_{nh} = 0.04391$). Ray tracing with an initial elevation angle of 3.3° is carried out and by inverting the continued fraction form the *a* coefficients can be determined as follow:

$$a = \frac{A_0 + A_1 + A_2 + A_3}{B_0 + B_1 + B_2} \tag{3.8}$$

where:

$$A_0 = b + c \cdot b + b^2 \tag{3.9.a}$$

$$A_1 = -mf \cdot b.\sin(\varepsilon) + c \cdot b \cdot \sin(\varepsilon) + mf \cdot b^2 \cdot \sin(\varepsilon) + c^2 \cdot \sin(\varepsilon) - mf \cdot b \cdot c \cdot \sin(\varepsilon) + c \cdot \sin(\varepsilon) \tag{3.9.b}$$

$$A_2 = -mf \cdot c^2 \cdot \sin^2(\varepsilon) + mf \cdot c \cdot \sin^2(\varepsilon) + b \cdot \sin^2(\varepsilon) + c \cdot \sin^2(\varepsilon) + \sin^2(\varepsilon) - mf \cdot b \cdot c \cdot \sin^2(\varepsilon) \tag{3.9.c}$$

$$A_3 = -mf \cdot b \cdot \sin^3(\varepsilon) - mf \cdot c \cdot \sin^3(\varepsilon) - mf \cdot \sin^3(\varepsilon) \tag{3.9.d}$$

$$B_0 = -c \cdot b - b + mf \cdot c + mf \cdot c^2 + mf \cdot b \cdot c \tag{3.9.e}$$

$$B_1 = -c \cdot \sin(\varepsilon) + mf \cdot \sin(\varepsilon) - c^2 \cdot \sin(\varepsilon) + mf \cdot c \cdot \sin(\varepsilon) + mf \cdot b \cdot \sin(\varepsilon) \tag{3.9.f}$$

$$B_2 = -c \cdot \sin^2(\varepsilon) - \sin^2(\varepsilon) \tag{3.9.g}$$

where *mf* is the mapping function value resulting from ray tracing (at a 3.3° initial elevation angle) and ε is the vacuum elevation angle of the desired direction.

Boehm et al. [2006] updated the VMF and called it VMF1 in which the *c* coefficients from ray tracing were fitted to a function of latitude and day of year to remove systematic errors. Boehm et al. [2006] also investigated the concept of a total mapping function in VMF1. However they mentioned the limitation of a total mapping function is that it is affected by bad a priori information about the non-hydrostatic part in the atmosphere

from NWP models. The coefficients for VMF1 total and hydrostatic mapping functions are as follows:

$$b_t = b_h = 0.0029 \tag{3.10}$$

$$c = c_0 + \left[\left(\cos\left(\frac{DoY - 28}{365}.2\pi + \psi \right) + 1 \right).\frac{c_{11}}{2} + c_{10} \right].(1 - \cos\varphi) \tag{3.11}$$

where φ is the latitude, and ψ specifies the northern or southern hemisphere. Values of c_0, c_{10}, c_{11} and ψ for hydrostatic and total VMF1 are given in Tables 3.2 and 3.3 respectively.

Table 3.2- Parameters in equation (3.11) for hydrostatic VMF1

Hemisphere	c_0	c_{10}	c_{11}	ψ
Northern	0.062	0.001	0.005	0
Southern	0.062	0.002	0.007	π

Table 3.3- Parameters in equation (3.11) for total VMF1

Hemisphere	c_0	c_{10}	c_{11}	ψ
Northern	0.063	0.000	0.004	0
Southern	0.063	0.001	0.006	π

The b_{nh} and c_{nh} coefficients of the non-hydrostatic VMF1 are the same as the non-hydrostatic VMF (i.e. those of NMF at 45° latitude).

3.1.4- Global Mapping Functions

Boehm et al. [2006] developed Global Mapping Functions (GMF), using 15°×15° global grids of monthly mean profiles from pressure, temperature, and humidity from the ECMWF 40 years reanalysis data (the same data that was used for GPT, see Chapter 2). This mapping function takes empirical equations for *b* and *c* from VMF1 and the coefficient *a* is calculated from spherical harmonics on a global grid from the following equations:

$$a = a_0 + A \cdot \cos\left(\frac{DoY - 28}{365} \cdot 2\pi\right) \tag{3.12}$$

where:

$$a_0 = \sum_{n=0}^{9}\sum_{m=0}^{n} P_{nm}(\sin\varphi) \cdot [A_{nm} \cdot \cos(m \cdot \lambda) + B_{nm} \cdot \sin(m \cdot \lambda)] \tag{3.13}$$

where DoY is day of year, a_0 is the global grid of mean values, A are the annual amplitudes, $P_{nm}(\sin\varphi)$ are the Legendre associated functions of *n* degree and *m* order, and A_{nm} and B_{nm} are the spherical harmonic coefficients.

Unlike VMF1, which requires real-time NWP data, GMF only requires station coordinates and day of year. As an example, hydrostatic and non-hydrostatic GMF for DoY 182 at 5 degree elevation angle are presented at Figures 3.4 and 3.5 respectively.

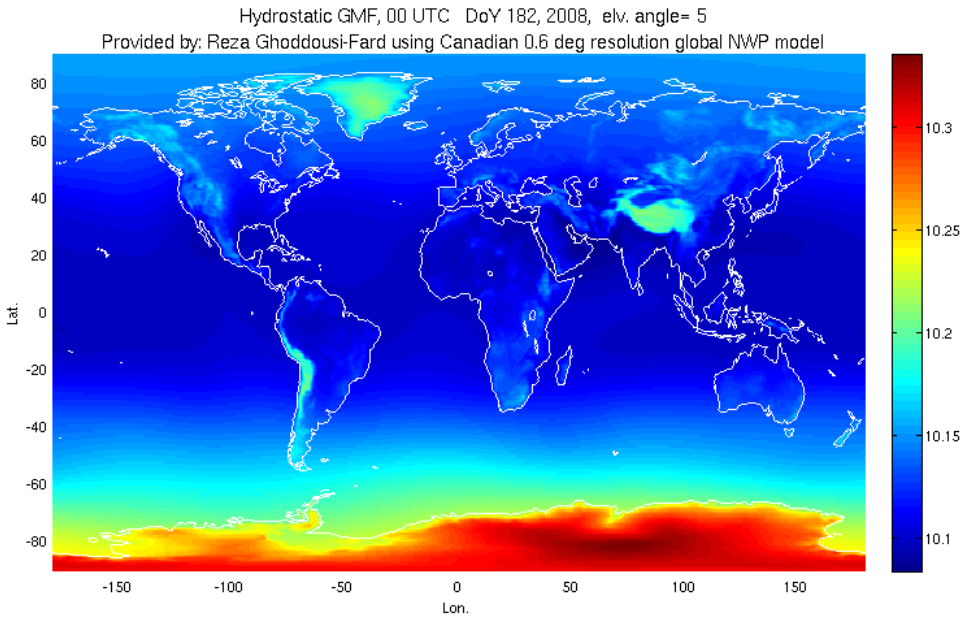

Figure 3.4– Hydrostatic GMF at 5 degree elevation angle on DoY 182 calculated on all grid points of Canadian high resolution global NWP model

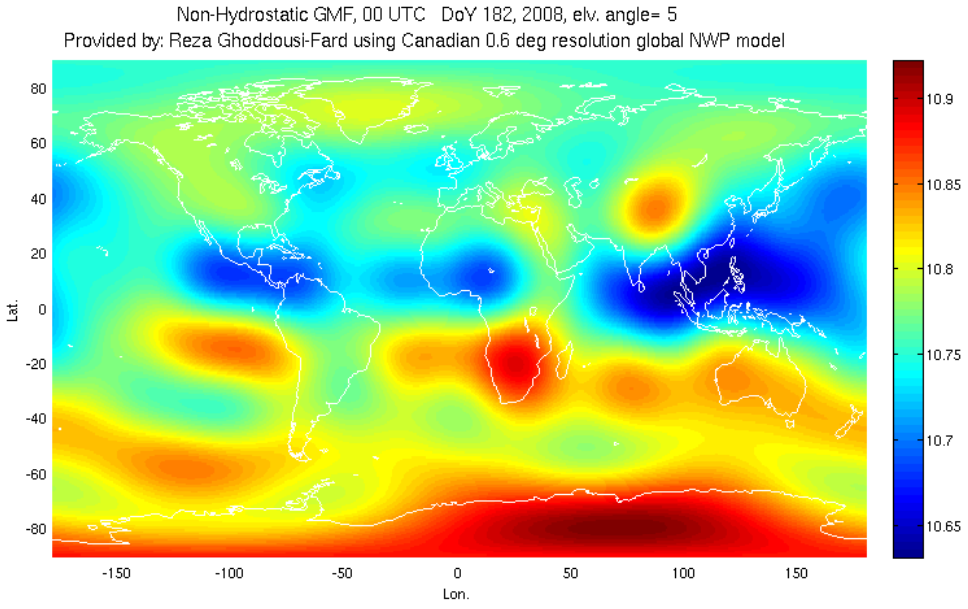

Figure 3.5– Non-hydrostatic GMF at 5 degree elevation angle on DoY 182 calculated on all grid points of Canadian high resolution global NWP model

3.1.5- Comparison of Recent Symmetric Mapping Functions

As mentioned before, while VMF1 and IMF are partly based on ray tracing through NWP models, NMF and GMF are empirical mapping functions and do not require real-time data. Hence, among these mapping functions, NMF followed by GMF are easiest to use but they are not tuned to day-to-day weather variations. In this regard, VMF1 and IMF have the advantage. What is practically of interest to the GNSS community is how much change in slant delay might arise as a result of using one mapping function as opposed to the other (as well as how easy they are to use).

The differences between hydrostatic and non-hydrostatic GMF and NMF at DoY 182 at 5 degree elevation angle are presented at Figures 3.6 and 3.7.

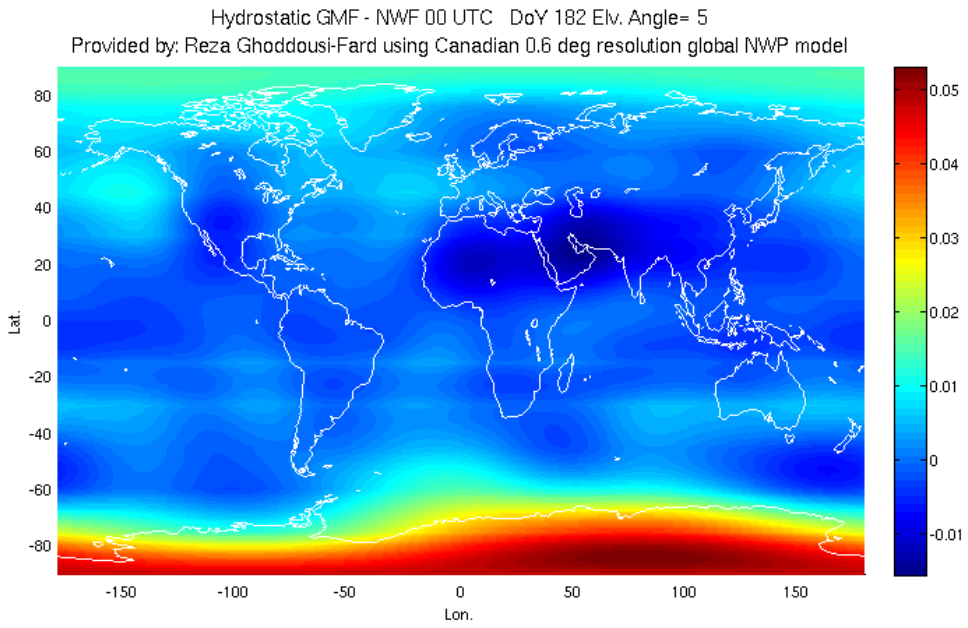

Figure 3.6- Difference between hydrostatic GMF and NMF on DoY 182

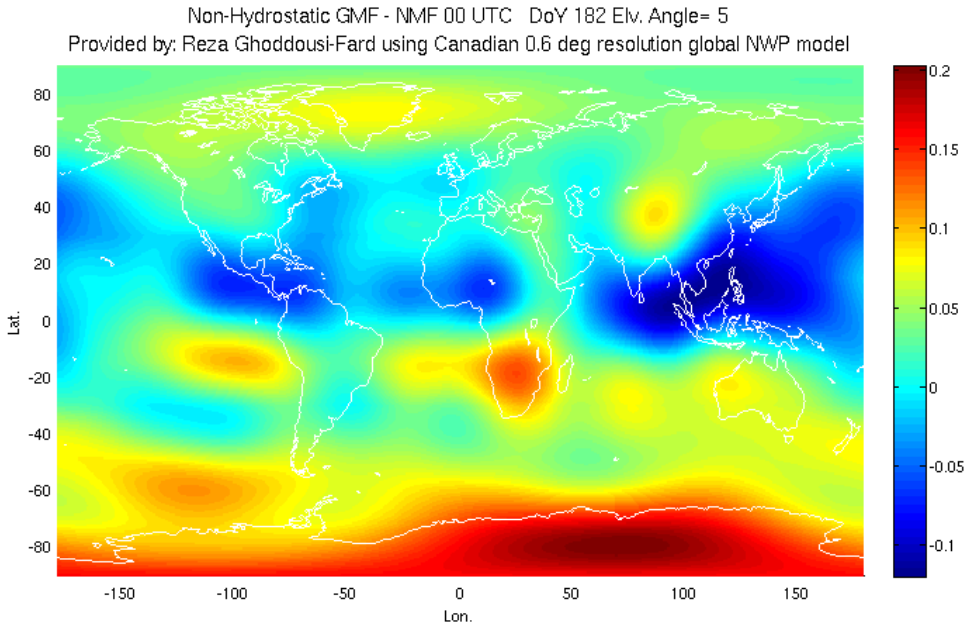

Figure 3.7- Difference between non-hydrostatic GMF and NMF on DoY 182

The differences shown in the above maps are multiplied by ZHD and ZWD from the Canadian global NWP model at the same epoch in 2008 and the results are the differences that these two mapping functions cause in slant delay. These are presented in Figures 3.8 and 3.9.

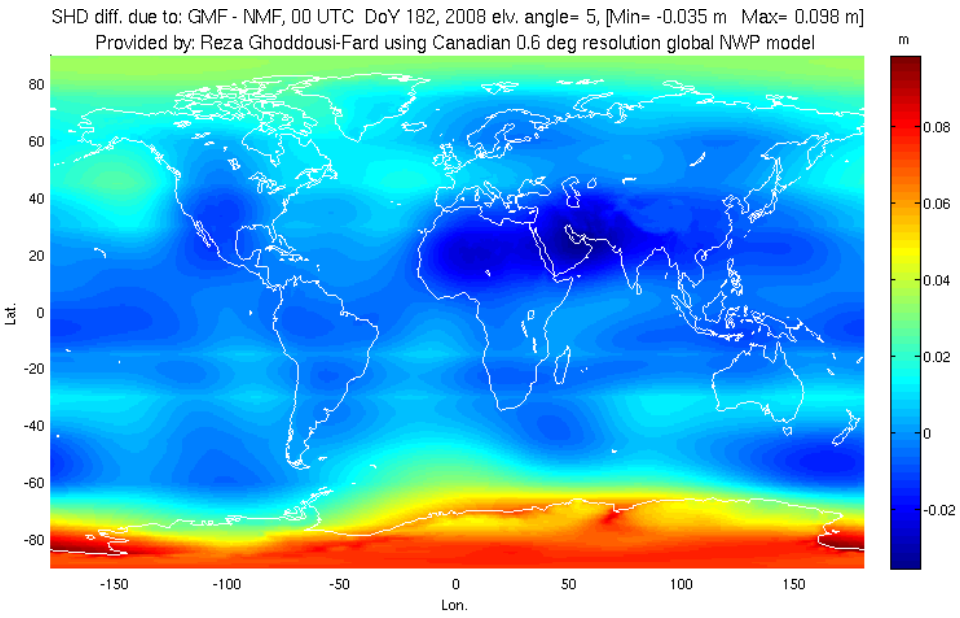

Figure 3.8- Difference between slant hydrostatic delays resulting from GMF and NMF on DoY 182, 2008

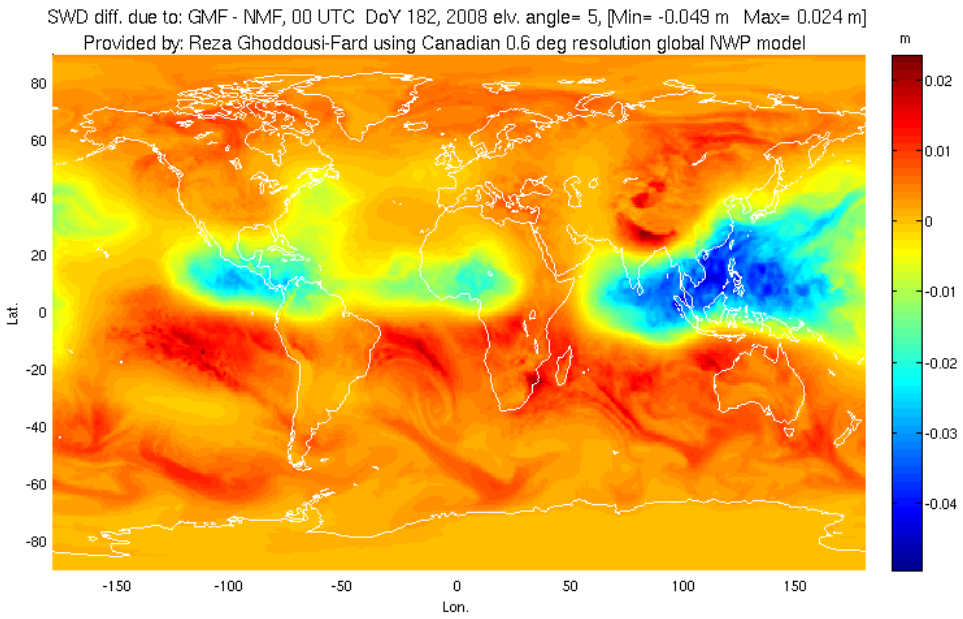

Figure 3.9- Difference between slant non-hydrostatic delays resulting from GMF and NMF on DoY 182, 2008

Since ZHD is one order of magnitude larger than ZWD, despite the smaller difference between hydrostatic mapping function values compared to non-hydrostatic (Figures 3.6 and 3.7), the resulting slant hydrostatic delay differences due to using GMF instead of NMF is larger than the slant non-hydrostatic delay. As can be seen in Figure 3.8 the use of GMF instead of NMF can cause up to about 10 cm slant hydrostatic delay difference at 5 degree elevation angle while the maximum slant non-hydrostatic delay difference in the investigated day is about 5 cm.

Figure 3.10 shows the slant hydrostatic delay differences at 5 degree elevation angle as a result of using IMF instead of NMF on the same day as above. Apart from large biases in

Antarctica which were also visible in Figure 3.8 (GMF vs. NMF), local anomalies also have caused differences of a few centimetres on the investigated day.

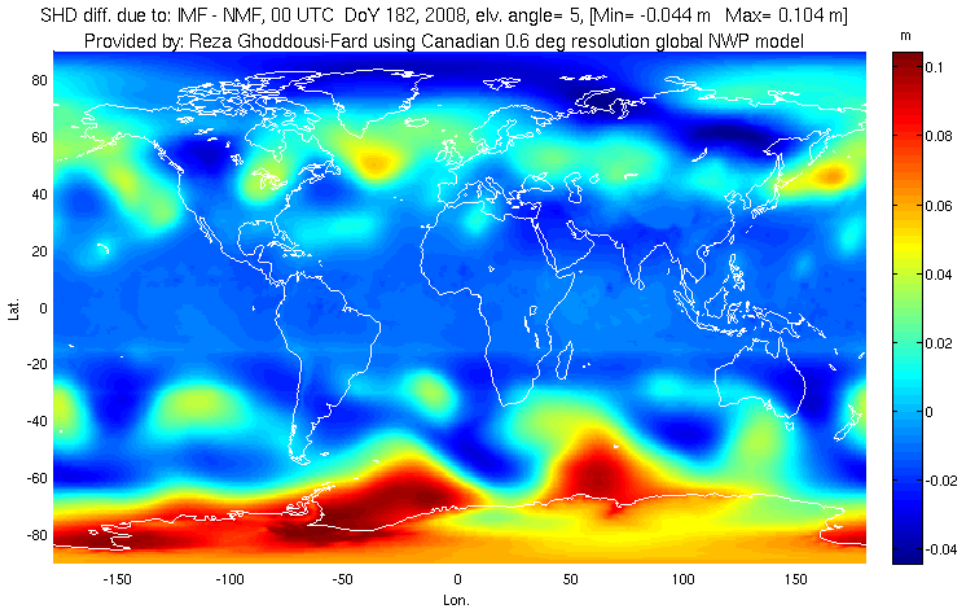

Figure 3.10- Difference between slant hydrostatic delays resulting from IMF and NMF on DoY 182, 2008

Based on the actual GPS constellation, slant delay differences as a result of changing mapping function are investigated. In all cases the mapping function differences are multiplied by the zenith delay from the global high resolution Canadian NWP model interpolated at each epoch (every 30 seconds) to present the results in units of delay (metre). One can see the differences of slant hydrostatic delay between the mapping functions mentioned in the previous sections at station ALGO, Canada over 24 hours on DoY 197, 2007 in Figures 3.11. The maximum difference and percentages of values larger than 1 cm with respect to the whole measurements over the day are quoted in the

title of the figures. Mapping functions based on NWP have smaller differences with each other compared to their differences with NMF. These can reach up to 127 mm at the lowest measured elevation angle on the investigated day and station in the case of VMF1. As can be seen in Figure 3.11.d VMF1 and IMF are in rather closer agreement. This is expected as both are partly based on the same NWP model although VMF1 is based on ray tracing at a 3.3° apparent elevation angle, while IMF is based on the 200 hPa isobaric height. One should note that in this study the 200 hPa isobaric height of the nearest 4 grid points to the station are averaged and then used in the IMF equations.

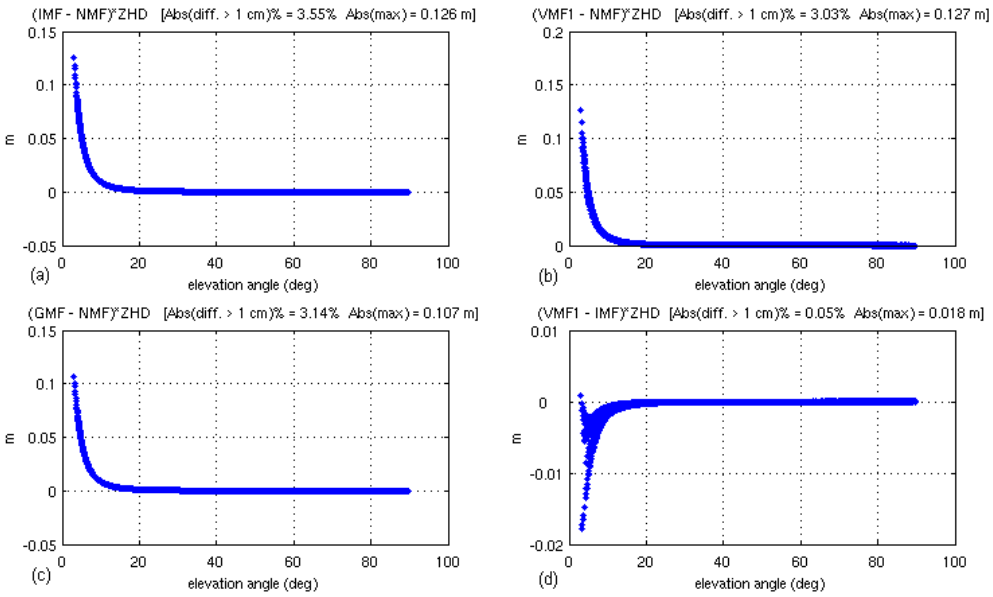

Figure 3.11- Slant hydrostatic delay difference at station ALGO, Canada, DoY 197, 2007 as a result of: a) IMF-NMF. b) VMF1-NMF. c) GMF-NMF. d) VMF1-IMF.

Similarly, slant non-hydrostatic delay between the mapping functions mentioned in the previous sections at station ALGO, Canada over 24 hours on DoY 197, 2007 are presented in Figures 3.12. As mentioned earlier, despite larger uncertainties in non-hydrostatic mapping functions in general, the slant non-hydrostatic delay differences are smaller due to the smaller ZWD compared to ZHD. The exception is the difference between non-hydrostatic VMF1 and IMF which is larger compared to hydrostatic values. The formulation of non-hydrostatic coefficients in IMF is derived from equations (3.7), while VMF1 is similar to NMF in the cases of b_{nh} and c_{nh} but a_{nh} is based on ray tracing.

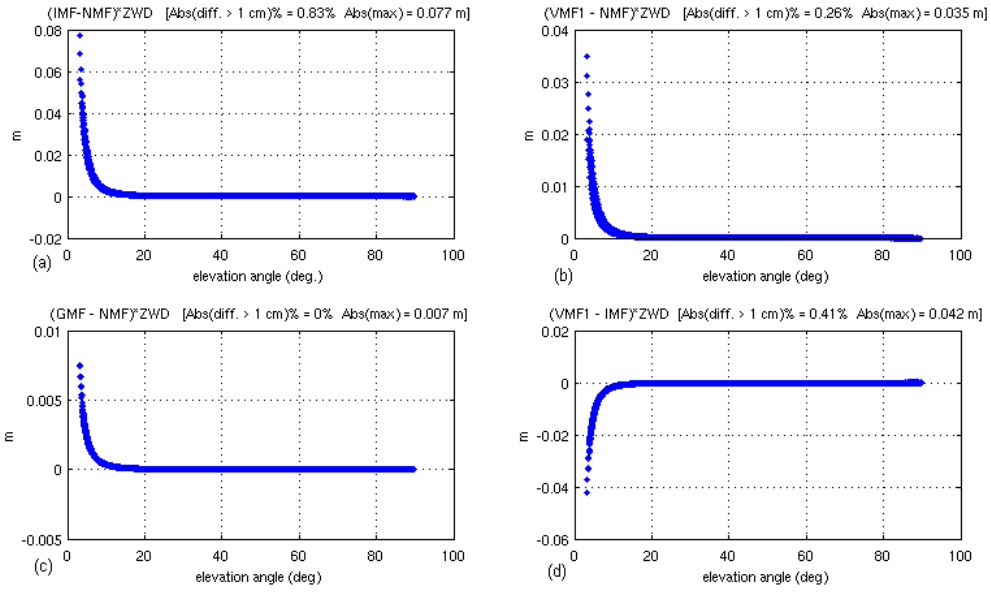

Figure 3.12– Slant non-hydrostatic delay difference at station ALGO, Canada, DoY 197, 2007 as a result of: a) IMF-NMF b) VMF1-NMF c) GMF-NMF d) VMF1-IMF

IERS Conventions Update [2007] (based on validation results of Niell [2006], Boehm [2007b] and Tesmer et al. [2007]) has recommended VMF1 for any global application, such as the determination of the terrestrial reference frame and Earth orientation parameters. As expected, and as it is clear in Figures 3.11 and 3.12, the choice of mapping function affects the slant delays significantly only at elevation angles below 15-20 degrees.

3.2- Gradient Models and Mapping Functions

Compared to the models and mapping functions used for the symmetric atmosphere, there are not many gradient models and mapping functions developed for the asymmetric part. In this section common gradient models and mapping functions are reviewed. A hydrostatic gradient model derived as a part of this dissertation research work will be introduced in Chapter 5.

Similar to the common approach to deal with the symmetric part of the delay, the use of an elevation-dependent function to map the horizontal azimuthally dependent delays has also been used to model the asymmetric part. The geodetic azimuth (α) and elevation angle (ε) between two points (with geometric distance *S*) can be related to local geodetic coordinate system as follows:

$$N = S \cdot \cos\varepsilon \cdot \cos\alpha \qquad (3.13.a)$$

$$E = S \cdot \cos\varepsilon \cdot \sin\alpha \tag{3.13.b}$$

$$h = S \cdot \sin\varepsilon \tag{3.13.c}$$

where N, E and h are north, east and height components respectively. From equations (3.13) the position vector of a point on the path can be written as follows:

$$\vec{x}(\varepsilon,\alpha) \cong h \cdot \cot\varepsilon \cdot (\cos\alpha \cdot \hat{n} + \sin\alpha \cdot \hat{e}) \tag{3.14}$$

where $\hat{n}$ and $\hat{e}$ are the unit vectors to the north and east respectively.

Equation (3.14) is the basis of available gradient models which will be reviewed in the following sections.

3.2.1- Davis et al.

Based on the above relations, Davis et al. [1993] (with the assumption of linear variation of refractivity with horizontal distance) defined a gradient model as follows:

$$d_{asym}(\varepsilon,\alpha) = m_{sym}(\varepsilon) \cdot \cot\varepsilon' \cdot (G_N \cdot \cos\alpha + G_E \cdot \sin\alpha) \tag{3.15}$$

where $m_{sym}(\varepsilon)$ is a symmetric mapping function (i.e. not a function of azimuth), ε' is the refracted elevation angle, and G_N and G_E are the delay gradients in the north and east directions respectively. Using an approximate relation between the refracted and unrefracted (vacuum) elevation angle given by Bean and Dutton [1966], the Davis gradient model in equation (3.15) is given as:

$$d_{asym}(\varepsilon,\alpha) \cong m_{sym}(\varepsilon) \cdot \cot\varepsilon \cdot (1 - 10^{-6} N_s \cdot \csc^2\varepsilon) \cdot (G_N \cdot \cos\alpha + G_E \cdot \sin\alpha) \tag{3.16}$$

where N_s is the total surface refractivity.

Later, MacMillan [1995] and MacMillan and Ma [1997] applied the gradient model of Davis in VLBI analysis (by replacing ε' simply by ε in equation (3.15)) and noted that the results are not sensitive to whether $m_{sym}(\varepsilon)$ is replaced by a hydrostatic or non-hydrostatic mapping function.

3.2.2- Chen and Herring

Chen and Herring [1997] showed that the gradient mapping function can be expressed approximately as a continued fraction expansion in the form of $\sin\varepsilon.\tan\varepsilon$ i.e.:

$$m_{asym}(\varepsilon) = \cfrac{1}{\sin\varepsilon\tan\varepsilon + \cfrac{c_1}{\sin\varepsilon\tan\varepsilon + \cfrac{c_2}{\sin\varepsilon\tan\varepsilon + \ldots}}} \tag{3.17}$$

They have retained just the first term i.e.:

$$m_{asym}(\varepsilon) = \frac{1}{\sin\varepsilon\cdot\tan\varepsilon + C} \tag{3.18}$$

where:

$$C = \frac{3\int \nabla N \cdot h^2 dh}{2\int \nabla N \cdot h(h+R) dh} \tag{3.19}$$

where ∇N is the gradient of refractivity, h is the height and R is the radius of Earth. Under the assumption of an exponential decay in the gradient with scale height of H_s,

equation (3.19) reduces to $\frac{3H_s}{2R}$ [Chen and Herring, 1997]. Hence assuming a hydrostatic gradient scale height of 13 km, and radius of the Earth equal to 6370 km, C = 0.0031. For a non-hydrostatic gradient scale height of 3 km, C=0.0007. However, Chen and Herring [1997] used a combined value of 0.0032 in their VLBI analysis as it is difficult to estimate the hydrostatic and non hydrostatic parts separately.

In order to use the Chen and Herring asymmetric mapping function, one may replace the $m_{sym}(\varepsilon).\cot\varepsilon'$ term in equation (3.15) with equation (3.18).

3.2.3- Tilting of the Atmosphere

Tilting the zenith direction in the mapping function by a small angle β may represent a tropospheric gradient (see e.g. Meindl et al. [2004]). The geometry of tilting the zenith direction is represented in Figure 3.13. In Figure 3.13 the tropospheric zenith is defined as normal to the tilted atmosphere while the geometric zenith is defined as normal to the untilted (symmetric) atmosphere. Based on the representation in Figure 3.13 and according to the first spherical law of cosines, we may write:

$$\cos(\hat{z}) = \cos(\beta)\cos(z) + \sin(\beta)\sin(z)\cos(A - A_0) \tag{3.20}$$

where A is the azimuth of the observation, A_0 is the azimuth of the tropospheric zenith direction ($\hat{z}$) with respect to the geometric zenith direction (z).

Since β is small we may write:

$\sin(\beta) \cong \beta$ and $\cos(\beta) \cong 1$

From equation (3.20) and considering a small value for β [Meindl et al., 2004] and assuming:

$$\hat{z} = z + \delta z \tag{3.21}$$

we can write:

$$\cos(z + \delta z) = \cos(z) + \beta \sin(z) \cos(A - A_0) \tag{3.22}$$

or:

$$\cos(z)\cos(\delta z) - \sin(z)\sin(\delta z) = \cos(z) + \beta \sin(z)\cos(A - A_0)\,. \tag{3.23}$$

Since δz is small we may write:

$$\cos(z) - \sin(z)\delta z = \cos(z) + \beta \sin(z)\cos(A - A_0) \tag{3.24}$$

which results in:

$$\delta z = -\beta \cos(A - A_0) \tag{3.25}$$

From (3.21) and (3.25) we can write:

$$\hat{z} = z - \beta \cos(A - A_0) \tag{3.26}$$

By defining: $x = -\beta \cos(A_0)$ and $y = -\beta \sin(A_0)$ we can write:

$$\hat{z} = z + x\cos(A) + y\sin(A) \tag{3.27}$$

hence:

$$\hat{z} - z = \delta z = x\cos(A) + y\sin(A) \tag{3.28}$$

Following (3.21), $f(\hat{z}) = f(z + \delta z)$ and by a linear approximation (using Taylor's theorem) we may write:

$$f(\hat{z}) = f(z) + \frac{\partial f}{\partial z}(z + \delta z - z) = f(z) + \frac{\partial f}{\partial z}\delta z \tag{3.29}$$

and considering (3.28) finally we have:

$$f(\hat{z}) = f(z) + \frac{\partial f}{\partial z} x\cos(A) + \frac{\partial f}{\partial z} y\sin(A) \tag{3.30}$$

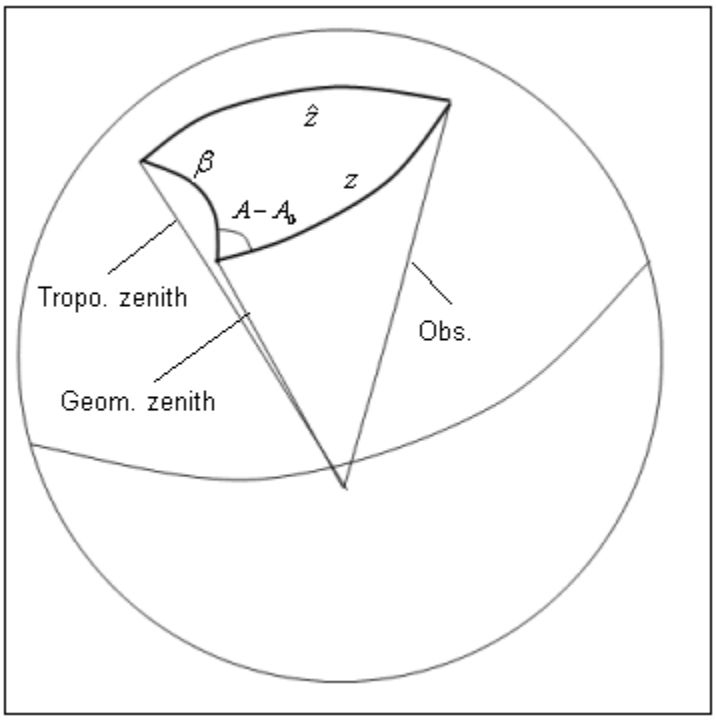

Figure 3.13- Geometry of spherical triangle as a result of tilting the zenith direction

Assuming a simple mapping function of $f = \frac{1}{\sin\varepsilon}$ equation (3.30) can be expressed in a similar form as equation (3.15).

3.2.4- Niell Hydrostatic Gradient Mapping Function

Niell [2001] proposed a hydrostatic gradient mapping function based on the same idea used in the IMF. Therefore this mapping function requires access to information from NWP models. The tilt of the hydrostatic atmosphere is defined as the direction of the normal to the surface defined by the geopotential height of the 200 hPa surface at the four nearest grid points. This direction is represented by gradient azimuth (α_g) and gradient zenith angle (z_g). The form of this mapping function is as follows:

$$GMFh(\varepsilon, \alpha_g, z_g) = MFh(\varepsilon - z_g \cdot \cos(\alpha_g)) \tag{3.31}$$

where *GMFh* is the hydrostatic gradient mapping function, *MFh* is an arbitrary azimuthally symmetric hydrostatic mapping function, and ε is the elevation angle of an observation. Following Niell [2003] the gradient azimuth and gradient zenith angle may be estimated by satisfying the following equation:

$$\vec{h} \cdot (\vec{W}_m - \vec{X}_0) = 0 \tag{3.32}$$

where $\vec{h} = \begin{bmatrix} h_x & h_y & h_z \end{bmatrix}$ is the normal to the plane that is fitted to 200 hPa geopotential heights at the grid points, $\vec{W}_m = \begin{bmatrix} w_{mx} \\ w_{my} \\ w_{mz} \end{bmatrix}$ is the position vector of the 200 hPa geopotential surface at the grid points, and $\vec{X}_0 = \begin{bmatrix} x_{0x} \\ y_{0x} \\ z_{0x} \end{bmatrix}$ is the position vector of the 200 hPa geopotential surface above the site.

From (3.32) one can derive the z component as follows:

$$w_{mz} = x_{0z} - \frac{h_x}{h_z}(w_{mx} - x_{0x}) - \frac{h_y}{h_z}(w_{my} - x_{0y}) \tag{3.33}$$

Since the normal vector is a unit vector, only the ratios of the components need to be estimated. Hence the vector of unknowns is defined as:

$\vec{y} = \lfloor x_{0z} \quad h_{xz} \quad h_{yz} \rfloor$, where $h_{xz} = \frac{h_x}{h_z}$ and $h_{yz} = \frac{h_y}{h_z}$.

The vector of observations is composed of the z component of the position vector of grid points.

A weighted least-squares approach can be used for estimation of the unknowns, where weights are calculated from the uncertainty in 200 hPa geopotential heights. The gradient azimuth (α_g) and gradient zenith angle (z_g) finally can be calculated in units of degrees by:

$$\alpha_g = \frac{180^\circ}{\pi} \cdot a\tan 2(h_{xz}, h_{yz}) \tag{3.34}$$

$$z_g = 90^\circ - \frac{180^\circ}{\pi} \cdot a\tan 2(1, r_{xy}) \tag{3.35}$$

where $r_{xy} = \left(h_{xz}{}^2 + h_{yz}{}^2\right)^{1/2}$ and atan2 is the four-quadrant inverse tangent function.

3.3- Summary

Comparison between recent mapping functions carried out in this chapter shows up to more than 10 cm difference between the NWP-based mapping functions and the NMF in low elevation angle measurements. Some of the symmetric and gradient mapping functions discussed in this chapter will be used later throughout this dissertation either for implementation in GPS software or in validation studies.

Chapter 4: Ray Tracing: Theory and Practice

In this chapter, the ray tracing algorithm developed for this research is reviewed. A web-based ray tracing package, accessible to the public and developed as a part of this research, will be discussed. Validation of data sources used in ray tracing in different locations and using different sensors - including surface met sensors and a water vapour radiometer (WVR) - will be addressed as well.

4.1- Ray Tracing: A Review

According to the American Meteorological Society's Glossary of Meteorology [AMS, 2007], ray tracing is:

"*a graphical or mathematical approximation scheme for determining the propagation of electromagnetic or sound waves by following the path of rays obeying the laws of reflection and refraction*."

Ray tracing has been a common approach for dealing with radio signal propagation through the atmosphere for a long time (see, e.g., Bean and Dutton [1966]). The term "ray tracing" is also used in other disciplines such as geophysics (see, e.g., Rucker and Ferré [2004]).

In order to estimate the delay along the signal path, numerical integration requires a series of thin spherical layers within which a constant refractivity is assumed. Assuming a symmetric atmosphere around a GNSS receiver, these layers are made by using vertical

profiles of measurements which are used for estimation of refractivity in each layer. Apart from the ray tracing algorithms themselves, the accuracy, resolution, and proximity of the data source have the most critical effect on achieving accurate results.

As mentioned in chapter 2, refractivity can be estimated using knowledge of pressure, temperature, and water vapour pressure (see Bean and Dutton [1966]; Davis et al. [1985]; Bevis et al. [1994]) along the signal path. However, in practice, only a small number of measurements may be available along a vertical profile. A sufficiently accurate numerical integration, however, requires a high vertical resolution of measurements. Increasing the vertical resolution of measurements (measurements here can refer to either RAOB data or available NWP model layers) is common practice (see, e.g., Rocken et al. [2001]).

Temperature and humidity may be assumed to change linearly between available data levels (which are usually provided at the altitude of significant change in the parameters). Hence they can be interpolated using:

$$l_z = l_i + \frac{l_{i+1} - l_i}{z_{i+1} - z_i}(z - z_i) \tag{4.1}$$

where l_z is the interpolated temperature or humidity at height of z, l_i and l_{i+1} are the temperature or humidity values at height z_i and z_{i+1} respectively.

Assuming an isothermal atmosphere (dry atmosphere of constant temperature) in hydrostatic equilibrium (see, e.g., Andrews [2000]), pressure values can be interpolated by using the following equations:

$$P = P_0 e^{\left(\frac{-gz}{R_d T_0}\right)} = P_0 e^{\left(\frac{-z}{\tilde{H}}\right)}, \tag{4.2a}$$

$$\text{where } \tilde{H} = \frac{R_d T_0}{g} \tag{4.2b}$$

In the above equations, P is the pressure at height z above the surface, P_0 is the surface pressure (or pressure at adjacent level), T_0 is surface temperature (or temperature at adjacent level), R_d is the specific gas constant for dry air, and g is the gravity acceleration that changes slightly with latitude and height (less than 1% for a height change of 30 km or latitude difference of 1 degree). One may refer to Marini and Murray [1973] and List [1966] for a gravity model that uses an effective Earth radius and height. $\tilde{H}$ is called "pressure scale height" (the height over which the pressure decreases by a factor of e). If the temperature is known as a function of height (e.g., at each level), the above equations may be used to find the pressure as a function of height. For moist air, virtual temperature (see, e.g., Wallace and Hobbs [1977]) rather than actual temperature should be used in equations (4.2a) and (4.2b).

The vertical interpolation approaches mentioned above are also used to derive surface values when the user (GPS antenna) height is not the same as the surface height of the meteorological profile. Some unavoidable errors in the determination of ZTD exist due to the vertical interpolation (or extrapolation, where the data source surface level is higher

than the GPS antenna). Exponential pressure interpolation is known to have a very good agreement with the vertical profile of the pressure. However, the temperature (and humidity measure) is interpolated linearly. This might be erroneous when there is a large height difference between the surface level of the data source and the GPS antenna. When there is temperature inversion[1], for example, the aforementioned issue might be of more concern. Figure 4.1 shows the vertical profile of temperature at station WHIT (YXY) in Whitehorse, Yukon, where a large height difference between GPS and radiosonde surface measurements exists (over 700 m). A zoomed view of the lower levels can be seen in Figure 4.2 where the GPS antenna level and radiosonde surface measurement have also been shown. The interpolated temperature values above the height of the GPS antenna do not consider any inversion layer (which may be incorrect). However, temperature errors are less important than pressure errors in ZTD determination and could be insignificant when compared to errors due to other assumptions.

In the ray tracing package developed as part of this dissertation research, the resolution of meteorological parameters was increased by using a step size of 10 m from the surface up to the altitude of 20 km and 50 m from 20 km to the top of the neutral atmosphere. Figure 4.3 shows the effect of changing the ray tracing integration step size for slant total delay

[1] Layers of air with negative lapse rates, i.e. where temperatures increases with height. Temperature inversion is a frequent phenomenon in the Arctic. The Arctic temperature inversion is usually because of snow and ice surfaces that exist in the Arctic regions. This low-level inversion is present almost continuously over the Arctic in winter and over snow and ice covered areas in summer [Maxwell, 1982].

at a 5 degree elevation angle compared to when a 5 m step size is used from the surface to the top of the neutral atmosphere. As can be seen in Figure 4.3, our integration step sizes provide almost the same results as the more time consuming step size of 5 m for the whole profile.

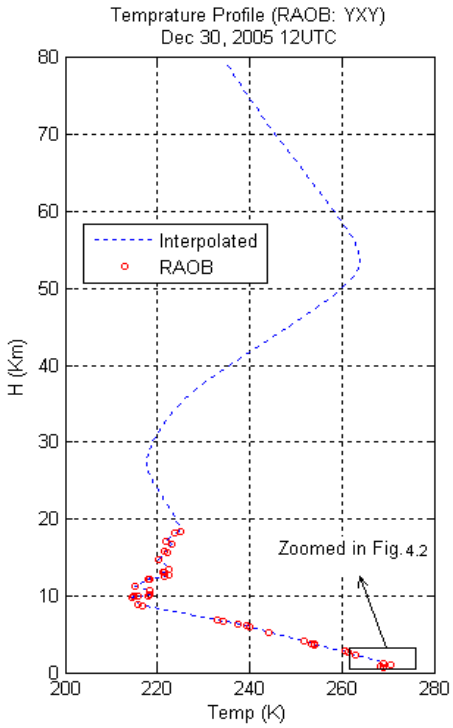

Figure 4.1- A sample temperature profile with inversion in low levels of the atmosphere.

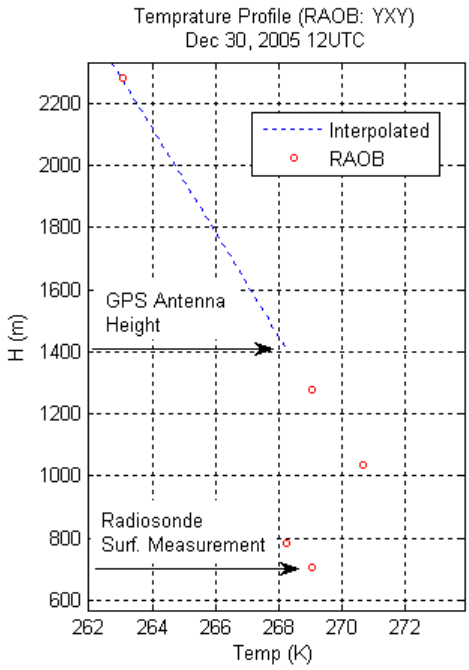

Figure 4.2- A Closer view at lower levels of Fig. 4.1.

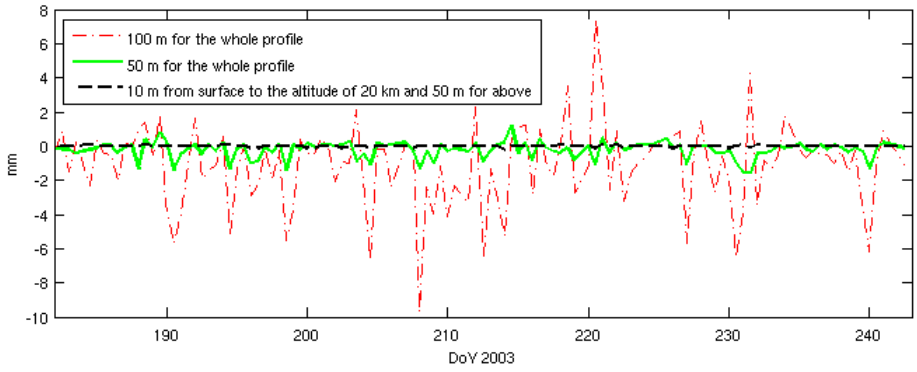

Figure 4.3- Effect of changing the integration step size for 5 degree slant total delay ray tracing result compared to a step sizes of 5 m for the whole profile. RAOB station: Churchill, Canada.

A horizontal interpolation may also be required when the user location is separated horizontally from the location of the data source profile(s). This is mainly the case when

NWP profiles are used for ray tracing. As will be discussed in section 4.2.2, NWP data can be available on a regular grid while the user location may not be necessarily collocated with one of the grid points. Hence horizontal interpolation approaches should be employed based on the 4 nearest neighbouring grid points. A final profile can be made using an inverse distance weighted interpolation approach where weights can be derived from:

$$w_{pi} = \frac{s_{pi}^{-c}}{\sum_{i=1}^{4} s_{pi}^{-c}} \tag{4.3}$$

where w_{pi} is the weight to be used for interpolation at user point p with respect to grid point i, s_{pi} is the spherical distance between user point p and grid point i and c is the power parameter. The power parameter is usually a positive value which affects the smoothness of the surface when surface fitting with polynomials [Lancaster and Šalkauskas, 1986]. In our case a larger power parameter, for example, causes the closer grid points to have a higher contribution to the interpolated values at the user point. Interpolated parameters at the user location can then be calculated using:

$$\psi_p = \sum_{i=1}^{4} w_{pi} \cdot \psi_i \tag{4.4}$$

where ψ_i is the meteorological parameter (e.g. temperature, humidity or pressure) at grid point i.

The effect of the power parameter on the retrieved values from NWP models can be investigated. Surface meteorological values from the nearest 4 grid points of NWP models with different resolutions (see section 4.2.2 for the specification of the regional and global NWP models used here) are interpolated to the location of UNB's Suominet[1] station (a Paroscientific MET3A meteorological sensor) using two different power parameters. Figures 4.4 to 4.6 show the difference between interpolated surface pressure, temperature and water vapour pressure respectively from NWP models (global and regional) using equations (4.3) and (4.4) with $c=1$ and $c=2$ and those from the met sensor. The mean and standard deviation of differences are given in the legend of the figures. It can be concluded from the figures that there is not a significant change in the interpolated values as a result of changing the power parameter when the regional NWP model (a rather high resolution model) is used. Furthermore, while in the case of the global model (with lower resolution) a slight change in the interpolated values might occur as a result of changing the power parameter from 1 to 2, the changes are still seen to be small and have insignificant effect on most ray tracing results. Statistical tests also show that differences between the means (met sensor – NWP) when the same model is used but the power parameter is changed from 1 to 2 are not significantly different at the 95% confidence level. Hence a power value of 1 may be used for most applications. One should note that the approximate distance of the location of the UNB met sensor to the nearest 4 grid points are 3.91 km, 10.88 km, 11.95 km and 15.69 km in the case of the

[1] http://www.suominet.ucar.edu/

regional model and 28.39 km, 49.80 km, 109.17 km and 116.49 km in the case of the global model.

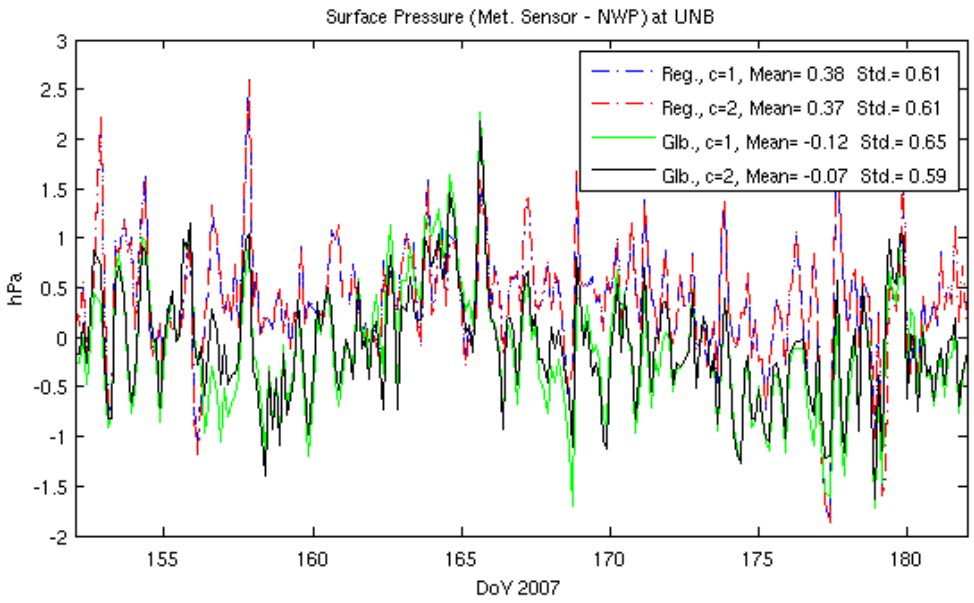

Figure 4.4- NWP (regional and global) surface pressure difference from UNB's met sensor under two different power parameters used for horizontal interpolation.

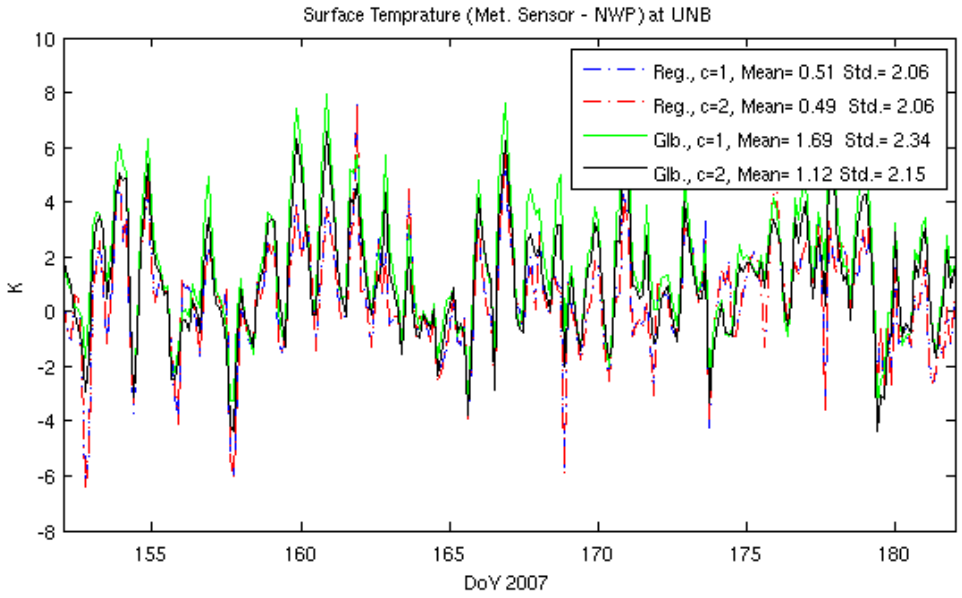

Figure 4.5- NWP (regional and global) surface temperature difference from UNB's met sensor under two different power parameters used for horizontal interpolation.

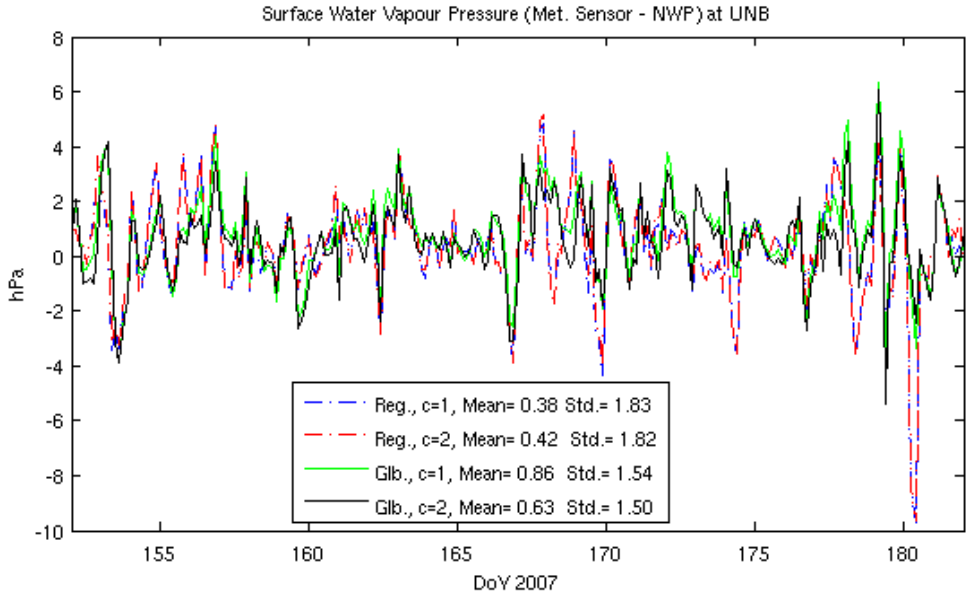

Figure 4.6- NWP (regional and global) surface water vapour pressure difference from UNB's met sensor under two different power parameters used for horizontal interpolation.

The mean difference in the values from global and regional models are significant at the 95% confidence level for both power parameters used[1]. Hence one may conclude that pressure from the global model provided closer average results to the independent measurements (met sensor) in the investigated month (see Figure 4.4). However, temperature and water vapour pressure from the met sensor are closer to the regional model than the global model (see Figures 4.5 and 4.6). The performance of regional vs. global models in zenith delay results will be investigated in section 4.4.3.

After calculating the pressure, temperature, and humidity at each level, and ignoring gas compressibility factors, one can use the following equation to derive refractivity at each level (see also equation (2.3)):

$$N_i = k_1 R_d \left(\frac{P_i - p_{wv_i}}{R_d T_i} + \frac{p_{wv_i}}{R_w T_i} \right) + \left(k_2' \frac{p_{wv_i}}{T_i} + k_3 \frac{p_{wv_i}}{T_i^2} \right) \tag{4.5}$$

where k_1, k_2' and k_3 are empirically determined constants introduced in equations (2.4); R_d and R_w are the specific gas constants for dry air and water vapour respectively; and P_i, T_i , and p_{wv_i} are pressure, temperature and water vapour pressure at level i respectively. Integration of the terms within the second parentheses in Equation (4.5) along the path results in the path non-hydrostatic (wet) delay while integration of the first

[1] Except for mean differences of water vapour pressure from NWP models with power parameter 2 which are not significantly different at the 95% confidence level. However, one should note that water vapour pressure is not the primary measurement in the met sensor or the primary humidity parameter available from NWP models. Relative humidity from the met sensor and specific humidity from the NWP models are both converted to water vapour pressure in order to be compared.

part of Equation (4.5) will result in the path hydrostatic delay. If the integrations are performed at the zenith, the resulting quantities are the ZWD and ZHD, respectively.

The neutral atmosphere contributes to the hydrostatic part of the delay up to an altitude of about 70-80 km. Figure 4.7 shows the effect of reducing the top level of integration in the zenith and 5 degree elevation slant delay. From the figure, one can conclude that ignoring the atmosphere above 60 km may result in a few mm slant delay error and less than 1 mm in the zenith delay.

The highest layers of both RAOB and NWP models end at about 20-30 km above the Earth's surface – below the top of the neutral atmosphere. The COSPAR International Reference Atmosphere (CIRA) 1986 model[1] has been used in the ray tracing package from the maximum height of RAOB (or NWP model) or 20 km above the Earth's surface (whichever is less). The values from CIRA are shifted to match the top level values of RAOB or NWP.

[1] http://modelweb.gsfc.nasa.gov/atmos/cospar1.html

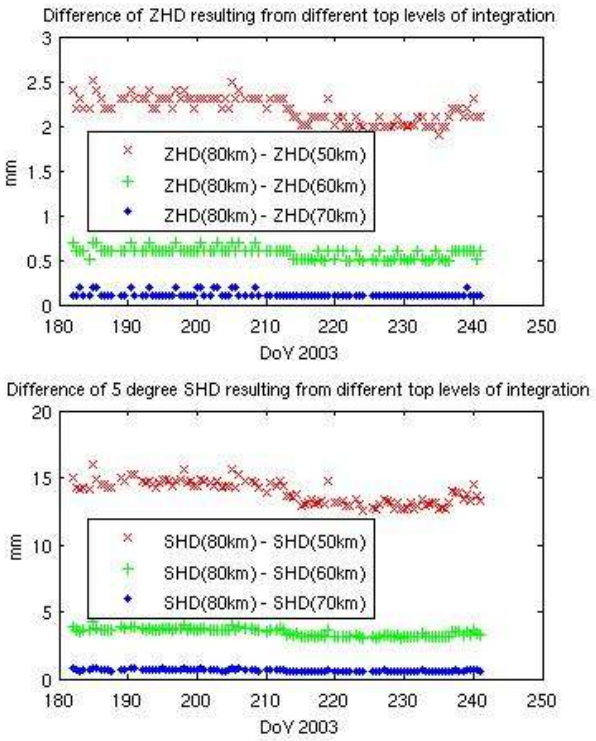

Figure 4.7- Change of zenith and slant hydrostatic delay (at 5° elevation angle) when top of the integration is 50, 60 and 70 km rather than 80km. RAOB: Churchill

4.1.1- Delay Integration

Practically speaking, ray tracing is solving the integrals in the basic equation of the neutral atmospheric delay presented in equation (2.1). In the zenith direction there is no bending effect and the distance traveled by the ray in each layer can be considered the same as user defined values (integration step size). Hence, the ZTD can be calculated simply by the following summation:

$$ZTD = 10^{-6} \sum_{i=Surface}^{80km} \left(\left(k_1 R_d \left(\frac{P_i - p_{wv_i}}{R_d T_i} + \frac{p_{wv_i}}{R_w T_i} \right) + (k_2' \frac{p_{wv_i}}{T_i} + k_3 \frac{p_{wv_i}}{T_i^2}) \right) \cdot dh_i \right) \tag{4.6}$$

where dh_i is the integration step size at level *i* and other parameters have already been introduced in equation (4.5).

In order to trace a ray in a direction other than zenith, one requires the slant distance that the ray travels in each layer. A simplified geometry of ray tracing in a symmetric atmosphere is represented in Figure 4.8. Using the initial angle of the ray at the surface, and applying Snell's law, by assuming spherical interface layers one can calculate the slant distance in each layer and also the angle at which the ray exits each layer (see, e.g., Boehm and Schuh [2003]) as follows:

$$s_i = -r_i \sin(\Theta_i) + \sqrt{r_{i+1}^2 - r_i^2 \cos^2(\Theta_i)} \tag{4.7}$$

where s_i is the distance of the traveled ray in layer *i*, r_i and r_{i+1} are the geocentric radius of middle points of two consecutives layers and Θ_i is angle of the ray at level *i* with local horizon which can be derived from the similar angle in the previous layer (e.g. in the first layer this is the user input value) and Snell's law as follows:

$$\Theta_{i+1} = \arccos\left(\frac{n_i}{n_{i+1}} \cos(\Theta_i + \delta_{i+1}) \right) \tag{4.8}$$

where n_i and n_{i+1} are the refractive indexes at two consecutive layers and:

$$\delta_{i+1} = \psi_{i+1} - \psi_i \tag{4.9}$$

where ψ_i and ψ_{i+1} are geocentre angles in two consecutive levels. The angle at which the ray exits each layer can be derived as:

$$e_{i+1} = \Theta_{i+1} - \psi_{i+1} \tag{4.10}$$

By performing the integration from the station (surface) toward the top of the neutral atmosphere one can finally calculate the angle at which the ray exits the neutral atmosphere. The geometric bending effect can be derived from the following equation and is then added to the hydrostatic delay [Boehm et al., 2006]:

$$\zeta = \sum_{i=1}^{k-1} \left[s_i - \cos(e_i - e_k) \cdot s_i \right] \tag{4.11}$$

Because of bending of the ray especially at low elevation angles, the initial elevation angle (at a user's location) is different from the geometric elevation angle of the straight direction from the user's position to a GNSS satellite, for example. The amount of bending at each layer depends on the refractivity of the layer and that of its neighbours. Hence any error in refractivity affects this angle and accumulates in consecutive layers[1]. However, one should note that the angle at which rays exit the neutral atmosphere (often known as the vacuum elevation angle) corresponds to the geometric angle which should be considered in GNSS analysis. Hence, an iterative approach can be employed to find the associated refracted elevation angle corresponding to a geometric angle at the user.

[1] This is probably a reason why integrating the path delay from surface toward the top of the neutral atmosphere has been common practice. For example, the software developed by J.L. Davis, T.A Herring, and A.E. Niell which was also used by Mendes [1999] also traces the path of a ray starting from the surface of the Earth travelling out of the neutral atmosphere. In this software, even though the user input is the vacuum elevation angle at the surface, an empirically determined relation is used to find the approximate corresponding refracted elevation angle (at the surface) to the user vacuum elevation angle. Three iterations are then carried out which result in three corresponding vacuum elevation angles and path delays. Finally a quadratic function is used for interpolation which results in the final path delay.

However for the purpose of implementing VMF1 (see Chapter 6) iteration is not required as the corresponding vacuum elevation angle to an initial elevation angle is used in the mapping function.

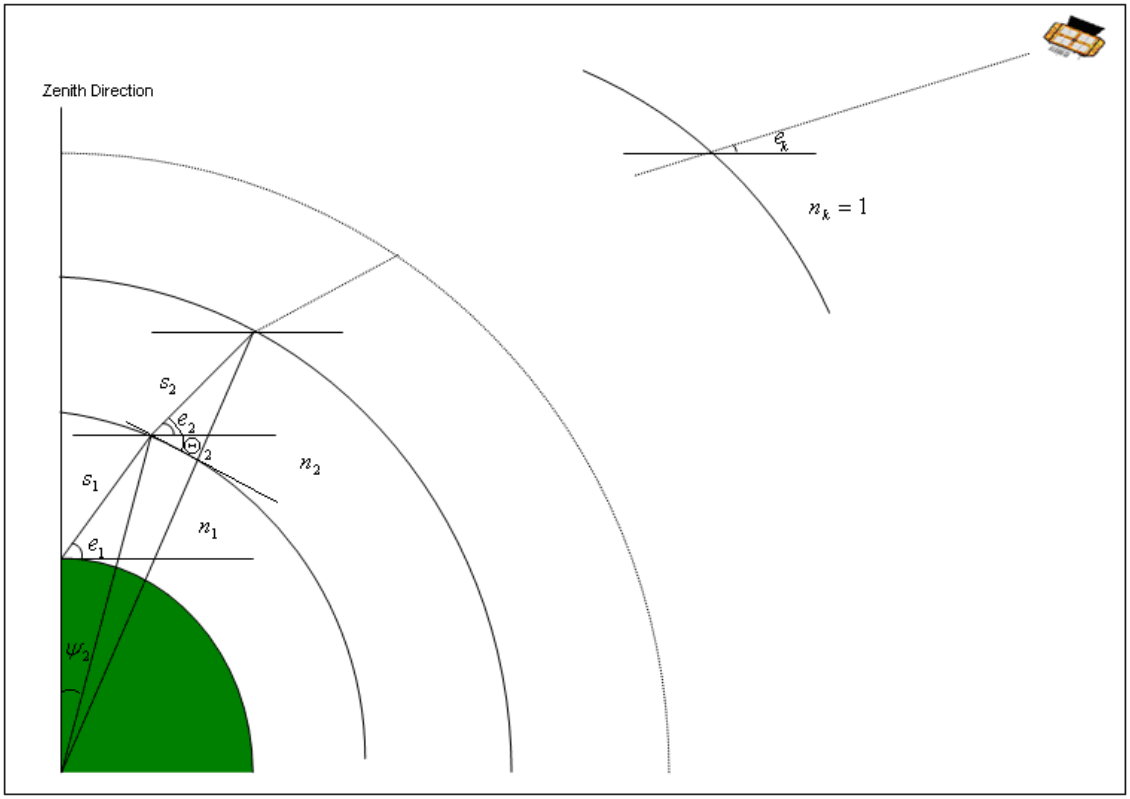

Figure 4.8- Geometry of ray tracing calculation (after Boehm and Schuh [2003, p.141]).

4.2- Data Sources for Ray Tracing

In the GNSS community, RAOB have been used for research purposes to validate atmospheric models and mapping functions (see, e.g., Mendes, [1999]; Rocken et al., [2001]). RAOBs are rather sparse in time and location. More recently, NWP models have

been used by researchers in order to assist GNSS neutral atmosphere error mitigation (see, e.g., Niell [2000]; Boehm et al. [2006]). However, performing the numerical integration of path delay in place of less challenging approaches (for example use of climate-based models) is most beneficial when there is real-time access to meteorological data sources virtually anywhere on the Earth.

4.2.1- Radiosonde

"*A radiosonde is a balloon-borne instrument used to simultaneously measure and transmit meteorological data while ascending through the atmosphere*" [FMH, 1997].

Radiosonde measurements usually include pressure, temperature and relative humidity. The wind information may also be retrieved by tracking the balloon's path. RAOB has been the main source of upper air measurements for over 70 years and still seems to be an important source of data for neutral-atmosphere studies. However, with only about 1000 RAOB sites worldwide, usually with launches twice a day, it faces spatiotemporal data sparseness. RAOB data in a ray tracing service can still be an option for research purposes, validation studies, and where the user location and time is close to an RAOB site and to launch times. Figure 4.9 shows the location of RAOB launch sites, whose data are accessible through the National Oceanic and Atmospheric Administration (NOAA) database[1].

[1] Radiosonde Database Access
http://raob.fsl.noaa.gov/

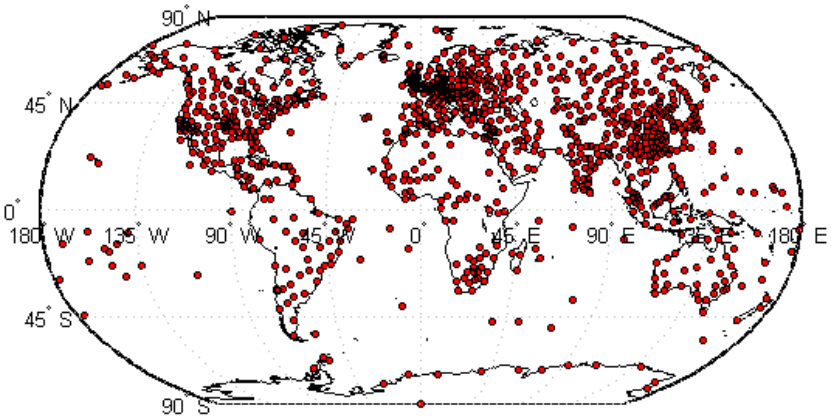

Figure 4.9- Location of RAOB launch sites whose data are accessible through NOAA database

4.2.1.1- Radiosonde Uncertainty Effects on Zenith Delay

Although the inherent uncertainties in the radiosonde measurements depend on the specific model and operational conditions, the minimum accuracy requirements for measured parameters may be adopted from FMH [1997] as stated in Table 4.1. Assuming random errors in the measured profiles and ignoring correlation among parameters one may apply the error propagation law for ZHD and ZWD as follows:

$$\sigma_{ZHD}^2 = \left(\frac{\partial ZHD}{\partial P}\right)^2 \cdot \sigma_P^2 + \left(\frac{\partial ZHD}{\partial T}\right)^2 \cdot \sigma_T^2 + \left(\frac{\partial ZHD}{\partial p_{wv}}\right)^2 \cdot \sigma_{p_{wv}}^2 \tag{4.12}$$

$$\sigma_{ZWD}^2 = \left(\frac{\partial ZWD}{\partial T}\right)^2 \cdot \sigma_T^2 + \left(\frac{\partial ZWD}{\partial p_{wv}}\right)^2 \cdot \sigma_{p_{wv}}^2 \tag{4.13}$$

where P, T and p_{wv} are pressure, temperature and water vapour pressure respectively.

Required derivations to be used in equations (4.12) and (4.13) are as follows (see equation (4.6)):

$$\frac{\partial(ZHD)}{\partial P_i} = 10^{-6}\sum_{i=1}^{n}\left(\left(\frac{k_1}{T_i}\right)dh_i\right) \tag{4.14}$$

$$\frac{\partial(ZHD)}{\partial T_i} = 10^{-6}\sum_{i=1}^{n}\left(\left(\frac{-k_1(P_i - p_{wv_i})}{T_i^{\,2}} - \frac{k_1 R_d\, p_{wv_i}}{R_w T_i^{\,2}}\right)dh_i\right) \tag{4.15}$$

$$\frac{\partial(ZWD)}{\partial T_i} = 10^{-6}\sum_{i=1}^{n}\left(\left(\frac{-k_2' p_{wv_i}}{T_i^{\,2}} - \frac{2k_3 p_{wv_i}}{T_i^{\,3}}\right)dh_i\right) \tag{4.16}$$

$$\frac{\partial(ZHD)}{\partial p_{wv_i}} = 10^{-6}\sum_{i=1}^{n}\left(\left(\frac{-k_1}{T_i} + \frac{k_1 R_d}{R_w T_i}\right)dh_i\right) \tag{4.17}$$

$$\frac{\partial(ZWD)}{\partial p_{wv_i}} = 10^{-6}\sum_{i=1}^{n}\left(\left(\frac{k_2'}{T_i} + \frac{k_3}{T_i^{\,2}}\right)dh_i\right) \tag{4.18}$$

However one should note that p_{wv_i} is not the primary radiosonde measurable. Hence first the propagation of errors in temperature and relative humidity on p_{wv_i} should be calculated. Using the following conversion equation adopted from FMH [1997]:

$$p_{wv_i} = \frac{U_i}{100}6.1121\exp\left(\frac{17.502 t_i}{240.97 + t_i}\right) \tag{4.19}$$

where U_i is the relative humidity and t_i is temperature in degrees Celsius, one can derive:

$$\frac{\partial p_{wv_i}}{\partial U_i} = 0.061121\exp\left(\frac{17.502 t_i}{240.97 + t_i}\right) \tag{4.20}$$

$$\frac{\partial p_{wv_i}}{\partial t_i} = \frac{257.7752 U_i}{\left(240.97 + t_i\right)^2} \exp\left(\frac{17.502 t_i}{240.97 + t_i}\right) \tag{4.21}$$

Using the derivations in equations (4.14) to (4.21) and assuming σ values as stated in Table 4.1 [FMH, 1997], the effect of radiosonde uncertainties (as random errors) in zenith delay integration can be calculated. ZHD and ZWD together with their propagated errors calculated from RAOB at Churchill, MB, for the month of June 2007 can be seen in Figures 4.10 and 4.11 respectively. It can be concluded that considering radiosonde measurements' uncertainties as random errors (and ignoring correlation among parameters) may only have sub-millimetre level effect on both ZHD and ZWD. While the effect is larger when the ZWD is increased, no such error variation can be seen in ZHD (mainly because the errors are small). One should note that uncertainties in CIRA values are assumed to follow those in Table 4.1, which might not be true. However, this should only have minor effect on ZHD error estimates. While the result of propagated random errors on zenith delay results seems to be promisingly small, the existence of systematic biases in RAOB is likely. Mendes [1999] simulated a constant bias based on World Meteorological Organization (WMO) accuracy limits on standard atmosphere profiles. It was concluded that a 2.3 mm bias in ZHD and biases of ~2 mm to almost 3 cm in ZWD were created. However, he stated that the accuracy of many of the current radiosonde instruments is better than the imposed WMO limits.

Table 4.1- Accuracy of related radiosonde measurements that shall be considered as minimum standard [FMH, 1997].

Variable	Accuracy
Temperature	0.5ºC
Relative Humidity	5%
Pressure	2.0 hPa (P > 300 hPa) 1.5 hPa (50 hPa < P ≤ 300 hPa) 1.0 hPa (P ≤ 50 hPa)

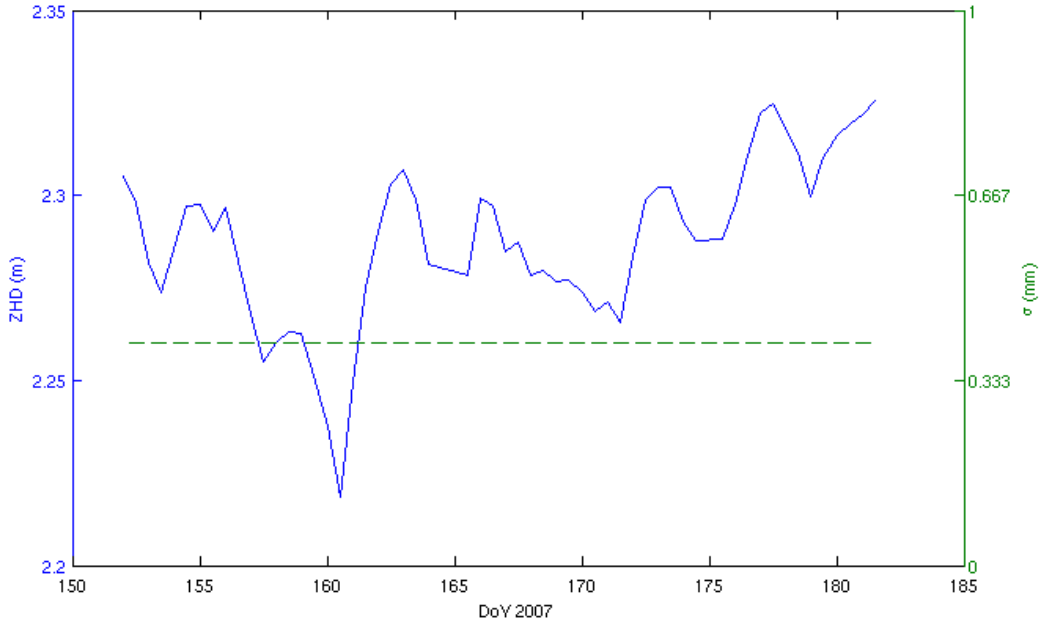

Figure 4.10- ZHD and propagated errors (dashed line scaled on the right side) calculated from RAOB at Churchill, MB.

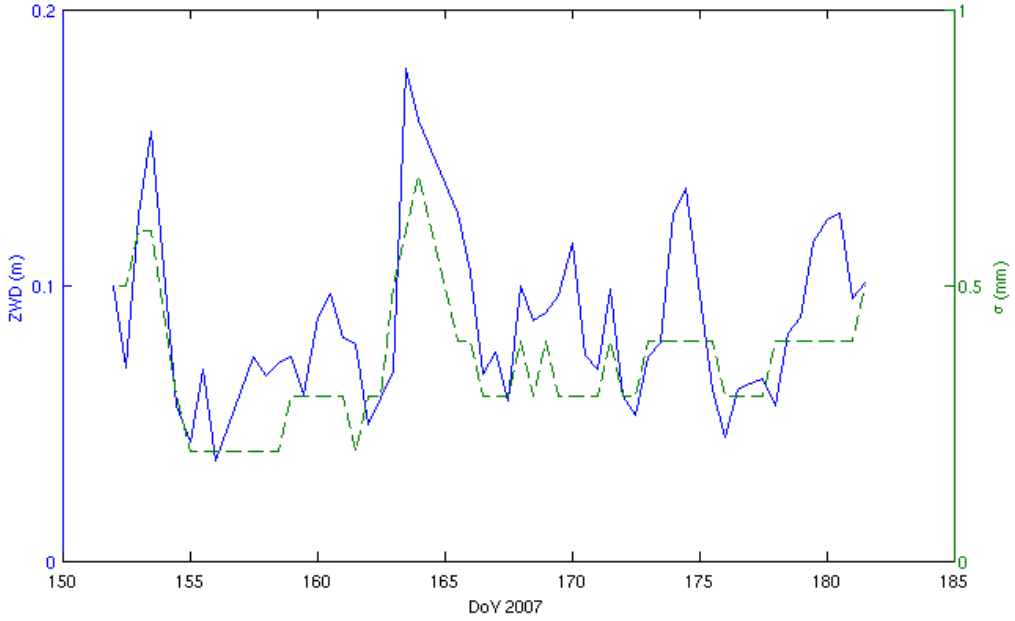

Figure 4.11- ZWD and propagated errors (dashed line scaled on the right side) calculated from RAOB at Churchill, MB.

4.2.2- NWP Models

NWP models are an alternative to RAOB with the advantage of virtually full global coverage in time and location. These models, developed by national weather offices, may cover a region of the world or the entire world. Among the models that have been used by the GNSS research community are the Canadian GEM, the European ECMWF and the US RUC models, to name a few. GEM models have been employed in this dissertation and will be briefly explained in this section.

The Canadian Meteorological Centre (CMC) has developed global and regional GEM models. Both the global and regional models are available at high and low resolutions.

However, the use of a high resolution NWP model seems to be more beneficial for GNSS applications due to proximity of grid points to user locations. Therefore high resolution models have been employed in this work and will be briefly explained here.

Before September 20, 2007 at 12 UTC (the initialization time), the global model was available at a resolution of 1°×1°. Subsequently, the global model became available on a 283 × 601 latitude-longitude grid (covering all the Earth except above 85°N and below 84.2°S) at a resolution of 0.6°×0.6° (which corresponds approximately to a 66 km × 66 km grid size at the equator). The model has 28 isobaric levels. As of June 3, 2008, at 12 UTC (the initialization time), the global model covers all the Earth and contains 301 × 601 grid points. The regional GEM model contains 501 × 399 grid points with a 15 km resolution at 60°N which is made available with 28 isobaric levels. This model covers most of North America and adjacent waters.

In addition to surface values (values at some fixed height above ground), vertical coverage of the three-dimensional fields for both global and regional models is provided for the following isobaric levels (hPa): 1015, 1000, 985, 970, 950, 925, 900, 875, 850, 800, 750, 700, 650, 600, 550, 500, 450, 400, 350, 300, 275, 250, 225, 200, 175, 150, 100 and 50. Most of these levels are the same as the standard mandatory reporting levels in RAOB. Also a few intermediate levels, especially near the surface and near the tropopause, are added to improve vertical resolution at those levels [Pelletier, 2008]. Regional 0-48 hour forecasts and global 0-144 hour forecasts are issued twice a day,

based on 00 UTC and 12 UTC initialization times. All fields are available at 3-hourly intervals[1].

4.3-Online Ray Tracing Package

An online ray tracing package (hereafter referred to as Online-RT) has been developed to provide zenith and slant delays at a user location using RAOB and NWP models. In addition, the online service provides latest maps of ZHD, ZWD and gradients using NWP models and provides comparisons with UNB3 and UNB3m models. The service is currently available at http://galileo.gge.unb.ca.

Code for data access and pre-processing has been written in Linux shell script, while the ray tracing and map-generation parts are written in MATLAB®. Although the basic ray tracing algorithm is the same for both RAOB and NWP models, data retrieval and manipulation are different and need to be addressed separately.

Online-RT provides automatic data access to the closest possible spatiotemporal RAOB to the user requested location and time via NOAA's online database. The user is informed of the distance and azimuth of the nearest possible RAOB. Currently, NOAA's online database provides RAOB data from 1994 up to today. Although these data have

[1] High-resolution CMC GRIB (see next page) dataset
http://www.weatheroffice.gc.ca/grib/High-resolution_GRIB_e.html

gone through extensive quality control analysis, further quality checks have been found to be necessary for our purpose.

Canadian NWP data is provided in gridded binary (GRIB) files. The files are based on parameters rather than coordinates; i.e., each file includes one specific parameter of just one specific isobaric layer for the whole set of grid points (180,901 and 199,899 points for the global and regional models respectively). Therefore, in order to achieve a vertical profile of meteorological parameters above a site, all GRIB files of related meteorological parameters need to be read. The GRIB files for each initialization time (00 and 12 UTC) are currently made available about 5 and 3 hours after the initialization time for the global and regional models respectively. Transferring all appropriate files from the Meteorological Service of Canada's[1] server to a local database also takes about 1-1.5 hours depending on network traffic. Therefore, in order to make sure that at any time the Online-RT can provide results at the current time, the GRIB files for forecasts up to 24 hours ahead are transferred. The total size of appropriate GRIB files is about 192.5 megabytes and 224.5 megabytes for global and regional models per initialization time respectively; i.e., a total size of about 834 megabytes per day for both global and regional models.

[1] The Meteorological Service of Canada makes CMC's GEM models output available to private sector meteorologists, academics and general public. http://www.weatheroffice.gc.ca/grib/index_e.html

Specific humidity is provided in the GEM models as the measure of humidity whereas dew point temperature is accessible by RAOB. However, both measures of humidity are converted to water vapour pressure. Dew point temperature can be converted to water vapour pressure through knowledge of saturation vapour pressure; large numbers of formulae are available to do this. Mendes [1999] tested four of the most widely used formulae and found differences as large as 3 mm for ZWD. He recommended the Wexler [1976] formula for use in saturated vapour pressure computations which is also the formula used here. For converting specific humidity to water vapour pressure the following approximate formula which is sufficiently accurate (see e.g. Cole [1975]) in normal conditions[1] can be used:

$$p_{wv} \cong \frac{P \cdot q}{0.622} \tag{4.22}$$

where p_{wv} *is* the water vapour pressure in hPa, P is the total pressure in hPa and q is the specific humidity in kg/kg.

A web interface to ask for a user input file (including user location and time) and email address has been developed. After accessing the data, and carrying out data manipulation and ray tracing, the results are sent back to the user by email. The output includes zenith and slant (at a user-requested elevation angle) hydrostatic and wet delays, predicted zenith values from the Saastamoinen model [Saastamoinen, 1972a, 1972b, 1973; Davis et

[1] In very humid condition the given formula may over estimate the ZWD by less than 1% compared to the accurate relation of : $p_{wv} = \frac{P \cdot q}{(1-0.622)\cdot q + 0.622}$.

al., 1985] with surface pressure interpolated to the user height from the models or radiosonde profiles and vacuum or unrefracted elevation angle (called VEA in Online-RT output). A sample output for a user request of two locations using RAOB can be seen in an example email message in Figure 4.12. As can be seen in this sample output, the closest available RAOB launch site information, which has been used for each requested location, is also provided.

```
Dear user:" c447j@unb.ca ", Thanks for your request from "ONLINE RAYTRACING"

User requested data source: RAOB
User submitted data (edited):
 47.80  -124.40   56.00  2007  7  20  0  2007  7  20  12   5.00
 74.95  -96.64   60.00  2007  7  19  0  2007  7  19  6   5.00
--------------------------------------------------------------------------------

*** RESULT for line "1" of user input file:

WMO: 72797  Cls. rnk.: 1  RAOB_Lat:  47.95 RAOB_Lon: -124.55 RAOB_H:  56.00 Dist. from User:  20.10
Km  Azim. from User to RAOB:  326.1

DoY,     YEAR,       USER H, ZHD(Sa.),ZWD(Sa.),VEA,ZHD(RT),ZWD(RT),SHD(RT), SWD(RT)
201.0000,2007.0000,56.0000,2.2922,0.1617,4.7987,2.2914,0.1698,23.9599,1.8970
201.5000,2007.0000,56.0000,2.2853,0.1535,4.7988,2.2846,0.1701,23.8940,1.8936

*** RESULT for line "2" of user input file:

WMO: 71924  Cls. rnk.: 1  RAOB_Lat:  74.72 RAOB_Lon: -94.98 RAOB_H:  40.00 Dist. from User:  54.87
Km  Azim. from User to RAOB:  117.1

DoY,     YEAR,       USER H, ZHD(Sa.),ZWD(Sa.),VEA,ZHD(RT),ZWD(RT),SHD(RT), SWD(RT)
200.0000,2007.0000,60.0000,2.2684,0.0687,4.8188,2.2686,0.0956,23.6614,1.0602

--------------------------------------------------------------------------------
"ONLINE RAYTRACING" is for limited research purposes with NO guarantee of any kind. Questions and
comments are welcome. Please contact: r.ghoddousi@unb.ca
```

Figure 4.12- A sample output file of the Online-RT package

Figure 4.13 shows the major steps carried out in the Online-RT package. The website also displays near real-time global maps of zenith hydrostatic and wet delays and total, NS and east-west (EW) gradients using the latest available Canadian global NWP model along with maps showing the differences between the hydrostatic, wet, and total zenith

delays computed using the NWP model and the values computed using the UNB3 and UNB3m climatological models.

In order to generate the latest global ZHD, ZWD, and comparison maps, almost all GRIB files are read and first converted to a 3D array of 24×4×180,901 cells where 24 is the number of layers, 4 represents the number of parameters (elevation, pressure, temperature, and specific humidity), and 180,901 is the number of grid points in the global model. One should note that there are a total of 29 layers available (including the surface layer). The layers above 200 hPa isobaric level make less than a 0.5 mm contribution to ZWD and hence can be ignored to speed up the map generation process. Each of the 180,901 matrices of 24×4 cells is then used for the ZWD calculation. It has been shown that the Saastamoinen model can provide ZHD with sub-millimetre accuracy provided that accurate (accuracy of better than ~0.4 hPa) surface pressure is available (see, e.g., Mendes [1999]). Therefore, the procedure for ZHD map generation uses only the surface pressure values and the Saastamoinen model. ZHD calculation is also carried out using mean sea level (MSL) pressure. These MSL ZHD and ZWD values at grid points are used for generating maps of NS and EW ZHD and ZWD gradients as well as the magnitude and azimuth of ZTD gradients.

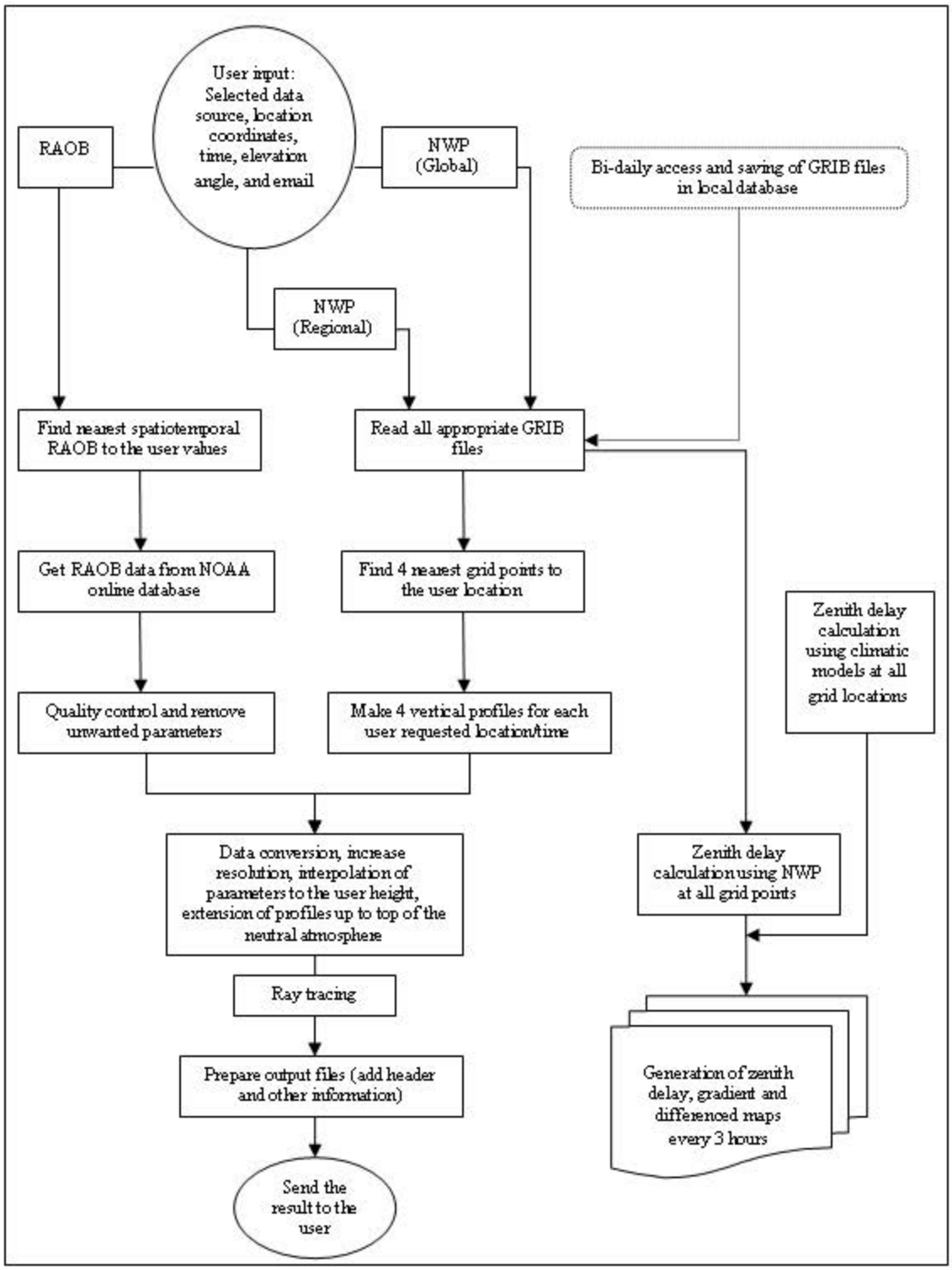

Figure 4.13- Major steps in Online-RT package.

The map generation procedure is repeated every 3 hours using the NWP data providing the shortest possible forecast time. Therefore, at any time, public users can have access to the near real-time global maps of ZHD, ZWD, gradients, and comparisons, which are being updated every 3 hours. The UNB climatological model values are also calculated at the location of grid points and then differenced from the NWP-calculated values in order to generate the difference maps. Sample maps provided by the Online-RT package at an arbitrary epoch are provided in Appendix III. All near-real-time maps are available publicly through the web site. A potential future use of the zenith delay map generation service could be in the Interferometric Synthetic Aperture Radar (InSAR) application (see, e.g., Foster et al. [2006]; Li et al. [2006]) where a high resolution weather model can be used to reduce the atmospheric effect on InSAR interferograms.

The performance of the climatological models may be evaluated using NWP results. For example, 3-hourly extreme differences of ZHD from global and regional NWP models and those from UNB3 are plotted in Figures 4.14 and 4.15 respectively. These result from monitoring of generated 3-hourly near-real-time maps over 16 months (from 1 July 2007 to 31 October 2008) such as those presented for an arbitrary epoch in Figures III.6 and III.7 (Appendix III). The average of positive and negative extreme values can be seen in the titles of Figures 4.14 and 4.15. Note that larger negative extreme difference values occur in the global model. These extreme negative differences typically occur in the belt

around Antarctica where UNB3, which is based on a standard atmosphere[1], usually overestimates mean sea level pressure. The increased variability in negative extreme values may indicate more variability in low pressure systems.

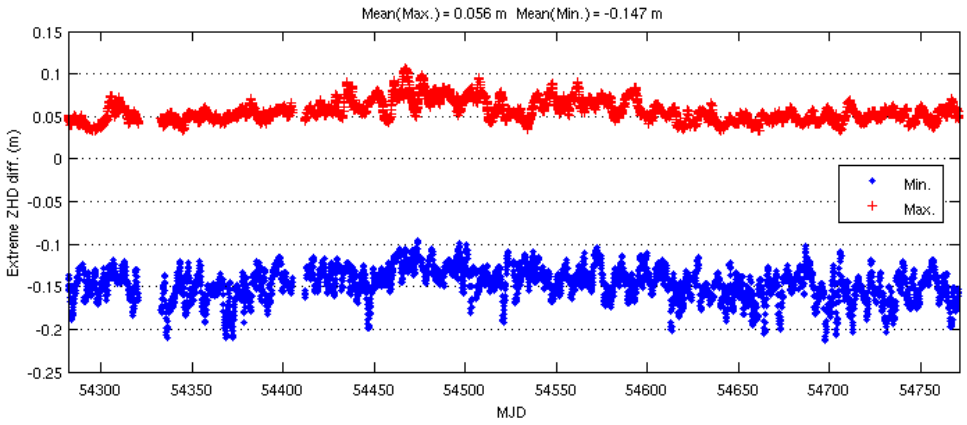

Figure 4.14– Extreme difference between ZHD from global high resolution Canadian NWP model and UNB3 calculated over 16 months.

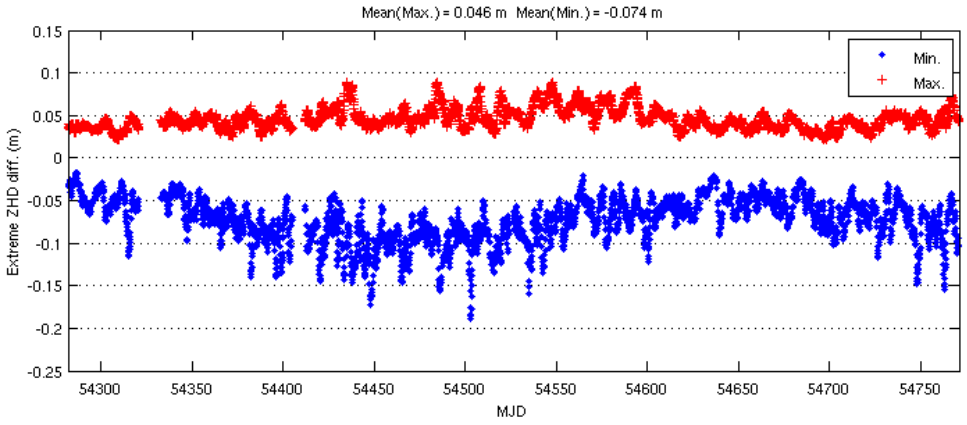

Figure 4.15– Extreme difference between ZHD from regional high resolution Canadian NWP model and UNB3 calculated over 16 months.

[1] UNB3 "*uses a look up table of meteorological parameters derived from the 1966 US Standard Atmosphere Supplements whose values vary over latitude and season*" [Collins, 1999].

4.4- Validation of Results

Results from available data sources in the ray tracing package (including global and regional Canadian NWP and RAOB) have been compared to each other and also compared with independent sensors including precise barometers and WVR. Retrieval of radio phase delay from WVR is discussed in section 4.4.1. A brief review of a unique project to validate the NWP zenith delay results in the marine areas of mid and high latitudes using sensors on a moving platform follows. A month long comparison of results from NWP, RAOB and WVR are presented in section 4.4.3.

4.4.1- Water Vapour Radiometer

WVR measures sky brightness temperature which is the temperature of a blackbody that is emitting at the same intensity as the sky (see e.g. Solheim [1993]). The atmospheric parameters which can usually be retrieved from a WVR are: integrated water vapour, integrated liquid water, and radio phase path delay. The latter is of interest to the GNSS community as it is usually treated as an independent observation of zenith or slant non-hydrostatic delay for validation of GNSS non-hydrostatic delay estimates or assisting processing scenarios.

An atmospheric spectrum in the vicinity of 22.235 GHz (where maximum atmospheric absorption occurs) shows that there exist two frequencies (about 20.4 GHz and 23.8 GHz) where the absorption is relatively independent of pressure (altitude). One of these

frequencies is usually used in WVRs[1] to minimize the sensitivity of brightness temperature to water vapour. Furthermore, in order to separate the effect of cloud liquid from water vapour, another frequency (usually 31.4 GHz) is also employed in dual frequency WVRs.

Radio phase path delay can be retrieved from opacity. Opacity may be defined as:

$$\tau_i = \ln\left(\frac{T_{mr} - T_{\cos}}{T_{mr} - T_{bi}}\right) \tag{4.23}$$

where T_{mr} is the mean radiation temperature, $T_{\cos} = 2.7K$ is the cosmic background temperature which results from the residual cosmic radiation from outer space that is left from the Big Bang (see e.g. Leick [2004]), and T_b is the sky brightness temperature which is the basic WVR observable and *i* represents the frequency.

By using opacities at two frequencies a linear retrieval equation for slant non-hydrostatic delay (*SWD*) from the opacities can be written as:

$$SWD = C_0 + C_1 \cdot \tau_{23.8} + C_2 \cdot \tau_{31.4} \tag{4.24}$$

where C_0, C_1 and C_2 are the retrieval coefficients. One way to derive the retrieval coefficients is by calculating the theoretical opacities by numerical integration through RAOB and then estimating the coefficients using a bilinear regression to opacities, liquid and vapour arrays (see e.g. Solheim [1993]). The brightness temperatures measured by

[1] In the Radiometrics WVR-1100, for example, the 23.8 GHz frequency is chosen because it is in a reserved research waveband where no radio transmission is allowed [Solheim, 1993].

WVR are used to calculate opacities at each of the two frequencies (see equation (4.23)). Using the retrieval coefficients and opacities one can calculate the SWD from equation (4.24).

From the retrieval approach briefly discussed above, one can conclude that WVR phase delay results are dependent on RAOB data at a particular location or locations. In practice, long term RAOB data from the same climatological region in which the WVR is operating are used for deriving the coefficients. While among the WVR retrievable parameters, phase delay is less dependent on the location of RAOB (and change of the retrieval coefficients), this dependence has been investigated during a field experiment carried out as part of this dissertation research work.

4.4.2- Precise Barometer and WVR on a Moving Platform for NWP Validation

There are very few reports on the performance of a WVR on a moving platform. Researchers at the University of Miami set up a WVR on the Royal Caribbean Cruise Line ship Explorer of the Seas [Minnett, 2004]. The experiment was also used to compare WVR and GPS results [Rocken et. al., 2005].

During the 2005 Canadian research icebreaker Canadian Coast Guard Ship (CCGS) Amundsen's mission in the Canadian Arctic an experiment was carried out by the author to investigate the performance of the Canadian regional NWP model. As a part of this experiment our Radiometrics WVR-1100 was set up on the ship's deck (see Figure 4.16)

and was programmed to record zenith as well as some specific slant measurements. A precise barometer[1] was also set up on the ship and provided a continuous record of the surface atmospheric pressure.

Figure 4.16- WVR onboard CCGS Amundsen

As mentioned in section 4.4.1 non-hydrostatic delays from a WVR are actually obtained from the observed brightness temperature and the estimated retrieval coefficients. These coefficients can be estimated from long term radiosonde measurements in the same climatological region as that in which the WVR operates. A retrieval program provided by Radiometrics Corporation has been used in this experiment. In order to investigate how different coefficients might affect the final WVR ZWD, three scenarios have been considered:

[1] A Honeywell Precision Barometer with accuracy of better than ±0.4 hPa (from -40 to 80°C) [Honeywell, 2005] was validated using the Suominet station barometer at UNB before installation on board the CCGS Amundsen.

1. Default retrieval coefficients derived from a radiosonde near UNB at a latitude of ~46° N.
2. Retrieval coefficients from the nearest radiosonde using the 3 months of data that span the date of measurement. Different sets of coefficients (from 6 years of data from 10 nearby radiosondes) were derived and used based on the proximity of the ship to a particular radiosonde site during the expedition (see Figure 4.17).
3. Same as 2 but using the entire 6 year radiosonde data sets.

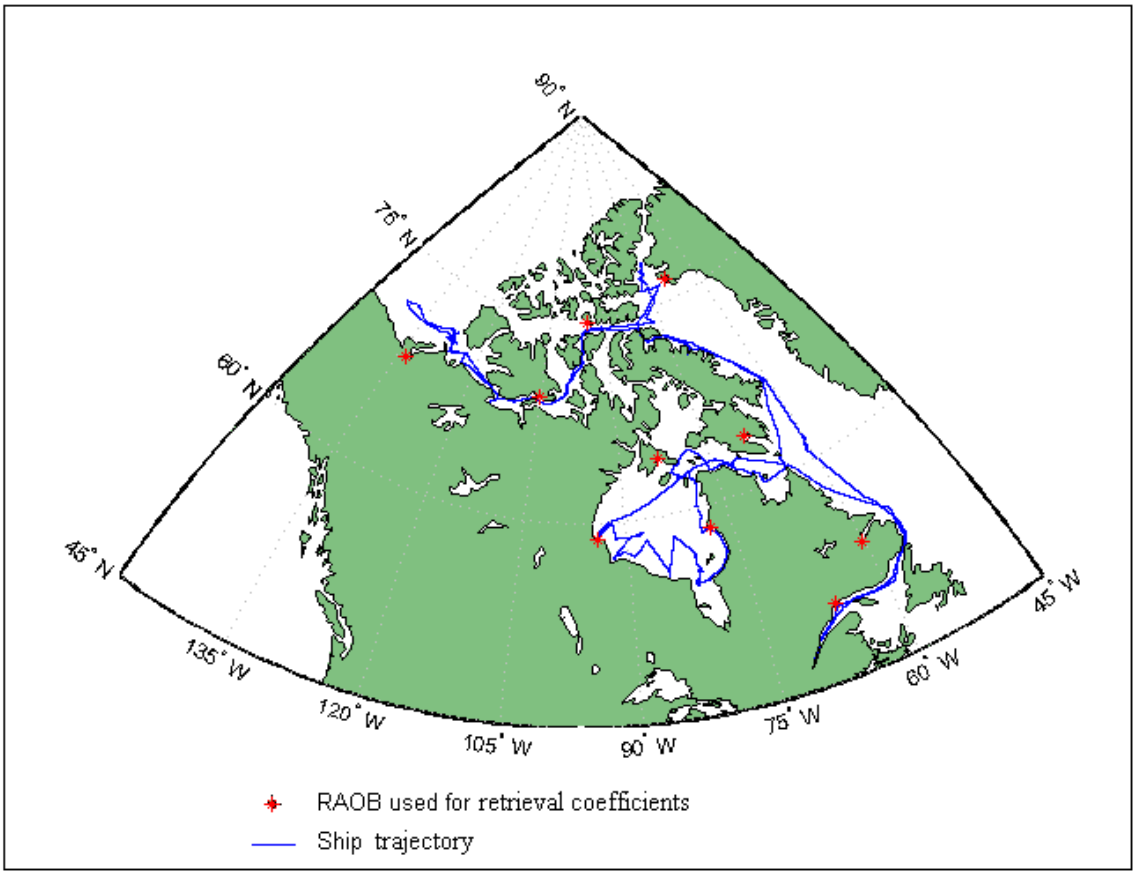

Figure 4.17- CCGS Amundsen expedition track on her 2005 mission and location of radiosonde sites used for retrieval coefficients.

The difference between the results from scenarios 2 and 3 was found to be negligible (about 0.04 cm in ZWD on average). Figure 4.18 shows the measured ZWD during the expedition as well as absolute and relative differences of ZWD resulting from scenarios 1 and 2. As can be seen in Figure 4.18c the change of retrieval coefficients affect the resulted WVR ZWD by less than 4% in most cases. The result from scenario 2 has been selected as the final WVR ZWD in this study.

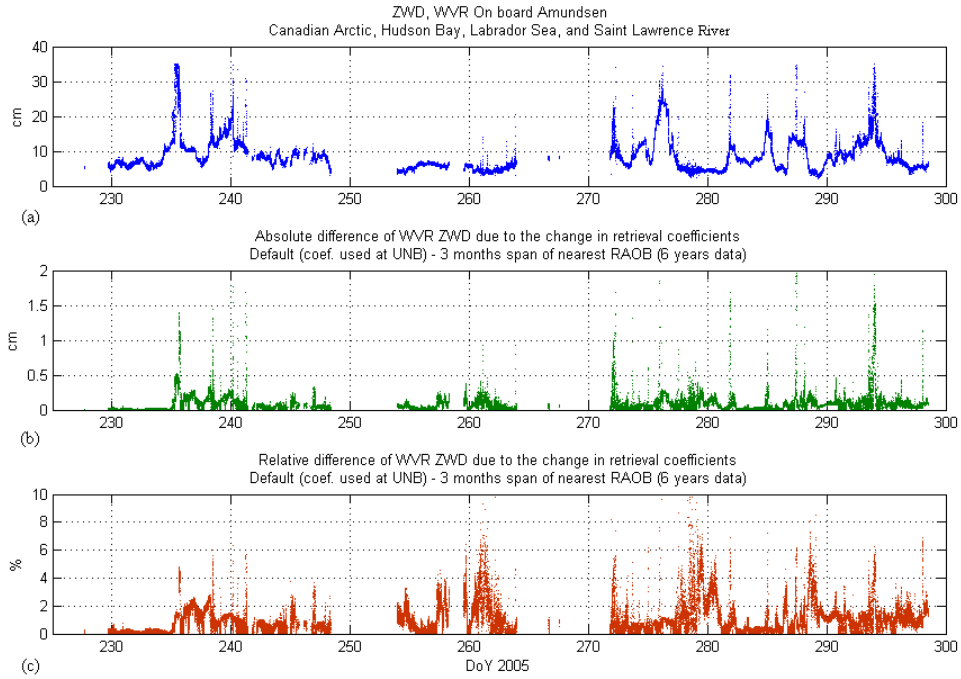

Figure 4.18– a) ZWD during the expedition. b) Absolute difference between ZWD from scenarios 1 and 2. c) Relative difference between scenarios 1 and 2.

In order to carry out the tip curve calibration[1] of the WVR noise diode injection temperatures, the WVR needs to be accurately levelled which was not possible on board the vessel. Therefore the calibration values obtained before the expedition were used.

Figures 4.19 and 4.20 show a comparison between NWP and barometer pressure measurements corrected to the GPS antenna height during parts of the expedition (Canadian Arctic, Sub-Arctic and mid-latitudes). The RMS of the differences is less than 1 hPa for the compared data series. Assuming no error in the Saastamoinen model, height and latitude, an uncertainty of less than 1hPa in surface pressure measurement will result in less than 2.3 mm error in the ZHD. The figures also include the predicted pressure from UNB3, a climate based neutral atmosphere model. The models and measurements are in closer agreement in Figure 4.20 (mid-latitudes) than in Figure 4.19 (high latitude). However, in the case of NWP, this may be partly due to the fact that only initialization (00 and 12 UTC) data were used in Figure 4.20.

[1] Tip curve calibration is a technique to calibrate instrument gain and accurate estimate of brightness temperature without any a priori knowledge of either. In this technique several sky observations are made at different elevation angles which provide observations through different air masses. The assumptions made are that the atmosphere is horizontally homogeneous and opacity is a linear function of air mass (hence the linear regression to line through the opacities must pass through the origin at zero air mass and zero opacity). The regression coefficient of the linear fit to opacities is an indicator of the calibration acceptance. One may refer to e.g. Solheim [1993] or Leick [2004] for more details on this technique.

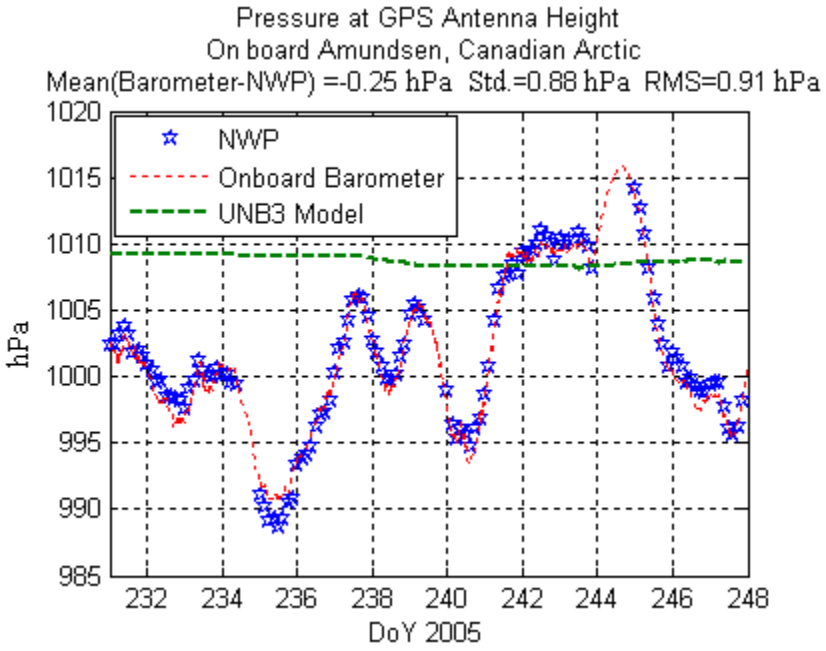

Figure 4.19– Measured and NWP Pressure values in the Canadian Arctic.

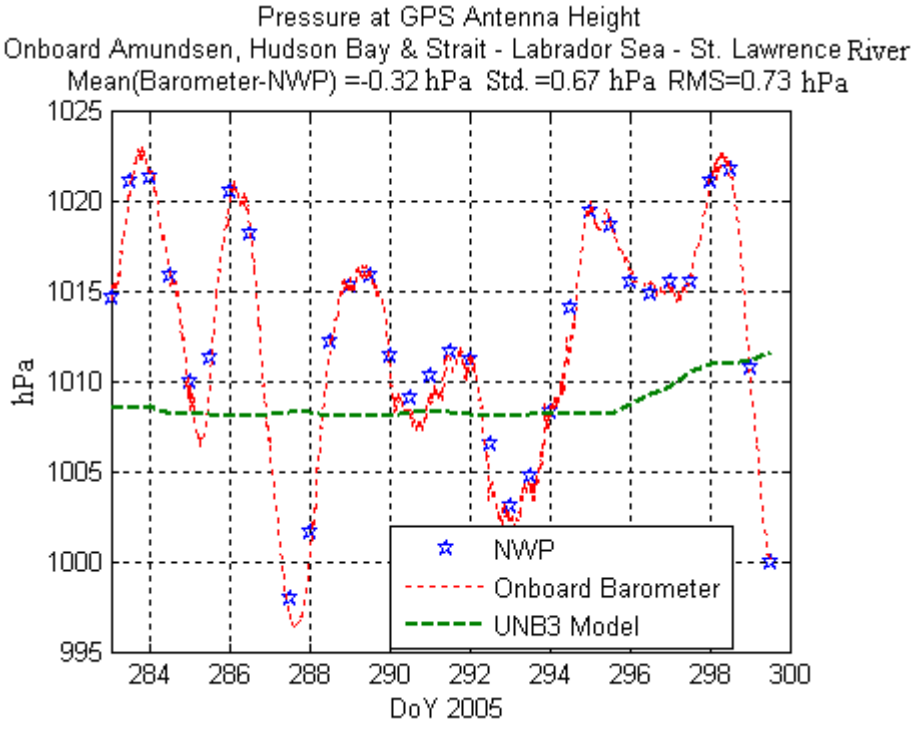

Figure 4.20– Measured and NWP Pressure values in the Canadian-Sub Arctic and mid-latitudes.

Figures 4.21 and 4.22 show the WVR ZWD results as compared with those calculated from the NWP. The RMS of the difference between smoothed WVR (using a MATLAB built-in function of 50^{th} order finite impulse response low pass filter which in this case is roughly close to a 1-hour moving average filter) and NWP are at the cm level. The figures also include the ZWD from the UNB3m model. As expected, the uncertainty in retrieving the wet delays in this study is about 1 order of magnitude larger than those of the hydrostatic delays. Liquid water or ice on a WVR antenna degrades the accuracy of brightness temperature measurements [Ware et al., 2004]. Therefore recorded data with liquid water values above 0.05 cm were removed before comparison. However, the largest difference usually occurs during the time of rapid change in wet delays at peak values. Apart from systematic and random errors that might exist in both the WVR and NWP, the larger differences at peak values might be due to local effects on the WVR measurements onboard and local scale weather phenomena which might not be detectable by the NWP with a 15 km resolution.

The values compared in Figures 4.21 and 4.22 are zenith measurements and not the slant–mapped-to-zenith values. This is of concern on a moving vessel as the true elevation angle of the WVR's line of sight may change due to the roll and pitch of the vessel. However, a maximum 7 degree roll or pitch which was the case during a few periods of the expedition does not have a significant effect on the WVR zenith measurements. Calculating the NMF for an 83 degree elevation angle shows that a 7 degree roll or pitch can cause about 0.75% error on the WVR ZWD results and is, therefore, insignificant.

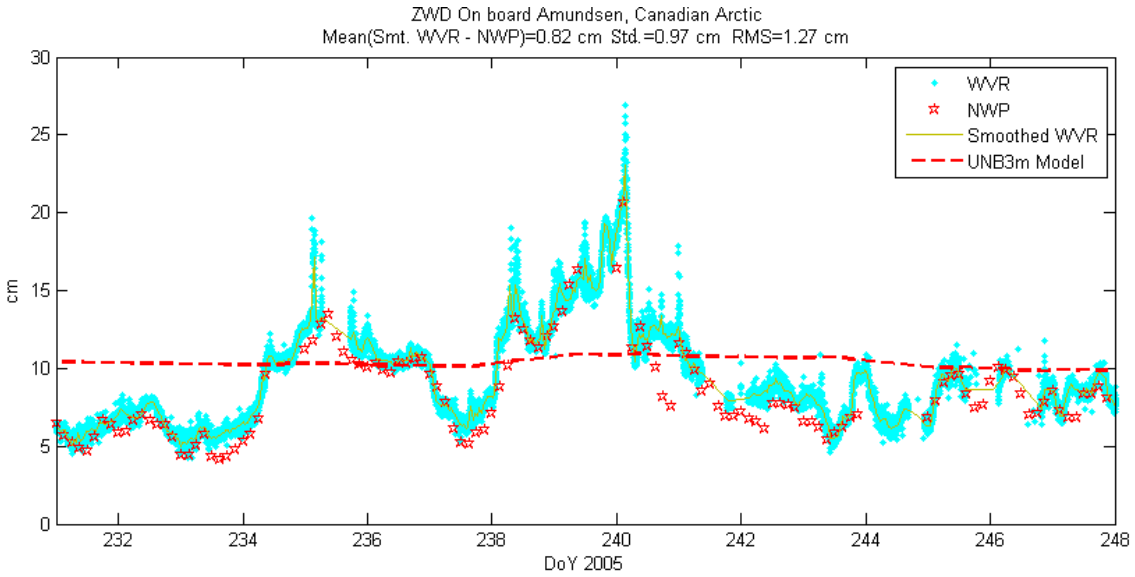

Figure 4.21– WVR and NWP ZWD in the Canadian Arctic

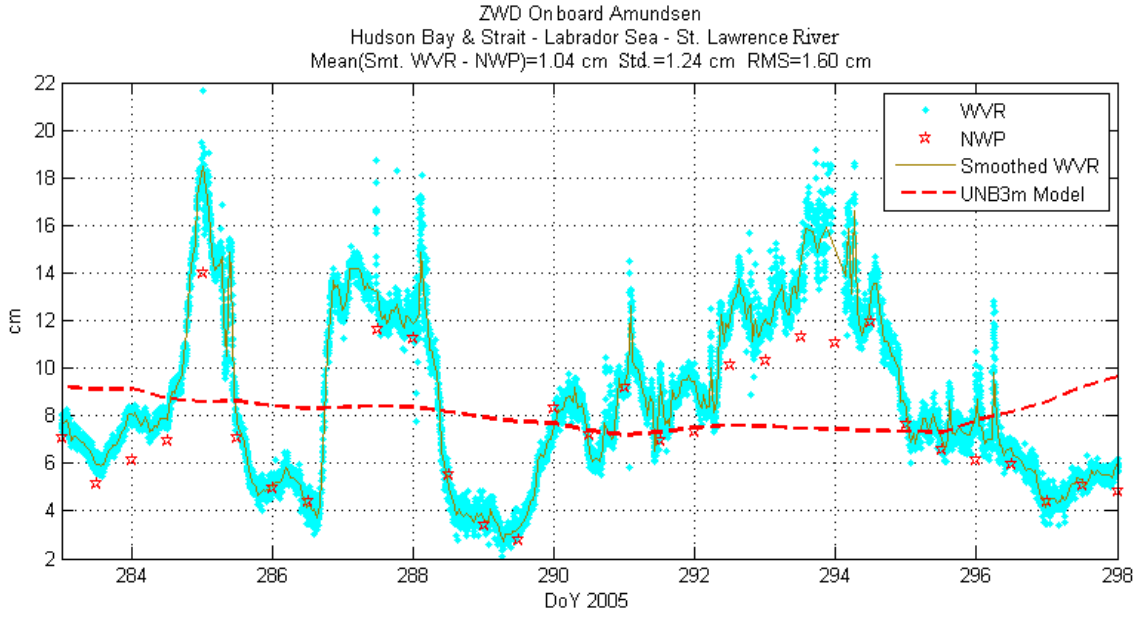

Figure 4.22– WVR and NWP ZWD in the Canadian Sub Arctic and mid latitudes

4.4.3- Validation at RAOB Locations and WVR at UNB

In order to compare the results of ray tracing from different available data sources in Online-RT, the package was employed to compute the results for zenith delays at over 66 radiosonde sites (see Appendix I) in the area covered by both regional and global models. The comparison took place using data over the month of June 2007. It should be noted that the compared data sets are highly correlated because the radiosonde data are assimilated into both models. However, currently there is a major difference in data assimilation schemes used by the two models[1]. Furthermore, data sources available for the two models are different due to the difference in time at which the models are run [Verner, 2008].

The relevant statistics resulting from a comparison of the global and regional models at the location of radiosonde sites are provided in Table 4.2. The resulting ZHD values from the two models are in good agreement. The RMS of the ZHD difference from the global and regional models over the compared month and locations is 1.7 mm. The RMS increases to 11.3 mm for ZWD.

[1] Currently, the regional model uses a three-dimensional variational data assimilation (3D-Var) system while the global model uses a four-dimensional variational data assimilation (4D-Var) system. One major difference between these two data assimilation approaches is that in the 4D-Var, observations are actually assimilated at their valid time of observation, while in 3D-Var observations received in a period of time are all used as if they were taken at the main synoptic time [Verner, 2008]. Hence the global model currently uses a more realistic data assimilation approach. This might be a reason why one may not simply expect more accurate zenith delay results from the regional model because of higher resolution.

Table 4.2- Difference between global and regional NWP model results

Global-Regional	Mean diff. (mm)	Std. (mm)	Abs. max diff. (mm)	No. of data points
ZHD	0.6	1.6	9.5	16080
ZWD	-0.4	11.3	76.5	16080

In Figure 4.23, one can see the histograms of the ZHD and ZWD differences between the values from the global and regional models and those from the radiosondes. Also in Table 4.3, the statistics of these comparisons are provided. The regional model has provided results slightly closer to the RAOB values. This is partly due to the higher resolution of the model and hence less uncertainty caused by our spatial interpolation techniques between grids. The disagreement in ZWD is about five times larger than ZHD (note the different horizontal scales in Figure 4.23). This is mainly due to the larger uncertainty in observation and prediction of humidity in all data sources. Furthermore, as mentioned before, linear interpolation of humidity and temperature (which might not always be valid) can be another source of error. However, all of the interpolation techniques may cause large errors under unusual local weather conditions. This is of more concern when there is a large difference between the user height and the surface level of the data source. This can also result in outlier values in some cases. The outlier values in the investigated data sets of regional and global NWP models compared to RAOB have occurred at the same times and locations. This can be due to local weather anomalies affecting a radiosonde or data quality issues.

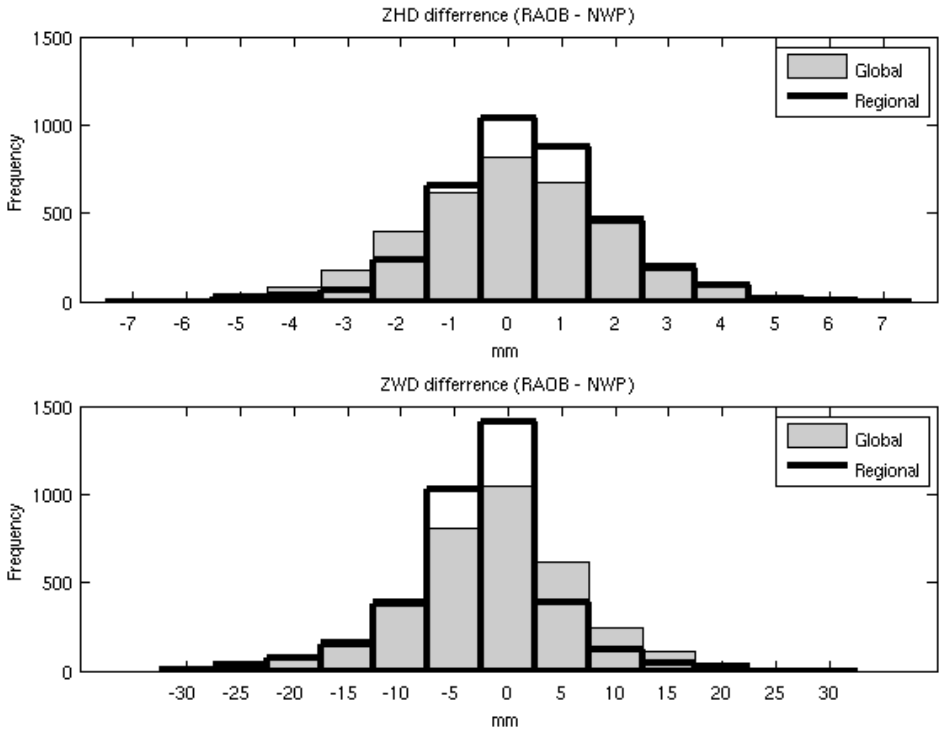

Figure 4.23- Histograms of differences of ZHD (upper plot) and ZWD (lower plot) computed from radiosonde data and NWP models.

Table 4.3- Statistics of comparison results between NWP models and RAOB.

	ZHD				ZWD			
	Mean diff. (mm)	Std. (mm)	Abs. max diff. (mm)	No. of data points	Mean diff. (mm)	Std. (mm)	Abs. max diff. (mm)	No. of data points
RAOB-NWP (Regional)	0.3	1.9	45.7	3688	-2.7	8.1	122.4	3688
RAOB-NWP (Global)	0.1	2.2	46.1	3688	-1.7	10.0	119.5	3688

In order to compare the NWP models' zenith delay results with independent approaches, WVR measurements and surface pressures from UNB's Suominet station were employed for ZWD and ZHD estimation respectively. The UNB Radiometrics WVR-1100 operates about 5 m (horizontally) from the UNB Suominet station. Brightness temperatures are measured by the WVR at different azimuths and elevation angles. In this study, slant wet delays above a 10 degree elevation angle at the WVR were converted to ZWD using the NMF. The resulting WVR ZWD data set was then averaged over 3-hour step sizes for comparison with NWP ZWD results. The Saastamoinen model together with pressure measurements from the Suominet station were used to estimate ZHD.

In Figure 4.24, ZWD at the location of the WVR resulting from the NWP models using the ray tracing package is compared to that from the WVR. The relevant statistics are provided in Table 4.4. We note that errors in WVR estimates of ZWD can reach 16-20 mm for very humid conditions [Coster et al., 1997]. Furthermore, we note that the larger difference of NWP results with respect to the WVR compared to those with respect to radiosondes (Table 4.3) is partly due to the fact that radiosonde launch times are limited to initialization times (00 and 12 UTC) and hence the radiosonde-NWP comparison was only based on NWP initialization times (and not the 3-hour forecast). The difference is also partly due to the fact that WVR-derived ZWD is responding to very local conditions in different azimuth and elevation angles whereas the NWP-derived results represent a weighted average over the nearest grid points. Figure 4.25 shows the difference between

ZHD resulting from surface pressure measurements and NWP models. The relevant statistics are provided in Table 4.4.

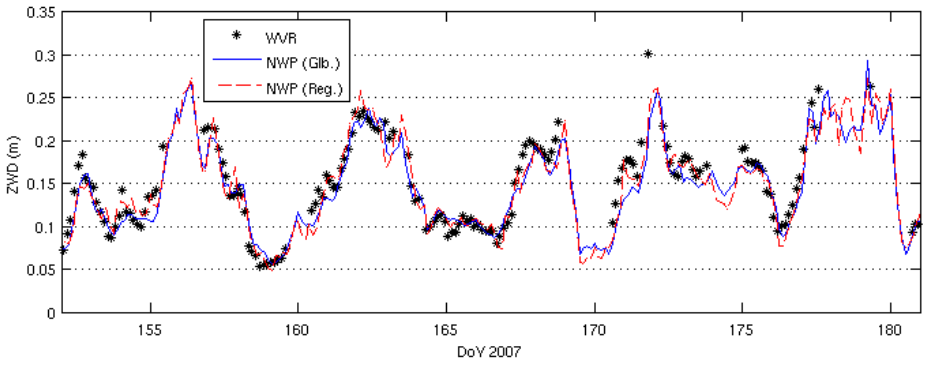

Figure 4.24- ZWD at the location of UNB's WVR using NWP models (global and regional) and the WVR.

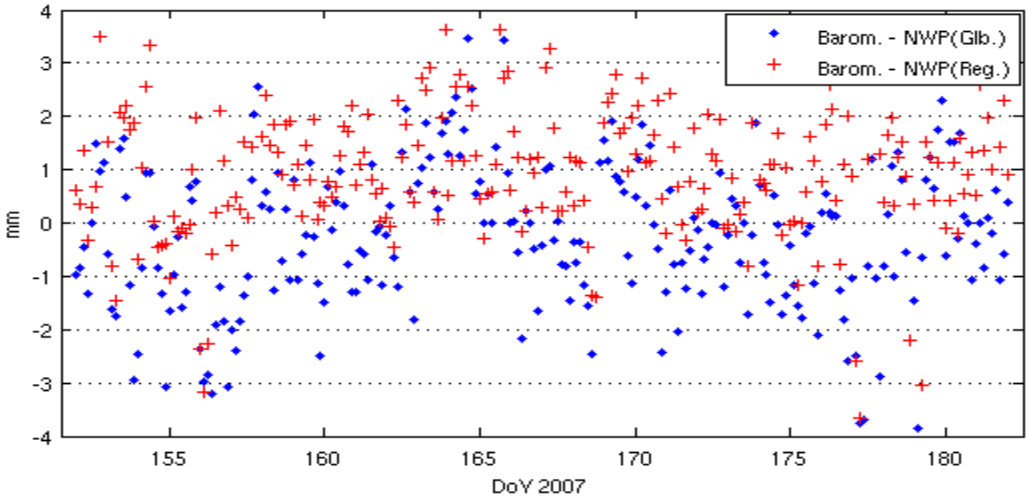

Figure 4.25- Difference of ZHD estimated from Saastamoinen model and pressure measurements (Barom.) and those from NWP models (global and regional).

Table 4.4- Difference between measurement (barometer and Saastamoinen model for ZHD and WVR for ZWD) and NWP models.

	ZHD		ZWD	
	Mean diff. (mm)	Std. (mm)	Mean diff. (mm)	Std. (mm)
Measurement - NWP (Regional)	1.0	1.4	5.4	15.3
Measurement – NWP (Global)	-0.3	1.4	8.1	15.5

4.4.4- Summary of Validation Results

Overall agreements of different models and sensors used in validation studies in various scenarios in previous sections show that ZWD determination still is not possible with uncertainties of better than about 1-2 cm. ZHD, on the other hand, can be derived with an uncertainty of better than 1-2 mm. Considering a nominal value of 2.3 m for ZHD and 0.2 m for ZWD, this means a 0.04-0.08 % and a 5-10 % relative error for ZHD and ZWD respectively. Current inherent uncertainties in the non-hydrostatic part of the delay justify the applicability of estimation approaches for residual delay in GNSS and other transatmospheric radiometric data.

Chapter 5: Modelling and Estimation of Neutral Atmospheric Delay Gradients

In this chapter the behaviour of hydrostatic gradients is studied using a dual radiosonde ray tracing approach over part of North America. A regional model is derived based on this approach. An algorithm developed to estimate gradients from NWP models is also discussed. A comparison of the gradients resulting from the aforementioned approaches is carried out. Using the developed NWP-based approach, the temporal variation of gradients is studied at different locations and times. GPS-estimated gradient approaches will be discussed at the end of the chapter.

5.1- Modelling Regional Hydrostatic Gradients Using a Dual Radiosonde Ray Tracing Approach

As mentioned in Chapter 4 the neutral atmosphere contributes to the hydrostatic part of the delay up to an altitude of about 70-80 km. Figure 5.1 shows the horizontal distance of a station from the point where the signal reaches the top of the neutral atmosphere. One can see that (for example) a ray with 3 degree apparent elevation angle first reaches the top of the neutral atmosphere (height of 80 km) at a horizontal distance of about 733 km from a station at mid-latitude. At a high latitude station, the GPS constellation allows observations at azimuths of both 0 and 180 degree. This means two rays at a 3° elevation angle might reach the top of the neutral atmosphere with a horizontal separation of about

1460 km from each other where the atmospheric conditions (including the thickness of the atmosphere which affects the hydrostatic component) could be significantly different.

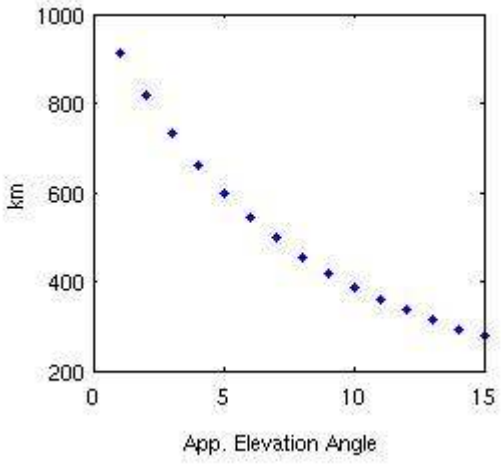

Figure 5.1- Horizontal distance of the slant path from the station at the top of the neutral atmosphere (80 km altitude).

Large scale azimuthal variation of the atmosphere around a site may be investigated using radiosonde observation profiles. Each radiosonde can be considered as a centre of a neighbourhood with a constant radius. All other radiosondes located in this neighbourhood could contain azimuthal atmospheric information in the direction made by the central and each adjacent radiosonde. Hence, each neighbourhood could contain directional information that could be useful for asymmetric studies in a statistical sense.

In this research, two meteorological profiles (resulting from two radiosondes launched at the same time) were used to retrieve more realistic parameters along the ray path. Figure 5.2 shows a schematic ray path from a GPS satellite to the location of a "receiver" (in this

case a radiosonde launch site labeled as r_1). The meteorological parameters for refractivity calculations at each integration step on the path (e.g. point p in Figure 5.2 which is on a ray path with geometric elevation angle of ε with a φ_p geocentric angle from r_1) were derived by linear interpolation between two radiosondes (r_1 and r_2 with geocentric angle of ϕ labelled in Figure 5.2) using equation (5.1), where ψ_1 and ψ_2 are meteorological parameters from the first and second radiosondes respectively, S_{r_1p} is the horizontal distance between radiosonde r_1 and point p on the ray path, and $S_{r_1r_2}$ is the horizontal distance between the two radiosondes. In the case when a ray passes the second radiosonde, only the values from the second radiosonde were used for refractivity calculations.

$$\psi_p = \psi_1 + (\psi_2 - \psi_1) \times \frac{S_{r_1p}}{S_{r_1r_2}} \tag{5.1}$$

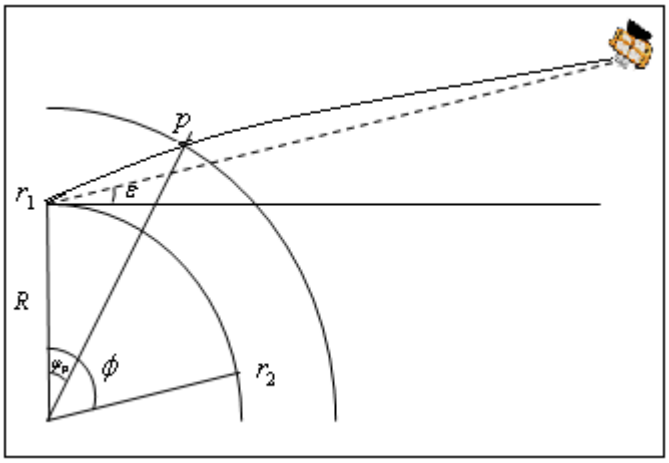

Figure 5.2- A schematic presentation of two radiosondes (r_1 and r_2) and ray path.

Software developed for single radiosonde ray tracing, explained in Chapter 4, was further enhanced to perform ray tracing using dual radiosondes. The software finds all radiosondes in a user-defined radius[1] around each one of the radiosondes. The difference between the slant delay from dual and single radiosonde ray tracing approaches contains information about the contribution of the atmosphere in the asymmetric part of the delay in the direction of the two radiosondes.

5.1.1- A Regional Study

Using 71 available radiosondes in the investigated area (see Figure 5.3) in 2004, 555 radiosonde pairs were formed. This resulted in 326,515 slant delays per elevation angle over the whole year. For all ray traced elevation angles (1-12 and 15 degrees) this made 4,244,695 slant delays for both the single and dual ray tracing approaches. This large database was then employed for statistical analysis. The list of radiosondes used for this study is given in Appendix I.

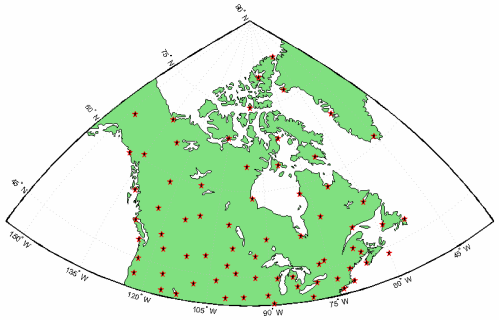

Figure 5.3- Location of radiosondes in the investigated area

[1] In this study a radius of 1000 km was chosen to investigate the effect of directional variations in low elevation angle ray paths.

Figure 5.4 shows the average difference between dual and single radiosonde ray tracing at a 3 degree apparent elevation angle for the slant hydrostatic delay. The error bars are the standard deviation over the whole year of 2004. It can be seen that all possible pairs of radiosondes provide almost a full range of azimuths. The black curve in the figure (in the polar plots as well) is the result of a nonlinear least-squares fit of a trigonometric function which will be discussed in the next section.

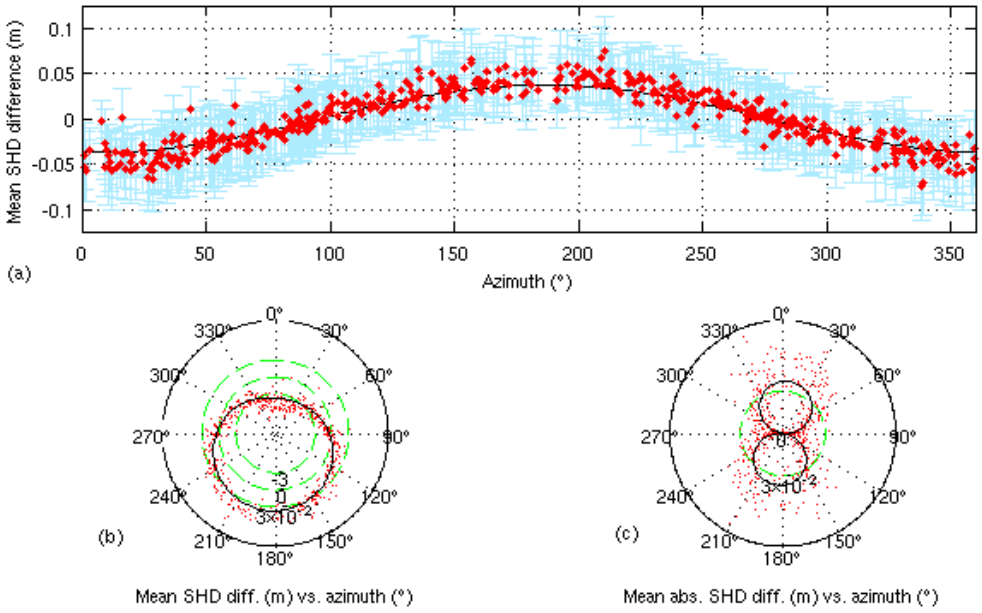

Figure 5.4- a) Average differences of dual – single ray tracing of slant hydrostatic delay (3° elevation angle) vs. azimuth (red dots with error bars) and fitted model (black curve). b) Same as above but in polar plot and without error bars. Note that the dashed concentric circles inside the polar form are representing -3, 0 and +3 cm from inside toward outside respectively. c): Same as above but for absolute differences.

Figure 5.4b shows a systematic decrease of SHD towards north (azimuths of 0°) and an increase towards south. Figure 5.4c shows values around zero in the EW direction. The variation of yearly averaged values vs. latitude and azimuth can be seen in the 3D plot in Figure 5.5. A clear systematic NS average gradient can be seen in Figures 5.4 and 5.5.

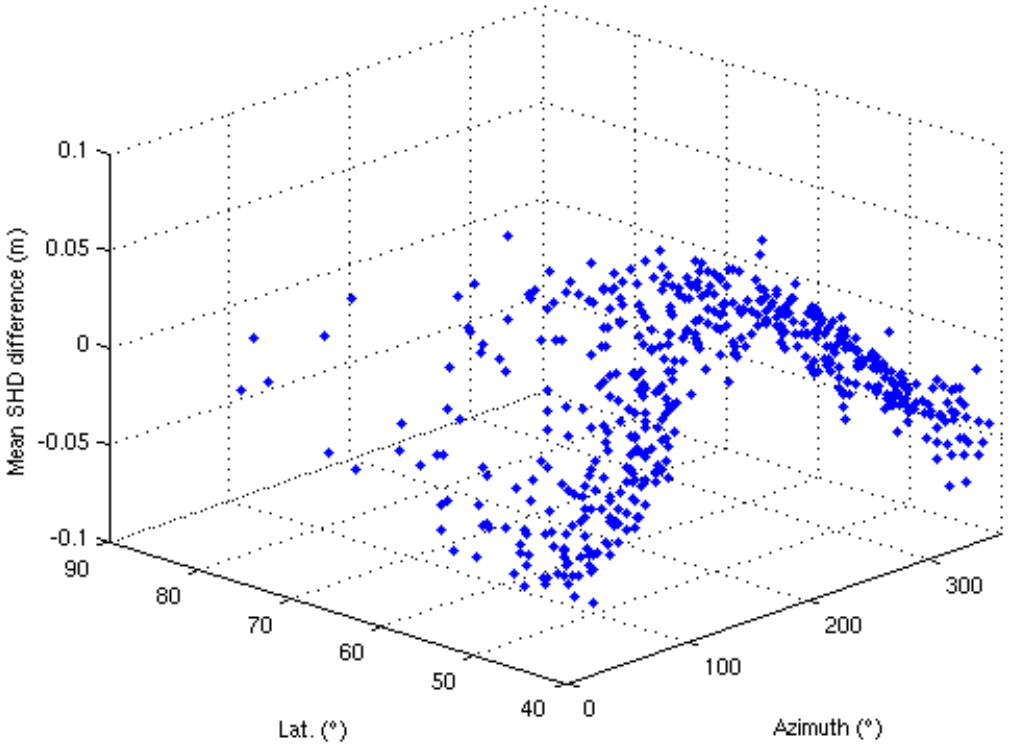

Figure 5.5- Yearly average differences of dual – single ray tracing of slant hydrostatic delay (3° elevation angle) vs. azimuth and latitude.

The results for slant wet delay (not shown here) do not show such a clear trend. This might be partly due to the limitation of the current approach in which the closest

radiosonde pairs in the investigated area are about 115 km from each other. Hence the current semi-3D ray tracing approach cannot detect the usually small scale variation in the wet delay behaviour. However, even with this approach, a slight NS wet gradient can be detected in some months. The NS gradient for both hydrostatic and wet components of the delay is expected. The former is mainly the result of the decreasing thickness of the atmosphere towards the pole and the later is due to the general decrease of humidity with increasing latitude in the investigated area. One can see as an example the thickness map of the atmosphere between the 500 and 1000 hPa isobaric levels and a ZWD map over Canada and northern US for an arbitrary epoch in Figures 5.6 and 5.7 respectively. The values used to produce the maps were calculated using the Canadian high resolution regional NWP model. It should be noted that the ZWD is also affected by surface height as seen in Figure 5.7 (e.g. the Rockies have low values).

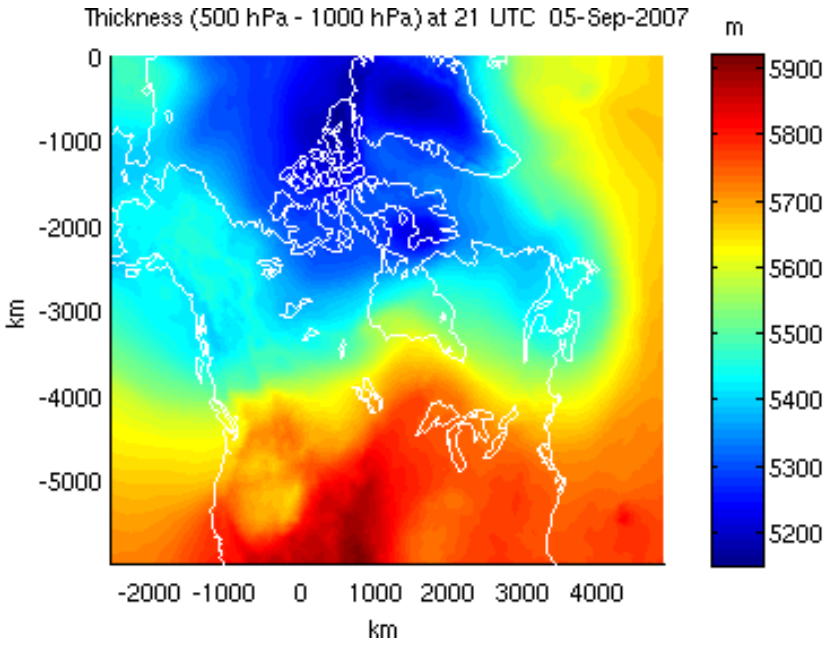

Figure 5.6- Thickness of the atmosphere between 500 and 1000 hPa at 21 UTC 05-Sep-2007 over area covered by regional Canadian NWP model.

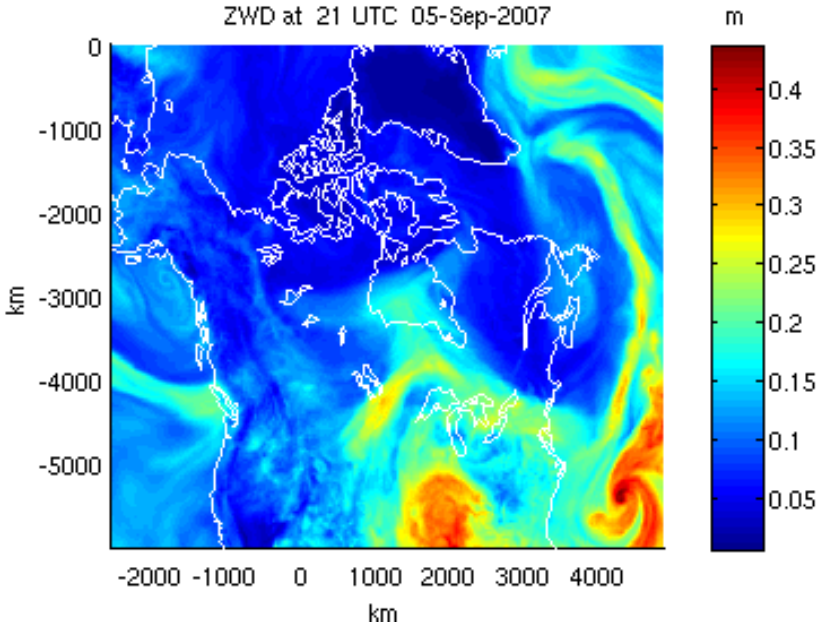

Figure 5.7- ZWD at 21 UTC 05-Sep-2007 over area covered by regional Canadian NWP model.

5.1.2- Modelling Azimuth-dependent Hydrostatic Slant Delays

Using the created database, an effort was made to model the nominal hydrostatic gradients in the investigated area. In order to study the monthly variation of the hydrostatic gradients the database is divided into 12 monthly periods. For each of the 555 radiosonde pairs, mean and variance of the difference between slant delays (dual – single RAOB ray tracing) over each month can be written as:

$$\begin{aligned} m_1 &= \frac{\sum_{j=1}^{n_1}\left(d^j_{i,c,az,\varepsilon} - d^j_{c,\varepsilon}\right)}{n_1} & \sigma_1^2 &= \left(\frac{1}{n_1-1}\sum_{j=1}^{n_1}\left(\left(d^j_{i,c,az,\varepsilon} - d^j_{c,\varepsilon}\right) - m_1\right)^2\right) \\ &\vdots & &\vdots \\ m_{12} &= \frac{\sum_{j=1}^{n_{12}}\left(d^j_{i,c,az,\varepsilon} - d^j_{c,\varepsilon}\right)}{n_{12}} & \sigma_{12}^2 &= \left(\frac{1}{n_{12}-1}\sum_{j=1}^{n_{12}}\left(\left(d^j_{i,c,az,\varepsilon} - d^j_{c,\varepsilon}\right) - m_{12}\right)^2\right) \end{aligned} \qquad (5.2)$$

where $n_1,\ldots,n_{12}$ are the number of simultaneous RAOB at the central RAOB *c* and directional RAOB *i* (which may vary for each pair of radiosondes) in months 1 to 12 respectively; $d^j_{i,c,az,\varepsilon}$ is slant delay (with elevation angle ε) calculated using RAOBs *i* and *c* which are at an azimuth *az* at observation epoch *j*, and $d^j_{c,\varepsilon}$ is the slant delay (with elevation angle ε) from single central RAOB *c*.

The following function is fitted to the monthly averaged values ($m_1,\ldots m_{12}$) for each ray traced elevation angle using a non-linear weighted least-squares approach:

$$d = g_N.\cos(az) + g_E \sin(az) \qquad (5.3)$$

Hence we can write:

$$\underline{d}_i = \begin{bmatrix} \cos(az_1) & \sin(az_1) \\ \vdots & \vdots \\ \cos(az_k) & \sin(az_k) \end{bmatrix}_i \cdot \begin{bmatrix} g_N \\ g_E \end{bmatrix}_i, \quad \underline{d}_i = \begin{bmatrix} m_{i1} & \dots & m_{ik} \end{bmatrix}^T, \qquad i = 1,\dots,12 \tag{5.4}$$

where k is the number of radiosonde pairs (in this case 555) and g_N and g_E are being estimated. The weights are calculated using the variance of monthly values as follow:

$$w_i = \frac{1}{\sigma_i^2}, \quad i = 1,\dots,12 \tag{5.5}$$

The estimated parameters are plotted in Figure 5.8. The NS elevation-angle-dependent gradients become significant at low elevation angles. There is also a yearly average change up to about 4 cm (at a 3 degree elevation angle) in this component with the largest values in the winter months. As expected, the EW component has a smaller average value and it is hard to interpret (lower plot in Figure 5.8).

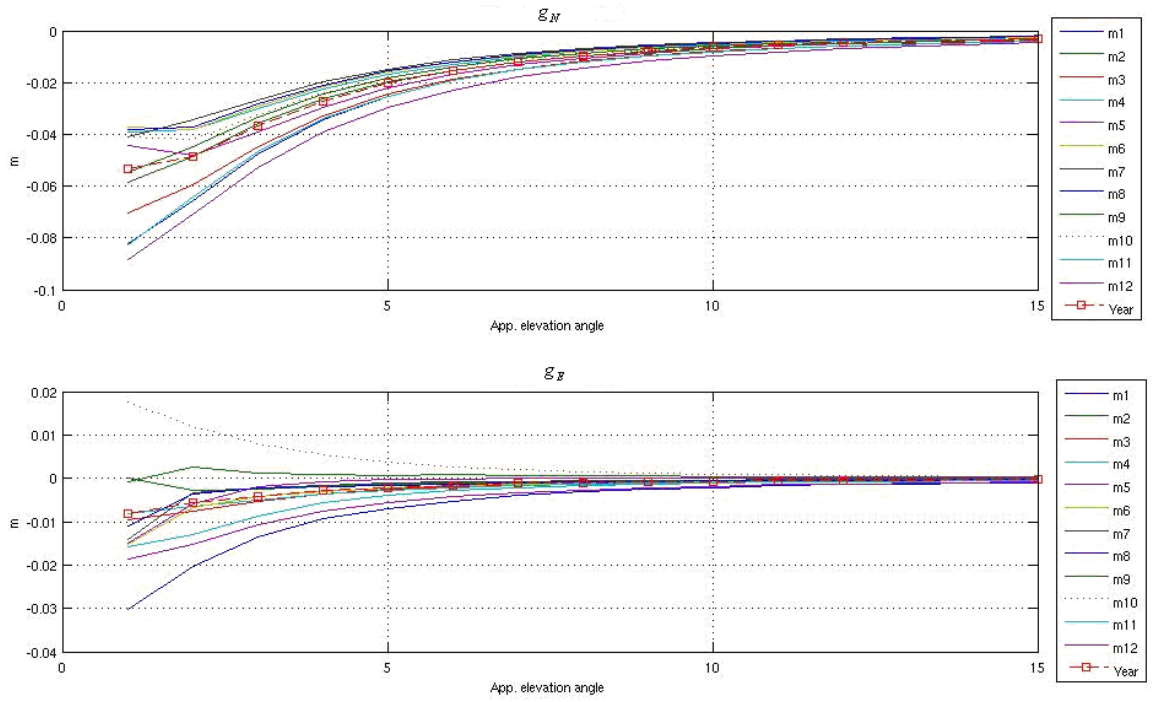

Figure 5.8- The estimated elevation-angle-dependent hydrostatic asymmetry at low elevation angles for each month and the whole year of 2004.

The following models are fitted to the results of 13 elevation angles (1-12 and 15 degrees) per each month:

$$\hat{g}_N = a_N \cdot \exp(b_N \cdot \varepsilon) \tag{5.6}$$

$$\hat{g}_E = a_E \cdot \exp(b_E \cdot \varepsilon) \tag{5.7}$$

where $\hat{g}_N$ and $\hat{g}_E$ are the elevation-angle-dependent gradients, a_N, b_N, a_E and b_E are given in Table 5.1 and ε is the elevation angle in degrees.

Table 5.1- Estimated parameters of exponential fit to NS (index N) and EW (index E) components together with RMS of the fits. Unit: metre.

Month	a_N	b_N	rms_N	a_E	b_E	rms_E
1	-0.1095	-0.2785	0.0015	-0.0419	-0.3554	0.0007
2	-0.0727	-0.2656	0.001	-0.001	-0.0312	0.0008
3	-0.0936	-0.2546	0.0015	-0.0133	-0.3149	0.0002
4	-0.0534	-0.223	0.0018	-0.0107	-0.258	0.0001
5	-0.063	-0.2045	0.0031	-0.0391	-0.9605	0.0001
6	-0.0519	-0.2241	0.0021	-0.0251	-0.5588	0.0007
7	-0.0542	-0.2503	0.0008	-0.0426	-1.1287	0.0007
8	-0.0524	-0.2317	0.0017	-0.0217	-0.7336	0.0008
9	-0.0772	-0.2571	0.0012	0.0006	-0.0198	0.0007
10	-0.0567	-0.2174	0.0022	0.0251	-0.3718	0.0003
11	-0.1096	-0.2814	0.0014	-0.0227	-0.3247	0.0005
12	-0.1157	-0.2614	0.0014	-0.025	-0.2806	0.0004
Year	-0.0721	-0.2416	0.0018	-0.0112	-0.3224	0.0002

The values in Table 5.1 may be considered for the middle of each month. For an arbitrary day a linear interpolation can be employed. The equations (5.6) and (5.7) together with Table 5.1 are hereafter referred to as UNBgr model. One can notice that due to the sparseness of radiosonde launch sites the model was not derived based on location. However, the model may represent an average regional behaviour of hydrostatic gradients over a year. One can see the monthly plots of the difference between dual and single ray tracing results - and a fitted model - in Appendix II.

5.2- Estimation of Horizontal Delay Gradients from NWP Models

With the assumption of a linear variation of refractivity with horizontal distance, the delay gradient contributions to the slant delay (often just referred to as delay gradients or horizontal gradients) can be defined as follows [Davis et al., 1993]:

$$G_{ew} = 10^{-6} \int_{Surf}^{H} h \nabla N_{ew} dh \tag{5.8a}$$

$$G_{ns} = 10^{-6} \int_{Surf}^{H} h \nabla N_{ns} dh \tag{5.8b}$$

where ∇N_{ew} and ∇N_{ns} are the gradients of refractivity in the EW and NS directions along the vertical profile respectively, h is the height along the vertical profile and H is the altitude of the top of the neutral atmosphere (hydrostatic or non-hydrostatic). The gradients in equations (5.8) have the same units as the path delay while the gradient of the zenith delay has units of path delay per unit of distance. The gradients defined in equations (5.8) are equivalent to those that can be achieved by a single GPS antenna parameter estimation process. The gradient of the zenith delay, on the other hand, may be estimated using GPS zenith delay estimates at more than one location. Both of the aforementioned types of gradients can be derived from NWP models. The latest global maps of the zenith delay gradients are currently provided every 3 hours on UNB's Online-RT website (see section 4.3 and appendix III for an example of zenith delay gradient maps). However, in order to correct slant delays by NWP gradients, the delay gradients need to be estimated at the location of the GPS antenna. An algorithm has been developed that enables the calculation of delay gradients using the NWP models at the user location.

Estimation of horizontal gradients defined in equations (5.8) requires a numerical gradient calculation of the refractivity field. Horizontal refractivity may be assumed in a two dimensional field where refractivity (N) is a function of easting (e) and northing (n) i.e.:

$$N = f(e,n) \tag{5.9}$$

Hence the gradient of refractivity in a flat earth approximation can be written as:

$$\nabla N = \left(\frac{\partial f}{\partial e}, \frac{\partial f}{\partial n} \right) = \frac{\partial f}{\partial e}\hat{i} + \frac{\partial f}{\partial n}\hat{j} \tag{5.10}$$

where $\hat{i}$ and $\hat{j}$ are the unit vectors in easting and northing directions respectively. The two terms on the right hand side of equation (5.10) define the EW and NS refractivity gradients as follows:

$$\nabla N_e = \frac{\partial f}{\partial e}\hat{i} \tag{5.11a}$$

$$\nabla N_n = \frac{\partial f}{\partial n}\hat{j} \tag{5.11b}$$

Equations (5.11a) and (5.11b) are the change of refractivity per unit of distance in the EW and NS directions respectively.

The refractivity gradient (weighted by height) along a profile at a grid point may be numerically integrated in the NS and EW directions as follows:

$$\nabla N_{ns}^{h} = \sum_{k=1}^{n} \left(\frac{h_k (N_{i+1,k} - N_{i-1,k})}{S_{i+1,i-1}} \cdot dh_k \right) \tag{5.12a}$$

$$\nabla N_{ew}^{h} = \sum_{k=1}^{n} \left(\frac{h_k (N_{j+1,k} - N_{j-1,k})}{S_{j+1,j-1}} \cdot dh_k \right) \tag{5.12b}$$

where:

- h_k is the height of level k,
- $N_{i+1,k}$ and $N_{i-1,k}$ are refractivities at one grid point to the north and one grid point to the south respectively both at level k,
- $N_{j+1,k}$ and $N_{j-1,k}$ are refractivities at one grid point to the east and one grid point to the west respectively both at level k,
- $S_{i+1,i-1}$ and $S_{j+1,j-1}$ are the distance between those grid points in the NS and EW directions, and
- dh_k is the integration step size at level k (see Figure 5.9 for a representation).

Equations (5.12) may then be used for estimation of horizontal gradients at each of the 4 nearest grid points to the user location, i.e.:

$$G_{ns}^{m} = 10^{-6} \cdot \nabla N_{ns}^{h,m} \qquad m = 1,\ldots,4 \tag{5.13a}$$

$$G_{ew}^{m} = 10^{-6} \cdot \nabla N_{ew}^{h,m} \qquad m = 1,\ldots,4 \tag{5.13b}$$

The horizontal gradient at the user location can finally be interpolated using the same approach used for zenith delay mentioned in Chapter 4, i.e.:

$$G_{ns}^{P} = \sum_{m=1}^{4} w_{Pm} \cdot G_{ns}^{m} \tag{5.14a}$$

$$G_{ew}^{P} = \sum_{m=1}^{4} w_{Pm} \cdot G_{ew}^{m} \tag{5.14b}$$

where weights can be calculated as:

$$w_{Pm} = \frac{\rho_{Pm}^{-c}}{\sum_{m=1}^{4} \rho_{Pm}^{-c}} \qquad m = 1,\ldots,4 \tag{5.15}$$

where ρ_{Pm} is the distance between user point P and each of the 4 grid points (see Figure 5.9), and c is the power parameter. A value of 1 is used here for the power parameter.

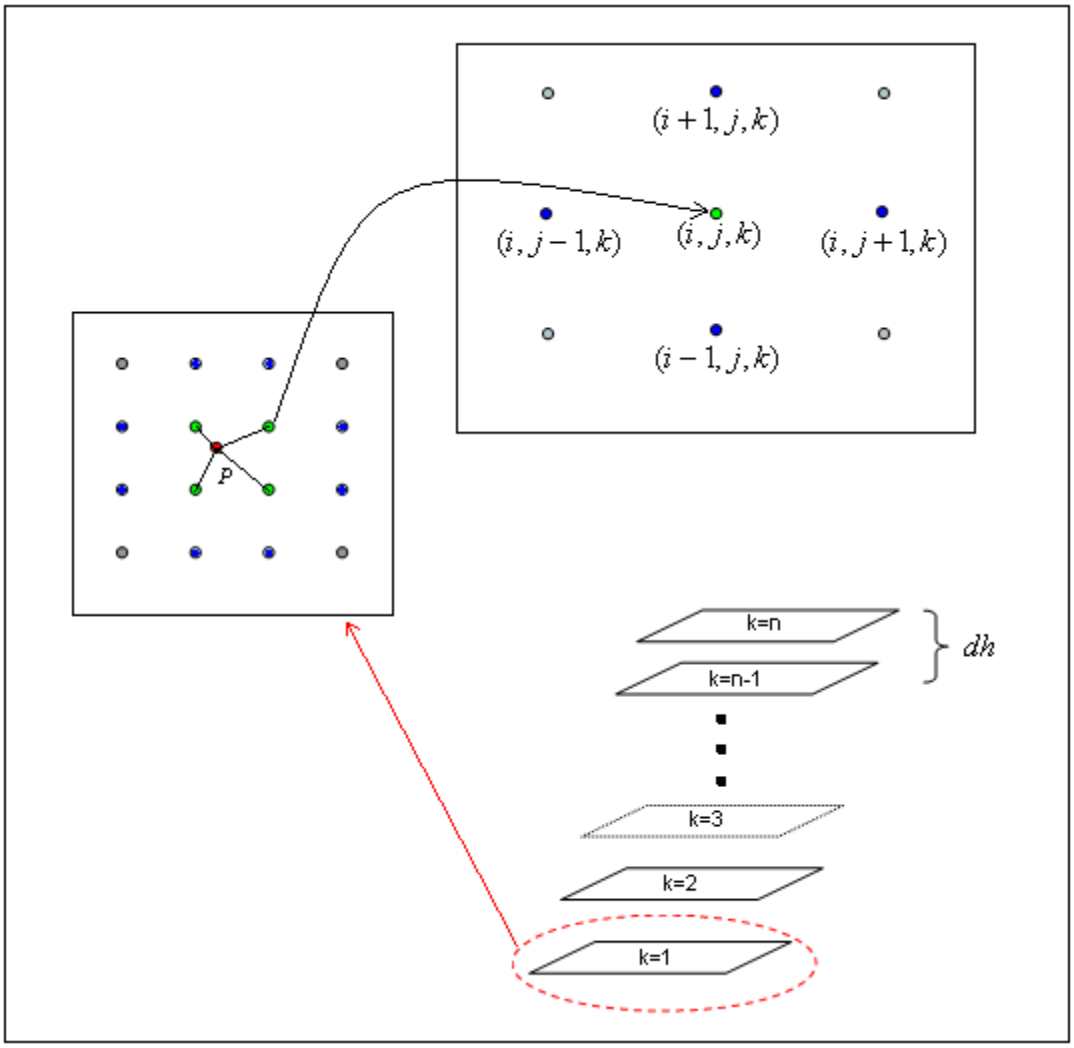

Figure 5.9- A schematic representation of horizontal gradient calculations from NWP grids.

5.3- Comparison of Different Gradient Retrieval Approaches

The dual radiosonde ray tracing approach explained in section 5.1 was applied in the same region (see Figure 5.3) but using data over the month of August 2007. This is chosen as a benchmark for comparing:

- NWP-based gradient retrieval,
- the UNBgr model,
- and the commonly used gradient mapping functions including:
    - Davis,
    - Chen and Herring (CH) and
    - derivative of non-hydrostatic VMF1 (VMFW1) with respect to zenith angle (see Chapter 3).

Gradient calculation using NWP was performed at locations collocated with the investigated radiosonde launch sites, including the central site shown in Figure 5.10 (The Pas, MB). The comparison between Davis, CH and the derivative of VMFW1 (all using NWP-retrieved hydrostatic horizontal delay gradients), the dual ray tracing approach and UNBgr are plotted in Figure 5.11 for each azimuth made between radiosonde pairs at a 5 degree elevation angle over the month of August 2007.

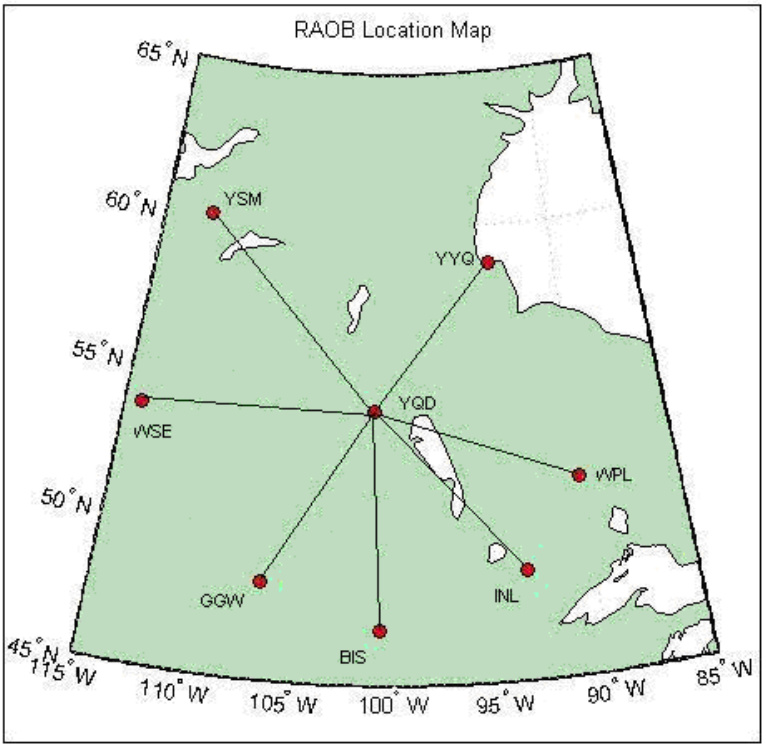

Figure 5.10- Locations of radiosonde sites used for validation of gradient retrieval approaches.

In Figure 5.12, a comparison with the dual RAOB ray tracing approach in each of the directions, then summarized as error bar plots (mean and standard deviation), is shown. One can see that in this investigated case the CH mapping function and derivative of VMFW1, followed by UNBgr, provided closer results to the dual RAOB ray tracing approach than the Davis mapping function. One should note that in CH, Davis and the derivative of VMFW1, NWP horizontal delay gradients were used while the elevation-angle-dependent part is included in UNBgr.

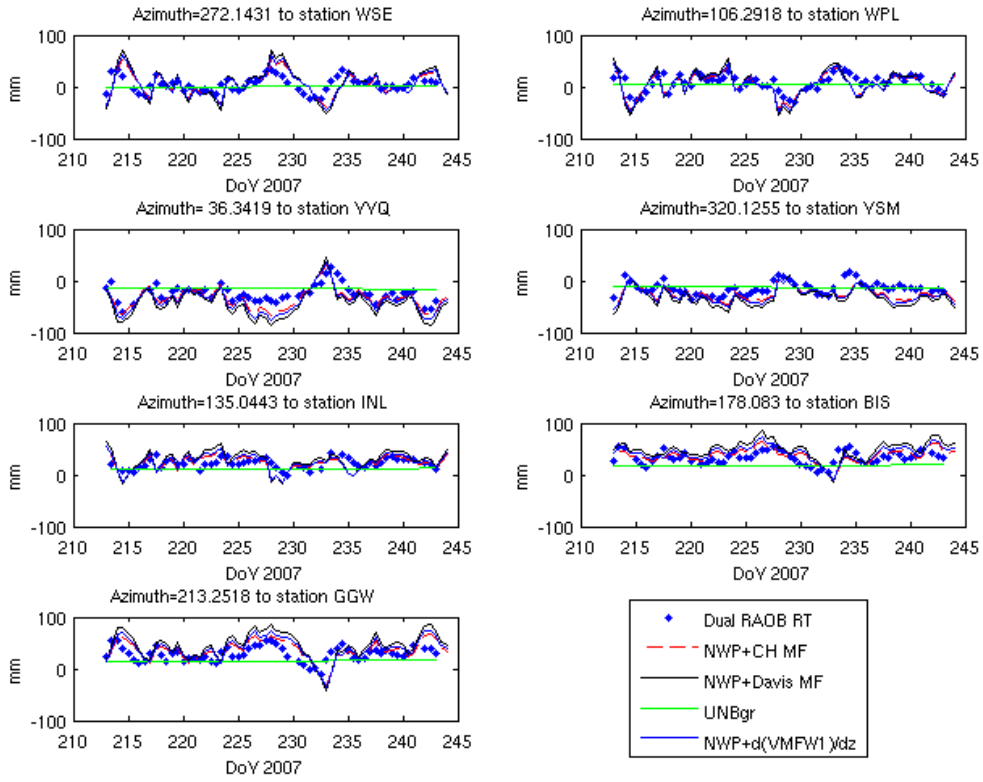

Figure 5.11- Comparison between Davis, CH and the derivative of VMFW1 (all using NWP-retrieved hydrostatic horizontal delay gradients), the dual RAOB ray tracing approach and the UNBgr model at central station YQD (The Pas, MB). Elevation angle: 5°.

Similar results were derived at other radiosonde pairs in the investigated region. One can see in Figure 5.11 that there is a generally good agreement between the dual radiosonde ray tracing approach and NWP-retrieved gradients mapped with gradient mapping functions. Despite the fact that UNBgr is based on an average fit to monthly data (and hence is not expected to represent daily variations), statistically speaking, it has provided

closer results to dual ray tracing than the Davis mapping function (which benefited from real-time NWP horizontal gradients) over the investigated month as seen in Figure 5.12.

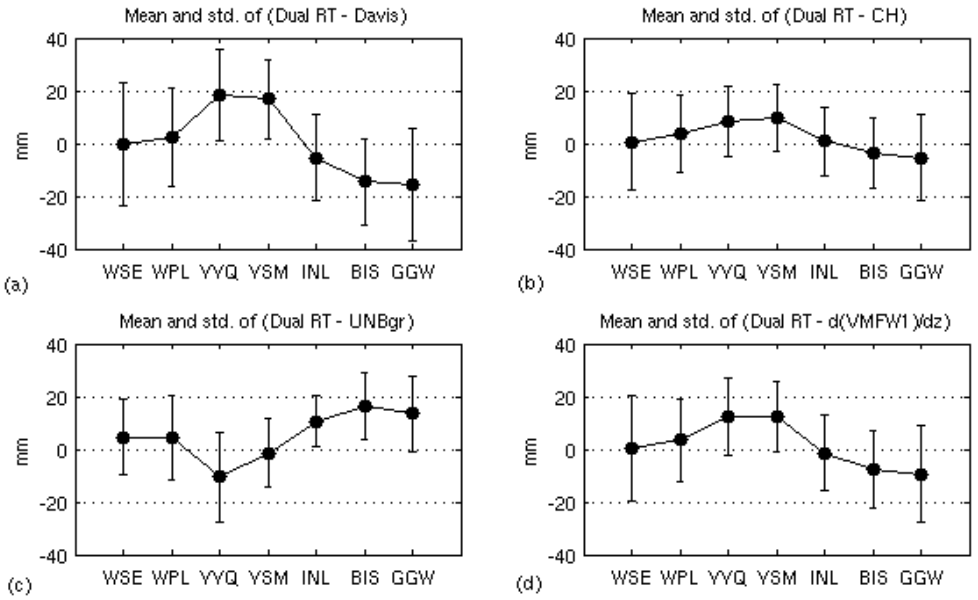

Figure 5.12- Mean and standard deviation of differences from dual RAOB ray tracing for each direction shown in Figure 5.10 with 5 degree elevation angle. a) Davis. b) CH. c) UNBgr. d) Derivative of VMFW1.

5.3.1- Comparison of NWP-retrieved Gradients from Two Different Models and Algorithms

Horizontal gradients retrieved from the Canadian global NWP model are compared with gradient calculations by Boehm and Schuh [2007] which use a 3-profile approach from the model of ECMWF. Figure 5.13 shows the comparison between the algorithm and model used in this dissertation (UNB) and those of the Boehm and Schuh (Vienna) over

the month of July 2007 at station ALGO, Canada. One should note that Boehm and Schuh [2007] used empirically determined reduction factors to their original NWP-derived gradients based on a comparison between their 3-profile approach results and a 3-D ray tracing during a VLBI campaign over 15 days in October 2002. However, it is found that use of their reduction factor (to their gradients) will deteriorate the agreement between the result of Vienna and UNB at least for the hydrostatic part. Hence their reduction factors are not used for the plots in Figure 5.13. A rather good overall agreement can be seen in the hydrostatic gradients between the two approaches and models in Figure 5.13a and 5.13b. The agreement is not as good in the non-hydrostatic gradients (see Figure 5.13c and 5.13d) which are partly due to the higher uncertainty in the non-hydrostatic part of the models. Similar results were found in other locations.

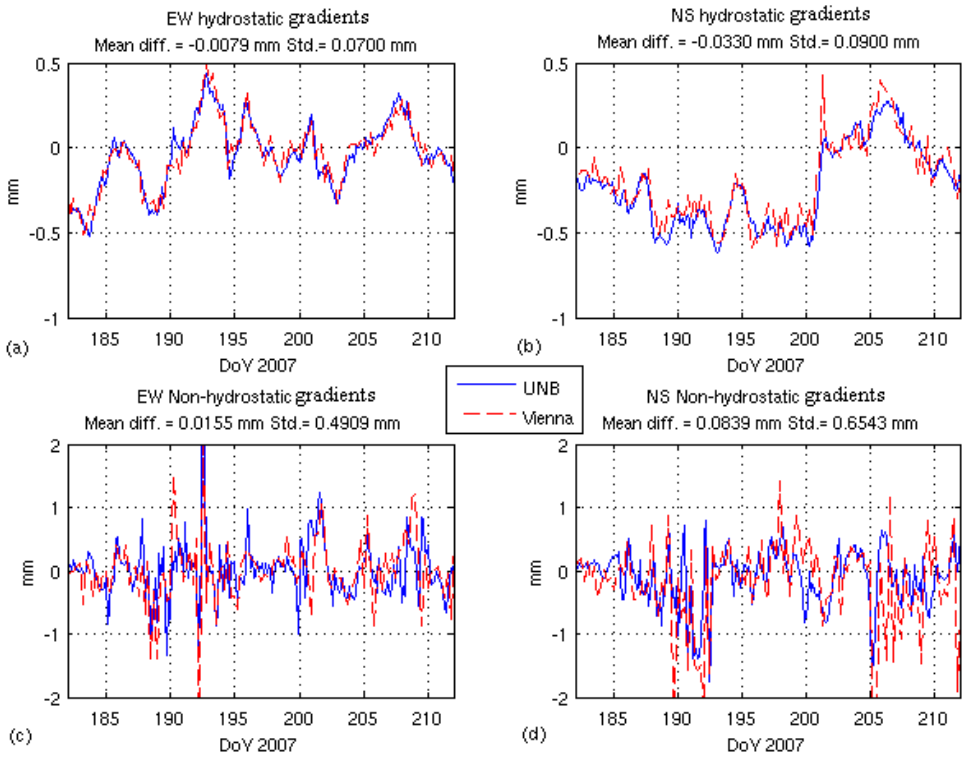

Figure 5.13- Comparison between gradients from Vienna and UNB (this dissertation) approaches at station ALGO over the month of July 2007. a) EW hydrostatic. b) NS hydrostatic. c) EW non-hydrostatic. d) NS non-hydrostatic.

5.4- Studying Temporal Variations of Gradients

Using NWP-retrieved gradients (based on the algorithm discussed in section 5.2) the temporal variation of gradients can be investigated. This may assist enhancing GNSS gradient estimation approaches as it provides a more physically meaningful behaviour of

gradients. An empirical cumulative distribution function[1] (ECDF) of the temporal variation of tropospheric parameters is employed for studying the variations in a number of locations spread over different latitudes in the northern and southern hemispheres. As an example, Figure 5.14 shows ECDFs for absolute change of NS and EW hydrostatic, non-hydrostatic and total gradients per 3 hours calculated over the month of July, 2007 at station ALGO. The value of 1 on the y axis of the ECDF plots corresponds to the extreme largest temporal variation in the sample (which can be extracted from the x axis). One may note that even though the cumulative distribution functions are monotonically increasing, the function may not be strictly increasing especially when it is close to 1. This is due to the contribution of a few large values in the sample which might not be representative values for studying the statistical population. Hence a corresponding value to 0.95 of ECDFs is considered in the studies tabulated in this section and referred to as 95% probability.

For comparison, ECDFs of ZWD and ZHD at the same station over the same period are presented at Figure 5.15. One can notice different horizontal scale between hydrostatic and non-hydrostatic gradients in Figure 5.14. As expected temporal variation (per 3 hours) of non-hydrostatic gradients is about one order of magnitude larger than the hydrostatic gradients. Similarly one can notice different horizontal scales between Figure 5.15.a and 5.15.b and may conclude that temporal variation of ZWD is more than 1 order

[1] Cumulative distribution functions represent "*the probability that a variable X takes on a value less than or equal to a number x*" [Mathworld, 2008], i.e.: $F(x) = P(X \leq x)$.

of magnitude larger than those for ZHD in the investigated station. The statistics for all investigated stations over the month of July (summer) 2007 can be seen in Table 5.2. Based on the ECDFs, the maximum absolute change in the gradient and zenith delays (per 3 hours) at 95% probability have also been calculated and are included in the table. Results calculated over the month of January (winter) 2008 can be seen in Table 5.3.

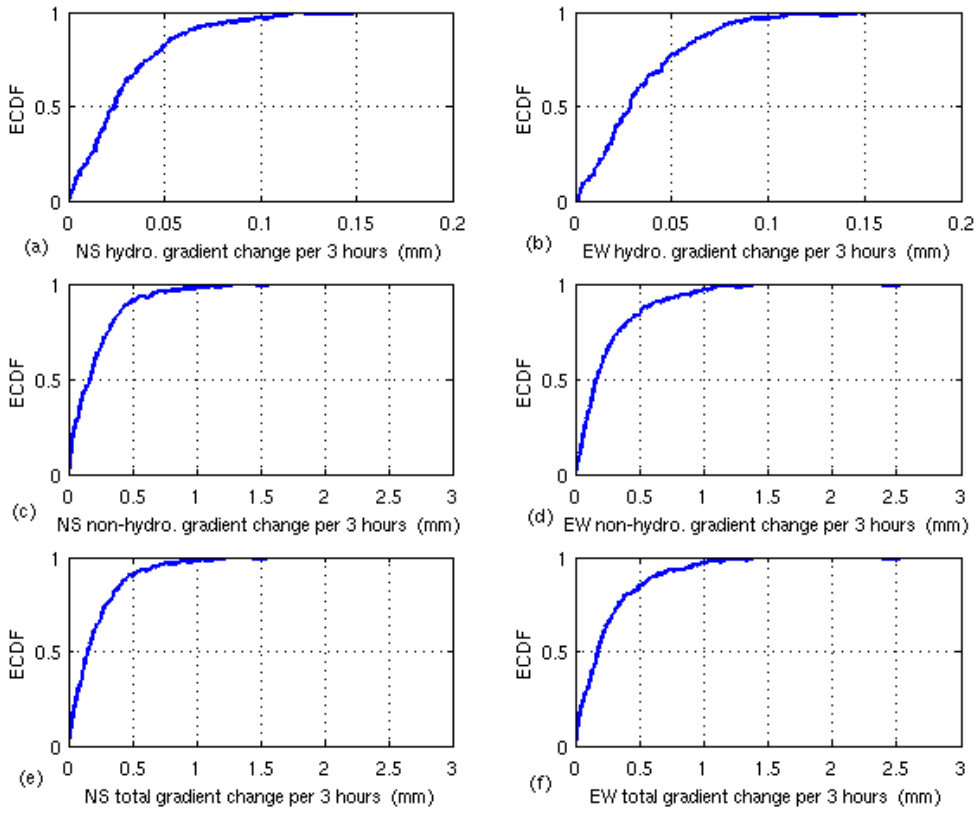

Figure 5.14- ECDF for absolute gradient change per 3 hours at station ALGO over month of July 2007. a) Hydrostatic NS. b) Hydrostatic EW. c) Non-hydrostatic NS. d) Non-hydrostatic EW. e) Total NS. f) Total EW.

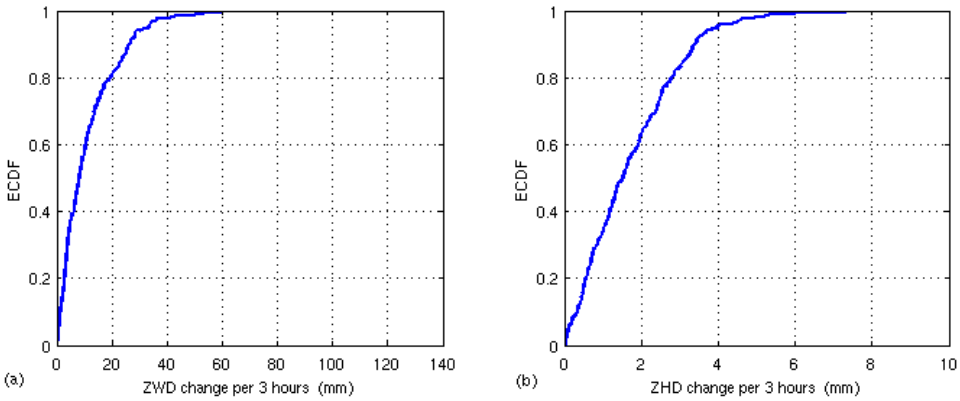

Figure 5.15- ECDF for absolute zenith delay change per 3 hours at station ALGO over month of July 2007. a) ZWD. b) ZHD.

Values in Table 5.2 are summarized in Figures 5.16 and 5.17 while those in Table 5.3 are summarized in Figures 5.18 and 5.19. Figure 5.16 shows mean and standard deviation of variation of hydrostatic, non-hydrostatic and total gradient calculated over the month of July 2007 and Figure 5.17 for the month of January 2008. As can be seen in Figure 5.16 the non-hydrostatic gradients and consequently the total gradient temporal variations are larger at the three northern hemisphere mid-latitude stations. One may note that the results presented in the figure are based on northern hemisphere summer month of July. In Figure 5.18, instead, one can see that the variations of non-hydrostatic and total gradients are larger in the southern hemisphere stations which are calculated during the southern hemisphere summer month of January 2008. Hence a seasonal dependency on the temporal variation in non-hydrostatic gradients may be concluded.

Table 5.2- Statistics of temporal variation of gradients and zenith delays (mm/3 hours) calculated over the month of July 2007. Pr(0.95) is the max absolute change (mm/3 hours) in 95% probability.

Stn. [Lat. °]	Stat. Parameter	Hydro. gradient		Non-hydro. gradient		Total gradient		ZWD	ZHD
		NS	EW	NS	EW	NS	EW		
ALRT [82.5]	Mean	0.021	0.025	0.065	0.114	0.071	0.122	4.039	1.216
	Std.	0.019	0.024	0.071	0.130	0.076	0.134	4.339	1.042
	Pr(0.95)	0.061	0.071	0.207	0.326	0.236	0.356	12.423	3.244
RESO [74.7]	Mean	0.018	0.024	0.084	0.170	0.087	0.173	5.948	0.826
	Std.	0.015	0.022	0.090	0.175	0.089	0.173	6.096	0.766
	Pr(0.95)	0.052	0.071	0.278	0.517	0.276	0.510	17.418	2.447
ALGO [46.0]	Mean	0.031	0.035	0.227	0.274	0.225	0.275	11.701	1.754
	Std.	0.027	0.028	0.247	0.329	0.241	0.331	12.688	1.335
	Pr(0.95)	0.084	0.086	0.692	0.923	0.680	0.908	33.277	3.970
UNBJ [46.0]	Mean	0.033	0.034	0.228	0.290	0.230	0.293	13.849	1.674
	Std.	0.029	0.029	0.240	0.301	0.246	0.300	13.484	1.302
	Pr(0.95)	0.081	0.087	0.713	0.923	0.705	0.899	40.223	4.227
NRC1 [45.5]	Mean	0.031	0.034	0.200	0.224	0.204	0.227	12.096	1.703
	Std.	0.026	0.027	0.202	0.272	0.201	0.270	11.396	1.270
	Pr(0.95)	0.086	0.091	0.565	0.696	0.609	0.704	31.742	4.117
AREQ [-16.5]	Mean	0.067	0.054	0.125	0.098	0.123	0.097	4.626	2.438
	Std.	0.054	0.042	0.103	0.084	0.104	0.093	3.935	1.913
	Pr(0.95)	0.166	0.131	0.303	0.262	0.311	0.280	12.604	6.326
RIO2 [-53.8]	Mean	0.040	0.040	0.066	0.088	0.080	0.096	5.038	3.074
	Std.	0.035	0.032	0.074	0.095	0.076	0.099	5.377	2.946
	Pr(0.95)	0.104	0.104	0.227	0.271	0.212	0.253	17.965	9.385
OHI2 [-63.3]	Mean	0.049	0.057	0.042	0.054	0.070	0.082	3.192	3.956
	Std.	0.043	0.053	0.061	0.072	0.075	0.084	3.989	3.501
	Pr(0.95)	0.140	0.162	0.124	0.210	0.219	0.274	12.079	11.116

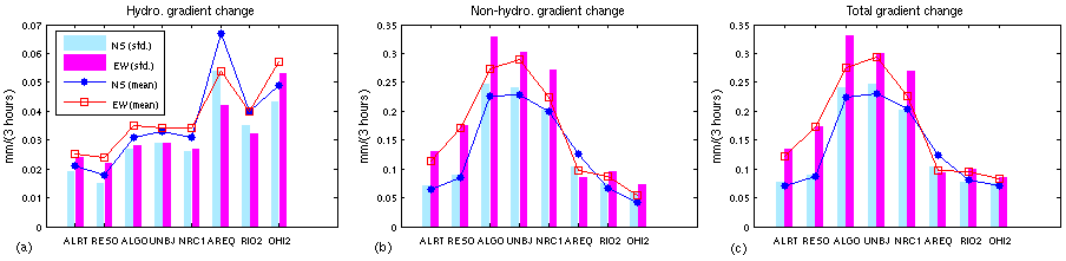

Figure 5.16- Mean and std. of temporal variation of gradients per 3 hours calculated over the month of July 2007. a) Hydrostatic. b) Non-hydrostatic. c) Total. Stations ordered by decreasing latitude.

Figure 5.17 shows the maximum absolute temporal variation of gradients and zenith delays per 3 hours at 95% probability calculated over the month of July 2007 (Figure 5.19 for month of January 2008). The variations of non-hydrostatic and total gradients are below 1 mm over 3 hours (at 95% probability) at all stations and in both investigated summer and winter months. The ZHD and ZWD variations can be seen for comparison in Figures 5.17d and 5.19d for the months of July 2007 and January 2008 respectively. As expected, the non-hydrostatic gradient and ZWD temporal variations are larger than the hydrostatic gradients and ZHD at most stations. This is not as clear for high (low) latitude stations in northern (southern) hemisphere winter months. This may be due to the low amount, and variability, of humidity in the winters in the Arctic and Antarctica.

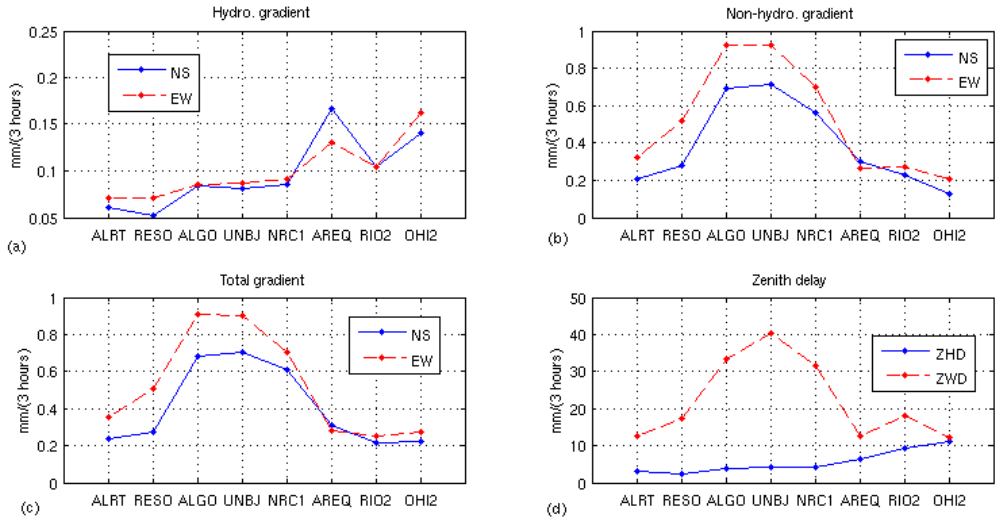

Figure 5.17- Maximum absolute temporal variation per 3 hours at 95% probability calculated over the month of July 2007. a) Hydrostatic gradient. b) Non-hydrostatic gradient. c) Total gradient. d) Zenith delay. Stations ordered by decreasing latitude.

Although temporal variation of gradients, as well as gradients themselves, depend on factors such as local weather conditions, topography and mountains[1] (which are probably among the reasons for larger gradient variations at some stations, e.g., AREQ[2]), a clear dependence on season and latitude can be concluded from the investigations presented in Figures 5.16 to 5.19 and Tables 5.2 and 5.3. Furthermore, one may notice a slightly larger average absolute temporal variation in EW gradients compared to NS gradients. The larger EW variation might be a reason for not having clear average systematic EW effects

[1] Orographic lifting, e.g., which is defined as lifting of air as it travels over a mountain [Ackerman and Knox, 2007] can cause different temperature and humidity in upwind and downwind sides of a mountain and hence it may cause delay gradients.

[2] One may also notice a lower variability in zenith delay at station AREQ which is likely to be due to the high altitude of this station (about 2447 m) which causes lower values of ZWD and ZHD as well.

as pointed out using the dual ray tracing study reported in section 5.1. The result of the empirical NWP-based study shown here for gradients and zenith delay temporal variations can be used to tune GNSS tropospheric parameter estimation strategies as will be shown in the next section.

Table 5.3- Statistics of temporal variation of gradients and zenith delays (mm/3 hours) calculated over the month of January 2008. Pr(0.95) is the max absolute change (mm/3 hours) at 95% probability.

Stn. [Lat.°]	Stat. Parameter	Hydro. gradient		Non-hydro. gradient		Total gradient		ZWD	ZHD
		NS	EW	NS	EW	NS	EW		
ALRT [82.5]	Mean	0.027	0.037	0.012	0.024	0.033	0.046	0.665	2.157
	Std.	0.024	0.032	0.018	0.032	0.032	0.041	0.790	2.063
	Pr(0.95)	0.070	0.094	0.039	0.077	0.088	0.129	2.304	5.947
RESO [74.7]	Mean	0.026	0.033	0.014	0.026	0.031	0.043	0.941	1.627
	Std.	0.025	0.033	0.017	0.031	0.029	0.045	1.233	1.879
	Pr(0.95)	0.074	0.105	0.041	0.086	0.085	0.144	3.278	4.354
ALGO [46.0]	Mean	0.048	0.063	0.090	0.107	0.107	0.132	6.172	3.936
	Std.	0.039	0.061	0.131	0.185	0.141	0.207	9.167	4.117
	Pr(.95)	0.126	0.180	0.347	0.451	0.372	0.532	25.027	11.609
UNBJ [46.0]	Mean	0.050	0.069	0.101	0.140	0.116	0.167	7.133	4.354
	Std.	0.043	0.066	0.123	0.243	0.127	0.266	11.521	4.728
	Pr(0.95)	0.128	0.189	0.326	0.626	0.358	0.553	30.991	11.412
NRC1 [45.5]	Mean	0.048	0.061	0.092	0.124	0.107	0.146	6.448	3.979
	Std.	0.038	0.065	0.145	0.226	0.148	0.239	9.986	4.313
	Pr(0.95)	0.133	0.182	0.374	0.510	0.370	0.657	25.039	10.520
AREQ [-16.5]	Mean	0.088	0.064	0.341	0.245	0.323	0.235	7.296	2.155
	Std.	0.065	0.049	0.276	0.205	0.259	0.202	5.378	1.401
	Pr(0.95)	0.206	0.165	0.867	0.662	0.837	0.632	17.923	4.956
RIO2 [-53.8]	Mean	0.040	0.052	0.160	0.221	0.168	0.228	11.655	2.837
	Std.	0.032	0.045	0.183	0.258	0.185	0.265	12.228	2.056
	Pr(0.95)	0.098	0.135	0.440	0.723	0.447	0.806	37.798	6.955
OHI2 [-63.3]	Mean	0.039	0.057	0.088	0.146	0.100	0.165	6.029	2.943
	Std.	0.031	0.054	0.106	0.197	0.114	0.205	6.970	3.320
	Pr(0.95)	0.101	0.167	0.274	0.514	0.279	0.568	19.775	7.251

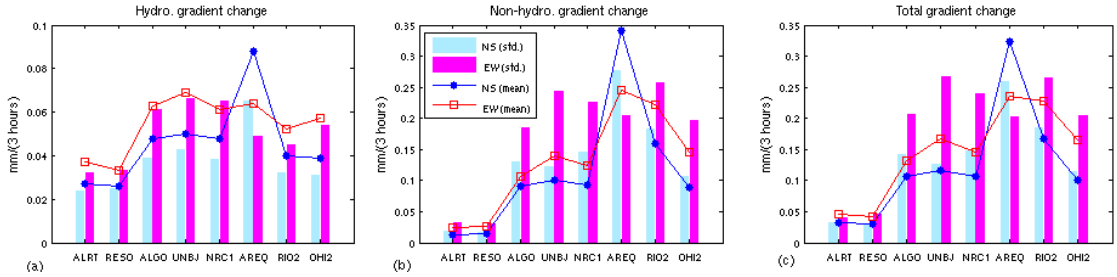

Figure 5.18- Mean and std. of temporal variation of gradients per 3 hours calculated over the month of January 2008. a) Hydrostatic. b) Non-hydrostatic. c) Total. Stations ordered by decreasing latitude.

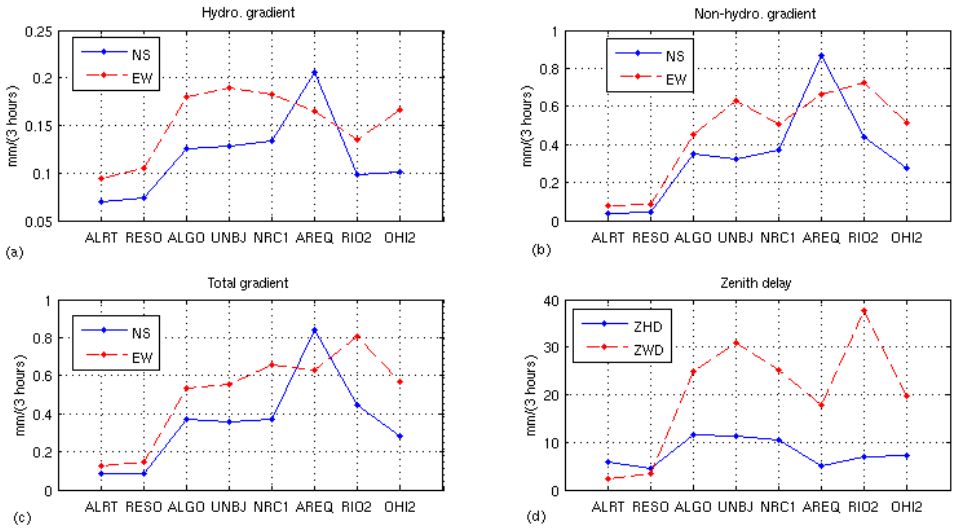

Figure 5.19- Maximum absolute temporal variation per 3 hours at 95% probability calculated over the month of January 2008. a) Hydrostatic gradient. b) Non-hydrostatic gradient. c) Total gradient. d) Zenith delay. Stations ordered by decreasing latitude.

5.5- GPS-estimated Gradients

Current scientific GPS software products usually use either stochastic (Kalman filter) or deterministic (least-squares adjustment) strategies to estimate tropospheric parameters, including horizontal gradients. The most common estimation strategies and parameterizations are summarized in Figure 5.20. One may refer to, for example, Gelb [1974] or Brown and Hwang [1997] for details on stochastic parameter estimation approaches. As shown in Figure 5.20, a first-order Gauss-Markov process is parameterized by state variation and correlation time while a random walk process is parameterized by process noise rate. However, a random walk process can be considered a special Gauss-Markov process with correlation time of infinity [Dodson et al., 1996] (e.g. 100 hours for a 24-hour GPS session [GAMIT, 2006]). Furthermore, a piece-wise linear parameterization when the parameters are assumed to be correlated is roughly equivalent to a random walk parameterization [Bock and Doerflinger, 2001]. It has been reported that current approaches of ZTD estimation perform at the same level of accuracy and precision (see e.g. Ware et al. [1993] and van der Wal [1995]).

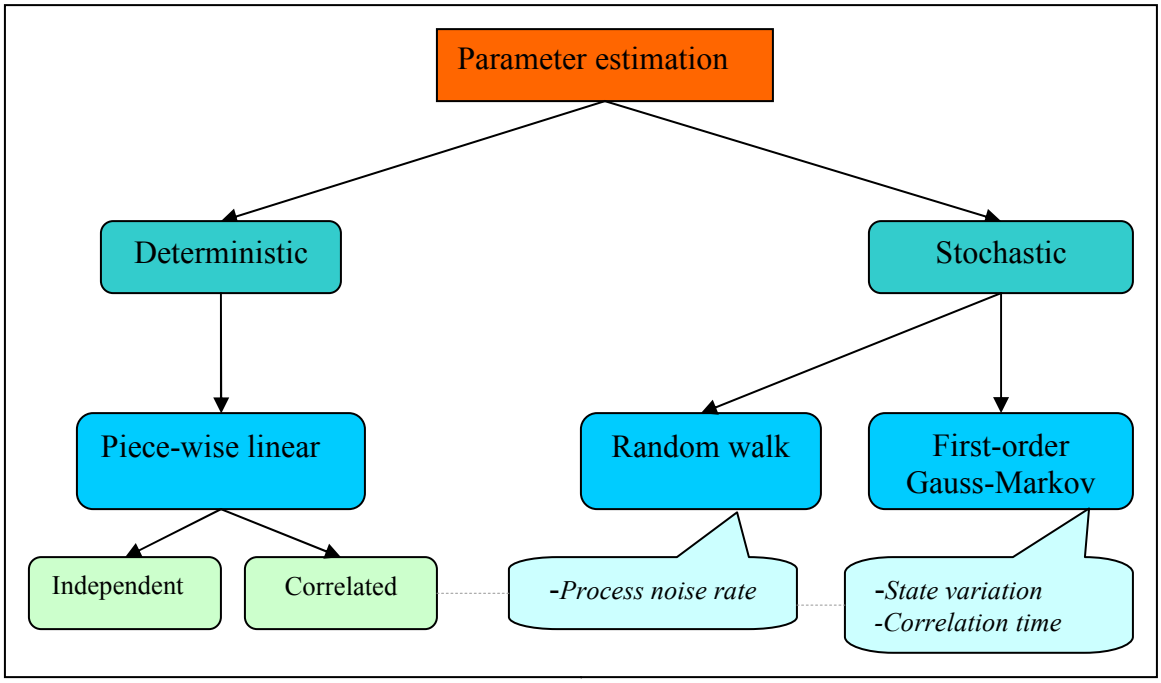

Figure 5.20- A schematic representation of current GPS tropospheric parameter estimation approaches.

Bernese GPS software Version 5.0 uses a deterministic approach for parameter estimation by least-squares. In this software the tropospheric zenith delay and gradients are treated as piece-wise linear parameters. The partial derivatives for tropospheric parameters (gradients and residual zenith delay) are as follows:

$$A_{G_{ns}} = \gamma \cdot \frac{\partial mf}{\partial z} \cdot \cos(az) \tag{5.16}$$

$$A_{G_{ew}} = \gamma \cdot \frac{\partial mf}{\partial z} \cdot \sin(az) \tag{5.17}$$

$$A_{ZTD} = \gamma \cdot mf \tag{5.18}$$

where $A_{G_{ns}}$, $A_{G_{ew}}$ and A_{ZTD} are the partial derivatives for NS gradient, EW gradient and ZTD respectively; z and az are the zenith angle and azimuth respectively and:

$$\gamma = 1 - \frac{|t_i - t_0|}{\Delta t}, \quad 0 \le \gamma \le 1 \tag{5.19}$$

where t_i is the current epoch, t_0 is the reference epoch of the estimation interval and Δt is the estimation interval. One may note that equations (5.16) and (5.17) result from the idea of tilting of the atmosphere (see section 3.2.3) where the gradient mapping function is equivalent to the derivative of a symmetric mapping function with respect to the zenith angle.

Partial derivatives based on equations (5.16) to (5.19) are calculated for 24 hours of GPS observations at two stations located at different latitudes. Figures 5.21 and 5.22 are partial derivatives at station ALGO (a mid-latitude station) vs. elevation angle and time respectively, with 2 hour tropospheric parameter estimation intervals. Figures 5.23 and 5.24 are those at station ALRT (a high latitude station). Figures 5.21 to 5.24 exemplify the importance of low elevation angle GPS measurements in the estimation of tropospheric parameters, as has already been stated by others (e.g. Bar-Sever et al. [1998] and Meindl et al. [2004]). This can also be explained by the similar partial derivatives of height and ZTD components at high elevation angles. One may notice from equation (3.13.c) that the partial derivative for the height component is $1/\sin(\varepsilon)$. For elevation angles above about 20°, this provides almost the same value as a mapping function. Only when low elevation angles are used the mapping function (partial derivative of ZTD) is becoming significantly different than $1/\sin(\varepsilon)$ and this can prevent ill-conditioning of the design matrix. From Figures 5.21 and 5.23 it is clear that observations below 15 degrees

are essential for gradient estimation. Furthermore, the GPS constellation (with a lack of visible satellites in the north direction from mid-latitude) may result in systematic effects on NS estimated gradients compared to the EW estimated gradients in mid-latitude stations (compare Figure 5.21a and 5.21b). For the same reason, the accuracy of gradients estimated at stations in different latitudes may also differ systematically (compare Figures 5.21 and 5.23 and note the different scales on the y-axes). Low elevation angle measurements at different azimuths are crucial for estimation of gradients. This fact may prevent reliable short interval estimation of gradients. In other words, over some short periods during a session, there may not be enough low elevation quality-control-passed observations to be used for estimation of gradients.

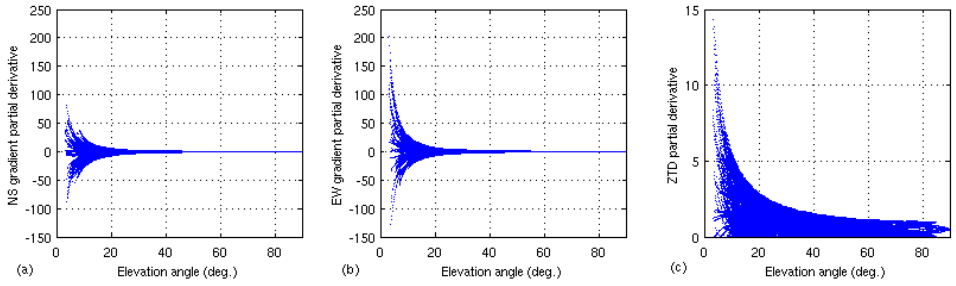

Figure 5.21- Partial derivative vs. elevation angle calculated for 2 hours estimation intervals at station ALGO, DoY 197, 2007. a) NS gradient. b) EW gradient. c) ZTD.

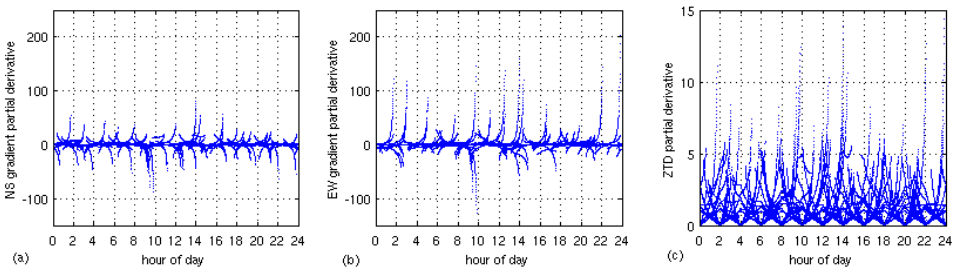

Figure 5.22- Partial derivative vs. time calculated for 2 hours estimation intervals at station ALGO, DoY 197, 2007. a) NS gradient. b) EW gradient. c) ZTD.

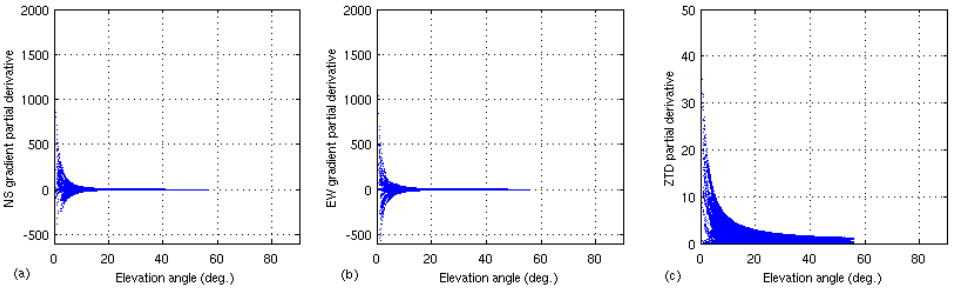

Figure 5.23- Partial derivative vs. elevation angle calculated for 2 hours estimation intervals at station ALRT, DoY 197, 2007. a) NS gradient. b) EW gradient. c) ZTD.

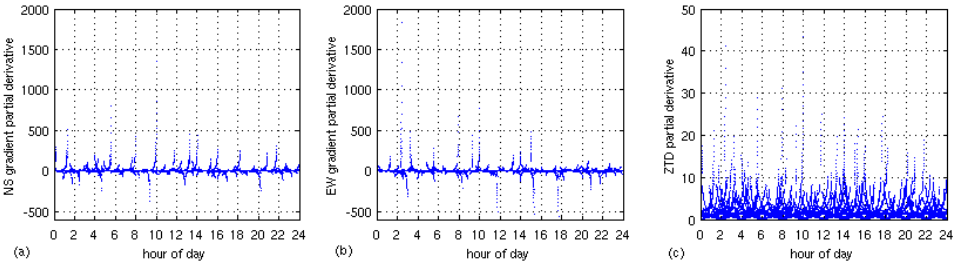

Figure 5.24- Partial derivative vs. time calculated for 2 hours estimation intervals at station ALRT, DoY 197, 2007. a) NS gradient. b) EW gradient. c) ZTD.

5.5.1- Gradient Estimation Interval Effect

Estimation of one set of unconstrained gradients for a 24-hour session has been a common practice in deterministic piece-wise estimation approaches such as the one used in Bernese. However, the NWP-based investigation results in the previous section shows that, depending on the location and season, gradients may vary at the sub-millimetre level over a much shorter period of time than 24 hours. Compared to the gradient values themselves the amount of the variation may seem significant. In this section, an investigation is carried out using the Bernese software to study the effect of shortening gradient estimation intervals on other estimated parameters including coordinates and ZTD. Based on the gradient temporal variation studies in the previous section, one may introduce relative constraints on the gradient to prevent large variations in estimated gradients. This can also be useful to study the effect of relative constraints on the results.

One month of GPS observations at station ALGO during July 2007 was processed using a Bernese precise point positioning engine[1] with different gradient estimation intervals, and with and without relative constraints. The relative constraint values are chosen based on the NWP-based study for the same month and station. The 31 sets of daily coordinates and 31 sets of 2-hourly ZTD estimates are compared with the International GNSS Service (IGS) cumulative solution[2] and IGS ZTD estimates. The mean and standard deviation of differences are presented in Table 5.4. As can be seen in Table 5.4, shortening gradient

[1] A modified version of the Bernese software capable of using NWP-based zenith delay and mapping function (VMF1) is used here without a priori gradient. See Chapter 6 for details of the modified software.
[2] IGS Analysis Centers' combined cumulative solution up to week 1445.

estimation intervals without relative constraints can result in larger standard deviations of differences from IGS solutions. Standard deviations are smaller when the gradients are relatively constrained. Based on the RMS of differences from IGS, horizontal and height components does not seem to be significantly affected (on average over a month) under different options shown in Table 5.4. However the ZTD estimates seems to be degraded when gradients were estimated every 2 hours without relative constraining. In this case, relative constraining has improved the ZTD estimates.

Table 5.4– Statistics of difference between PPP estimation results under various gradient estimation intervals and IGS solution. Station: ALGO, July, 2007. N/A indicates relative constraining is not applied.

Gradient estimation interval	2 hours				6 hours			
Rel. const.	0.3 mm		N/A		0.5 mm		N/A	
Diff. from IGS	Mean (mm)	Std. (mm)	Mean (mm)	Std. (mm)	Mean (mm)	Std. (mm)	Mean (mm)	Std. (mm)
Lat.	-2.90	2.63	-2.90	2.63	-2.88	2.59	-2.86	2.59
Lon.	3.70	3.68	3.80	4.00	3.72	3.65	3.91	3.70
Ht.	-1.28	6.64	-2.48	6.67	-0.73	7.07	-1.71	7.22
ZTD	-3.10	7.50	-1.24	12.70	-3.87	7.08	-2.86	8.46
Gradient estimation interval	12 hours				24 hours			
Rel. const.	0.5 mm		N/A		0.7 mm		N/A	
Diff. from IGS	Mean (mm)	Std. (mm)	Mean (mm)	Std. (mm)	Mean (mm)	Std. (mm)	Mean (mm)	Std. (mm)
Lat.	-3.01	2.60	-3.00	2.60	-3.01	2.60	-3.01	2.61
Lon.	3.18	3.71	3.10	3.70	3.14	3.72	3.13	3.73
Ht.	0.21	7.07	-0.05	7.20	0.33	6.96	0.31	6.96
ZTD	-5.14	6.26	-4.91	6.75	-5.40	5.78	-5.34	5.84

5.6- Summary

The behaviour of hydrostatic gradients has been studied in a statistical sense by using radiosonde data sets. The results showed clear average NS hydrostatic gradients over the region studied. There was not such a clear trend in EW gradients. For real-time gradients an algorithm has been developed to retrieve gradients from NWP models. Temporal variation of gradients and zenith delays were investigated using the NWP-based approach. The results were used for tuning relative constraints in gradient estimation. In Chapter 6 implementation of NWP-based gradients, zenith delays and mapping functions in scientific GNSS software will be discussed.

Chapter 6: NWP-based Parameters in GPS Software: Analysis and Results

In this chapter, the use of a semi-3-D NWP-based approach by means of implementing gradients as a priori to the code pseudorange and phase observations will be discussed. Modifications that have been carried out on Bernese GPS software to make it capable of using NWP products in all processing options will be reviewed. The effect of the NWP implemented option on some pre-processing results will be investigated as well. The effect of NWP-based parameters on a month long data set at a number of stations was carried out to investigate the change of GPS-estimated parameters under these implementations.

6.1- A Semi-3-D NWP-Based Neutral Atmospheric Correction

Although independent observations reported in Chapter 4 show good accuracy of ZHD derived from NWP models especially in low altitude regions, the accuracy of ZWD derived from these models is usually far less than that of ZHD. While NWP models provide a far more realistic 3-D atmospheric structure than standard atmosphere models, slant delays derived from NWP models are still not accurate enough for high precision GNSS positioning applications without estimation of residual tropospheric delay. Hence 3-D ray tracing trough NWP models may not be worth the effort.

An alternative approach with less computational difficulty, yet still taking into account the asymmetry of the atmosphere through the use of NWP models, could be achieved by implementing the NWP gradients in the GNSS phase and code observation equations. The ray tracing software discussed in Chapter 4 was further enhanced with the implementation of the NWP-based gradient retrieval algorithm discussed in Chapter 5. This enables the calculation of zenith delays, slant delays at a single elevation angle[1], vacuum elevation angle, as well as NS and EW gradients, at virtually any location at or near the surface of the Earth. These can be calculated at every 3 hour interval (NWP initialization and forecast times) which later can be linearly interpolated at every GNSS observation epoch to be used in processing.

Re-writing equation (2.12) at epoch t_r between receiver *r* and satellite *s*, we have:

$$T_r^s(t_r, \varepsilon_r^s, az_r^s) = ZHD_{t_r} \cdot mfh_{t_r}(\varepsilon_r^s) + ZWD_{t_r} \cdot mfnh_{t_r}(\varepsilon_r^s) + mfG(\varepsilon_r^s) \cdot (G_{ns_{t_r}} \cdot \cos(az_r^s) + G_{ew_{t_r}} \cdot \sin(az_r^s)) \quad (6.1)$$

where:

- ZHD_{t_r} and ZWD_{t_r} are ZHD and ZWD respectively at epoch t_r;
- $mfh_{t_r}(\varepsilon_r^s)$ and $mfnh_{t_r}(\varepsilon_r^s)$ are hydrostatic and non-hydrostatic symmetric mapping functions respectively at epoch t_r and elevation angle ε_r^s;

[1] Following VMF1, ray-traced slant delays at the lowest apparent elevation angle and the associated vacuum elevation angle will suffice in the calculation of the symmetric mapping functions (see chapter 3).

- $mfG(\varepsilon_r^s)$ is the gradient mapping function at elevation angle ε_r^s (depending on the gradient mapping function it can be a function of t_r too);
- $G_{ns_{t_r}}$ and $G_{ew_{t_r}}$ are NS and EW horizontal gradients at epoch t_r; and
- az_r^s is the azimuth between satellite *s* and receiver *r*.

As reviewed in Chapter 3 a number of gradient mapping functions have been developed. Figure 6.1 shows the difference between commonly used gradient mapping functions and the hydrostatic gradient mapping function of Chen and Herring [1997] referred to as *CH(h)*. The compared mapping functions include the non-hydrostatic Chen and Herring (*CH(nh)*), Davis [1993] with the hydrostatic NMF (*Davis(NMFh)*), Davis with the non-hydrostatic NMF (*Davis(NMFnh)*), and the derivative of the hydrostatic and non-hydrostatic NMF and VMF1 with respect to zenith angle.

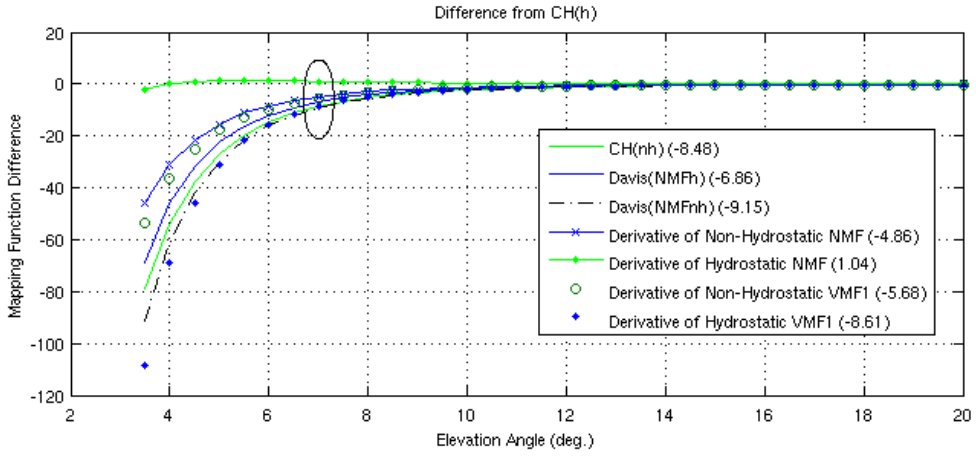

Figure 6.1- Differences of the most commonly used gradient mapping functions from *CH(h)* during DoY 197, 2007 at station ALGO (Canada). As an example, values in parentheses in the legend are the differences at 7 degree elevation angle.

The large difference between gradient mapping functions at low elevation angles might be significant. The validation of gradient mapping functions is not a trivial task. Studies reported in Chapter 5 show that *CH(h)* and the derivative of non-hydrostatic VMF1 provided closer results to the dual radiosonde ray tracing for hydrostatic asymmetric delay. One may note that the derivative of VMF1 has the advantage of being a function of location and the real time of the measurement.

Current strategies for high precision GNSS processing usually down-weight the low elevation angle measurements by an elevation-angle-dependent function. This makes the choice of gradient mapping function less critical. A number of authors have reported that the results of VLBI and GPS are not sensitive to the choice of gradient mapping function (see e.g. Bock and Doerflinger [2001], Bar-Sever et al. [1998] and MacMillan [1995]). These references all refer to the effect of the gradient mapping function when it is only used for estimation of gradients; i.e., as a part of the design matrix. The effect of the gradient mapping functions in the current approach; i.e., when it is also used to correct the slant delay a priori (in equation (6.1)) is investigated. Figure 6.2 shows the difference that using the derivative of the hydrostatic or non-hydrostatic VMF1 as a gradient mapping function can cause in the slant hydrostatic delays over 24 hours of measurements. Only 0.15% of measurements in the day were affected by more than 0.5 cm.

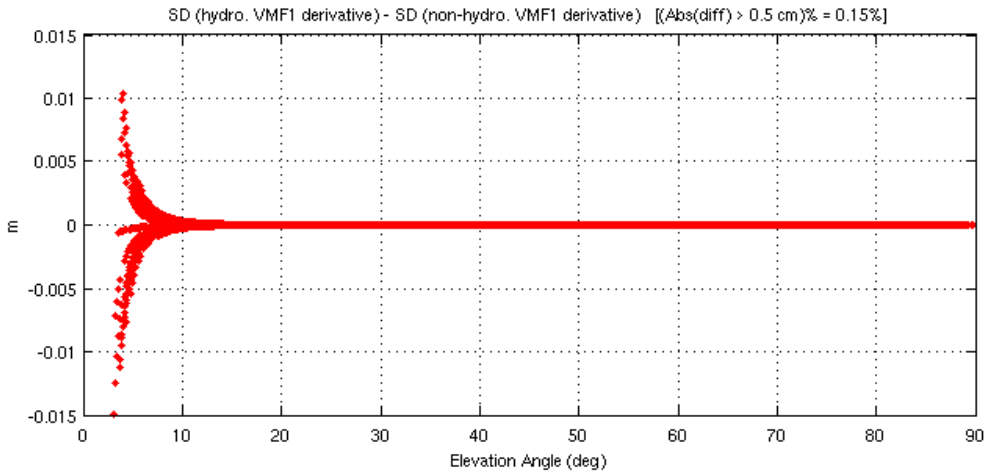

Figure 6.2- Difference in slant hydrostatic delay as a result of using the derivative of the hydrostatic or non-hydrostatic VMF1 as a gradient mapping function. Station: ALGO (Canada), DoY 197, 2007.

6.2- Software Implementation

Equation (6.1) can be used to apply a correction for neutral atmospheric delay on phase and code pseudorange observables. This provides a more accurate phase and code pseudorange which are corrected based on the real time and azimuth of measurement in addition to the elevation angle. In order to investigate the effect of NWP-based parameters on GPS estimated parameters, I have modified the Bernese GPS software. Bernese is a high quality software package for GNSS applications which is being used by many research centres including some of the IGS analysis centres. The software is well-suited for processing long data sets and is capable of considering almost all current state-of-the-art post-processing options.

Figure 6.3 shows major steps that have been carried out for implementation of NWP parameters in the Bernese software. Zenith delays, mapping functions[1] and gradients retrieved from NWP models based on the algorithms mentioned in previous chapters are entered through a newly defined Bernese input file[2]. As can be seen in the lower part of Figure 6.3 implementing the NWP-corrected phase and code pseudoranges in the software includes modifications to 4 main parts of the software:

- Synchronization of receiver clocks with GPS time and determination of approximate station coordinates using code zero-difference measurements.
- Preprocessing of the phase observation on the zero- and single-difference level and cycle slip detection and repair.
- Main parameter estimation program.
- Combination of results achieved by sequential solutions using normal equation files.

[1] VMF1 mapping functions used as symmetric NWP-based mapping functions while derivative of non-hydrostatic VMF1 is used as a gradient mapping function.
[2] A file with extension NWP is defined and introduced in all related programs and menus. See Appendix V for the format of this file.

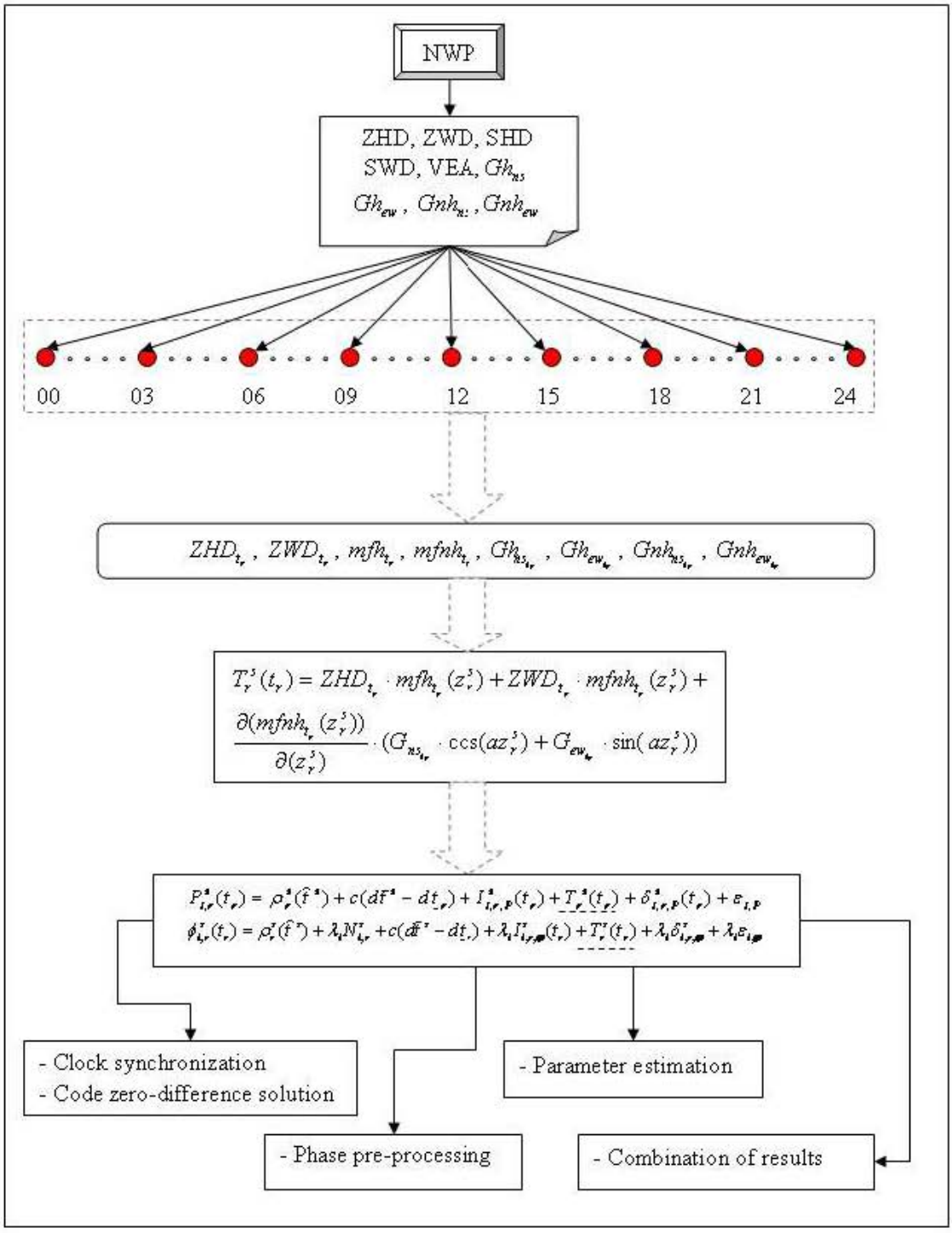

Figure 6.3- A simplified representation of implementation of NWP-based parameters in the Bernese GNSS software.

6.2.1- Clock Synchronization and Code Zero-Difference Solution

An accuracy of 1 microsecond (μs) for the receiver clock error can result in a geometric distance (between satellite and receiver) error of smaller than 1 mm [Bernese, 2007]. A code observation with RMS error of less than about 300 m may fulfill the requirement for receiver clock error accuracy of $1\,\mu s$. Therefore even C/A code measurements are sufficient for this purpose. Within the Bernese software a program named CODSPP uses least-square adjustments to estimate receiver clock errors using zero-difference code (or smoothed code) measurements (linear combinations such as ionosphere-free are usually used). The estimated receiver clock errors in program CODSPP are used as a priori values for the main parameter estimation program. The effect of an enhanced a priori neutral atmosphere model on a priori clock estimation is marginal and is more visible when low elevation angle measurements are used. Figure 6.4 shows the receiver clock error estimated at station ALGO using the author-modified version of the Bernese software (see Figure IV.1 for a flow diagram of the modified and newly added subroutines to the CODSSP program capable of correcting pseudoranges using the NWP-based approach) and original software options including the default option of Saastamoinen[1]. The minimum elevation angle used in the results presented in Figure 6.4 was set to 10 degrees. As can be seen in the title of the figure the RMS of the estimated

[1] In program CODSPP of Bernese Version 5.0, the Saastamoinen option for neutral atmosphere model means: constant values of temperature (18°C), relative humidity (50%) and pressure (1013.25 hPa) at zero height are interpolated to the station height and used in the Saastamoinen model and mapping function.

clock error differences is 0.0012562 μs . The RMS increased to 0.0015585 μs when the minimum elevation angle was decreased to 3 degrees (see Figure 6.5). Some effects which are likely to be due to the larger errors in low elevation angle measurements under the Saastamoinen approach can be seen in Figure 6.5. ZHD and ZWD from NWP and Saastamoinen (as implemented in the original Bernese) at station ALGO in the investigated day can be seen in Figure 6.6. A clear correlation between the larger ZWD difference between the two neutral atmospheric modeling approaches from DoY 192 to 192.6 (see Figure 6.6b) and the larger difference between the estimated clocks can be seen. However it should be mentioned that a priori receiver clock error estimates under either of the neutral atmospheric modeling strategies are usually sufficiently close to be able to provide similar final clock and coordinate results from the main parameter estimation program (in a PPP approach for example).

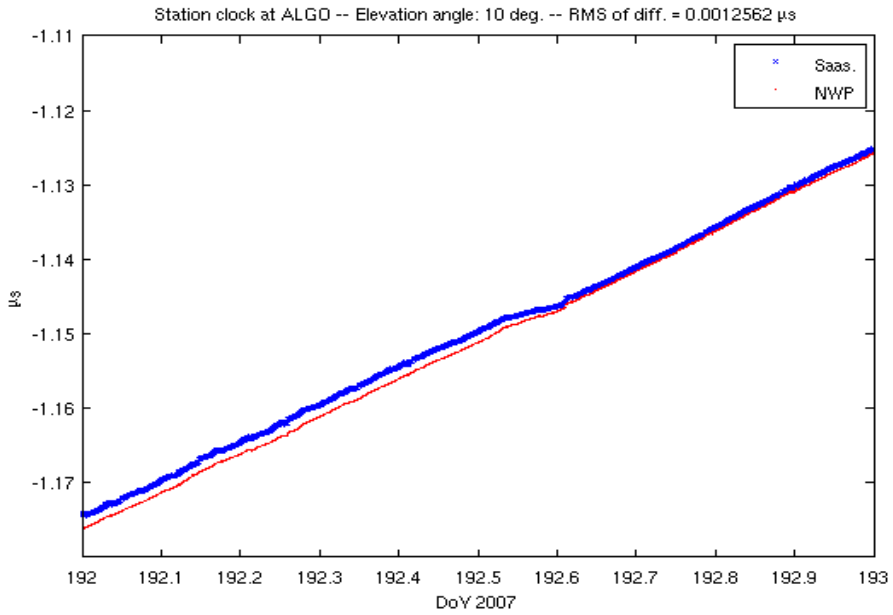

Figure 6.4– Receiver clock error estimated using smoothed code with a minimum of 10 degree elevation angle at station ALGO under Saastamoinen and NWP neutral atmospheric correction methods.

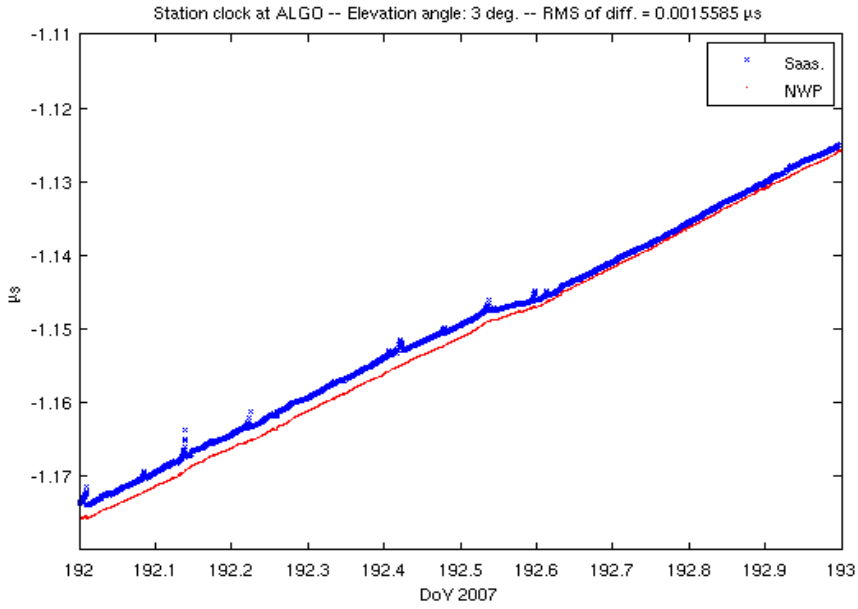

Figure 6.5- Receiver clock error estimated using smoothed code with a minimum of 3 degree elevation angle at station ALGO under Saastamoinen and NWP neutral atmospheric correction methods.

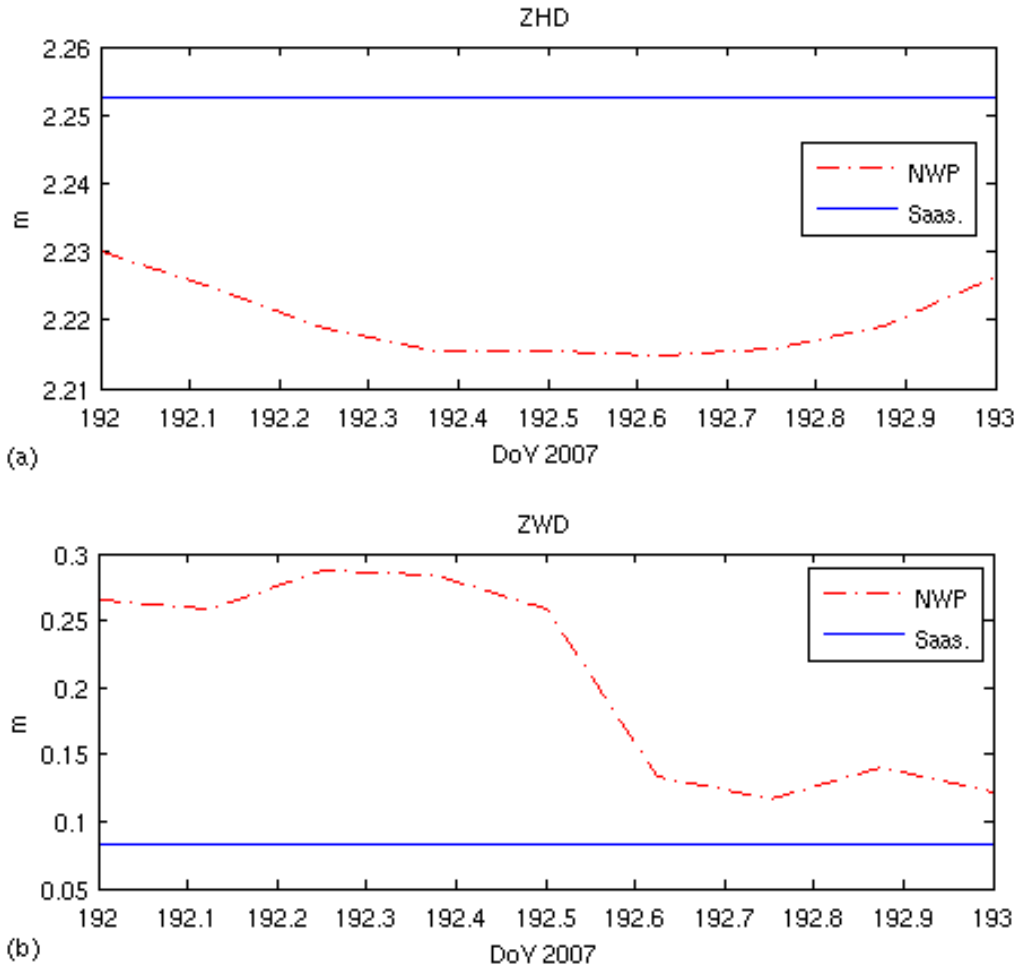

Figure 6.6- Zenith delay from NWP and Saastamoinen model (with Bernese default parameter values) at station ALGO. a) ZHD. b) ZWD.

Estimation of a priori coordinates using code (or smoothed code) is also being carried out in program CODSPP. The effect of the NWP-based neutral atmospheric correction is investigated in an epoch by epoch solution of the zero-difference ionosphere-free linear

combinations of the smoothed code[1] (see equation (2.9) for ionosphere-free linear combination of code measurements). Figure 6.7 shows coordinate differences from IGS cumulative solutions[2] when an elevation cut off angle of 10° is imposed. The RMS of the differences can be seen in the title of the subplots. The RMS is smaller when the NWP option is used, especially in the height component. The results when observations are down to 3° are processed can be seen in Figure 6.8. The difference between the two solutions is larger and the effect of the NWP approach becomes more significant. The large discrepancies of the Saastamoinen solution in some periods in Figure 6.8 are likely to be due to the low elevation angle measurements which are more vulnerable to an inaccurate neutral atmosphere modelling. The use of the NWP approach in this investigated scenario resulted in a decrease of the RMS by about 30 cm in the height component when low elevation angle measurements are used (see Figure 6.8c). Again one can notice that the differences between the two solutions are larger during the period when ZWD values from Saastamoinen differ greatly from the NWP values (compare Figures 6.6, 6.7 and 6.8). A similar result for smoothed code solutions under different neutral atmosphere models was found for other stations. Even though the accuracy of coordinate results from a code solution are not sufficient for high accuracy applications, improved results under the NWP-based neutral atmospheric modeling approach may be

[1] Observation of each satellite arc can be smoothed using the RNXSMT program of Bernese software which employs a number of linear combinations and screening approaches for outliers and cycle slip detection and finally uses carrier phase data to smooth the code data. See Bernese [2007] for details.
[2] In this chapter the IGS cumulative solution refers to IGS Analysis Centers' combined cumulative solution up to week 1445.

useful for providing better a priori kinematic coordinates. A least-squares adjustment approach used in Bernese can be enhanced by improving a priori coordinates.

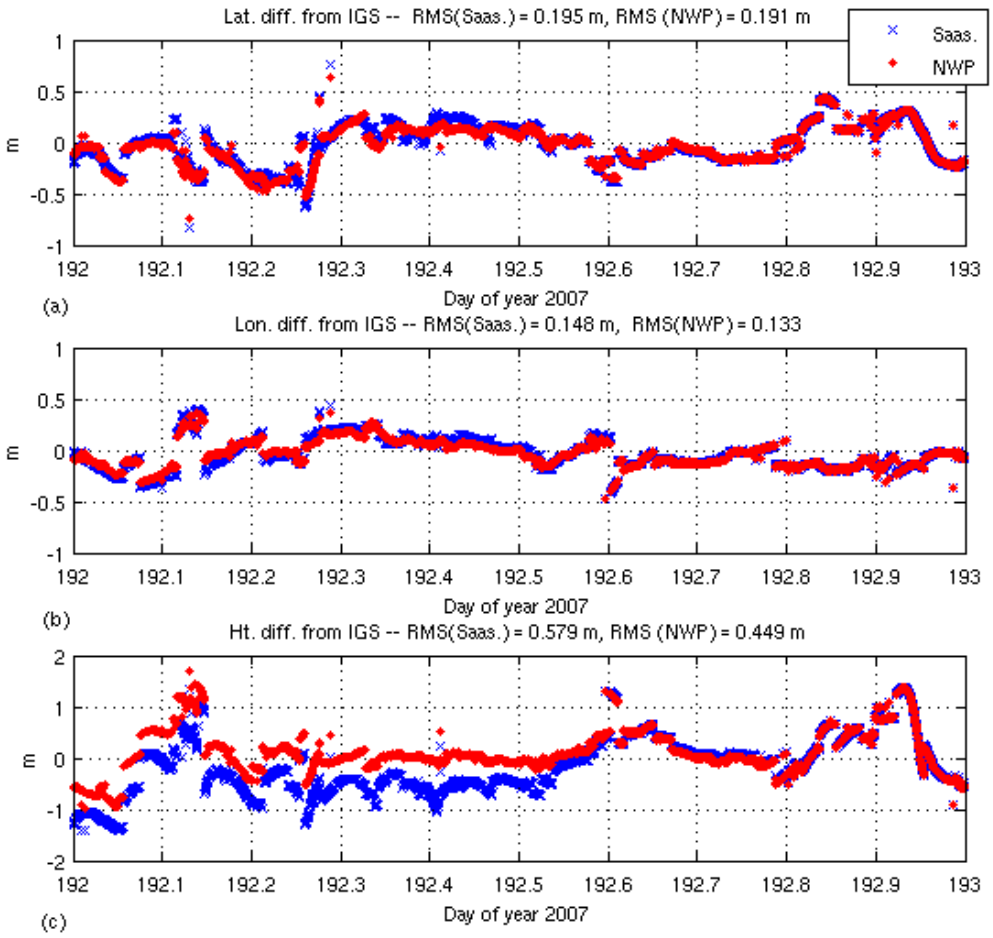

Figure 6.7– Difference of code solution using Saastamoinen and NWP approaches at station ALGO from IGS cumulative solution, elevation angle cut off: 10°. a) Latitude. b) Longitude. c) Height.

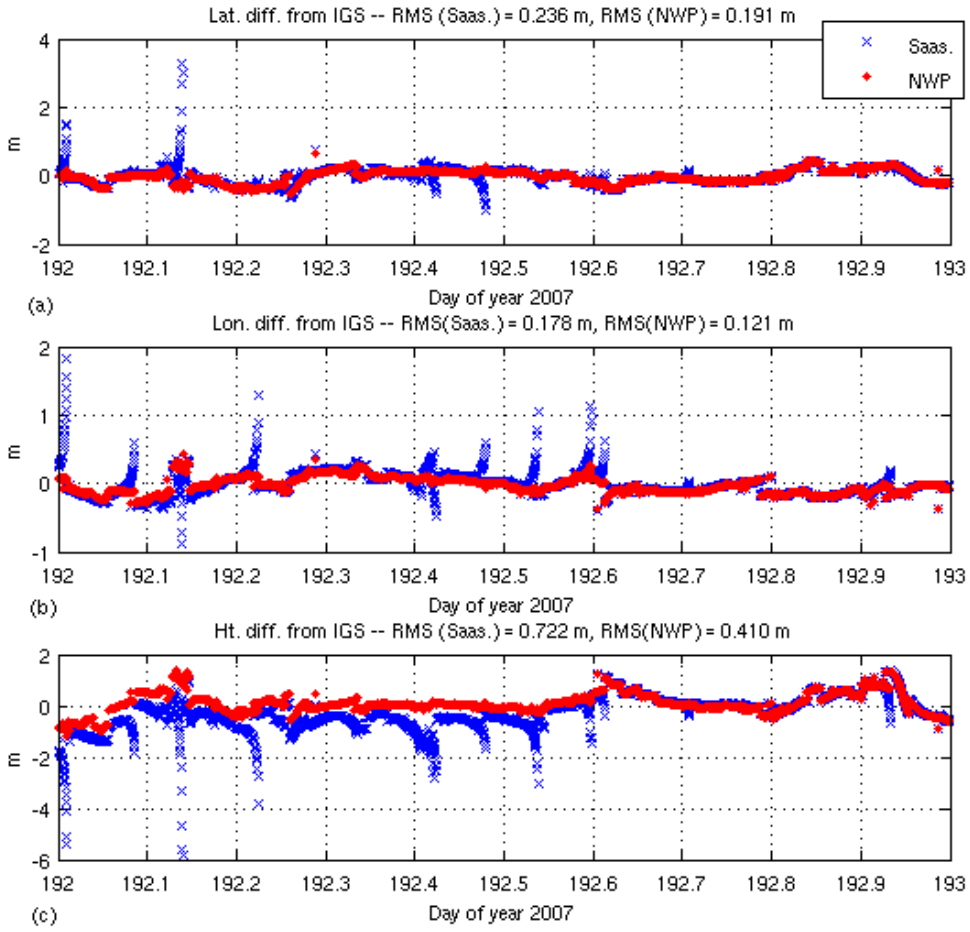

Figure 6.8– Difference of code solution using Saastamoinen and NWP approaches at station ALGO from IGS cumulative solution, elevation angle cut off: 3°. a) Latitude. b) Longitude. c) Height.

6.2.2- Pre-Processing of Phase Observations

Within the Bernese GPS software a program named MAUPRP is also capable of identifying cycle slips without the need for code observations. Although this program is able to process both zero-difference and single-difference observation files, it is not

usually used for zero-differences unless high accuracy (better than 0.1 ns) satellite clocks with the same sampling rate as the observations are available [Bernese, 2007]. The program performs a number of screening approaches to identify outliers and compute a triple-difference solution to be used for cycle slip detection.

Hydrostatic, non-hydrostatic and total delay NWP options have been implemented in the MAUPRP program. In Figure IV.2 the flow diagram of newly added and modified subroutines in this program are shown. As an example a baseline made by stations ALGO and NRC1 (about 199 km) was processed using the modified program twice: under the total delay NWP option and the default option of Niell[1]. The a priori coordinates of both stations were chosen from the IGS cumulative solution and station ALGO was considered as fixed. Assuming the IGS coordinates as true values, the difference between the triple-difference solution and IGS may represent the accuracy of the solution. Figure 6.9 shows the NRC1 position difference from IGS (used as a priori) for both solutions. It can be seen that the NWP option provided more accurate triple-difference solutions.

[1] In MAUPRP, Niell option means total zenith delay from Saastamoinen model together with hydrostatic NMF.

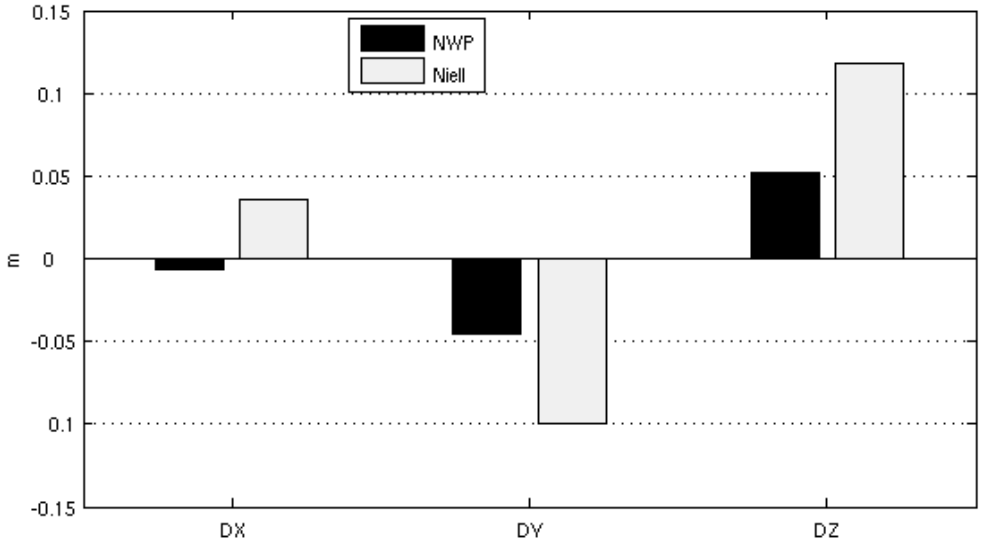

Figure 6.9– Difference of coordinate components from IGS at NRC1 in a triple-difference solution by program MAUPRP. Baseline: ALGO-NRC1, DoY 192, 2007.

6.2.3- Main Parameter Estimation

The main parameter estimation program of Bernese, namely GPSEST, sets up the observation equations and solves the normal equations based on a least-squares approach. The program deals with the neutral atmospheric delay in two parts: a priori modelling, and estimation of residual zenith delay and gradients. Similar to the above mentioned programs, new options have been added to GPSEST for correcting observation equations based on equation (6.1) where VMF1 (hydrostatic and non-hydrostatic) together with the derivative of non-hydrostatic VMF1 are used as symmetric and gradient mapping functions respectively. The possibility of choosing a priori gradients (hydrostatic, non-hydrostatic or total from NWP) is also provided through the newly defined input file.

The hydrostatic and non-hydrostatic VMF1 are added as new options for mapping functions in order to be used as partial derivatives in the estimation of the residual neutral atmospheric delay. Figure IV.3 shows a flow diagram of the newly added and modified subroutines in the GPSEST program. The effect of these added options are partly investigated in a month-long PPP processing example as will be discussed in section 6.3.

6.2.4- Combination of Solutions

Multi-session solutions are combined in the Bernese software in a program named ADDNEQ2. The main inputs to this program are the normal equations resulting from the sequence of solutions from GPSEST. One may refer to Bernese [2007] for details on the sequential least-squares estimation approach used in ADDNEQ2. Modifications to this program were carried out to make it capable of handling the results from the modified GPSEST. Figure IV.4 represents a flow diagram of the modified parts of this program.

6.3- Effect of NWP-Based Corrected Pseudo-ranges on PPP Estimates

As mentioned before, even though NWP models provide a more realistic state of the atmosphere, due to the uncertainties that are associated with them (especially in the non-hydrostatic part) the estimation of residual neutral zenith delay is still unavoidable for high accuracy applications. Hence the hydrostatic zenith delay together with a hydrostatic mapping function is preferred as an a priori correction. In this case a non-hydrostatic mapping function can be safely used for the partial derivative for estimation of residuals

which, in this case, are the non-hydrostatic delays. In other words, in the absence of an accurate met sensor collocated with the GNSS antenna, NWP is probably the most accurate available option for ZHD (see Chapter 4). Hence, the residual outputs can be considered as ZWD without need for further corrections. Similarly, regarding the use of NWP-based gradients, it may be more practical to implement hydrostatic gradients rather than non-hydrostatic or total gradients for two reasons:

1. The higher accuracy of hydrostatic gradients derived from NWP models compared to the non-hydrostatic gradients.
2. As mentioned in Chapter 5, for GNSS measurements down to a 3 degree elevation angle, the atmosphere contributing to the hydrostatic path delay has a horizontal radius of about 700 km around the station. Therefore even low resolution NWP models may be able to provide useful hydrostatic gradient estimates.

Hence, considering the hydrostatic zenith delay and gradients (and using hydrostatic VMF1 as a symmetric mapping function and the derivative of the non-hydrostatic VMF1 as a gradient mapping function in equation (6.1)), the a priori slant delay (SD) at epoch *i* to satellite *j* (SD_i^j) can be written as:

$$SD_i^j = ZHD_i \cdot VMFH1_i^j + \frac{\partial VMFW1_i^j}{\partial z_i^j}(Gh_{NS_i} \cdot \cos(az_i^j) + Gh_{EW_i} \cdot \sin(az_i^j)) \qquad (6.2)$$

where ZHD_i is the zenith hydrostatic delay from the NWP model interpolated to epoch *i*, $VMFH1_i^j$ and $VMFW1_i^j$ are the hydrostatic and wet VMF1 (partly from NWP) for

satellite *j* interpolated at epoch *i*, z_i^j *and* az_i^j are the zenith angle and azimuth at epoch *i* to satellite *j* respectively, and Gh_{NS_i} and Gh_{EW_i} are the hydrostatic NS and EW gradients from NWP interpolated at epoch *i* respectively.

Figure 6.10a shows the a priori SD resulting from a standard atmosphere, Saastamoinen zenith hydrostatic model, and hydrostatic NMF (hereafter referred to as the default) at station ALGO on DoY 197, 2007. Figure 6.10b shows the difference of SD from NWP ZHD and VMFH1 (equation (6.2) without gradient components) from the default. Figure 6.10c shows the difference between SD from equation (6.2) and the default. As can be seen in Figure 6.10b the use of a priori ZHD from NWP caused a difference varying from 10.6 mm to 150 mm with respect to the default scenario (Figure 6.10a) in this case. The range of differences further increased from 10.5 mm to 179.6 mm when hydrostatic gradients were also considered. The differences between the NWP option with and without hydrostatic gradients as a priori can be seen in Figure 6.10d. One might expect larger differences in situations like the passage of weather fronts or, in case of ZHD, where the sea-level pressure is very different from that of the standard models used in GNSS software. One such location is the belt around Antarctica where the annual average sea-level pressure is of the order of 985 hPa [Peixoto and Oort, 1993], far less than what is usually considered in models based on a standard atmosphere.

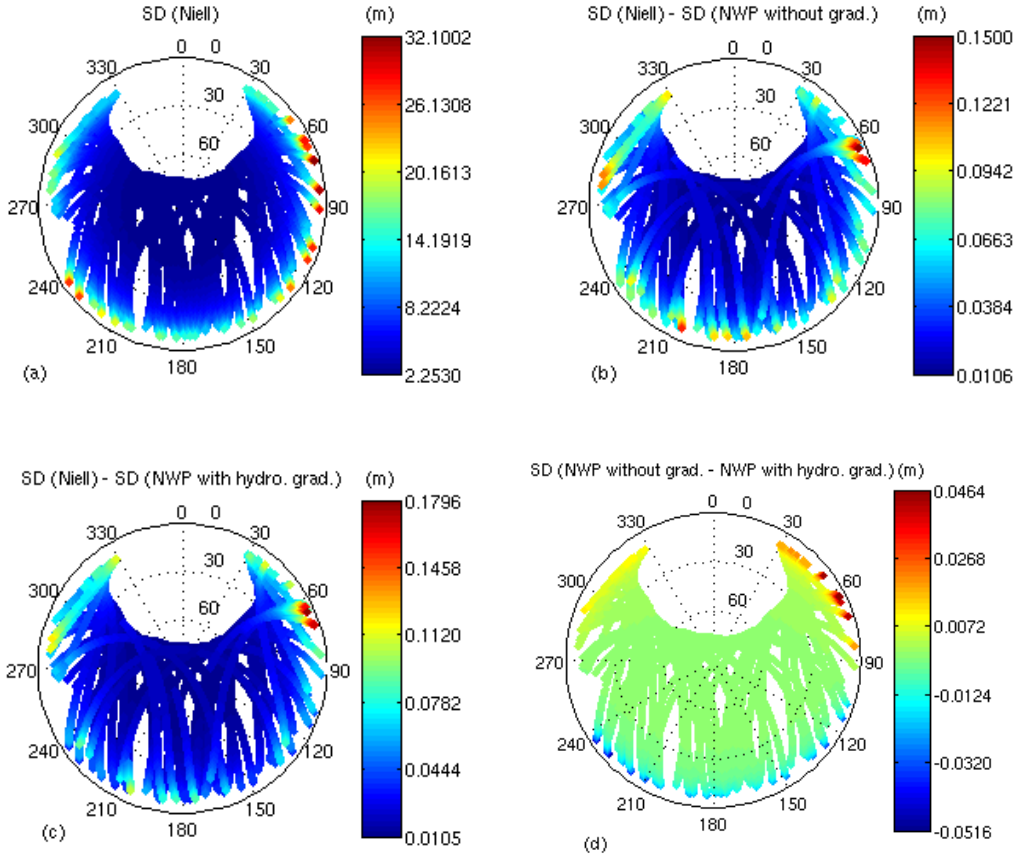

Figure 6.10- a) A priori slant delay from the Saastamoinen model with hydrostatic NMF. b) Difference between slant delay resulting from NWP hydrostatic zenith delay with VMF1 and (a). c) Difference between slant delay resulting from NWP hydrostatic zenith delay, gradient and VMFH1, and (a). d) Difference between slant delay resulting from NWP hydrostatic zenith delay with VMF1, with and without hydrostatic gradients. All at station ALGO on DoY 197, 2007.

6.3.1- Data Analysis and Results

A PPP processing engine using the modified Bernese has been employed in three scenarios:

1. Default processing options: Extrapolated standard constant atmosphere parameters (see the footnote on section 6.2.1 for constant values) used in the Saastamoinen model multiplied by the hydrostatic NMF as a priori SD. Non-hydrostatic NMF used for estimation of ZTD residuals and tropospheric gradients every 2 and 24 hours respectively.
2. Use of NWP ZHD and hydrostatic VMF1 as a priori SD, non-hydrostatic VMF1 for estimation of ZTD residuals and tropospheric gradients every 2 and 24 hours respectively.
3. Same as 2 but further correcting the a priori SD by adding NWP hydrostatic gradients following equation (6.2).

In all scenarios, zero difference ionosphere-free linear combinations of phase and code were used as the basic observables. While observations down to a 3 degree elevation angle were used, a weighting function of $\sin^2(e)$, where e is the elevation angle, was used to down-weight the low elevation angle measurements. IGS absolute phase-centre models for satellite and receiver antennas that are dependent on both the elevation angle and azimuth were used. Schmid et al. [2005] reported that a transition from relative to absolute phase-centre models could cause jumps of up to 5 mm in the horizontal position and up to 1 cm in the height component. They also mentioned that an absolute antenna phase-centre model has the advantage of reducing the dependence of the coordinate results on the elevation cut-off angle. IGS has switched to an absolute phase-centre model

since GPS week 1400 [IGS, 2005]. The antenna phase-centre change, which was carried out as a part of an updating of the IGS reference frame realization, mainly affects the height component and caused a decrease of weekly average estimated scale bias [IERS, 2006]. Earth rotation parameters, and final satellite clocks and orbits from IGS were used. Corrections for ocean tide loading were also applied. RINEX files from the IGS stations shown in Figure 6.11 covering the whole month of July 2007 were processed three times according to the above described scenarios. Receiver and antenna types together with approximate coordinates of the investigated stations are presented in Table 6.1. IGS cumulative solution and final IGS ZTD[1] estimates were adopted for comparisons made in the rest of this chapter.

The PPP results are from a free network solution and hence the resulting coordinates share the reference frame defined by the orbits and clocks. Since GPS week 1400, the IGS products are available in the IGS05 reference frame which is an IGS realization of the Conventional Terrestrial Reference System. However, one should note that as already pointed out by others (see e.g. Teferle et al. [2007]), no GPS software is fully consistent with the combined IGS products. While results presented in this chapter are not from any kind of transformation between current coordinate results and those of the IGS, the statistics regarding differences with respect to IGS cumulative solutions may be considered as a reference for inter-comparison.

[1] Final IGS ZTD estimates are at 5 minute intervals provided by Jet Propulsion Laboratory.

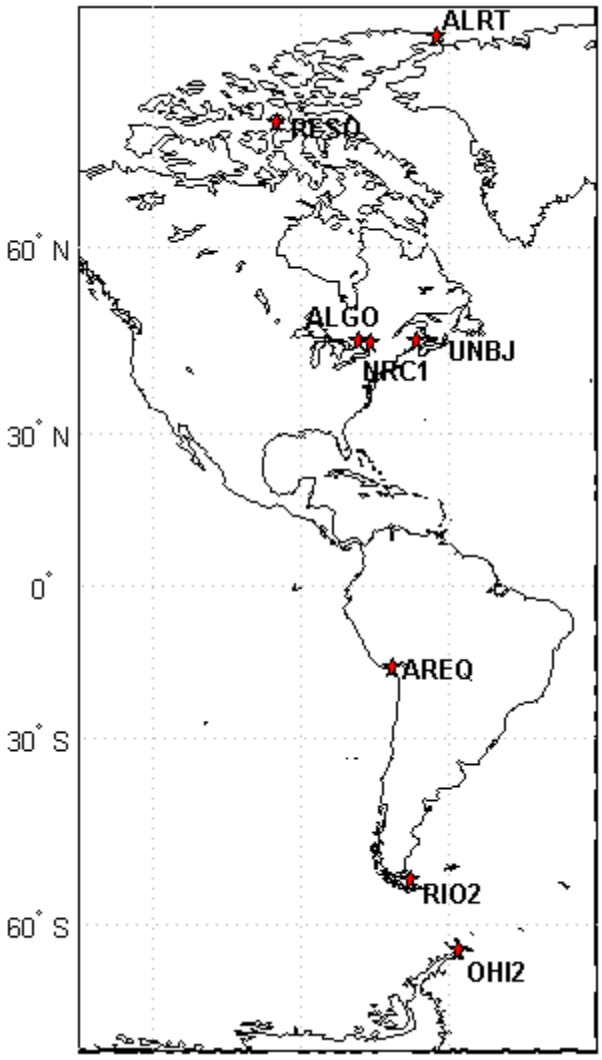

Figure 6.11- Location of investigated stations.

Table 6.1- Approximate position, receiver and antenna type of the investigated stations.

Station	Approximate Position			Receiver type	Antenna type	Antenna radome type
	Lat. (°-'-")	Lon. (°-'-")	Ellips. ht. (m)			
ALRT	82-29-40	-62-20-26	78.1	ASHTECH UZ-12	ASH701945C_M	---
RESO	74-41-27	-94-53-36	34.90	ASHTECH UZ-12	ASH700936A_M	---
ALGO	45-57-32	-78-04-17	202.0	AOA BENCHMARK ACT	AOAD/M_T	---
UNBJ	45-57-01	-66-38-30	22.75	TPS LEGACY	JPSREGANT_DD_E	---
NRC1	45-27-15	-75-37-26	82.48	AOA SNR-12 ACT	AOAD/M_T	---
AREQ	-16-27-56	-71-29-34	2488.9	ASHTECH UZ-12	AOAD/M_T	JPLA
RIO2	-53-47-08	-67-45-04	32.04	ASHTECH Z-XII3	ASH700936C_M	SNOW
OHI2	-63-19-16	-57-54-05	33.1	AOA SNR-8000 ACT	AOAD/M_T	DOME

6.3.1.1- Effect of NWP-based ZHD and Mapping Function

In Table 6.2, one can see the extreme differences of estimated parameters between scenario 1 (default) and scenario 2 (NWP ZHD and mapping function without gradients). As expected, scenario 2 mainly affects the height and ZTD values while there is no significant effect on horizontal components. One may also note larger differences in height and ZTD in southern latitude stations. This can be explained partly by Table 6.3 which includes RMS and maximum absolute difference between ZHD from NWP and Saastamoinen calculated over the month of July 2007 at investigated stations. As can be seen in Table 6.3 the discrepancy of ZHD from the two approaches increased at southern latitudes. This is partly because of using constant (regardless of season) default meteorological parameter values in the Saastamoinen model in the original Bernese

software. However even use of some latitude-based look-up tables such as the one used in UNB3, provides large discrepancies in some southern latitude regions (see Figures 4.14 and III.6). Another explanation for the larger differences for southern latitude stations can be related to the mapping functions (for the same reason as mentioned for UNB3, a mapping function like NMF may causes systematic errors in some southern latitude regions). As also stated by e.g. Vey et al. [2006] the largest impact of mapping functions based on NWP models compared to NMF can be seen in high southern latitude regions.

Table 6.2- Extreme differences between results of scenarios 1 and 2.

Station	Max. abs. lat. diff. (mm)	Max. abs. lon. diff. (mm)	Max. abs. ht. diff. (mm)	Max. abs. ZTD diff. (mm)
ALRT	0.08	0.09	2.50	1.83
RESO	0.09	0.08	1.90	1.47
ALGO	0.15	0.15	2.45	3.84
UNBJ	0.24	0.31	2.74	4.11
NRC1	0.09	0.25	1.47	2.01
AREQ	0.27	0.44	3.69	4.93
RIO2	0.16	0.41	5.68	6.19
OHI2	0.16	0.46	5.65	6.32

Table 6.3- RMS and max. abs. diff. between ZHD from NWP and Saastamoinen calculated over month of July 2007 at the investigated stations.

Station	RMS diff. (mm)	Max. abs. diff. (mm)
ALRT	10.4	27.7
RESO	13.8	26.4
ALGO	16.5	38.0
UNBJ	14.0	28.9
NRC1	16.1	37.5
AREQ	36.2	45.8
RIO2	39.6	110.9
OHI2	50.8	124.9

6.3.1.2- Effect of NWP-based A Priori Hydrostatic Gradients

As an example, the EW and NS hydrostatic gradients estimated from the NWP model at ALGO over the month of July 2007 are presented in Figures 6.12a and 6.12b respectively. Rapid changes of hydrostatic gradients are likely to be a result of the passage of low or high pressure systems around the investigated location. By taking a closer look at Figure 6.12b one can notice, for example, a rapid change of the NS hydrostatic gradient from about -0.5 to 0 mm during 19 to 20 July (DoY 200.5 to 201.5) at station ALGO. Surface weather maps at these two days are presented in Figures 6.13 and 6.14 while the thickness of the atmosphere between the 500 and 1000 hPa isobaric levels (hereafter referred to as thickness) and mean sea level (MSL) pressure maps produced using the Meteorological Service of Canada regional NWP model are also presented in Figures 6.15 and 6.16. Passage of a cold front from north to south and a low pressure system near the location of ALGO can be seen in Figure 6.13 and are likely to be partly responsible for the NS gradient on that day. Features in thickness and MSL

pressure maps may be more correlated with hydrostatic gradients. As can be seen in Figure 6.14a, during DoY 200, the thickness is changing in an NS direction near the location of ALGO. Furthermore a low MSL pressure area exists at this location while a higher pressure area is located toward the north of the station (see Figure 6.15b). These are likely to be the reason for the considerable NS gradient at ALGO. During DoY 201, however, the edge of thickness change moves further to the south (see Figure 6.15a) and a low pressure system moves to the east of ALGO (see Figure 6.16b) resulting in a slightly increased EW hydrostatic gradient which has been quantified by the gradient estimation algorithm and can be seen in Figure 6.12a.

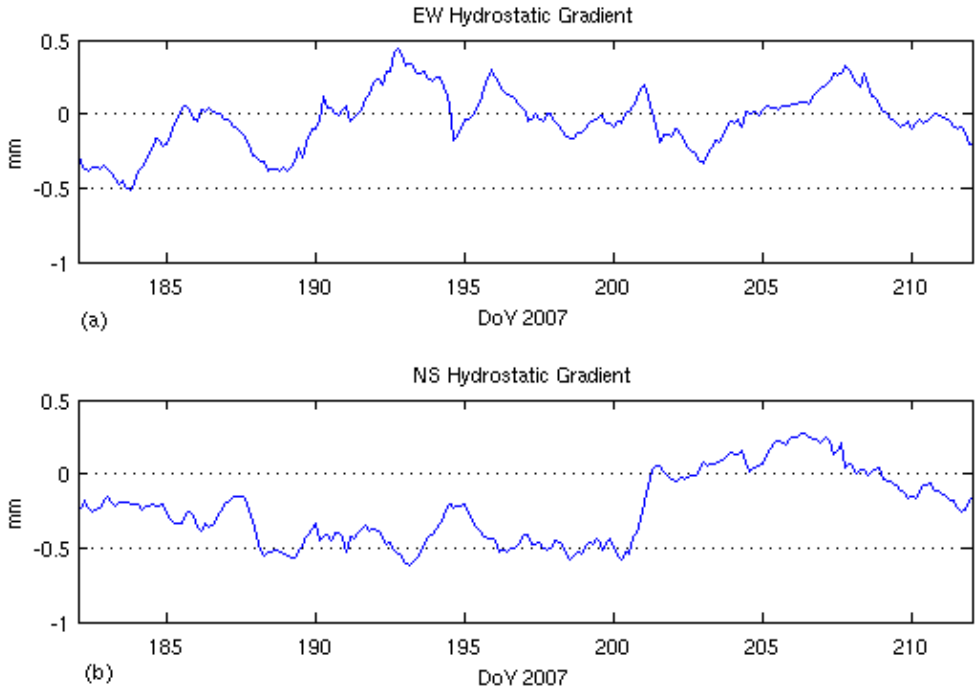

Figure 6.12- NWP hydrostatic gradients at station ALGO over month of July 2007; a) EW b) NS.

The effect of these gradients on daily estimated coordinates and 2-hour ZTD estimates can be seen in Figures 6.17 to 6.19. Figure 6.17a shows the correlation between latitude differences resulting from scenarios 3 and 2 (processing with and without hydrostatic gradients) and the magnitude of hydrostatic gradients. Figure 6.17b shows the correlation between latitude differences and NS hydrostatic gradients. Figures 6.17c and 6.17d show the correlations with longitude and height component differences respectively. It is clear from Figure 6.17b that there is a strong correlation between NS hydrostatic gradients and latitude differences. No such correlation exists with EW hydrostatic gradients as can be seen in Figures 6.18a to 6.18c. This may be partly explained by the effect of the GPS satellites' sky distribution. Regarding ZTD differences, one can see in Figures 19a to 19c that NS gradients have a higher correlation with ZTD differences than EW gradients and magnitudes at this station, although this is much lower than the latitude correlation shown in Figure 6.17b.

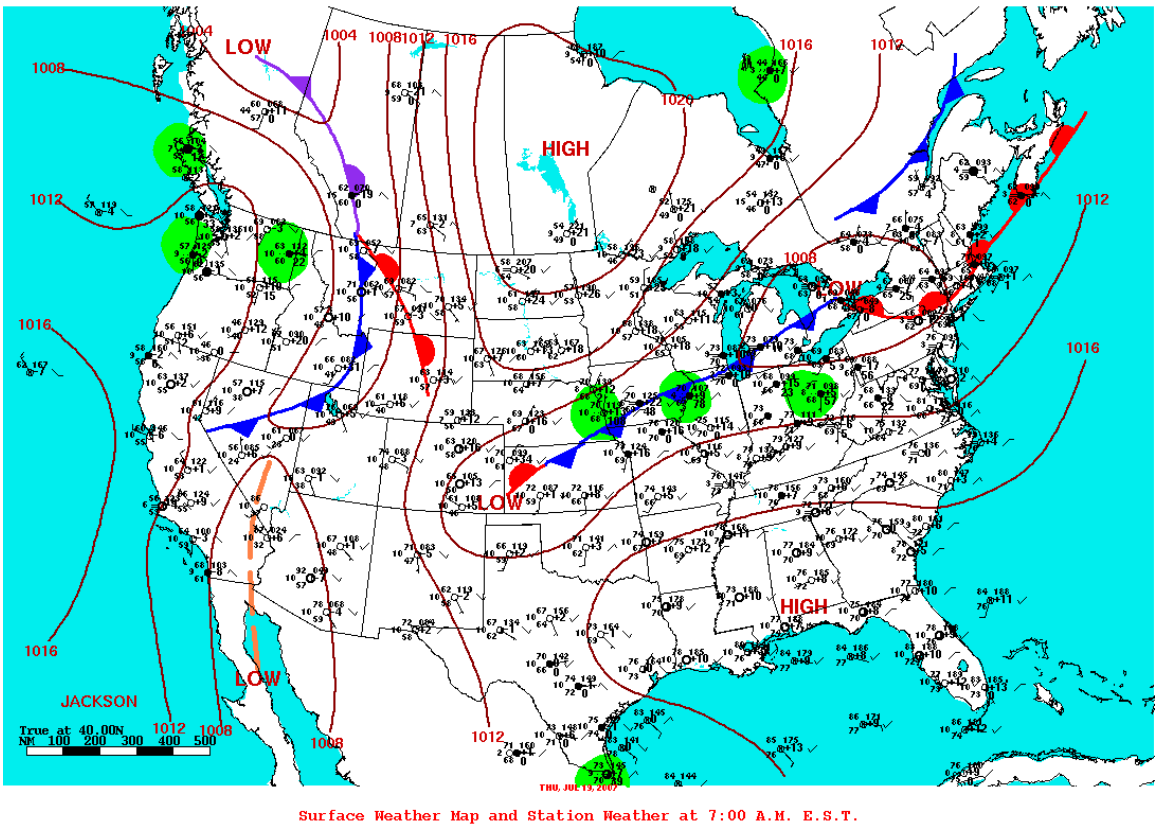

Figure 6.13- Surface weather map on DoY 200, 2007 (from NCDC [2008a]).

Statistics for all investigated stations are presented in Table 6.4, which includes correlation coefficients of the estimated daily coordinate absolute differences between scenarios 2 and 3 and absolute mean daily NS and EW hydrostatic gradients. Also included are correlation coefficients of absolute ZTD differences and absolute NS and EW hydrostatic gradients.

The significance of all correlation coefficient values have been tested using the following statistic (see e.g. Spiegel and Stephens [1998]):

$$t = \frac{r \cdot \sqrt{N-2}}{\sqrt{1-r^2}} \tag{6.3}$$

where r is the sample correlation coefficient, and N is the number of values. The statistic in equation (6.3) has the Student's distribution with *N-2* degrees of freedom. Correlation coefficients significantly different than zero at a 0.05 significance level, are presented in bold font in Table 6.4. As can be seen in the table, for all investigated stations there is a significant and strong correlation between NS hydrostatic gradients and latitude differences. For most stations, longitude components have not been affected significantly with the implementation of gradients. The height component and ZTD are also affected but the correlations with implemented gradients are not as strong as those with latitude, as previously mentioned.

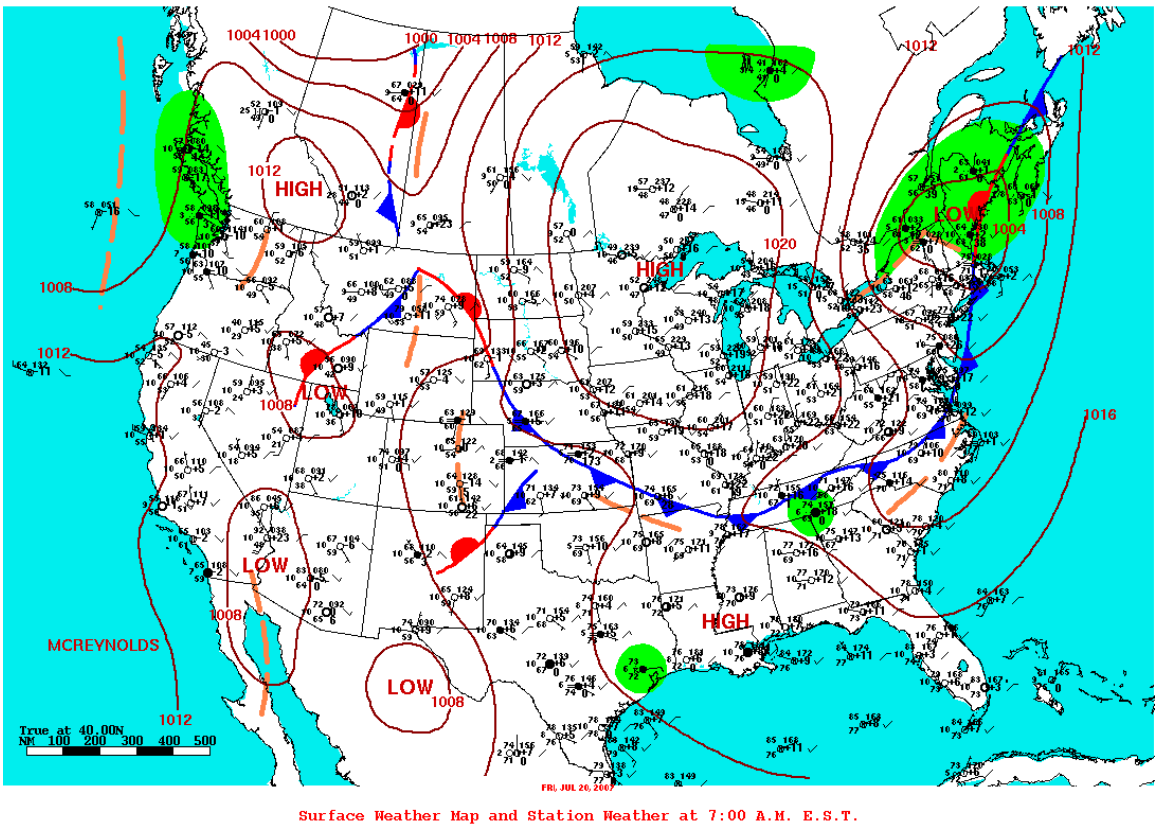

Figure 6.14- Surface weather map on DoY 201, 2007 (from NCDC [2008a]).

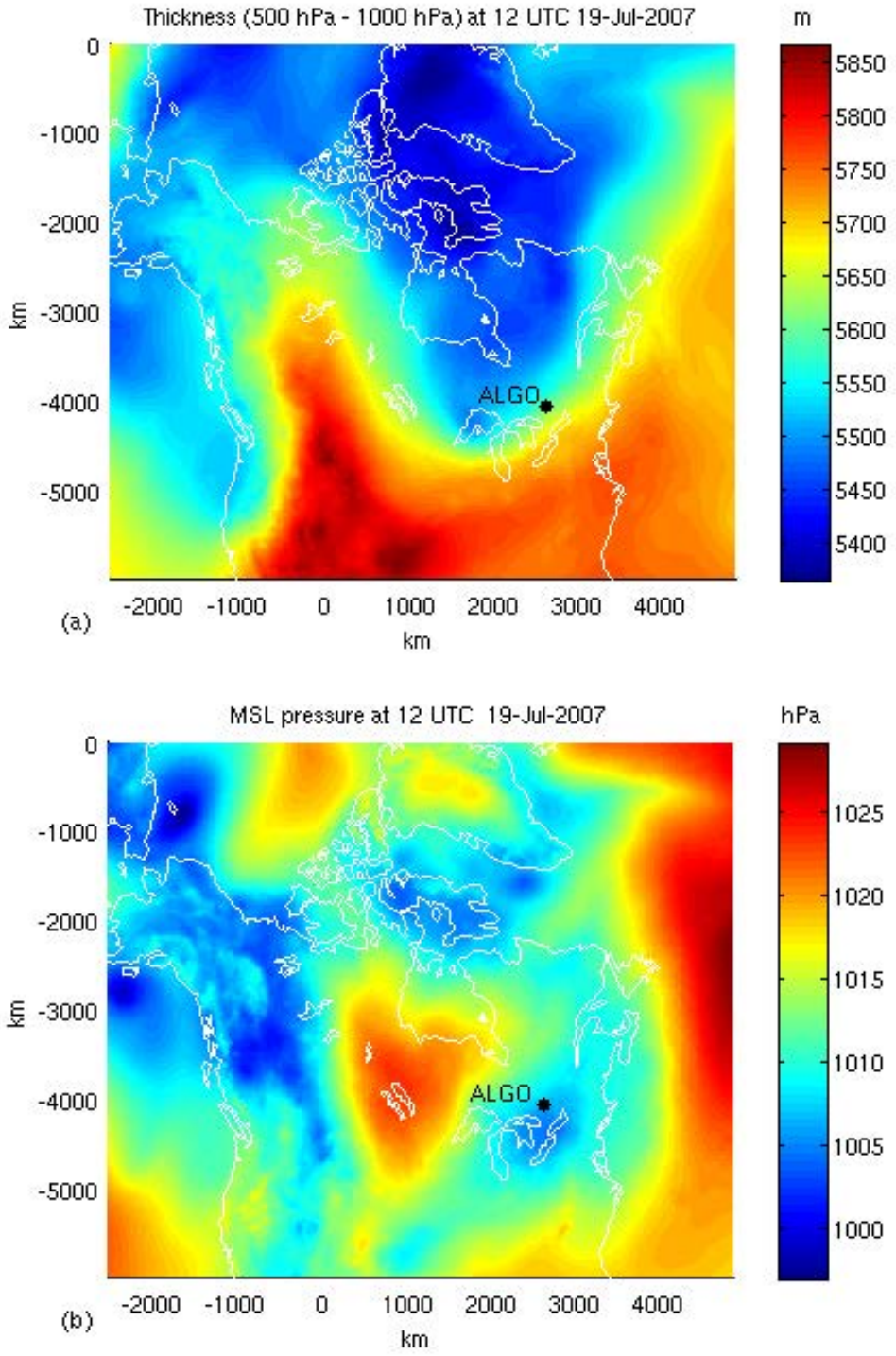

Figure 6.15- a) Thickness and b) MSL pressure maps produced using Meteorological Service of Canada regional NWP model on DoY 200.5, 2007.

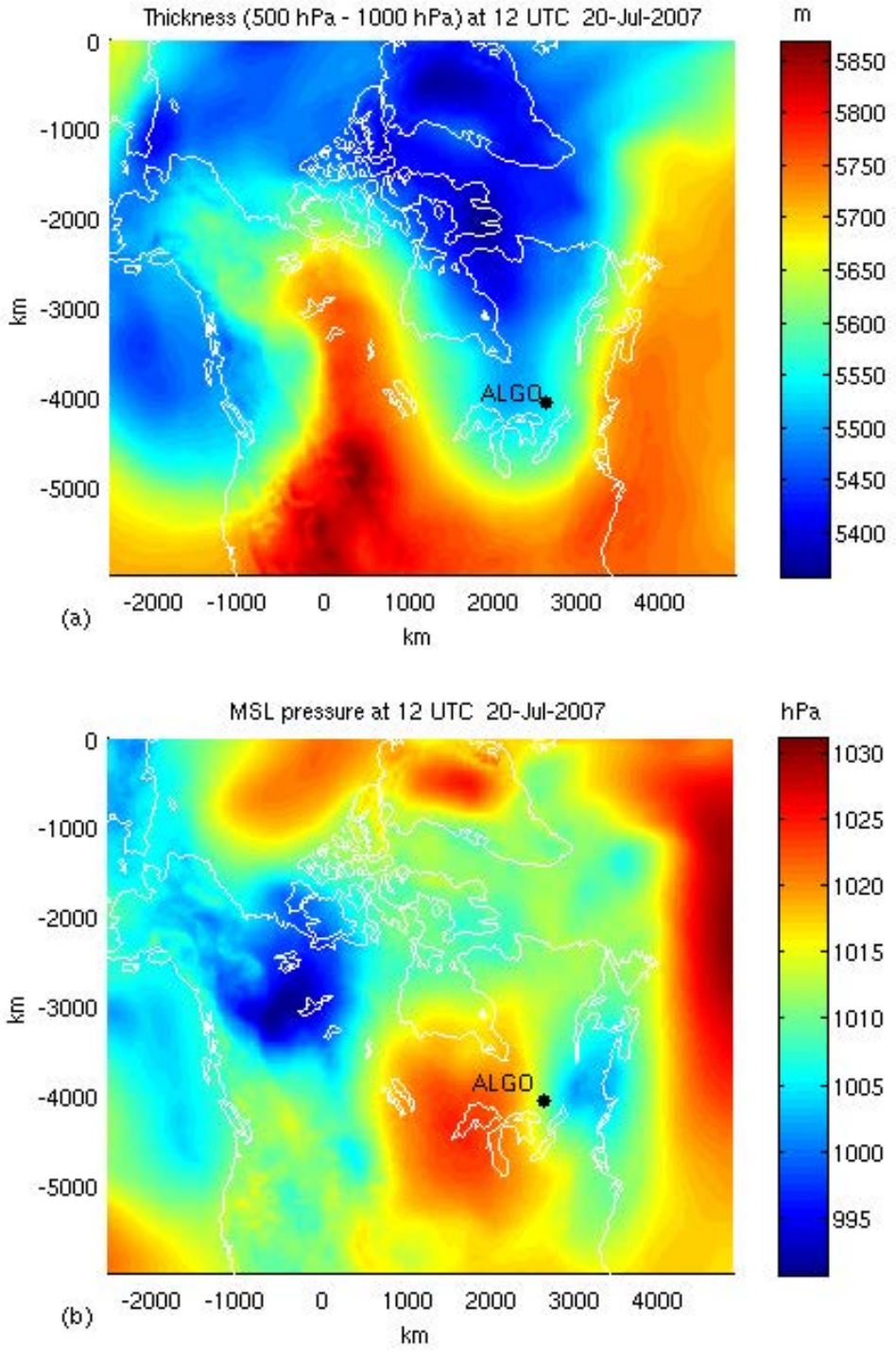

Figure 6.16- a) Thickness and b) MSL pressure maps produced using Meteorological Service of Canada regional NWP model on DoY 201.5, 2007.

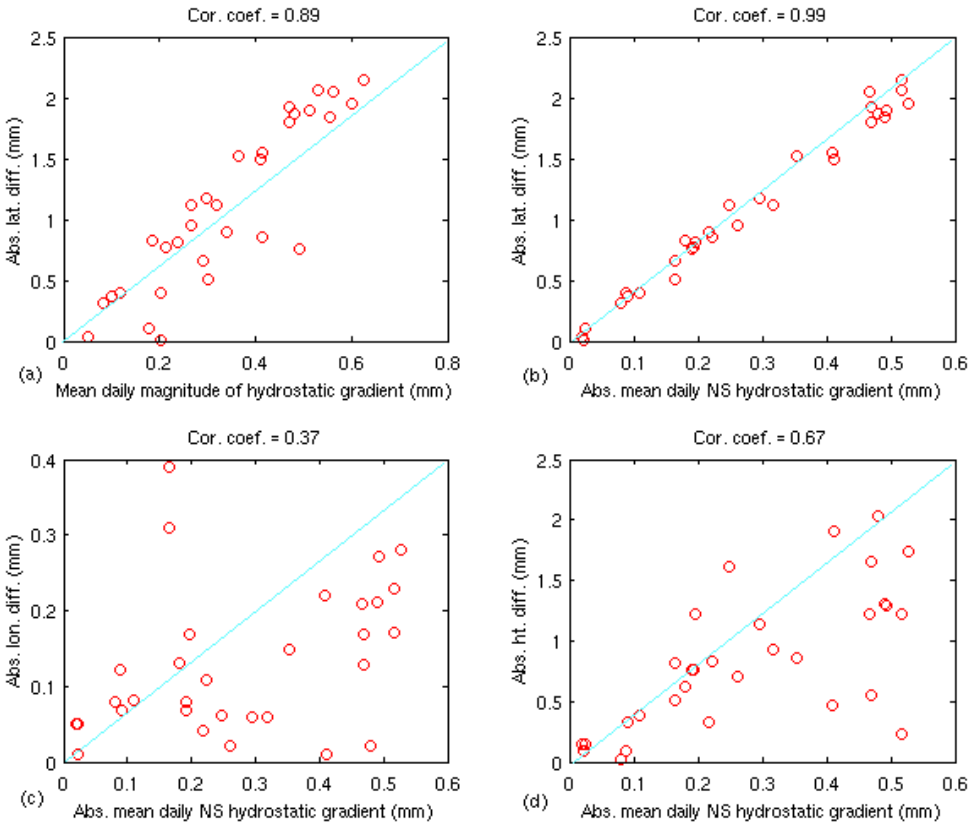

Figure 6.17- Absolute coordinate component differences between scenarios 2 and 3 vs. absolute mean daily hydrostatic gradients at station ALGO over the month of July 2007: a) gradient magnitude vs. latitude; b) NS gradient vs. latitude; c) NS gradient vs. longitude; d) NS gradients vs. height.

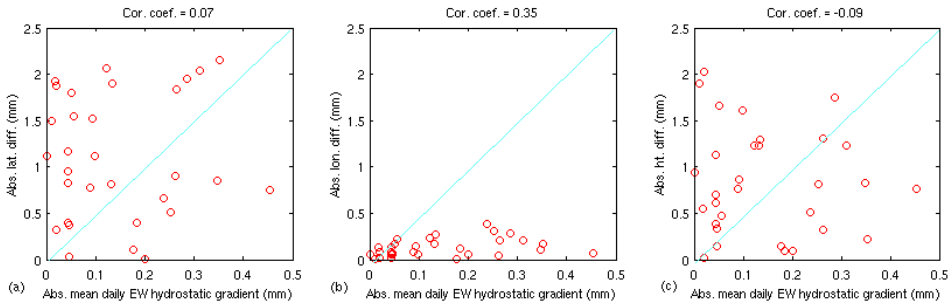

Figure 6.18- Absolute coordinate component differences between scenarios 2 and 3 vs. absolute mean daily EW hydrostatic gradients at station ALGO over the month of July 2007: a) latitude; b) longitude; c) height.

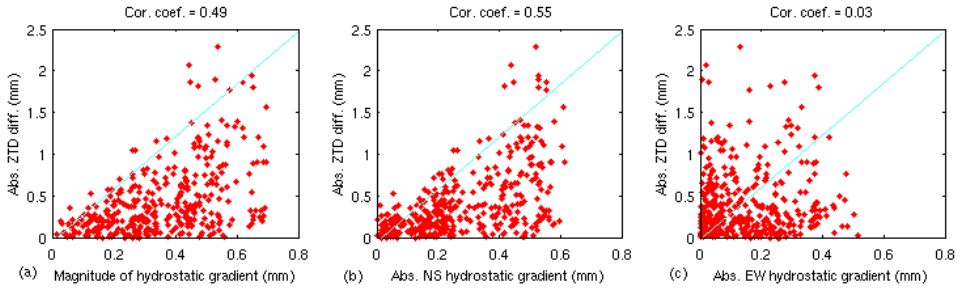

Figure 6.19- Absolute ZTD differences between scenarios 2 and 3 vs. absolute hydrostatic gradients at station ALGO over the month of July 2007: a) magnitude; b) NS; c) EW.

Table 6.4- Statistics of the comparisons between scenarios 2 and 3.

Station	Lat.			Lon.			Ht.			ZTD		
	Corr. with abs. mean daily NS grad.	Corr. with abs. mean daily EW grad.	Abs. max. diff. (mm)	Corr. with abs. mean daily NS grad.	Corr. with abs. mean daily EW grad.	Abs. max. diff. (mm)	Corr. with abs. mean daily NS grad.	Corr. with abs. mean daily EW grad.	Abs. max. diff. (mm)	Corr. with abs. NS grad.	Corr. with abs. EW grad.	Abs. max. diff. (mm)
ALRT	**0.99**	-0.04	3.39	**0.87**	0.03	0.86	**0.82**	0.13	4.41	**0.48**	0.03	7.43
RESO	**0.98**	-0.03	1.42	0.20	0.27	0.26	**0.77**	0.17	3.03	**0.27**	**0.18**	1.84
ALGO	**0.99**	0.07	2.15	**0.37**	**0.35**	0.39	**0.67**	-0.09	2.03	**0.55**	0.03	2.28
UNBJ	**0.98**	**0.42**	2.72	0.28	0.19	0.78	**0.45**	**0.38**	2.46	**0.40**	**0.22**	3.97
NRC1	**0.99**	0.19	2.25	0.20	-0.08	0.32	**0.78**	0.06	2.45	**0.57**	**0.14**	2.23
AREQ	**0.83**	0.25	0.67	0.26	0.17	1.11	**0.31**	**0.51**	2.83	**0.10**	**0.14**	6.04
RIO2	**0.99**	-0.02	5.14	0.13	**-0.41**	1.63	**0.55**	0.02	3.32	**0.59**	-0.04	3.04
OHI2	**0.99**	-0.01	3.78	0.19	**0.57**	1.35	**0.53**	-0.27	3.41	**0.74**	-0.04	4.62

Mean monthly differences between results from the three scenarios and IGS results have also been investigated. The results from all 3 scenarios agree with the IGS cumulative estimates in all three components at the mm level (except for station AREQ whose rather larger differences need further investigation). Tables 6.5 to 6.7 include mean and

standard deviation of estimated parameters from the scenarios (except for station RIO2 which did not have an IGS cumulative solution) and those of the IGS. These are also shown in Figure 6.19 to 6.22. While in a monthly comparison most of the NWP parameters' effects might average out, at some stations (namely ALGO, UNBJ, NRC1 and OHI2) the third scenario (NWP with hydrostatic gradients) still caused millimetre level mean latitude differences compared to the other scenarios. This may indicate that hydrostatic gradients can have systematic effects on long term latitude estimates.

Table 6.5- Statistics of scenario 1 results vs. IGS values.

Station	Mean diff. from IGS (mm)				Std of diff from IGS (mm)			
	Lat.	Lon.	Ht.	ZTD	Lat.	Lon.	Ht.	ZTD
ALRT	0.41	-4.61	-6.8	0.87	3.59	1.76	10.12	3.98
RESO	-3.66	-1.86	-4.77	-2.44	2.43	2.80	8.82	4.30
ALGO	-2.99	3.16	-0.47	-3.83	2.61	3.72	7.10	6.00
UNBJ	-2.44	-7.03	-6.10	5.66	3.76	3.64	6.87	8.89
NRC1	-2.51	1.06	-4.69	1.86	2.87	3.42	8.16	6.42
OHI2	5.91	1.90	-7.08	4.23	3.57	6.31	12.27	6.70

Table 6.6- Statistics of scenario 2 results vs. IGS values.

Station	Mean diff. from IGS (mm)				Std. of diff. from IGS (mm)			
	Lat.	Lon.	Ht.	ZTD	Lat.	Lon.	Ht.	ZTD
ALRT	0.44	-4.61	-6.60	0.47	3.59	1.76	10.02	3.77
RESO	-3.66	-1.87	-4.77	-2.67	2.43	2.80	8.64	4.34
ALGO	-3.01	3.13	0.31	-5.34	2.61	3.73	6.96	5.84
UNBJ	-2.39	-6.97	-5.95	5.02	3.77	3.67	6.99	8.53
NRC1	-2.53	1.16	-4.67	1.20	2.86	3.40	8.07	6.37
OHI2	5.88	1.94	-5.03	1.15	3.58	6.31	11.65	6.05

Table 6.7- Statistics of scenario 3 results vs. IGS values.

Station	Mean diff. from IGS (mm)				Std of diff. from IGS (mm)			
	Lat.	Lon.	Ht.	ZTD	Lat.	Lon.	Ht.	ZTD
ALRT	0.56	-4.67	-6.60	0.57	3.05	1.84	10.09	3.91
RESO	-3.86	-1.86	-5.10	-2.54	2.38	2.77	8.70	4.28
ALGO	-2.12	3.14	-0.19	-5.07	2.62	3.75	6.93	5.71
UNBJ	-1.08	-7.23	-6.63	5.17	3.81	3.61	6.98	8.53
NRC1	-1.49	1.16	-5.44	1.63	2.68	3.36	7.68	6.35
OHI2	4.25	1.73	-6.14	2.61	3.23	6.25	11.31	5.86

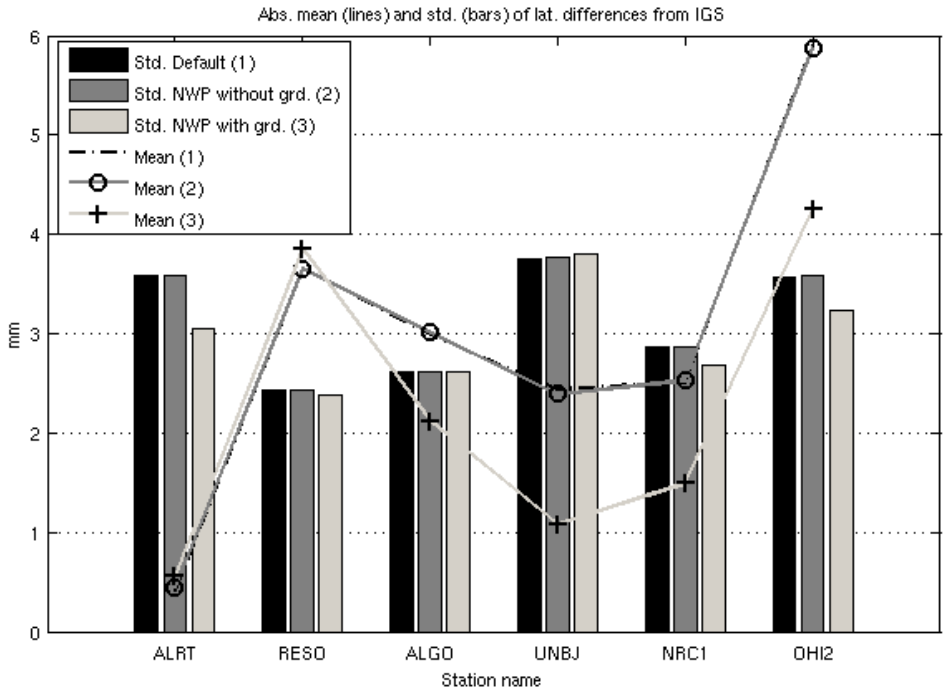

Figure 6.20- Absolute mean and std. of latitude difference between the results of the three scenarios and IGS values.

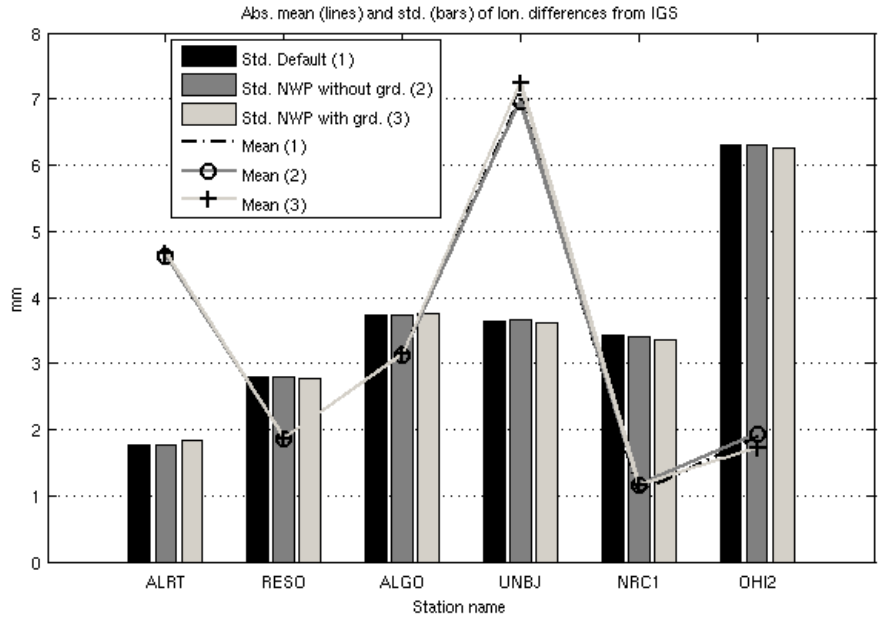

Figure 6.21- Absolute mean and std. of longitude difference between the results of the three scenarios and IGS values.

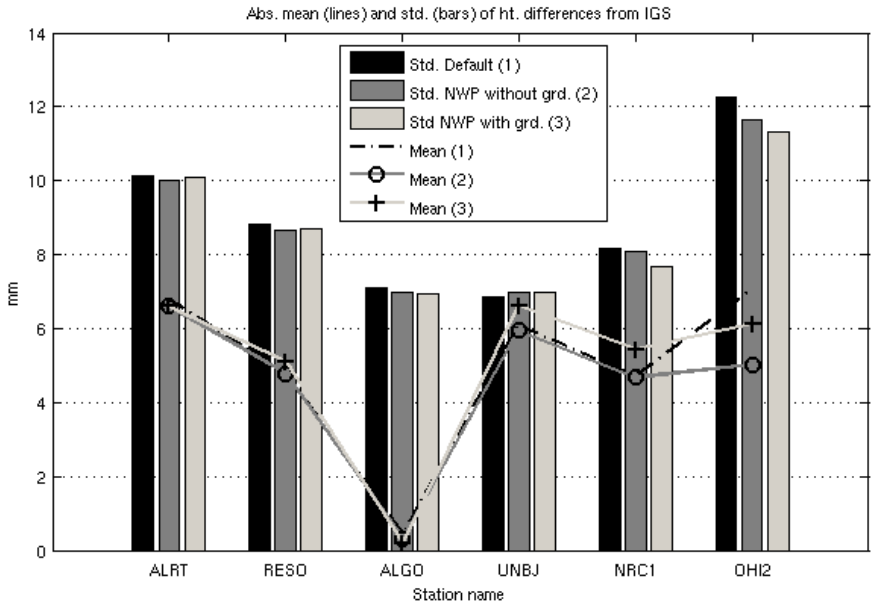

Figure 6.22- Absolute mean and std. of height difference between the results of the three scenarios and IGS values.

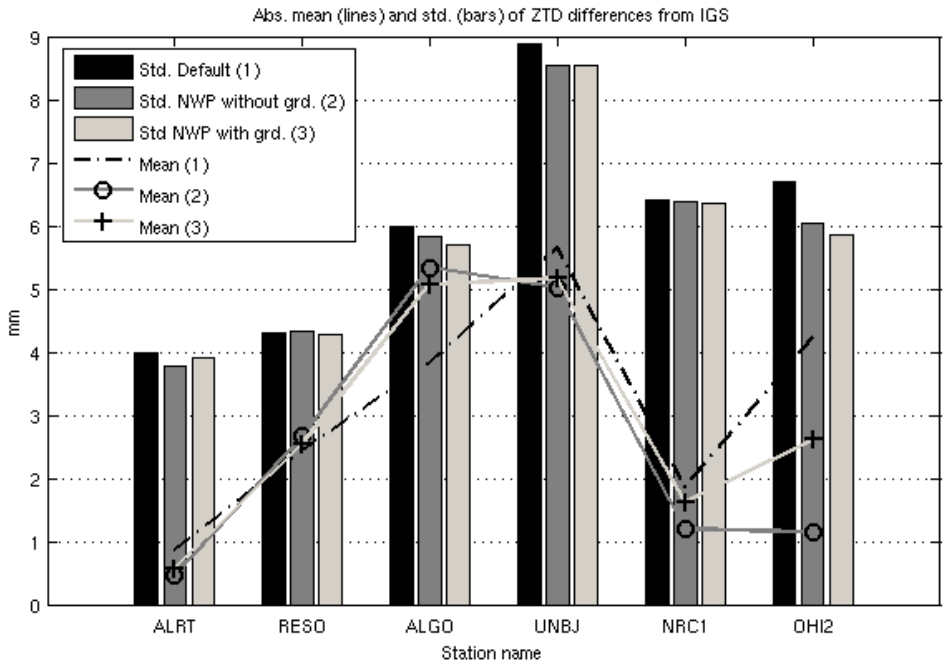

Figure 6.23- Absolute mean and std. of ZTD difference between the results of the three scenarios and IGS values.

6.3.2- Discussion

Estimated parameters from the PPP scenarios show strong correlation between NS hydrostatic gradients and latitude differences at all investigated stations. A 0.5 mm absolute mean daily NS gradient at station ALGO, for example, resulted in about 2 mm latitude difference. Overall, mean ratios of about 4-6 were found between the absolute latitude difference and the absolute mean daily NS gradient at all investigated stations. Weaker but still significant correlations also exist between NS gradients and both height and ZTD. Among the estimated parameters, longitude was the one with least change

under implementation of gradients. Although NS and EW hydrostatic gradients are of the same order of magnitude, the NS gradients seem to have a systematic behaviour as was studied in Chapter 5.

Monthly averaged estimated parameters show minor changes under the different scenarios considered. This change is larger for the latitude component at most stations. The monthly mean latitude results are closer to the reference (IGS) values when the hydrostatic gradients implemented as a priori (except for the two high latitude stations where the monthly mean NS hydrostatic gradients were close to zero and no significant mean latitude differences were found). The standard deviations of latitude, height and ZTD differences from IGS values slightly decrease at most stations when the third scenario (NWP with gradients) is used. Based on the estimation algorithms employed in the Bernese software and PPP results reported in this chapter, implementing hydrostatic gradients as a priori can cause millimetre level improvement in long term positioning at least for the latitude component. Estimation of at least one set of gradients per 24 hours still seems beneficial to absorb the non-hydrostatic gradients.

Chapter 7: Conclusions and Recommendations

In this dissertation, recent developments in neutral atmospheric modelling using NWP models have been reviewed. The performance of Canadian NWP models were validated using independent approaches at different locations including the Canadian Arctic. These include the use of a WVR and precise barometer on a moving platform in Canadian high latitudes, comparison with radiosonde data sets, and routine 3-hourly comparison of NWP and climate-based models. In general, uncertainties of 0.04-0.08% and a 5-10% for NWP-based ZHD and ZWD respectively can be expected.

The online ray tracing service developed as a part of this research is an example of a NWP-for-GNSS operational service. Generated near-real-time maps as a part of this service is an example of the feasibility of NWP models for zenith delay corrections on a global scale. The performance of UNB's widely used climate-based models can be monitored on a routine basis with NWP-based generated maps.

Behaviour of hydrostatic gradients has been studied in a statistical sense by using radiosonde data sets. The results showed clear average NS hydrostatic gradients over the region studied. There was not such a clear trend in EW gradients. For real-time gradients an algorithm has been developed to retrieve gradients from NWP models. The algorithm uses NWP profiles in all 4 cardinal directions around the station. In order to show the

effect of NWP-based parameters on GPS estimates as well as the practicality of the approach in real applications, the Bernese GPS software has been modified to be able to handle NWP-based zenith delays, mapping functions and gradients in all related programs and subroutines. This made the software capable of using a priori NWP data in all processing options. The modified software provides an eligible tool for research on the effect of enhanced neutral atmosphere information on the pre- and final processing of GNSS data.

The effect of NWP-based parameters on a month-long dataset of observations from a number of stations spread over northern and southern hemispheres was investigated in three different PPP scenarios. The processing strategies differ in the a priori hydrostatic slant delay handling. The results show strong correlation between NS hydrostatic gradients and latitude differences with weaker correlation between NS hydrostatic gradients and both height component and ZTD differences. Even though NS and EW gradients are the same order of magnitude it is found that longitude is not sensitive to either of the hydrostatic gradient components. The effect of ZHD and mapping function values from NWP when the gradients are not implemented was only seen on height and ZTD estimates. The largest effect of NWP-based ZHD and mapping functions was found for southern latitude stations.

Based on the processing results at the investigated stations mean ratios of about 4-6 were found between absolute latitude difference and absolute mean daily NS gradient. For

example, the estimated latitude component could be affected by more than 2 mm as a result of a 0.5 mm a priori NS hydrostatic gradient. Although the effect in terms of absolute maximum value might be larger for height and ZTD, the correlation of those with either gradient component was not as clear as the correlation with latitude. Furthermore, this may partly be due to higher uncertainty in height and ZTD estimations compared to horizontal components.

While it is shown in this dissertation that correcting the a priori SD with hydrostatic gradients can have a millimetre level effect in some estimated components, the modified Bernese software is capable of considering NWP hydrostatic, non-hydrostatic and total gradients as a priori in GPS observables as well as zenith delay and mapping functions based on NWP models in all processing strategies. Considering such effects on latitude, height and ZTD estimates might be crucial in applications such as deformation monitoring, long term geodynamic and crustal movements studies, sea-level change monitoring, defining terrestrial reference frames and climatology and consequential interpretations. Hence implementing hydrostatic gradients as a priori values is recommended in GPS processing when the highest accuracy is required in long-term positioning. Furthermore, in the event of passage of a weather front, the use of NWP-based parameters can provide more reliable solutions.

A clear dependence of the temporal variation of gradients on season and latitude has been found based on the NWP-based gradient retrieval approach. Furthermore, a slightly larger

average absolute temporal variation in EW gradients compared to NS gradients was found. This can probably be explained by the unsystematic average EW gradient behaviour. It was found that shortening the gradient estimation interval (to 12 hours and less) in the Bernese software decreases the precision of the estimated parameters. Relative constraining of gradients based on the NWP-based studies may prevent a degradation of the solution.

Although the UNBgr model, which has been derived from radiosonde data sets in part of North America, is a monthly averaged model without dependence on location, implementing this model as a correction to pseudoranges might be a simpler alternative to the NWP-based gradient approach. This might only be beneficial if long term (longer than a month) static data sets are needed to be processed and has yet to be investigated.

Other approaches for real-time access to neutral atmosphere corrections such as IP data streaming may be considered in the future as an alternative to the current online ray tracing service. A potential future use of the zenith delay map generation service could be in InSAR applications where a high resolution weather model can be used to reduce the atmospheric effect on InSAR interferograms.

The effect of current implementations on different processing strategies, and the use of higher resolution NWP models in order to investigate the effect of local weather anomalies, are among the future works that could be carried out with the modified

Bernese software. Another recommendation for future work is the enhancement of gradient estimation approaches by choosing modified process noise values by empirical determination from the NWP-based approach developed in this dissertation. If applicable, depending on the estimation algorithm, an investigation of the use of higher order functions rather than piece-wise linear ones in the gradient estimation might improve the resultant gradients and other estimates.

References

Ackerman, S.A., and J.A. Knox (2007). *Meteorology: Understanding the Atmosphere.* 2nd ed., Thomson Brooks/Cole, Belmont, CA.

AMS (2007). Glossary of Meteorology. American Meteorological Society. [On-line] 6 April 2007. http://amsglossary.allenpress.com/glossary

Andrews, D.G. (2000). *An Introduction to Atmospheric Physics*. 1st ed., Cambridge University Press, Cambridge.

Baby, H.B., P. Golé, and J. Lavergnat (1988). "A model for the tropospheric excess path length of radio waves from surface meteorological measurements." *Radio Science*, Vol. 23, No. 6, pp. 1023-1038.

Bar-Sever, Y.E., P.M. Kroger, and J.A. Borjesson (1998). "Estimating horizontal gradients of tropospheric path delay with a single GPS receiver" *Journal of Geophysical Research.* Vol. 103, No. B3, pp. 5019-5035.

Bean, B.R., and E.J. Dutton (1966). *Radio Meteorology*. National Bureau of Standards Monograph 92, Government Printing Office, Washington D.C.

Bernese (2007). User manual of the Bernese GPS Software Version 5.0. Edited by: Dach, R., U. Hugentobler, P. Fridez and M. Meindl, Astronomical Institute, University of Bern, Bern, Switzerland, 612 pp.

Bevis, M., S. Businger, S. Chiswell,T. Herring, R.A. Anthes, C. Rocken, and R.H Ware (1994). GPS meteorology: mapping zenith wet delays onto precipitable water, Journal of Applied Meteorology, Vol. 33, No. 3, 379-386.

Bock, O., and E. Doerflinger (2001). Atmospheric modeling in GPS data analysis for high accuracy positioning. *Phys. Chem. Earth (A)*, Vol. 26 No. 6-8, pp. 373-383.

Boehm, J., R. Heinkelmann, and H. Schuh (2007a). "Short Note: A global model of pressure and temperature for geodetic applications." *Journal of Geodesy*, Vol. 81, pp. 679-683, DOI: 10.1007/s00190-007-0135-3.

Boehm, J., P.J. Mendes-Cerveira, Schuh, H., and P. Tregoning (2007b). "The impact of mapping functions for the neutral atmosphere delay based on numerical weather models in GPS data analysis." *Dynamic Planet: Monitoring and Understanding a Dynamic*

Planet with Geodetic and Oceanographic Tools, IAG Symposium Series, 130, Springer-Verlag, Rizos, C. and Tregoning, P. (eds.), pp. 837-743.

Boehm, J., A. Niell, P. Tregoing, and H. Schuh (2006). "Global Mapping Function (GMF): A new empirical mapping function based on numerical weather model data." *Geophysical Research Letters,* Vol. 33, L07304, DOI: 10.1029/2005GL022546.

Boehm, J., and H. Schuh (2003). "Vienna mapping functions." *Proceedings of 16th Working Meeting on European VLBI for Geodesy and Astrometry*. Edited by W. Schwegnann and V. Thorandt, Bundesamt für Kartographie und Geodäsie, Leipzig, 2003, Germany, pp. 131-143.

Boehm, J., and H. Schuh (2004). "Vienna mapping functions in VLBI analyses." *Geophysical Research Letters*, Vol. 31, L01603, DOI: 10.1029/2003GL018984.

Boehm, J., and H. Schuh (2007), "Troposphere gradients from the ECMWF in VLBI analysis." *Journal of Geodesy*, 81:403-408 DOI 10.1007/S00190-007-0144-2.

Boehm, J., B. Werl, and H. Schuh (2006). Troposphere mapping function for GPS and very long baseline interferometry from European Centre for Medium-Range Weather Forecasts operational analysis data. *Journal of Geophysical Research*, Vol.111, B02406. DOI: 10.1029/2005JB003629.

Brown, R.G., and Hwang P.Y.C (1997). *Introduction to Random Signals and Applied Kalman Filtering*. 3rd Edition, John Wiley & Sons, New York.

Chen, G., and T.A. Herring (1997) "Effects of atmospheric azimuthal asymmetry on the analysis of space geodetic data" *Journal of Geophysical Research.* Vol. 102, No. B9, pp. 20489-20502.

Cole, F.W. (1975). *Introduction to Meteorology.* 2nd ed. John Wiley and Sons, Inc. New York.

Collins, J.P. (1999). *Assessment and Development of a Tropospheric Delay Model for Aircraft Users of the Global Positioning System*. M.Sc.E. thesis, Department of Geodesy and Geomatics Engineering Technical Report No. 203, University of New Brunswick, Fredericton, Canada, 174 pp.

Coster, A.J., A.E. Niell, F.S. Solheim, V.B. Mendes, P.C. Toor, and R.B. Langley (1997). "The effect of gradients in the GPS estimation of tropospheric water vapour." *Proceedings of The Institute of Navigation 53rd Annual Meeting*, Albuquerque, NM, U.S.A., 30 June – 1 July 1997; pp. 107-114.

Cucurull, L., P. Sedo, D. Behnard, E. Cardellach, and A. Rius (2002) "Integrating NWP Products into the Analysis of GPS Observables", Physics and Chemistry of the Earth, Vol. 27, pp. 377-383, DOI: 10.1016/S1474-7065(02)00015-3.

Davis, J.L., G. Elgered, A.E. Niell, and C.E. Kuehn (1993). "Ground-based measurement of gradients in the "wet" radio refractivity of air." *Radio Science*, Vol. 28, No. 6, pp. 1003-1018.

Davis, J.L., T.A. Herring, I.I. Shapiro, A.E.E Rogers, and G. Elgered (1985). "Geodesy by radio interferometry: effects of atmospheric modeling errors on estimates of baseline length." *Radio Science,* Vol. 20, No. 6, 1593-1607.

de Haan, S., and van der Marel H. (2004). "The influence on GPS estimates of NWP-derived mapping functions" *Physics and Chemistry of the Earth*, Vol. 29 pp. 159-166.

Dodson, A.H., P.J. Shardlow, L.C.M. Hubbard, G. Elgerd, and P.O.J. Jarlemark (1996). "Wet tropospheric effects on precise relative GPS height determination." *Journal of Geodesy*, Vol. 70, No. 4, pp.188-202.

Emardson, T.R., and P.O.J. Jarlemark (1999). "Atmospheric modelling in GPS analysis and its effect on the estimated geodetic parameters." *Journal of Geodesy.* Vol. 73 pp. 322-331.

FMH (1997). Federal Meteorological Handbook No. 3. Office of the Federal Coordinator for Meteorological Services and Supporting Research. Washington DC.

Foster J., B. Brookes, T. Cherubini, C. Shacat, S. Businger, and C.L. Werner (2006). Mitigating atmospheric noise for InSAR using a high resolution weather model. Geophysical Research Letters, Vol. 33, L16304, DOI: 10.1029/2006GL026781.

GAMIT (2006). Reference Manual, GPS Analysis at MIT, Release 10.3, Department of Earth, Atmospheric, and Planetary Sciences, Massachusetts Institute of Technology, 182 pp.

Gelb, A. (1974). *Applied Optimal Estimation.* The MIT Press, Massachusetts Institute of Technology, Cambridge, Mass., 374 pp.

Guo, J, and R.B. Langley (2003). "A new tropospheric propagation delay mapping function for elevation angles down to 2°." Proceedings of ION GPS/GNSS 2003, 16th International Technical Meeting of the Satellite Division of The Institute of Navigation, Portland, OR, 9-12 September 2003; pp. 386-376.

Herring, T.A. (1992). "Modelling atmospheric delays in the analysis of space geodetic data." *Proceedings of Symposium on Refraction of Transatomspheric Signals in Geodesy*,

J.C. de Munck and T.A.Th. Spoelstra (Eds.), The Netherlands, 19-22 May, Netherlands Geodetic Commission, Publications on Geodesy, Delft, The Netherlands, No 36, New Series, pp. 157-164.

Hobiger, T., R. Ichikawa, T. Takasu, Y. Koyama, and T. Kondo (2008). "Ray-traced troposphere slant delays for precise point positioning." *Earth Planets Space*, 60, e1-e4.

Honeywell (2005). "Honeywell Pressure Products Manual" [CD-ROM], Honeywell Precision Barometer.

Hopfield, H.S. (1969). "Two-quartic tropospheric refractivity profile for correcting satellite data." *Journal of Geophysical Research*, Vol. 74, No. 18, pp. 4487-4499.

IERS (2006). IERS Annual Report 2006. [On-line] 10 September 2008. http://www.iers.org/documents/publications/ar/2006/ar2006_341.pdf

IERS Conventions Update (2007). Chapter 9: Tropospheric Model, [On-line] 10 September 2008. http://tai.bipm.org/iers/convupdt/convupdt_c9.html

Ifadis, I. (1986). "The atmospheric delay of radio waves: Modeling the elevation dependence on a global scale." Technical Report No. 38L, School of Electrical and Computer Engineering, Chalmers University of Technology, Göteborg.

Ifadis, I.M., and P. Savvaidis (2001). "Space to earth observations: approaching the atmospheric effect." *Phys. Chem. Earth (A)*, Vol. 26, No. 3, pp. 195-200.

IGS (2005). IGSMAIL-5272 Switch the absolute antenna model within the IGS, Mon., 19 Dec 2005 14:25:53 +0100 (CET).

Iwabuchi, T., S. Miyazaki, K. Heki, I. Naito, and Y. Hatanaka (2003). "An impact of estimating tropospheric delay gradients on tropospheric delay estimations in the summer using the Japanese nationwide GPS array". *Journal of Geophysical Research*. Vol. 108, No. D10, DOI: 10.1029/2002JD002214.

Jensen, A.O.B (2002). Numerical Weather Predictions for Network RTK. Publication Series 4, Volume 10, National Survey and Cadastre, Denmark.

Jupp, A., S. Healy, M. Powe, J. Owen, and J. Butcher (2003). "Use of numerical weather prediction fields for the improvement of tropospheric corrections in global positioning applications" ION GPS/GNSS, 9-12 September 2003, Portland, OR, USA.

Kalnay, E. (2003). Atmospheric Modeling, Data Assimilation and Predictability. Cambridge University Press, Cambridge.

Lancaster P. and K. Šalkauskas (1986). *Curve and Surface Fitting: An Introduction.* Academic Press Ltd, London.

Langley, R.B. (1998). "Propagation of the GPS signals." In *GPS for Geodesy*, 2nd ed., Eds. P.J.G. Teunissen and A. Kleusberg. Springer-Verlag, Berlin Heidelberg, pp. 112-149

Leandro, R.F., Langley, R.B., Santos M. (2008). "UNB3m_pack: a neutral atmosphere delay package for radiometric space techniques." *GPS Solutions*, Vol. 12, pp. 65-70.

Leandro, R.F., M.C. Santos, and R.B. Langley (2006). "Wide Area Neutral Atmosphere Models for GNSS Applications." Proceedings of ION GNSS 2006, the 19th International Technical Meeting of the Satellite Division of The Institute of Navigation, Forth Worth, TX, 26-29 September 2006; pp. 1910-1924.

Leick, A. (2004). *GPS Satellite Surveying*. 3rd ed., John Wiley & Sons, Inc., Hoboken, New Jersey.

Li Z., P. Muller, P. Cross, P. Albert, J. Fischer, and R. Bennartz (2006). Assessment of the potential of MERIS near-infrared water vapour products to correct ASAR interferometric measurements. International Journal of Remote Sensing, Vol. 27, No. 2, 349-365.

List, R.J. (1966). *Smithsonian Meteorological Tables*. 6th revised ed. (third reprint), The Smithsonian Institution, Washington, D.C.

MacMillan, D.S. (1995). "Atmospheric gradients from very long baseline interferometry observations." *Geophysical Research Letters*, Vol. 95, No. 9, pp. 1041-1044.

MacMillan, D.S., and C. Ma (1997). "Atmospheric gradients and the VLBI terrestrial and celestial reference frames." *Geophysical Research Letters*, Vol. 24, No. 4, pp. 453-456.

Marini, J.W. (1972). "Correction of satellite tracking data for an arbitrary tropospheric profile." *Radio science*, Vol. 7, No. 2, pp. 223-231.

Marini, J.W., and C.W Murray (1973). Correction of Laser Tracking Data for Atmospheric Refraction at Elevation above 10 degrees. NASA-TM-X-70555, Goddard Space Flight Center, Greenbelt, MD, U.S.A., 59pp.

Mathworld (2008). Wolfram Mathworld. [On-line] 24 October 2008. http://mathworld.wolfram.com/DistributionFunction.html.

Maxwell, J.B. (1982). The Climate of the Canadian Arctic Islands and Adjacent Waters. Canadian Government Publishing Centre, Supply and Services Canada, Ottawa, Canada.

Meindl, M., S. Schaer, U. Hugentobler, and G. Beutler (2004). "Tropospheric gradient estimation at CODE: Results from global solutions." *Journal of the Meteorological Society of Japan*. Vol. 82(1B), pp. 331-338.

Mendes, V.B. (1999). *Modeling The Neutral-Atmosphere Propagation Delay in Radiometric Space Techniques*. Ph.D. dissertation, Department of Geodesy and Geomatics Engineering Technical Report No. 199, University of New Brunswick, Canada, 353 pp.

Minnett, P.J. (2004) WVR on a moving vessel. [On-line] to R. Ghoddousi-Fard <c447j@unb.ca> from <pminnett@rsmas.miami.edu>, 31 December.

NCDC (2008a). Daily Weather Maps, National Climatic Data Center, National Oceanic and Atmospheric Administration, U.S. Department of Commerce. [On-line] 4 September 2008. http://www.ncdc.noaa.gov/oa/climate/research/dwm/

NCDC (2008b). Locate Weather Observation Station Record, National Climatic Data Center, National Oceanic and Atmospheric Administration, U.S. Department of Commerce. [On-line] 4 November 2008. http://lwf.ncdc.noaa.gov/oa/climate/stationlocator.html

Niell, A.E. (1996). "Global mapping functions for the atmosphere delay at radio wavelengths." *Journal of Geophysical Research,* Vol. 101, No. B2, pp. 3227-3246

Niell, A.E. (2000). "Improved atmospheric mapping functions for VLBI and GPS." *Earth, Planets and Space*, Vol. 52, No. 10, 699-702.

Niell, A.E. (2001). "An a priori Hydrostatic Gradient Model for Atmospheric Delay." In: D. Behrend and A Rius (Eds.): *Proceedings of the 15th Working Meeting on European VLBI for Geodesy and Astrometry*, Institut d'Estudis Espacials de Catalunya, Consejo Superior de Invetigaciones Cientificas, Barcelona, Spain, 2001.

Niell, A.E. (2003). "The IMF mapping function-Rev. 2" GPSMet Workshop, Tsukuba, Japan, May. [On-line] 8 July 2008. http://www.haystack.mit.edu/geo/pubs/index.html

Niell, A.E. (2006). "Interaction of atmosphere modeling and analysis strategy." Proceedings of IVS 2006 General Meeting, Behrend, D. and Baver, K. (ed.), NASA/CP-2006-214140.

Niell A., and L. Petrov (2003). "Using a Numerical Weather Model to Improve Geodesy." *Proceedings of the workshop: State of GPS Vertical Positioning Precision*, Luxembourg, 2-4 April.

Orliac, E. (2002). *Troposphere delay models for satellite navigation applications*. Unpublished Diploma thesis, École Polytechnique Fédérale de Lausanne, Lausanne, Switzerland. 93pp.

Owens, J.C. (1976). "Optical refractive index of air: Dependence on pressure, temperature and composition." *Applied Optics*, Vol. 6, No. 1, pp. 51-59.

Pany T. K. (2002). Development and Application of Tropospheric GPS Slant Delay Models Based on Numerical Weather Prediction Models and Turbulence Theory. PhD. dissertation, Graz University of Technology, Graz, Austria.

Peixoto, J.P., and A.H. Oort (1993). *Physics of Climate.* 3rd printing, American Institute of Physics, New York.

Pelletier Y. (2008). Isobaric levels. [On-line] to R. Ghoddousi-Fard <c447j@unb.ca> from <yves.pelletier@ec.gc.ca>, 05 February.

Rocken, C., J. Johnson, Teresa Van Hove, and T. Iwabuchi (2005). "Atmospheric water vapour and geoid measurements in the open ocean with GPS." *Geophysical Research Letters*, 32, L12813, DOI: 10.1029/2005GL022573.

Rocken, C., S. Sokolovskiy, J.M. Johnson, and D. Hunt (2001). "Improving mapping of tropospheric delays." *Journal of Atmospheric and Oceanic Technology*, Vol. 17, Issue 7, 1205-1213.

RTCA, (2006). Minimum Operational Performance Standards for Global Positioning System/Wide Area Augmentation System Airborne Equipment, RTCA DO-229D, RTCA, Inc., Washington, D.C., U.S.A., December.

Rucker, D.F., and T.P.A Ferré (2004). "BGPR_Reconstruct: a MATLAB® ray-tracing program for nonlinear inversion of first arrival travel time data from zero-offset borehole radar." *Computers and Geosciences.* Vol. 30, pp. 767-777. DOI:10.1016/j.cageo.2004.05.009.

Saastamoinen, J. (1972a). "Contributions to the theory of atmospheric refraction." *Bulletin Géodésique*, No. 105, pp. 279-298.

Saastamoinen, J. (1972b). "Introduction to practical computation of astronomical refraction." *Bulletin Géodésique*, No. 106, pp. 383-397

Saastamoinen, J. (1973). "Contributions to the theory of atmospheric refraction, part II: refraction corrections in satellite geodesy." *Bulletin Géodésique*, No. 107, pp. 13-34.

Schmid, R., M. Rothacher, D. Thaller, and P. Steigenberger (2005). "Absolute phase center corrections of satellite and receiver antennas: Impact on global GPS solutions and estimation of azimuthal phase center variations of the satellite antenna." *GPS Solutions*, Vol. 9, pp.283-293, DOI: 10.1007/s10291-005-0134-x.

Schüler, T. (2001). "On the Ground-Based GPS Tropospheric Delay Estimation." Ph.D. dissertation, Universität der Bundeswehr Munchen. [On-line] 14 November 2004. http://forschung.unibw-muenchen.de/info.php?&id=591

Schüler T., G. W. Hein and B. Eissfeller (2001). "A new tropospheric correction model for GNSS navigation." *Proceedings of GNSS 2001, V GNSS International Symposium*, Spanish Institute of Navigation, Seville, Spain, May 8-11.

Seko, H., H. Nakamura, and S. Shimada (2003). "Evaluation of the GPS positioning error due to the inhomogeneous distribution of atmospheric delay using a numerical weather model data." International Workshop on GPS Meteorology, Tsukuba, Japan, Jan 14-17.

Solheim, F. S. (1993). "Use of pointed water vapour radiometer observations to improve vertical GPS surveying accuracy." PhD dissertation, University of Colorado, Colorado, USA, 128 pp.

Spiegel, M.R., and L.J. Stephens (1998). *Schaum's Outline of Theory and Problems of Statistics.* 3rd edition, McGraw-Hill, New York.

Teferle, F.N., E.J. Orliac, and R.M. Bingley(2007). "An assessment of Bernese GPS software precise point positioning using IGS final products for global site velocities." *GPS Solutions*, Vol. 11, pp. 205-213, DOI: 10.1007/s1091-006-0051-7.

Tesmer, V., J. Boehm, R. Heinkelmann, and H. Schuh (2007). "Effect of different tropospheric mapping functions on the TRF, CRF and position time-series estimated from VLBI." *Journal of Geodesy*, Vol. 81, pp. 409-421, DOI: 10.1007/s00190-006-0126-9.

Thayer, G. D. (1974). "An improved equation for the radio refractive index of air." *Radio Science*, Vol. 9, No. 10, pp 803-807.

van der Wal, A.D. (1995). Evaluation of Strategies for Estimating Residual Neutral-Atmosphere Propagation Delay in High Precision Global Positioning System Data Analysis. M.Sc.E. thesis, Department of Geodesy and Geomatics Engineering Technical Report No. 177, University of New Brunswick, Fredericton, New Brunswick, Canada.

Verner G. (2008). Radiosonde data assimilation. [On-line] to R. Ghoddousi-Fard <c447j@unb.ca> from <Gilles.Verner@ec.gc.ca>, 18 January.

Vey, S., R. Dietrich, M. Fritsche, and A. Rülke (2006). "Influence of mapping function parameters on global GPS network analyses: Comparisons between NWF and IMF." *Geophysical Research Letters*, Vol. 33, L01814, DOI:10.1029/2005GL024361.

Wallace, J.M., and P.V. Hobbs (1977). *Atmospheric Science: An Introductory Survey*, Academic Press Inc., New York.

Ware, R., D. Cimini, P. Herzegh, F. Marzano, J. Vivekanandan and E. Westwater (2004), Ground-based Microwave Radiometer Measurements During Precipitation. Presented at the 8th Specialist Meeting on Microwave Radiometry, 24-27 Feb 2004, Rome, Italy. [on-line] August 16 2006. http://www.radiometrics.com/ware_microrad04.pdf.

Ware, R., C. Rocken, F. Solheim, T. Van Hove, C. Alber, and J. Johson (1993). "Pointed water vapor radiometer corrections for accurate global positioning system surveying." *Geophysical Research Letters*, Vol. 20, No. 23, pp. 2635-2638.

Wexler, A. (1976). "Vapour pressure formulation for water in range 0 to 100ºC. A revision." *Journal of Research of the National Bureau of Standards- A. Physics and Chemistry*, Vol. 80A, Nos. 5 and 6, pp. 775-785.

Appendix I: List of Radiosonde Stations Used in Dual Ray Tracing and Validation Studies

Table I.1 includes list of radiosondes used in dual ray tracing explained in section 5.1.1. Those shown in bold were also used for validation studies explained in section 4.4.3.

Table I.1– Location and code of radiosondes

Init.	WBAN[1]	WMO[2]	Lat.°	Lon.°	Elev. (m)	Station name
BGTL	99999	4202	76.53	-68.75	77	THULE,GL
BGEM	**99999**	**4220**	**68.7**	**-52.75**	**40**	**EGEDESMINDE,GL**
BGBW	**99999**	**4270**	**61.18**	**-45.43**	**4**	**NARSSARSSUAQ,GL**
FAI	**26411**	**70261**	**64.82**	**-147.87**	**135**	**FAIRBANKS,US**
YAK	**25339**	**70361**	**59.52**	**-139.67**	**10**	**YAKUTAT,US**
ANN	**25308**	**70398**	**55.03**	**-131.57**	**37**	**ANNETTE ISLAND, US**
YVQ	**26214**	**71043**	**65.28**	**-126.75**	**95**	**NORMAN WELLS, CA**
YUX	**16895**	**71081**	**68.78**	**-81.25**	**7**	**HALL BEACH, CA**
YLT	**18601**	**71082**	**82.5**	**-62.33**	**66**	**ALERT, CA**
YZT	**25223**	**71109**	**50.68**	**-127.37**	**17**	**PORT HARDY, CA**
WSE	**25145**	**71119**	**53.55**	**-114.1**	**766**	**EDMONTON PLAIN, CA**
WIQ	25154	71124	54.8	-110.08	703	PRIMROSE LAKE, CA
YLW	**94151**	**71203**	**49.97**	**-119.38**	**454**	**KELOWNA APT, CA**
YSA	**14642**	**71600**	**43.93**	**-60.02**	**4**	**SABLE ISLAND, CA**
WQI	**94620**	**71603**	**43.87**	**-66.05**	**9**	**YARMOUTH, CA**
YWA	54706	71625	45.95	-77.32	130	PETAWAWA, CA
YCX	**14685**	**71701**	**45.83**	**-66.43**	**52**	**GAGETOWN, CA**
YOY	54724	71716	46.9	-71.5	178	VALCARTIER, CA
YMW	**4734**	**71722**	**46.38**	**-75.97**	**170**	**MANIWAKI, CA**
YYT	**14531**	**71801**	**47.67**	**-52.75**	**140**	**TORBAY, CA**
YZV	**15636**	**71811**	**50.22**	**-66.27**	**52**	**SEPT ILES, CA**
YJT	**14503**	**71815**	**48.53**	**-58.55**	**60**	**STEPHENVILLE, CA**

[1] The "*five-digit station identifier, which is an acronym, invented in the 1950's, stands for: Weather-Bureau-Army-Navy*" [NCDC, 2008b].

[2] "*A five-digit station identifier assigned by the World Meteorological Organization, used for international weather data exchange and station documentation*" [NCDC, 2008b].

Table I.1- …Continued

YYR	**15601**	**71816**	**53.3**	**-60.37**	**36**	**GOOSE BAY, CA**
YAH	**15708**	**71823**	**53.75**	**-73.67**	**307**	**LA GRANDE, CA**
YMO	**15803**	**71836**	**51.27**	**-80.65**	**10**	**MOOSONEE, CA**
WPL	**15907**	**71845**	**51.47**	**-90.2**	**386**	**PICKLE LAKE, CA**
YLO	94921	71853	49.82	-99.65	382	SHILO, CA
YQD	**25004**	**71867**	**53.97**	**-101.1**	**273**	**THE PAS, CA**
YVP	**15641**	**71906**	**58.1**	**-68.42**	**60**	**KUUJJUAQ, CA**
YPH	**15704**	**71907**	**58.45**	**-78.12**	**26**	**INUKJUAK, CA**
ZXS	**25206**	**71908**	**53.9**	**-122.8**	**601**	**PRINCE GEORGE, CA**
YVN	**16607**	**71909**	**63.75**	**-68.55**	**35**	**IQALUIT, CA**
YYQ	**15901**	**71913**	**58.75**	**-94.07**	**29**	**CHURCHILL, CA**
YZS	**16801**	**71915**	**64.2**	**-83.37**	**57**	**CORAL HARBOUR, CA**
YEU	**18801**	**71917**	**79.98**	**-85.93**	**10**	**EUREKA, CA**
YRB	**17901**	**71924**	**74.72**	**-94.98**	**40**	**RESOLUTE, CA**
YCB	**26005**	**71925**	**69.1**	**-105.12**	**25**	**CAMBRIDGE BAY, CA**
YBK	**16910**	**71926**	**64.3**	**-96**	**49**	**BAKER LAKE, CA**
YSM	**26118**	**71934**	**60.03**	**-111.95**	**203**	**FT SMITH, CA**
YYE	**25262**	**71945**	**58.83**	**-122.6**	**377**	**FORT NELSON, CA**
YEV	**22258**	**71957**	**68.32**	**-133.53**	**103**	**INUVIK, CA**
YXY	**26316**	**71964**	**60.72**	**-135.07**	**704**	**WHITEHORSE, CA**
OKX	**94703**	**72501**	**40.87**	**-72.87**	**20**	**BROOKHAVEN, US**
ALY	**54775**	**72518**	**42.69**	**-73.83**	**94**	**ALBANY, US**
PIT	**94823**	**72520**	**40.53**	**-80.23**	**360**	**PITTSBURGH, US**
BUF	**14733**	**72528**	**42.93**	**-78.73**	**218**	**BUFFALO, US**
OAX	**94980**	**72558**	**41.32**	**-96.37**	**350**	**OMAHA, US**
LBF	**24023**	**72562**	**41.13**	**-100.68**	**847**	**NORTH PLATTE, US**
SLC	**24127**	**72572**	**40.77**	**-111.97**	**1288**	**SALT LAKE, US**
LKN	**4105**	**72582**	**40.87**	**-115.73**	**1608**	**ELKO, US**
MFR	**24225**	**72597**	**42.37**	**-122.87**	**397**	**MEDFORD, US**
DTX	**4830**	**72632**	**42.7**	**-83.47**	**329**	**DETROIT, US**
APX	**4837**	**72634**	**44.55**	**-84.43**	**448**	**GAYLORD, US**
GRB	**14898**	**72645**	**44.48**	**-88.13**	**210**	**GREEN BAY, US**
MPX	**94983**	**72649**	**44.83**	**-93.55**	**287**	**MINNEAPOLIS, US**
ABR	**14929**	**72659**	**45.45**	**-98.42**	**397**	**ABERDEEN, US**
UNR	**94043**	**72662**	**44.07**	**-103.21**	**1037**	**RAPID CITY, US**
RIW	**24061**	**72672**	**43.06**	**-108.47**	**1688**	**RIVERTON, US**
BOI	**24131**	**72681**	**43.57**	**-116.22**	**871**	**BOISE, US**
SLE	**24232**	**72694**	**44.92**	**-123.02**	**61**	**SALEM, US**
CAR	**14607**	**72712**	**46.87**	**-68.02**	**191**	**CARIBOU, US**
INL	**14918**	**72747**	**48.57**	**-93.38**	**359**	**INTERNATIONAL FALLS, US**
BIS	**24011**	**72764**	**46.77**	**-100.75**	**503**	**BISMARCK, US**

Table I.1 …Continued

GGW	**94008**	**72768**	**48.2**	**-106.62**	**693**	**GLASGOW, US**
TFX	**4102**	**72776**	**47.45**	**-111.38**	**1130**	**GREAT FALLS, US**
OTX	**4106**	**72786**	**47.68**	**-117.63**	**728**	**SPOKANE INTNL, US**
UIL	**94240**	**72797**	**47.95**	**-124.55**	**56**	**QUILLAYUTE, US**
GYX	**54762**	**74389**	**43.89**	**-70.25**	**125**	**GRAY, US**
DVN	**94982**	**74455**	**41.6**	**-90.57**	**229**	**DAVENPORT MUNICIPAL, US**
CHH	**14684**	**74494**	**41.67**	**-69.97**	**16**	**CHATHAM, US**
ILX	**4833**	**74560**	**40.15**	**-89.33**	**178**	**LINCOLN-LOGAN COUNTY, US**

Appendix II: Monthly Plots of Differences between Dual and Single RAOB Ray Tracing and a Fitted Function

In each of the following figures in the specified month, the upper plot represents the average differences of dual minus single RAOB ray tracing of slant hydrostatic delay at 3° elevation angle vs. azimuth (dots with error bars) and a fitted model (black curve). The lower plot (left) is the same as the above one but in polar plot form and without error bars. Note that the dashed circles inside polar form are representing -3, 0 and +3 cm from inside toward outside respectively. The lower plot (right) is the same as the above one but for absolute differences. *a* and *b* in the title of each upper plot refer to the fitted function as: $d = a \cdot \cos(az) + b \cdot \sin(az)$.

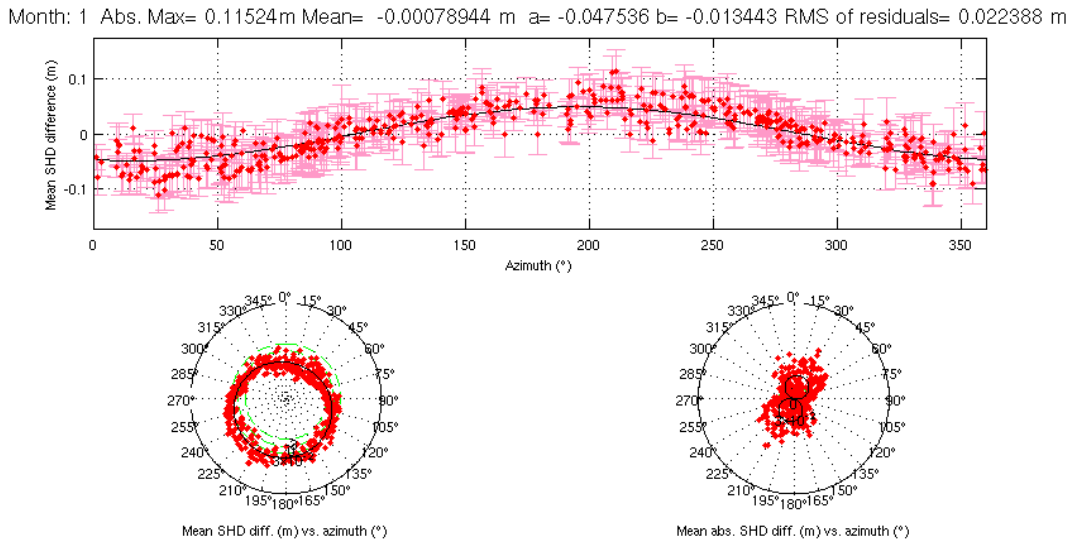

Figure II.1– Mean and standard deviation of SHD difference and the fitted model for the month of January 2004.

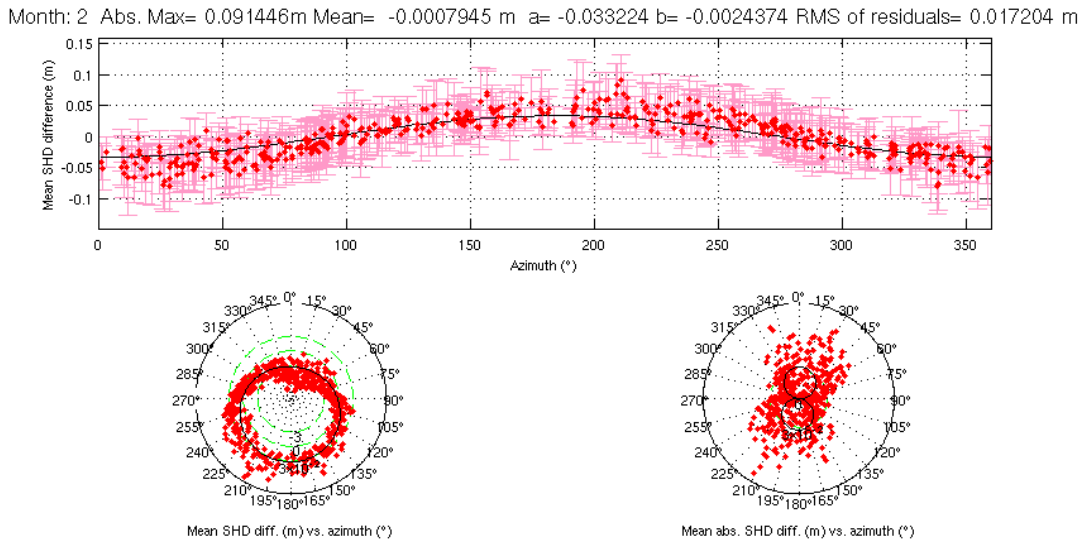

Figure II.2– Mean and standard deviation of SHD difference and the fitted model for the month of February 2004.

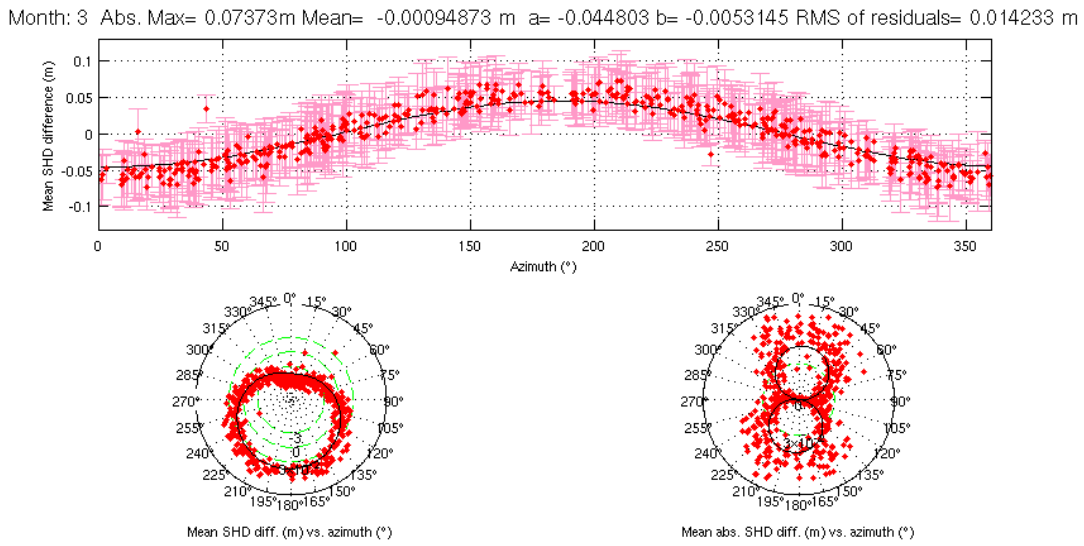

Figure II.3– Mean and standard deviation of SHD difference and the fitted model for the month of March 2004.

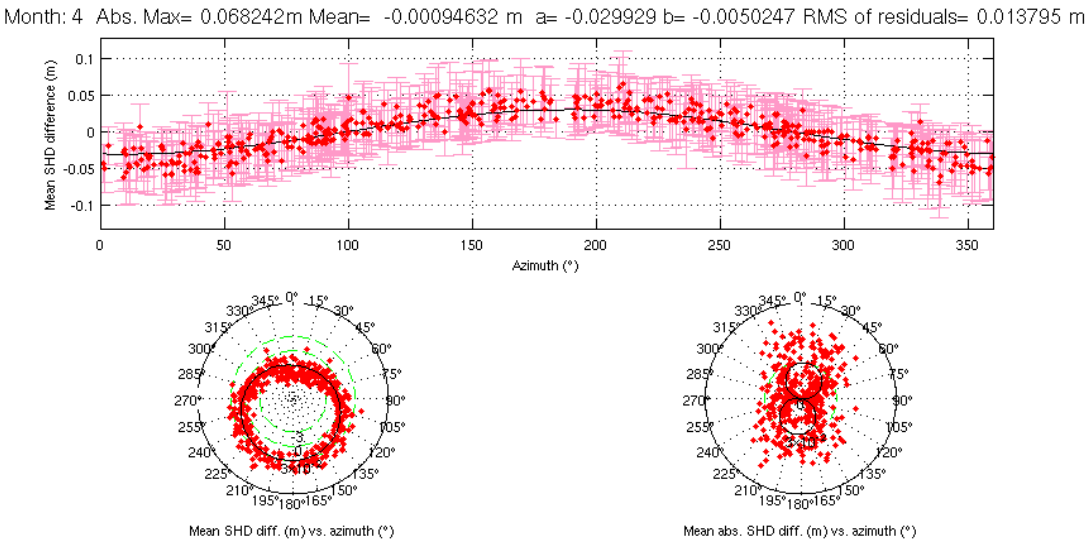

Figure II.4– Mean and standard deviation of SHD difference and the fitted model for the month of April 2004.

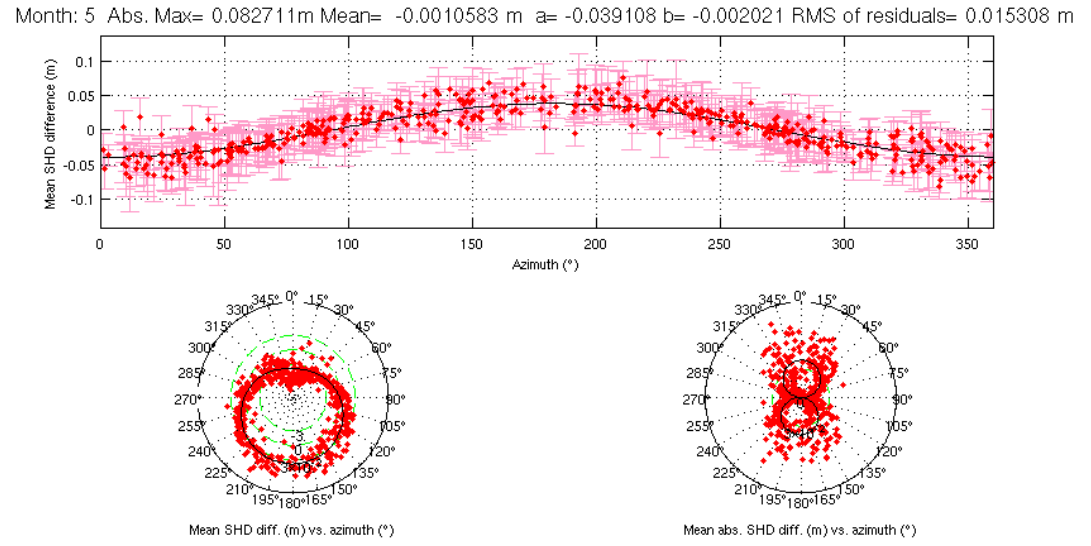

Figure II.5– Mean and standard deviation of SHD difference and the fitted model for the month of May 2004.

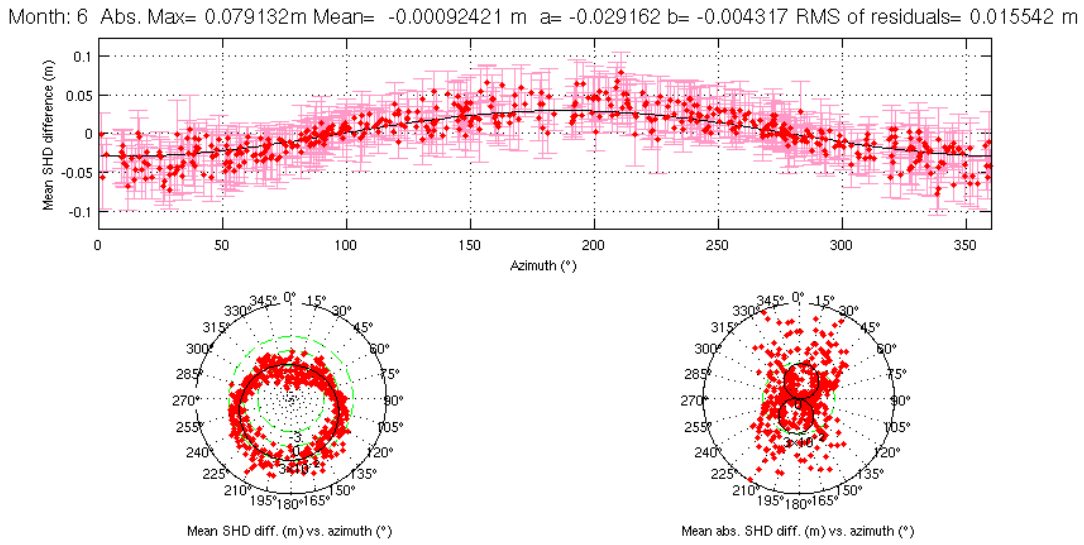

Figure II.6– Mean and standard deviation of SHD difference and the fitted model for the month of June 2004.

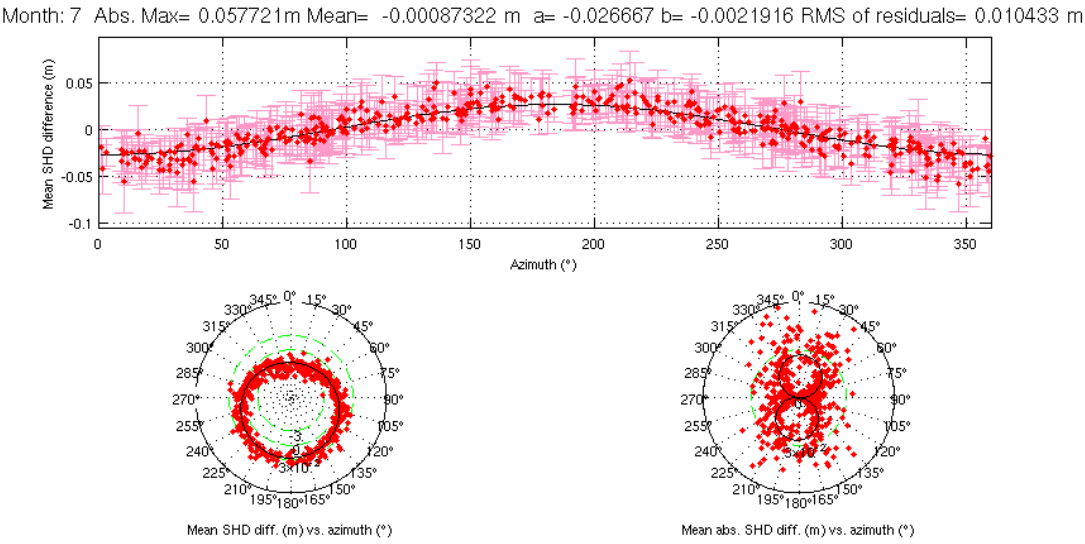

Figure II.7– Mean and standard deviation of SHD difference and the fitted model for the month of July 2004.

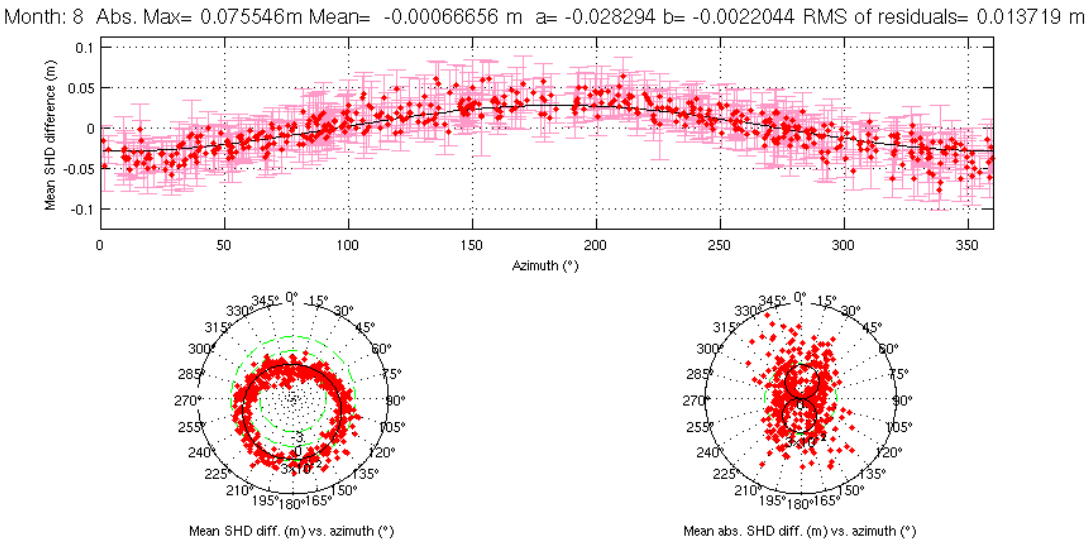

Figure II.8– Mean and standard deviation of SHD difference and the fitted model for the month of August 2004.

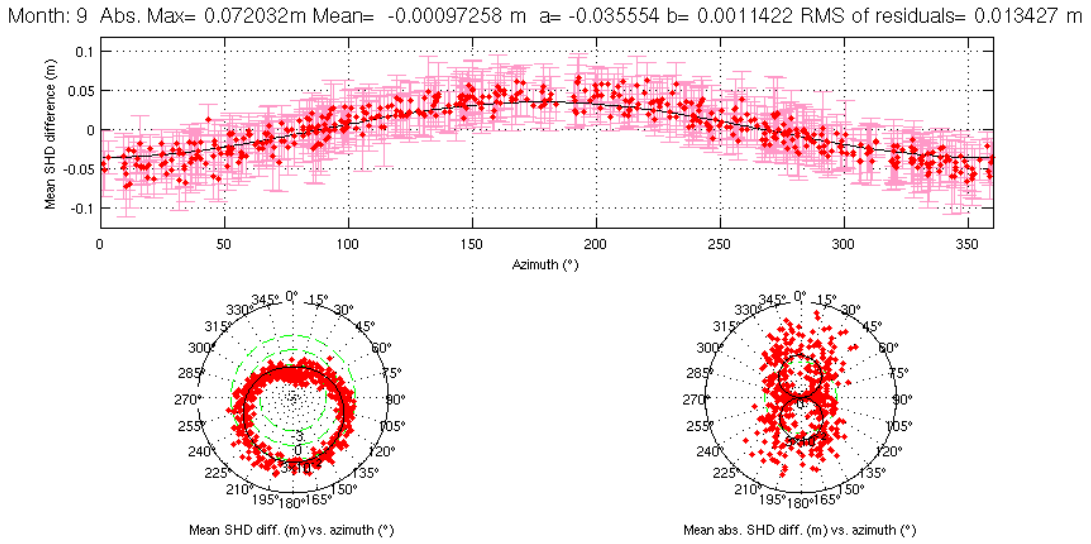

Figure II.9– Mean and standard deviation of SHD difference and the fitted model for the month of September 2004.

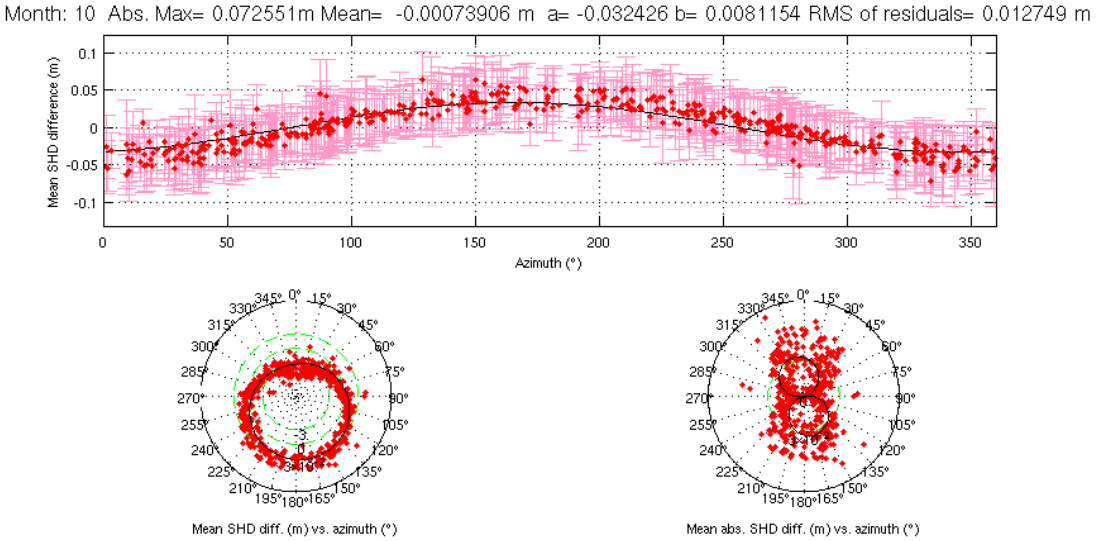

Figure II.10– Mean and standard deviation of SHD difference and the fitted model for the month of October 2004.

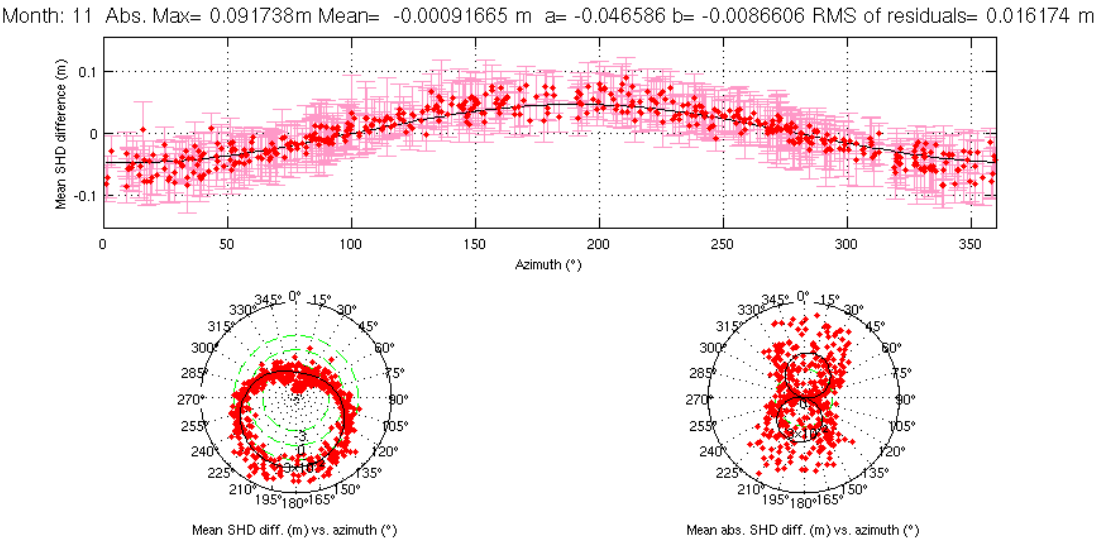

Figure II.11- Mean and standard deviation of SHD difference and the fitted model for the month of November 2004.

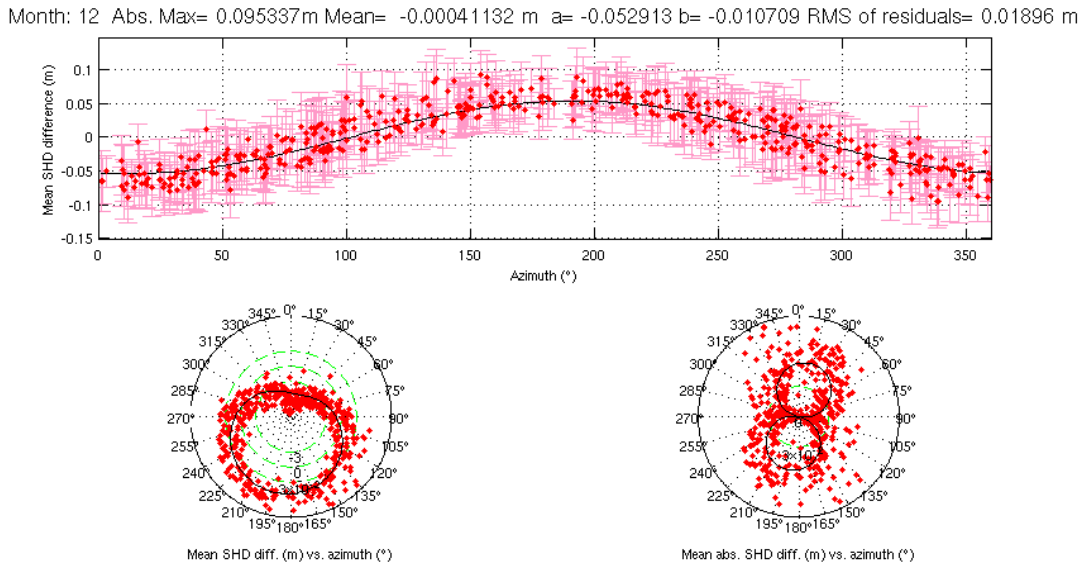

Figure II.12– Mean and standard deviation of SHD difference and the fitted model for the month of December 2004.

Appendix III: Sample Online-RT Maps

The following are near-real-time maps provided by Online-RT at an arbitrarily chosen epoch, as examples of the available maps.

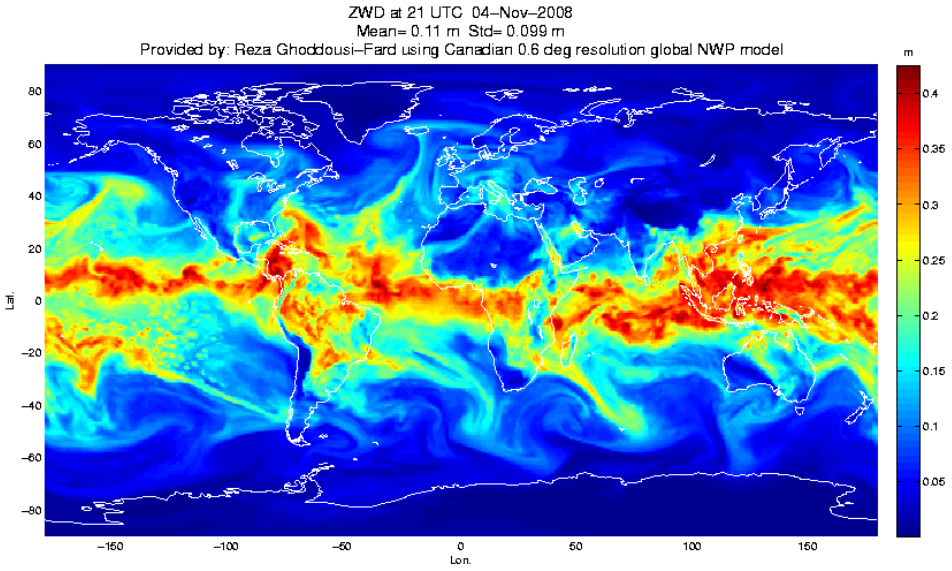

Figure III.1- ZWD from global NWP.

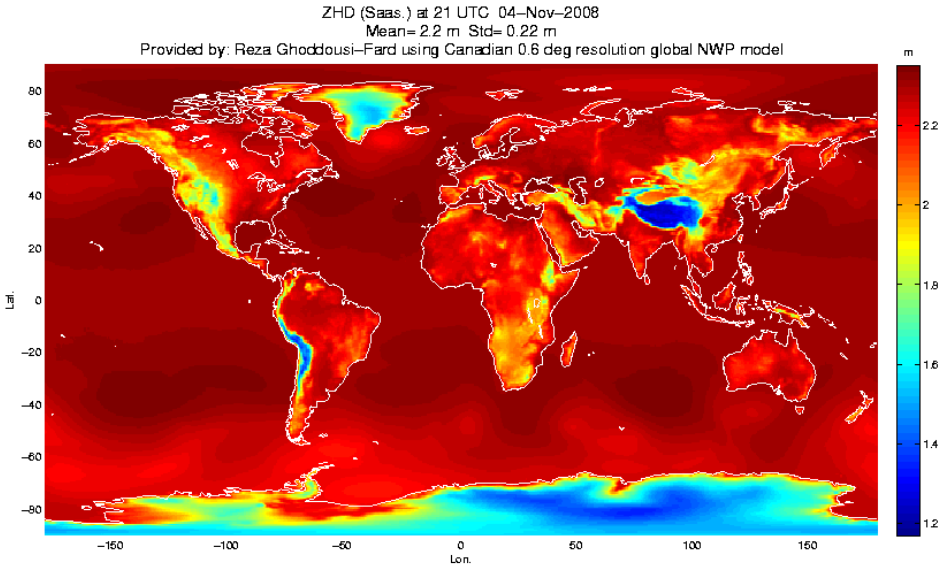

Figure III.2- ZHD from global NWP.

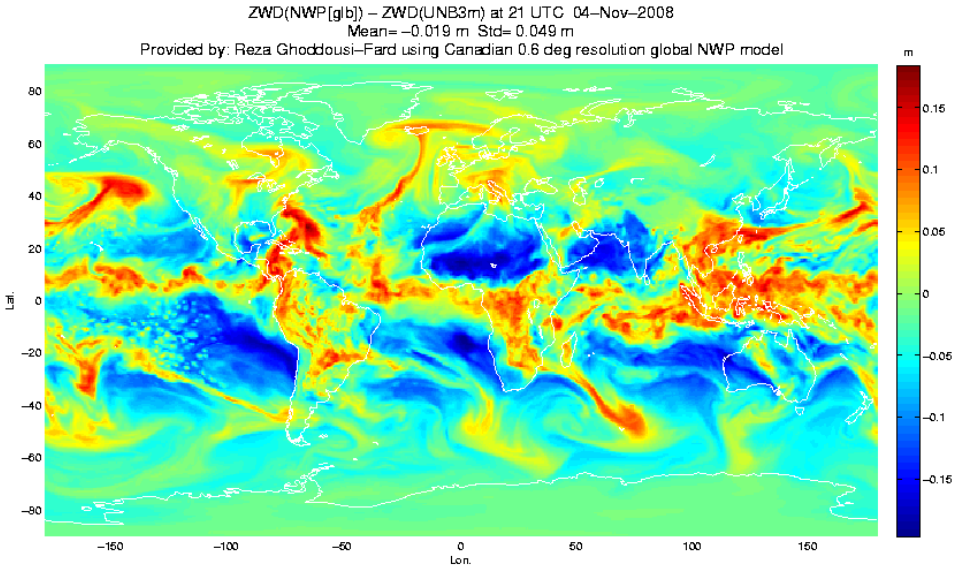

Figure III.3- Difference between ZWD from global NWP and UNB3m model.

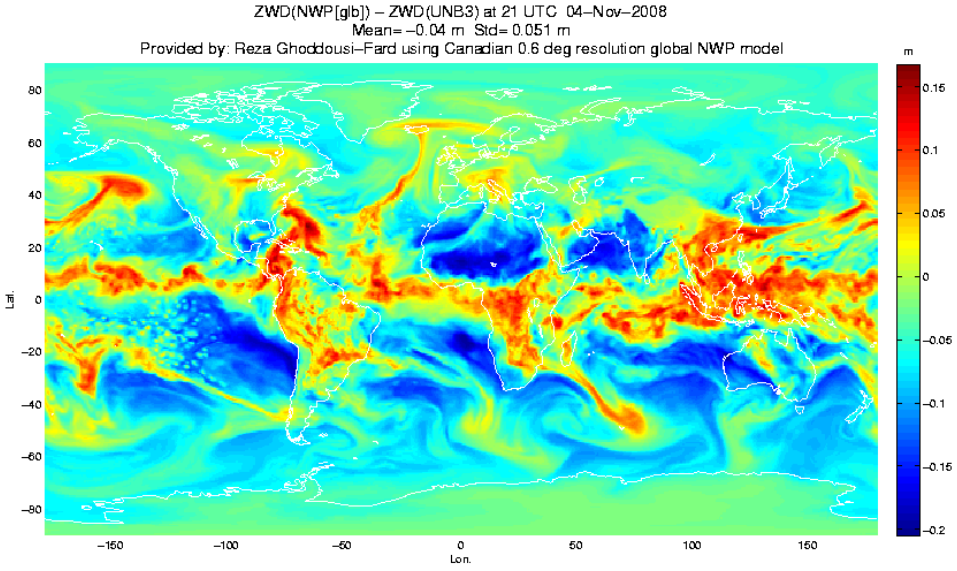

Figure III.4- Difference between ZWD from global NWP and UNB3 model.

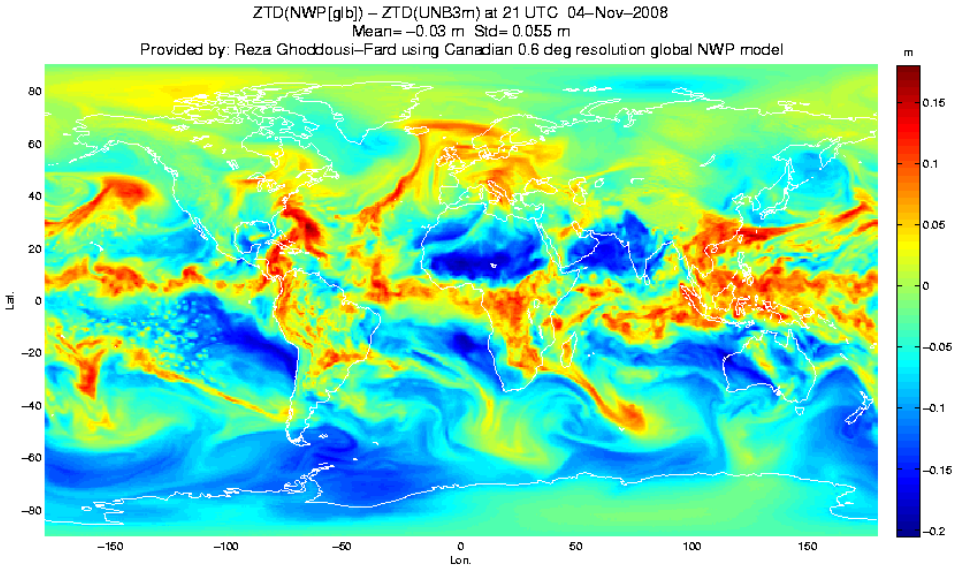

Figure III.5- Difference between ZTD from global NWP and UNB3m model.

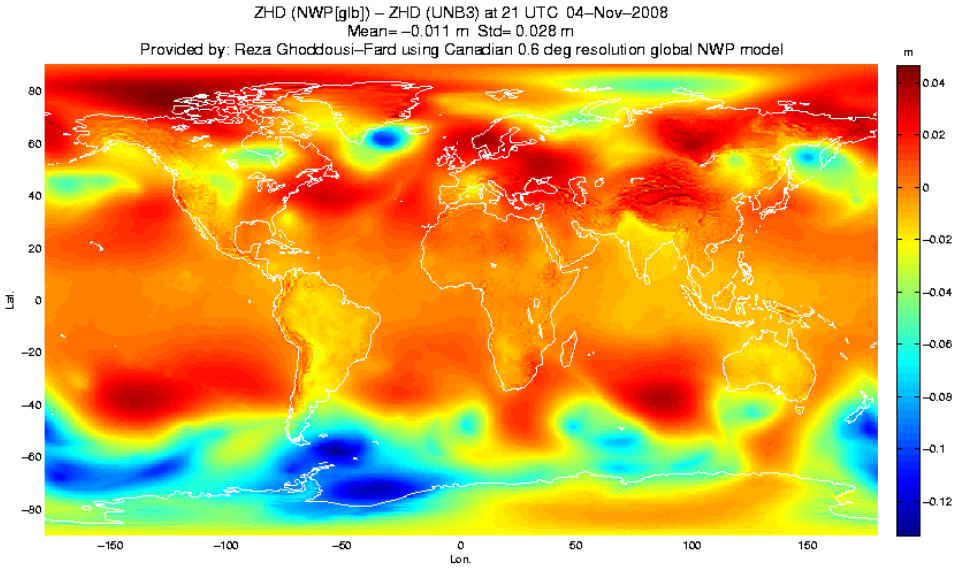

Figure III.6- Difference between ZHD from global NWP and UNB3 model.

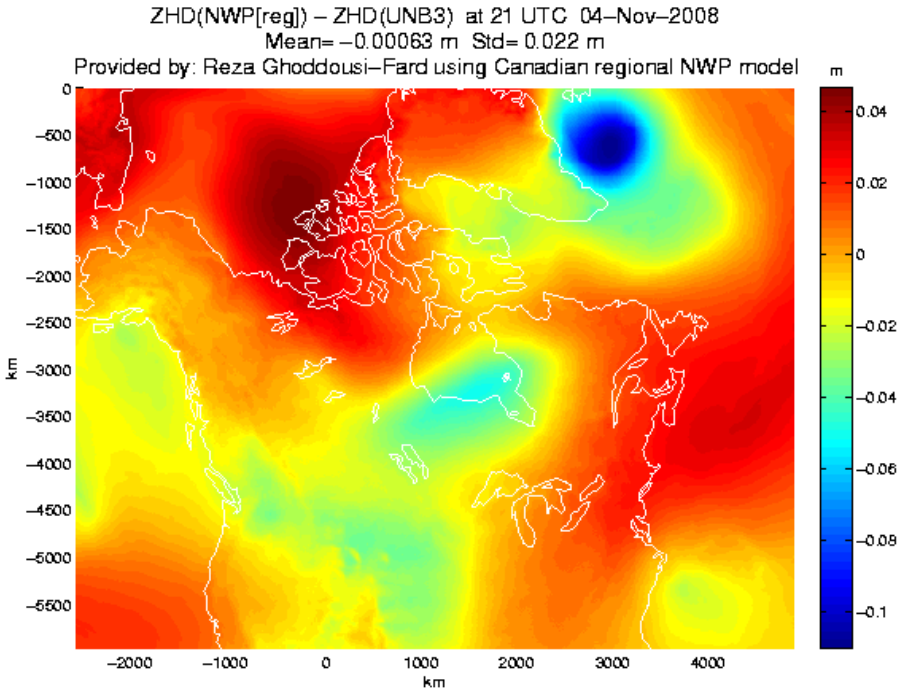

Figure III.7- Difference between ZHD from regional NWP and UNB3 model.

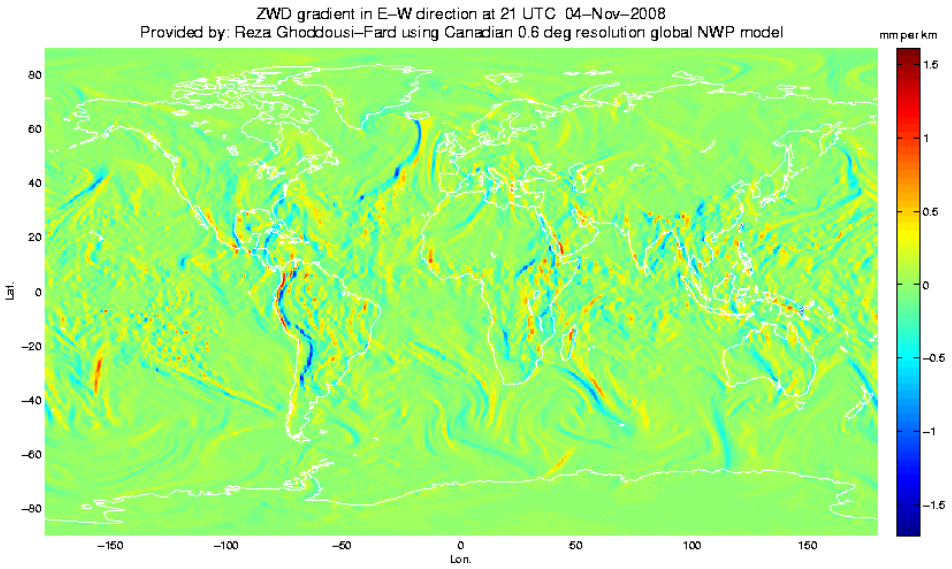

Figure III.8- EW gradient of ZWD from global NWP.

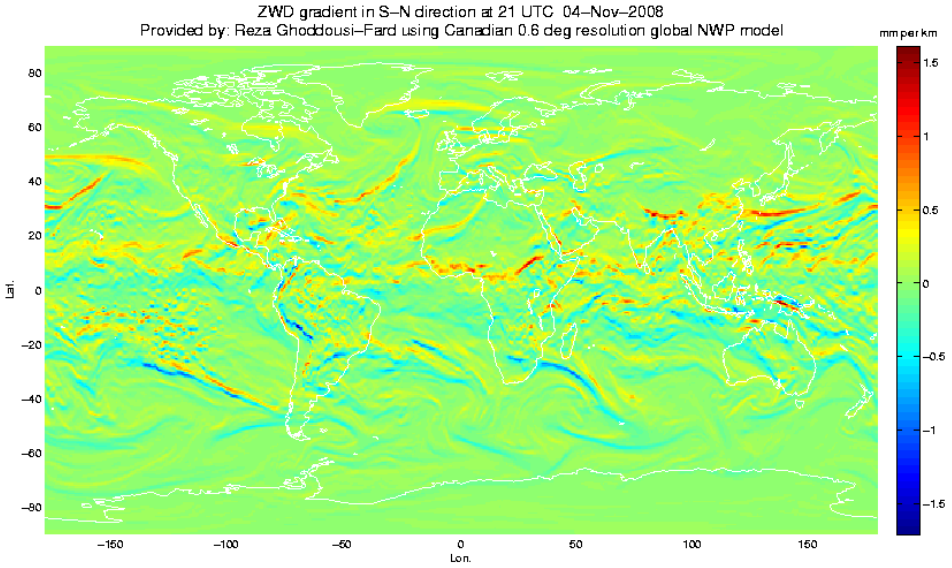

Figure III.9- NS gradient of ZWD from global NWP.

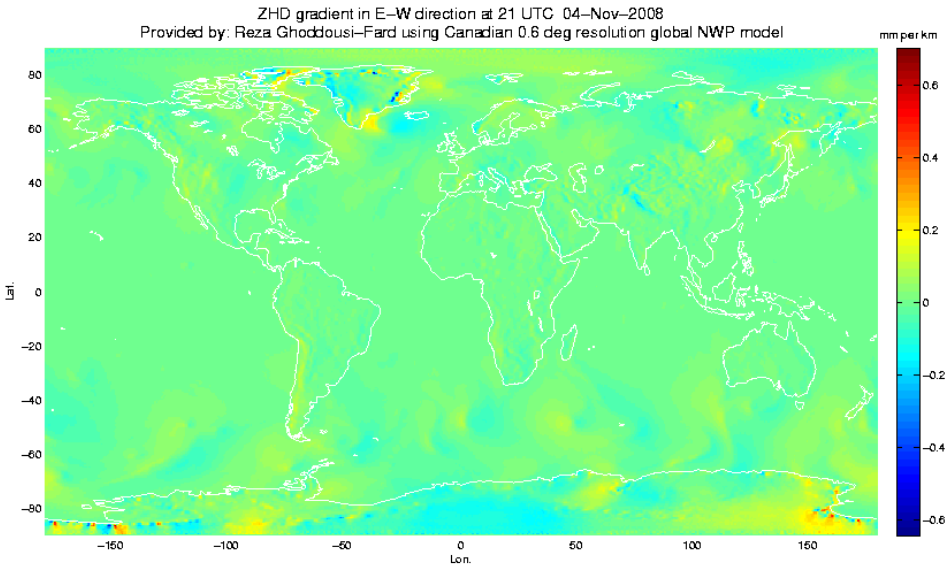

Figure III.10- EW gradient of ZHD from global NWP.

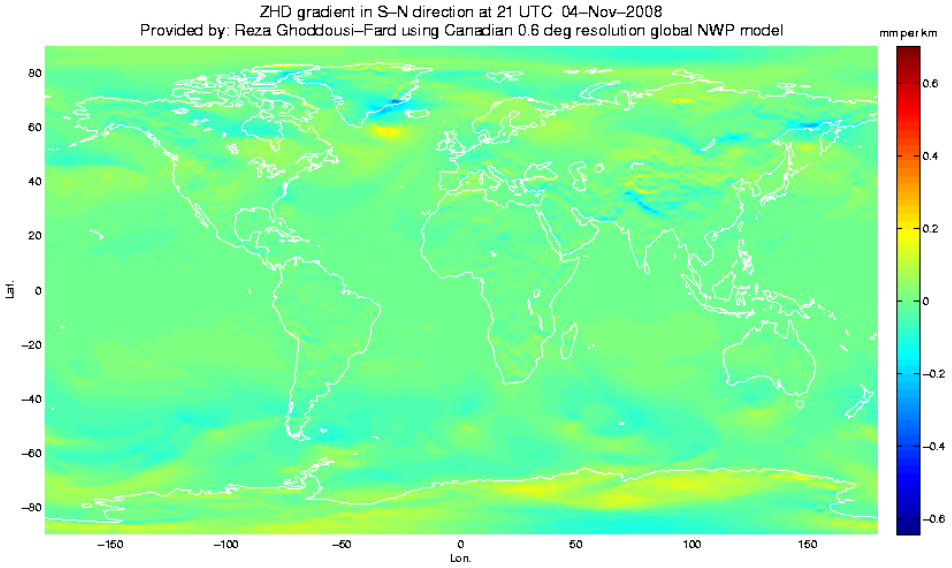

Figure III.11- NS gradient of ZHD from global NWP.

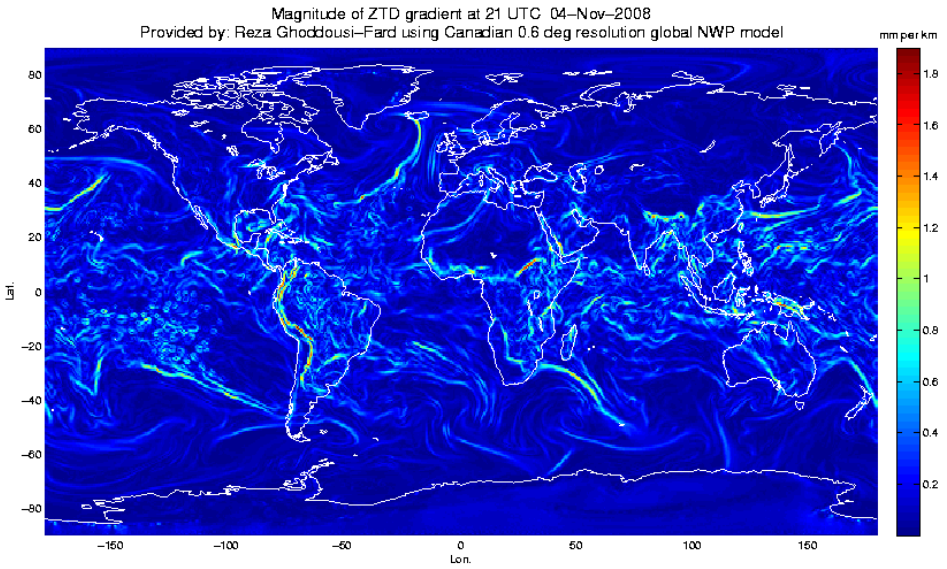

Figure III.12- Magnitude of ZTD gradient from global NWP.

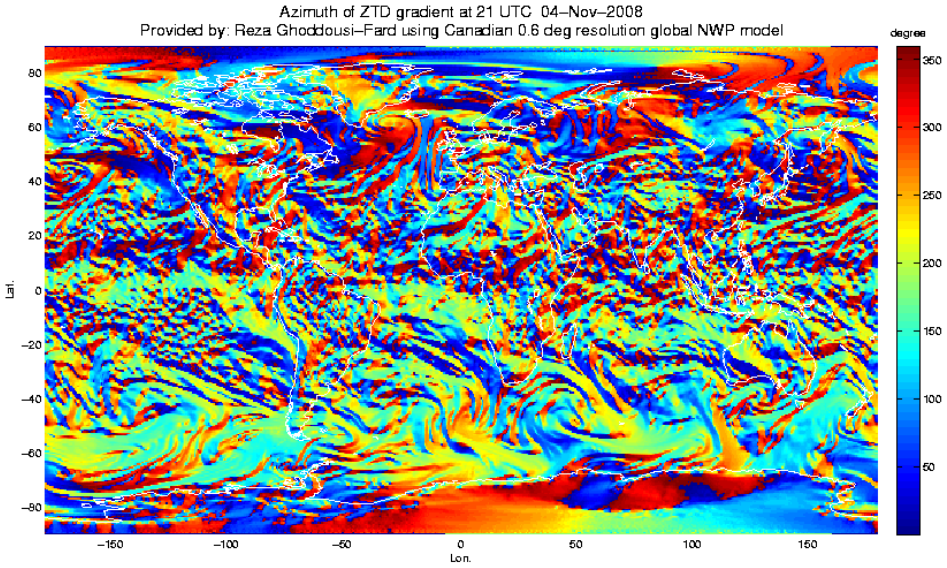

Figure III.13- Azimuth of ZTD gradient from global NWP.

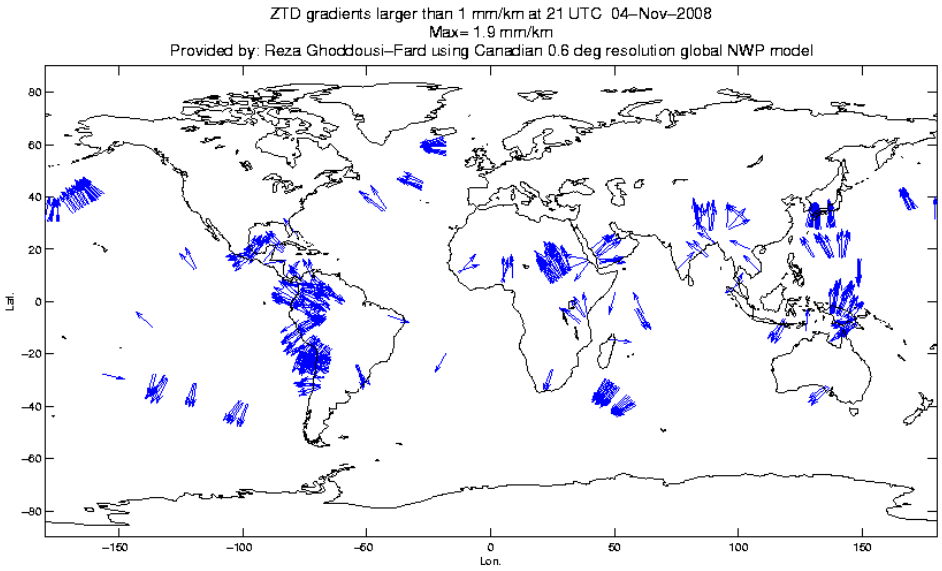

Figure III.14- ZTD gradients larger than 1 mm/km

Appendix IV: Bernese Modification Flow Diagrams

The following are flow diagrams of modified subroutines and newly added ones for the four main programs of the Bernese GPS software Version 5.0. Bold boxes are the newly added subroutines while other boxes are modified subroutines.

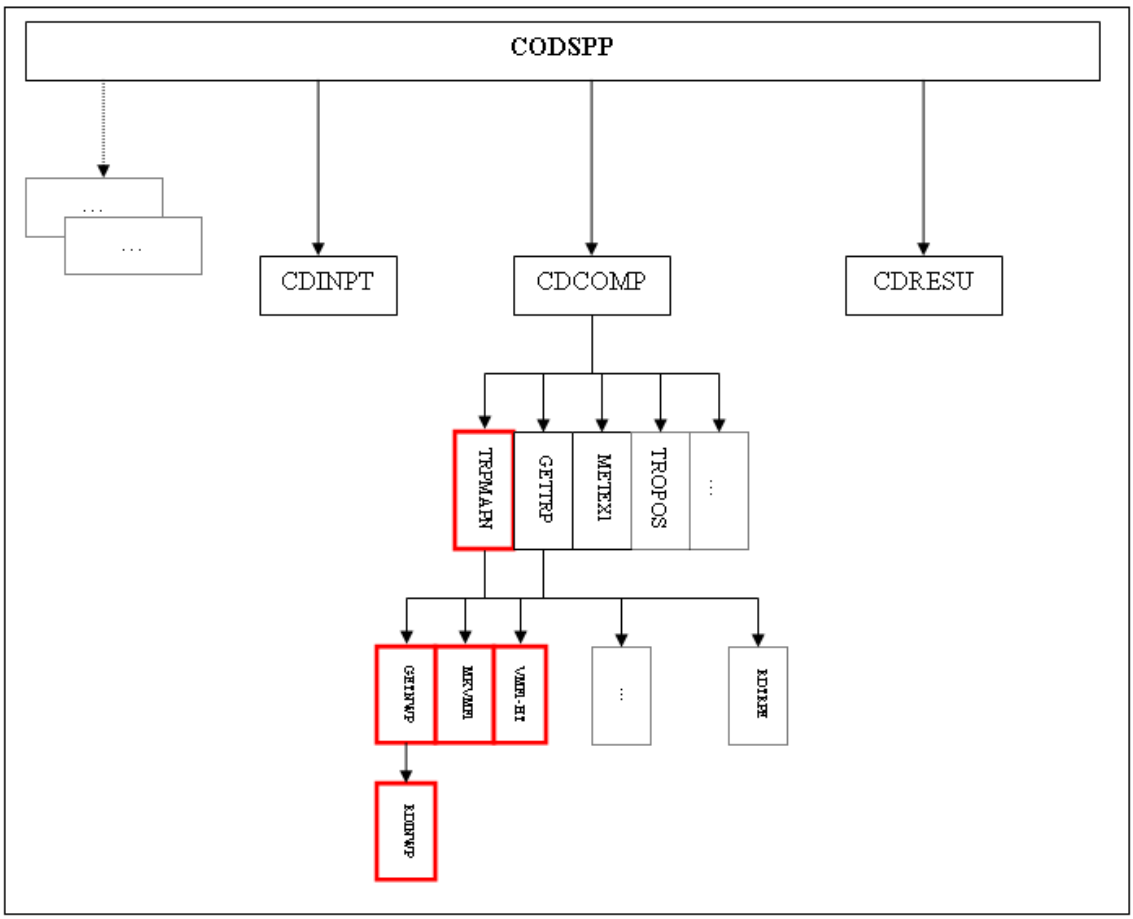

Figure IV.1– CODSPP: Synchronization of receiver clock with GPS time and determination of approximate coordinates using zero-difference observations.

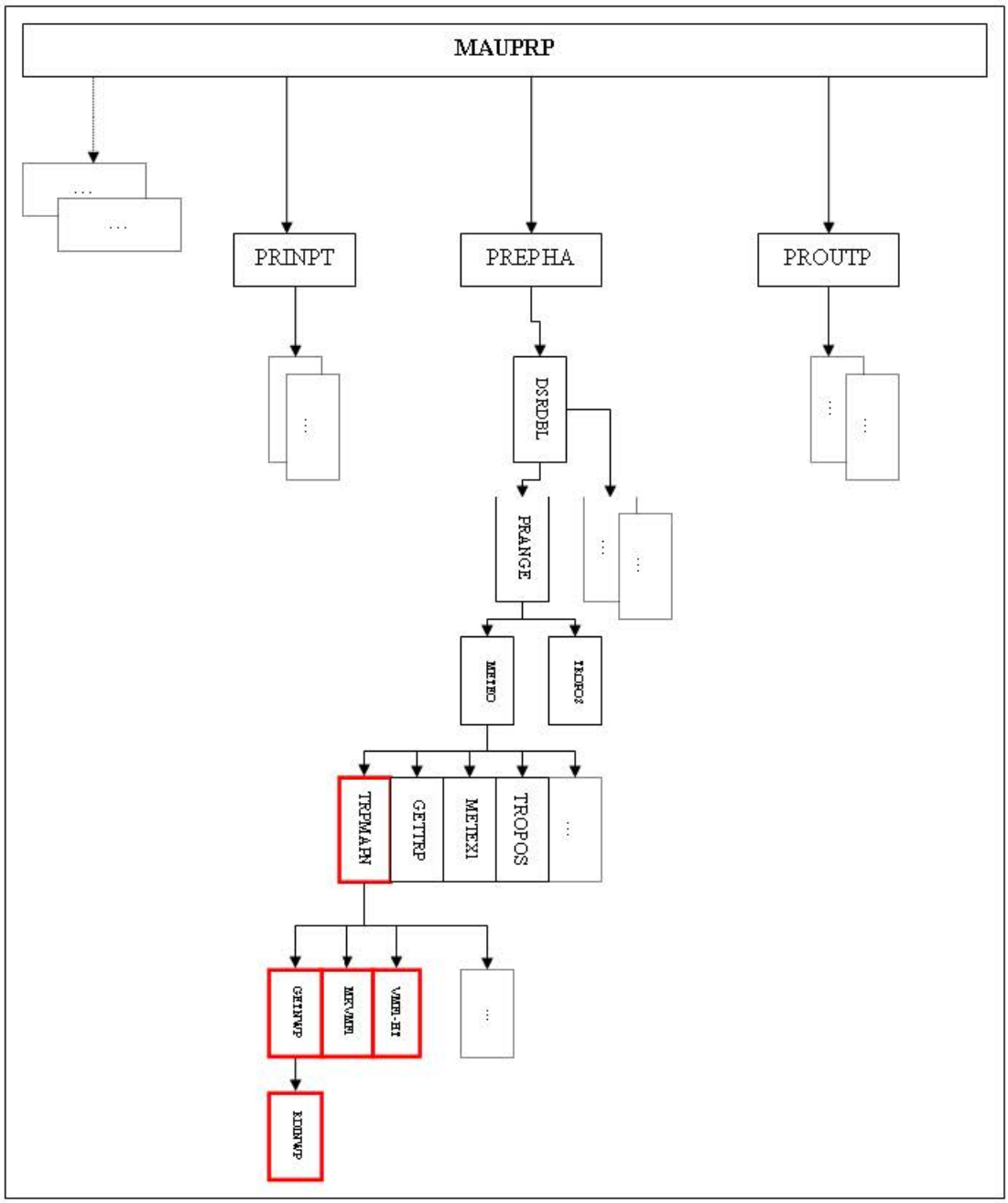

Figure IV.2– MAUPRP: Pre-processing of phase observations on the zero- and single-difference level for cycle slip detection and repair.

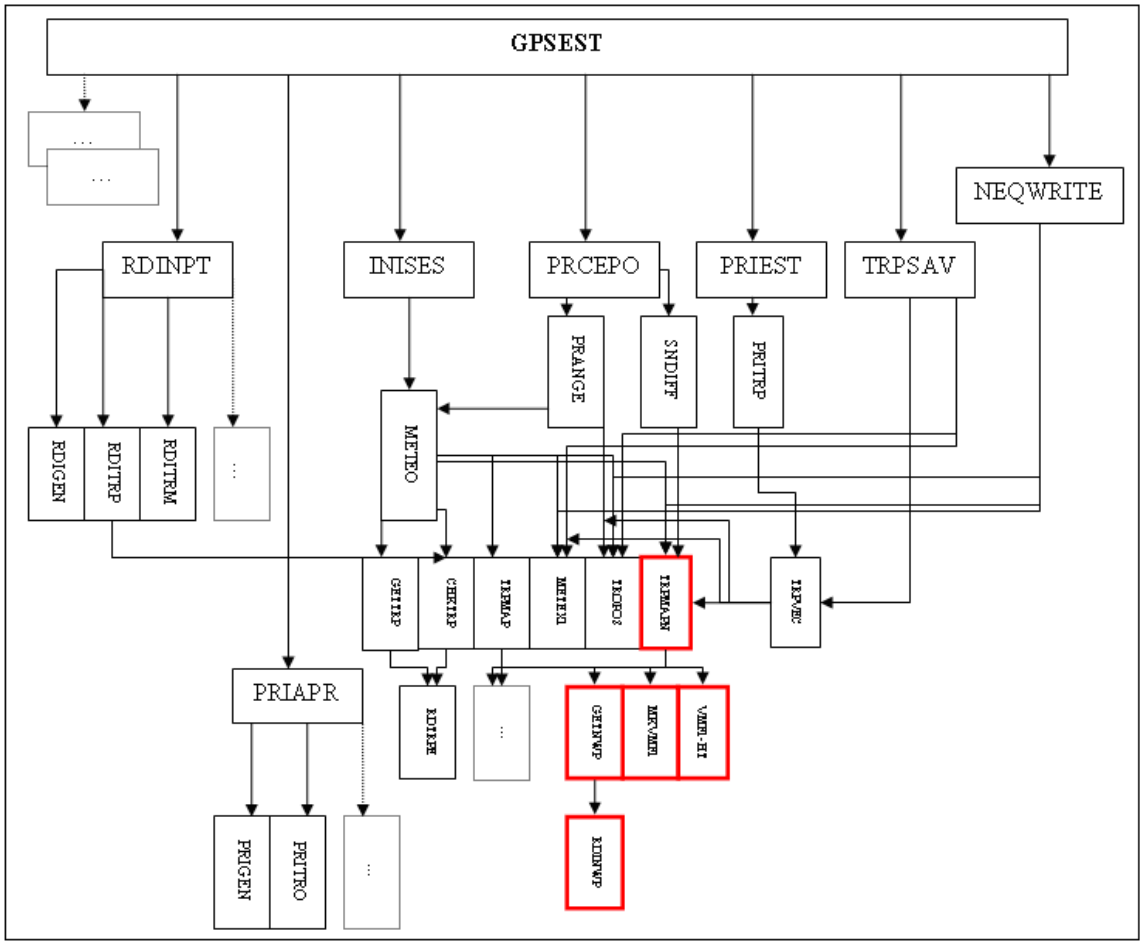

Figure IV.3– GPSEST: The main parameter estimation program.

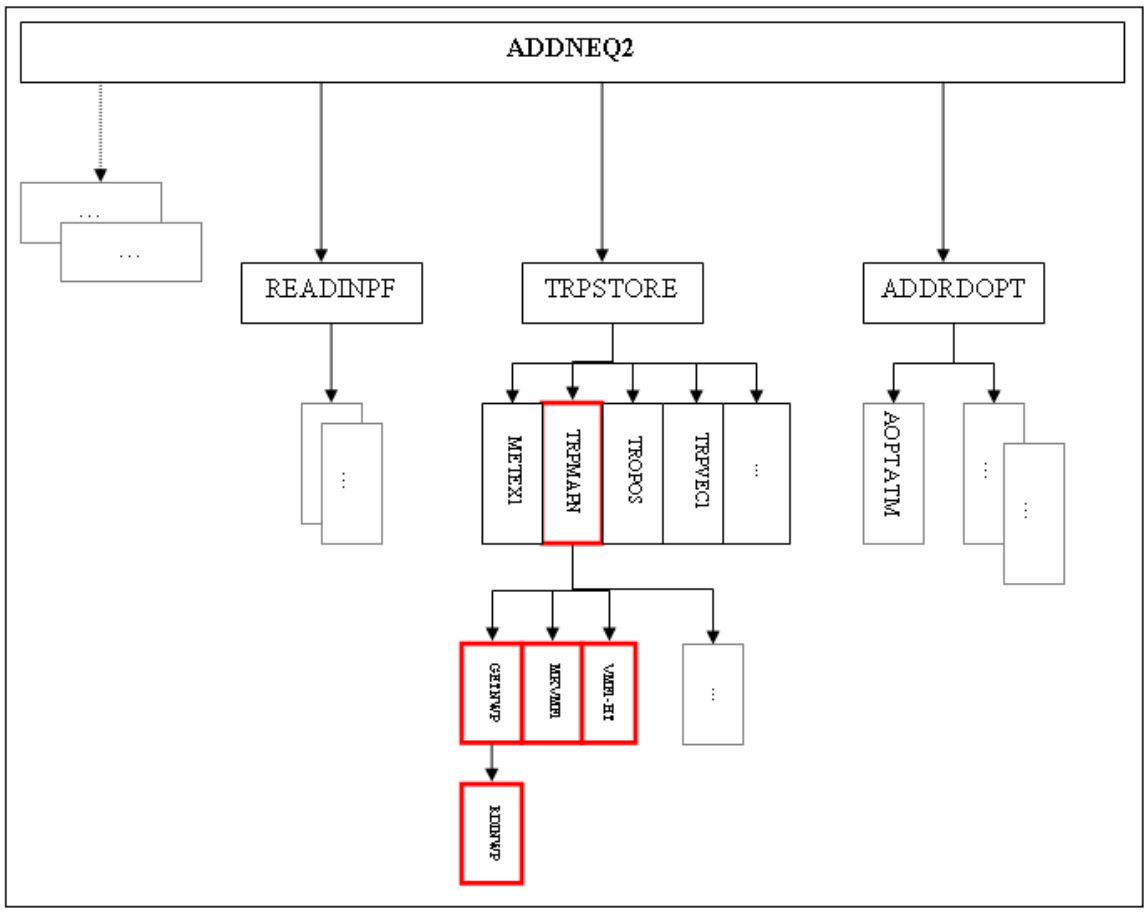

Figure IV.4– ADDNEQ2: Combination of results using normal equation files.

Appendix V: NWP Input File Format Defined for Modified Bernese

Type: ASCII

Directory: Campaign-specific directory ATM

Extension: NWP

Created by: Ray tracing software

Used by: The file may be introduced in CODSPP, MAUPRP, GPSEST and ADDNEQ2.

Example: Figure V.1

The NWP file should contain the following information:

1. Title line: Data source and date of run (any text is accepted)
2. Gradient code (1 means file includes gradients, 0 means no gradients) and step size (in units of day)
3. Data part:
    - Station name.
    - Modified Julian Date.
    - ZHD (m).
    - SHD (m).
    - ZWD (m).
    - SWD (m).
    - VEA (rad).
    - Hydrostatic EW gradient (m).
    - Hydrostatic NS gradient (m).
    - Non-hydrostatic EW gradient (m).
    - Non-hydrostatic NS gradient (m).

```
Global 1 deg NWP (GEM)--Ray tracing run at: 08-Jun-2008
1 0.1250
ALGO       54297.000  2.232243 32.441938  0.132108  2.181081  0.052956  0.000016 -0.000408  0.000066  0.000055
UNBJ       54297.000  2.283089 33.113076  0.219556  3.548012  0.052856  0.000408 -0.000546 -0.000465  0.000185
NRC1       54297.000  2.262958 32.856516  0.139808  2.293354  0.052950  0.000120 -0.000519  0.000080  0.000037
ALRT       54297.000  2.295735 33.371476  0.095577  1.563332  0.053088 -0.000286  0.000192  0.000314 -0.000229
ALGO       54297.125  2.235234 32.532246  0.120313  1.998074  0.052846 -0.000055 -0.000418  0.000109  0.000309
UNBJ       54297.125  2.283320 33.181013  0.233896  3.791371  0.052725  0.000445 -0.000597 -0.000659  0.000490
NRC1       54297.125  2.266685 32.964699  0.133376  2.198541  0.052838  0.000090 -0.000488  0.000219  0.000007
ALRT       54297.125  2.295021 33.357155  0.089495  1.465971  0.053086 -0.000309  0.000260  0.000384 -0.000263
ALGO       54297.250  2.237234 32.560345  0.113920  1.888219  0.052851 -0.000035 -0.000481 -0.000032  0.000487
UNBJ       54297.250  2.283368 33.234705  0.228488  3.715738  0.052613  0.000468 -0.000614  0.000735 -0.000653
NRC1       54297.250  2.269047 33.017061  0.123965  2.054584  0.052799  0.000073 -0.000551  0.000178  0.000118
ALRT       54297.250  2.294434 33.345589  0.086281  1.414403  0.053090 -0.000294  0.000292  0.000279 -0.000250
ALGO       54297.375  2.239656 32.582921  0.109501  1.816874  0.052885  0.000002 -0.000475  0.000113  0.000526
UNBJ       54297.375  2.284913 33.280238  0.199098  3.252210  0.052575  0.000405 -0.000618  0.001529 -0.001077
NRC1       54297.375  2.272229 33.066519  0.116809  1.940297  0.052792  0.000061 -0.000586  0.000085  0.000086
ALRT       54297.375  2.295775 33.365294  0.083121  1.361520  0.053085 -0.000301  0.000344  0.000245 -0.000217
ALGO       54297.500  2.241555 32.629696  0.111893  1.853939  0.052841 -0.000031 -0.000467 -0.000039  0.000314
UNBJ       54297.500  2.288581 33.345104  0.131125  2.175134  0.052551  0.000321 -0.000663 -0.000049 -0.000096
NRC1       54297.500  2.274586 33.123878  0.114781  1.909235  0.052736  0.000102 -0.000576  0.000076 -0.000067
ALRT       54297.500  2.297090 33.389660  0.081488  1.335906  0.053075 -0.000279  0.000356  0.000071 -0.000074
....
```

Figure V.1- An example of NWP input file to the modified Bernese.

Curriculum Vitae

Candidate's full name: Reza Ghoddousi-Fard

Universities attended: B.Sc.E. (Surveying), K.N.Toosi University of Technology, 1995

M.Sc.E. (Geodesy), K.N.Toosi University of Technology, 1999

Publications:

Ghoddousi-Fard R., P. Dare, and R.B. Langley (2008). "Tropospheric Delay Gradients from Numerical Weather Prediction Models: Effects on GPS Estimated Parameters." Submitted to *GPS Solutions*.

Ghoddousi-Fard R., P. Dare, and R.B. Langley (2008). "A Web-Based Package for Ray Tracing the Neutral atmosphere Radiometric Path Delay." *Computers and Geosciences*, In Press, DOI: 10.1016/j.cageo.2008.02.027.

Ghoddousi-Fard R. and P. Dare (2007). "A Climatic Based Asymmetric Mapping Function Using a Dual Radiosonde Raytracing Approach." Proceedings of ION GNSS 2007, 20th International Technical Meeting of the Satellite Division of The Institute of Navigation, Fort Worth, Texas, Sept. 25-28, 2007, pp. 2870-2879.

Ghoddousi-Fard R. and P. Dare (2006). "Online GPS Processing Services: An Initial Study." *GPS Solutions*, 10: 12-20, DOI: 10.1007/s10291-005-0147-5.

Ghoddousi-Fard R. (2006). "Comparison of IGS and Radiosonde Determination of ZTD in the Canadian Arctic." Proceedings of ION GNSS 2006, 19th International Technical Meeting of the Satellite Division of The Institute of Navigation, Fort Worth, Texas, Sept. 26-29, 2006, pp. 1936-1944. [Student Paper Competition Winner]

Ghoddousi-Fard R. and P. Dare (2006). "Comparing Various GNSS Neutral Atmospheric Delay Mitigation Strategies: A High Latitude Experiment." Proceedings of ION GNSS 2006, 19th International Technical Meeting of the Satellite Division of The Institute of Navigation, Fort Worth, Texas, Sept. 26-29, 2006, pp. 1945-1953.

Ghoddousi-Fard R. and P. Dare (2005). "The effectiveness of online GPS processing services." Proceedings of the 33rd CSCE annual conference, The Canadian Society for Civil Engineering, Toronto, Canada, June 2-4, 2005, pp. GC249-1-10.

Ghoddousi-Fard R. (2002). "Comparison of Terrestrial and GPS Observation Results in a Geodetic Control Network." Proceedings of the 2nd Symposium on Geodesy for Geotechnical and Structural Engineering, Berlin, Germany, May 21-24, 2002, pp. 515-521.

Ghoddousi-Fard R. (1996). "Solving of GPS Carrier Phase Ambiguity." Proceedings of the 4th Civil Engineering Student Conference, Iran University of Science & Technology, Tehran, Iran, October (In Persian).

Conference Presentations:

Ghoddousi-Fard R. and P. Dare (2005). "An Investigation on the performance of regional GEM zenith delay products in the Canadian Arctic." CMOS 2005, Canadian Meteorological and Oceanographic Society, Vancouver, Canada, May. [Abstract published]

Ghoddousi-Fard R. (1994). **"**Applications of GPS in Geomatics." 2nd Civil Engineering Student Conference, University of Tehran, Tehran, Iran, October. [Abstract published in Persian]